PONTIFICIA UNIVERSIDAD CATOLICA DE CHILE
ESCUELA DE INGENIERIA

COMPARATIVE BOND PULLOUT PERFORMANCE OF CFRP AND STEEL REINFORCING BARS IN CONCRETE AT ELEVATED TEMPERATURE

CRISTIÁN HERNÁN MALUK ZEDÁN

Thesis submitted to the Office of Research and Graduate Studies in partial fulfilment of the requirements for the Degree of Master of Science in Engineering.

Advisor:
DR. HERNÁN SANTA MARÍA OYANDEL

Santiago de Chile, (May, 2010)

PONTIFICIA UNIVERSIDAD CATOLICA DE CHILE
ESCUELA DE INGENIERIA

COMPARATIVE BOND PULLOUT PERFORMANCE OF CFRP AND STEEL REINFORCING BARS IN CONCRETE AT ELEVATED TEMPERATURE

CRISTIÁN HERNÁN MALUK ZEDÁN

Members of the Committee:

DR. HERNÁN SANTA MARÍA OYANEDEL

DR. RODRIGO JORDAN SAINTE-MARIE

DR. LUKE A. BISBY

DR. CARLOS VIDELA CIFUENTES

Thesis submitted to the Office of Research and Graduate Studies in partial fulfilment of the requirements for the Degree of Master of Science in Engineering.

Santiago de Chile, (May, 2010)

Para aquellos que nos cuidan desde arriba,
sin ellos nada de esto hubiese sido posible.

ABSTRACT

Novel structures are emerging utilizing high performance, self-consolidating, fibre-reinforced concrete (HPSCC) reinforced with high-strength, lightweight, and non-corroding prestressed reinforcement. One example of this is a new type of HPSCC precast panels, with pretensioned carbon fibre reinforced polymer (CFRP) tendons, intended as load-bearing panels for building envelopes. As for all load-bearing structural members in building applications, the performance of these members under fire conditions must be understood before they can be used with confidence. In particular, the bond performance of CFRP prestressing reinforcement at elevated temperatures is not well known, although available research on the bond between glass fibre reinforced polymer bars and concrete at elevated temperatures suggests that loss of bond may govern the response.

The study presented in this thesis examines the performance of these new types of structural elements at high temperature or during exposure to fire, placing particular emphasis on the bond performance of CFRP tendon compared to that of steel wire prestressing reinforcement at elevated temperatures. The results of bond pullout tests executed at high temperature on CFRP and steel prestressing bars embedded in HPSCC, the thermal and mechanical properties of CFRP, steel, and HPSCC, and large scale fire tests on CFRP prestressed HPSCC panels are presented and discussed to shed light on the fire performance of these structural elements.

A heat transfer model was developed with the objective of predicting the temperatures within a pullout sample subjected to bond-pullout executed at high temperature. A thermal incompatibility model was created to predict the longitudinal crack formation in large scale fire tests.

Result suggested that degradation of the bond strength of CFRP bars at high temperature is governed by the degradation of the epoxy matrix from which the CFRP bar is made from. From the pullout test results, a relationship was found between the temperatures of bond failure and the prestress load at which the sample were sustained.

Keywords: CFRP, HPSCC, advanced composites, bond strength, pullout test, fire endurance, high temperature, large scale fire test, image correlation analysis.

RESUMEN

La aparición de novedosos elementos estructurales han emergido utilizando hormigón de alto desempeño, auto-compactante y con fibras, HPSCC (por sus siglas en ingles) reforzados con barras de alta resistencia, livianas y con alta resistencia a la corrosión. Ejemplo de lo anterior son paneles prefabricados de HPSCC, pretensados con barras de polímero reforzado con fibras de carbono, CFRP (por sus siglas en ingles), usados como elementos estructurales perimetrales en edificios. Al igual que para otros elementos estructurales de un edificio, el comportamiento de estos novedosos elementos debe ser estudiado y analizado antes de que puedan ser usados con confianza. Particularmente, el efecto de las altas temperaturas en la adherencia de las barras de CFRP con el hormigón, fenómeno que aún no se conoce en detalle.

Este proyecto examina el desempeño de estos elementos, bajo condiciones de incendio, poniendo particular énfasis en el efecto de las altas temperaturas en la adherencia de las barras de CFRP con el HPSCC y realizando un análisis comparativo con barras de acero. Este trabajo presenta los resultados de ensayos de extracción en barras de CFRP y acero embebidas en cilindros de hormigón sometidos a altas temperaturas, ensayos de las propiedades mecánicas y térmicas de las barras de CFRP y acero, así como del hormigón. También se presentan los resultados de ensayos a escala real de a altas temperaturas.

Un modelo de transferencia de calor fue desarrollado con el objetivo de predecir las temperaturas en las probetas sometidas a los ensayos de extracción a altas temperaturas. También se desarrolló un modelo para predecir la aparición de grietas longitudinales observadas en los ensayos a escala real ejecutados.

En el proyecto se propuso que la degradación de la adherencia entre las barras de CFRP y el HPSCC, a altas temperaturas, está regida por la degradación de la resina epóxica, componente fundamental de las barras de CFRP. A partir de los resultados de los ensayos de extracción, se encontró una relación entre la temperatura a la cual se produce la falla de la adherencia y la tensión a la que es sometida la barra durante el ensayo.

Palabras Claves: CFRP, hormigón de alto desempeño, adherencia, ensayo de extracción, resistencia al fuego, altas temperaturas, ensayo de incendio a escala real, análisis de correlación de imágenes.

ACKNOWLEDGEMENTS

It is amusing to reflect on how life has taken us in directions we could previously never have imagined. For me, it was just three years ago that I was finishing a semester abroad at The University of Leeds. Just as my stay in the United Kingdom was coming to an end, I was offered the chance to do an internship at the BRE Centre for Fire Safety Engineering at The University of Edinburgh. It was here where I was first introduced to the discipline of Fire Engineering, which I complemented with my undergraduate studies in Structural Engineering at Pontificia Universidad Católica de Chile. I must thank Dr Pedro Reszka for giving me my first opportunity to visit Edinburgh, and for sharing with me his passion for Fire Engineering.

Back in Chile I began my master's studies under the supervision of Dr Hernán Santa María, whom I thank for his support and thoughtful comments. I then had the opportunity to visit Edinburgh for a second time, and work on the development of this thesis with Dr Luke Bisby, whom I thank for his guidance, kindness and patience. I am deeply grateful to Professor José Luis Torero for his support which made my stays in Edinburgh possible, and I thank Dr Giovanni Terrasi from EMPA, Switzerland and Dr Mark Green from Queen's University for their technical support.

I must thank the students, technicians, staff, and lecturers in the Structures Department at Pontificia Universidad Católica de Chile and in the Fire Group at The University of Edinburgh, for helping in one way or another with the outcome of this thesis.

I'd also like to thank my family and friends for their unconditional support in the last couple of years, and Nicolas Bal and Francesco Colella, flatmates and friends with whom I experienced life in Edinburgh.

LIST OF CONTENTS

LIST OF TABLES

LIST OF FIGURES

1 INTRODUCTION

1.1 Background

Current trends in construction are forcing the development of more durable and sustainable concrete structures. Careful selection, design, and optimization of both the concrete mixtures and the reinforcing materials used are now commonplace. From this, structural elements have emerged, incorporating optimized, high-performance, self-compacting, fibre-reinforced concrete (HPSCC) and novel reinforcing and prestressing materials such as carbon fibre reinforced polymer (CFRP) tendons, which are high-strength, creep resistant, lightweight, non-corroding, and magnetically invisible. One example of this is a new type of HPSCC precast panels, with pretensioned carbon fibre reinforced polymer (CFRP) tendons, intended as load-bearing panels for building envelopes (Terrasi, 2007). However, the performance of these HPSCC precast members under fire conditions is not well known and must be understood before they can be used with confidence.

The bond between both steel and CFRP reinforcing bars (prestressed and non-prestressed) and concrete deteriorates at elevated temperature (Morley & Royles, 1983; Katz, Berman & Bank, 1999). Indeed, for fibre reinforced polymer (FRP) reinforcement, bond strength reductions are thought to be a limiting factor for the fire-safety of FRP reinforced or prestressed concrete (Bisby, Green & Kodur, 2005), although the precise magnitude of bond strength reductions and their impacts on the load-bearing capacity of heated reinforced (or prestressed) concrete structures have not been studied and remain unknown. The tensile strength of steel and CFRP is also reduced by exposure to elevated temperatures; the reductions are well known for steel tendons (Eurocode 2, 2002) but remain largely unknown for CFRP tendons.

National design codes (ACI, 2004; CNR, 2006; fib, 2007; ISIS, 2006) which include sections on the design of FRP reinforced concrete structures, have as a fundamental hypothesis that perfect bond exists between FRP reinforcement and concrete. Nonetheless, special recommendations are suggested for the fire resistance analysis, which must be carried our taking into account the value of the glass transition temperature of the FRP's polymer matrix.

1.2 Objective

The primary objective of this study was to experimentally investigate the bond deterioration of CFRP tendons and steel prestressing wire at high temperature. Concentric pullout tests were executed at high temperature and used for comparison purposes, rather than for characterizing the bond phenomenon of reinforcement in concrete. Although the pullout tests were the main experiments performed for this research, various ancillary tests were also performed to determine the mechanical and thermal properties of the CFRP tendons, steel prestressing wire and HPSCC.

Analytical and numerical, mechanical and heat transfer models were developed using the experimental parameters to better comprehend the phenomena taking place as the pullout tests were executed at high temperature.

1.3 Methodology

An efficient and reliable force transfer between reinforcement and concrete is always assumed in reinforced concrete construction design. For commonly used deformed steel reinforcement, the transfer of forces from the concrete to the reinforcement or vice versa occurs by chemical adhesion, frictional forces and mechanical anchorage.

ACI (2003) recommended that pullout tests should not be performed with the objective of determining development length of reinforcement in concrete. In a common pullout test in which the bar is put in tension, the concrete is placed in compression. This stress state differs markedly from most reinforced concrete members, in which both the bar and the surrounding concrete are in tension.

In any case, in both pullout tests and in real concrete members, the concrete in direct contact with the reinforcement is under compressive force (ACI, 2003). For the concrete members, the surrounding concrete is subjected to a compressive force due to relative movement of the reinforcement with respect to the concrete.

Taking into account that ACI (2003) does not recommend the use of pullout tests for determining development length, pullout tests were carried out in the current project for comparative purposes in studying the relative performance of FRP tendons and deformed steel prestressing wires in concrete. Special effort was made to keep the same mechanical and thermal conditions between the pullout tests executed with steel and the ones with CFRP reinforcements.

Additional tests were performed to determine the mechanical and thermal properties of steel prestressing wire, CFRP tendons and HPSCC used during the pullout tests. Compressive and splitting tensile strength tests were carried out on HPSCC samples. Digital image correlation analysis was used to determine compressive strain and sample failure in compressive and splitting tensile strength tests, respectively.

Transient thermal tensile tests were performed on CFRP tendons at high temperature. These tests consisted in tensile stressing of the tendons to a typical service stress under ambient temperature and then increasing the tendons' temperature until failure occurred under constant sustained load.

Dynamic Mechanical Analysis (DMA) was performed on the CFRP tendons used in the pullout tests to determine the epoxy's elastic modulus deterioration as a function of temperature. This analysis was performed by measuring load and deformation during sinusoidal flexural loading of the sample in the elastic range of the CFRP tendon, as the temperature of the sample increased at a given rate.

The thermal conductivity of the concrete used in the pullout tests was determined by steady state tests executed on small concrete samples, and did not consider the moisture migration, decomposition of cement hydration products, and melting of the polypropylene fibres which occurred as the concrete's temperature increased. The data obtained from this test was complemented with past literature's tests executed for similar concrete mixtures, and values obtained were used as input for the heat transfer model.

As a complementary research project (performed by others), seven large scale fire tests were performed on CFRP prestressed HPSCC slabs in a floor furnace at the Swiss Federal Laboratories for Materials Testing and Research (EMPA), with an ISO 834 (ISO, 1999) heating curve. Six of the HPSCC slabs were prestressed with CFRP tendons and one with steel prestressing wire (identical to the reinforcing materials used in the pullout tests).

1.4 Scope of the Research

A total of eighteen pullout tests were executed for this study, nine with steel reinforcement and nine with CFRP reinforcement. The pullout test setup was designed to prevent, as much as possible, the influence of forces arising from the pullout's border conditions from stresses at the reinforcement-concrete interface. The way in which the pullout tests were executed resulted in the determination of the temperatures for which bond failed, since bond stress was maintained constant at a certain level during heating (load-then-heat testing).

A novel digital image correlation analysis technique was used to measure slip during the pullout tests, compressive strain and elastic modulus in compressive strength tests on HPSCC, and crack openings in splitting tensile strength tests on HPSCC. This measuring technique was used in this study with the objective of presenting a new area of application of this innovative measurement technology, which has not been considered in past studies.

The results from the pullout tests executed with CFRP reinforcement were used to develop a correlation between the sustained bond stress and the residual elastic modulus of the CFRP's epoxy. The residual elastic modulus was determined by the DMA done on the CFRP tendons.

A finite element analysis was performed, using experimentally determined input parameters as well as those available from past studies, to develop a heat transfer model of the pullout experiment and determine the profile of temperatures in both the concrete and the reinforcement.

An adaptation of an analytical model was developed to determine the effects of CFRP tendons' transverse thermal expansion effect on the concrete cover in the large scale fire tests, in which longitudinal splitting cracks were observed in the tested slabs' surface.

2 LITERATURE REVIEW

2.1 Advanced Fibre Reinforced Polymer Composites

Advanced composites have become a promising alternative construction material with significant advantages in non-corrosiveness, high strength-to-weight ratios and high stiffness-to-weight ratios. Firstly used in military, aerospace and automotive applications, the development of new manufacturing techniques known as pultrusion, filament winding and layup (Lubin, 1998), allowed advanced composites to find their way into civil engineering in the form of fibre reinforced polymers (FRPs).

FRPs' use in various forms in construction has been developing for more than 40 years with the potential of replacing reinforcing steel in areas where corrosion, weight or the magnetic properties of steel pose problems. FRPs are currently used as externally bonded FRP sheets and plates to increase shear, flexural and/or confinement strength of deficient concrete members. Near surface mounted (NSM) FRP is another application in which FRP strips are used to improve the flexural or shear capacity of concrete members by being inserted into slots cut in the concrete cover. Another very promising and now reasonably widely implemented application of FRPs is their use for the partial or total replacement of steel with FRP bars for reinforced or prestressed concrete members.

2.2 FRP Bars

2.2.1 Overview

FRP bars have become widely used, for more than 15 years, as a potential replacement for steel reinforcement in concrete. This seems, on first glance, to be a good idea to replace steel with a lighter and non-corrosive material, but FRPs' behaviour as a concrete reinforcement must be fully understood before they can be used with the confidence with which we use steel.

One of the biggest concerns with the use of FRP bars as concrete reinforcement is the fact that no plasticity of their stress-strain response occurs before failure, even though FRP bars have a high strength and relatively high strain capacity (Burgoyne, 2001). It should also be considered that different manufacturing processes could mean that stiffness and strength might significantly vary amongst different FRP products.

2.2.2 Composition

FRP bars are mainly made of fibre reinforcement and a polymer resin matrix. The most common types of fibres used in advanced composites are glass, carbon and aramid (commercially known as Kevlar) fibres, which generally occupy 30%-70% of the overall volume of the bar. The longitudinal tensile strength and stiffness of FRP bars is highly dependent in the type of fibre and fibre volume fraction. The manufacturing process may also affect the mechanical characteristics of the bar.

Glass fibres, being non conductive, have the advantage of insulating properties to prevent galvanic corrosion of metals in structures, although they have shown to be sensitive to moisture attacks, leading to creep-rupture, under certain conditions of exposure and under certain threshold stress levels (Reinhart, 1998).

Glass fibre reinforced polymers (GFRPs) commonly have a larger nominal mass with the disadvantage that glass fibres have comparatively low creep resistance. Aramid fibre reinforced polymers (AFRPs) usually exhibit a higher tensile strength and stiffness than GFRPs, with excellent creep resistance. Carbon fibre reinforced polymers (CFRPs) have the higher tensile strength and stiffness than all other commonly used FRP bars. Carbon fibres behave very well against creep deformation and relaxation (Seica & Packer, 2007).

The polymer resin matrix is the adhesive binder which transfers the loads within and between the fibres. The most common resins used in advanced composites are unsaturated polyester, epoxy and vinyl ester.

2.2.3 Properties

The tensile strength determination of FRP bars is complicated because stress concentrations generally occur in and around the anchorage points and adequate testing grips must be designed to allow failure to occur in the middle of the test specimen, away from the grips.

Fibre reinforced polymer bars are made from aligned fibres which work together by the adhesion and force transfer provided by the polymer resin matrix. FRP bars have an anisotropic mechanical behaviour, with the transverse properties noticeably inferior to those in the axial direction. In the longitudinal direction, FRP bars have a high tensile strength (3500 MPa for some commercial FRP bars) and high stiffness with a linear elastic response up to failure, with little or no ductility, as opposed to steel reinforcing bars which show a considerable reduction in stiffness (plasticity) at high loads.

There has been a considerable amount of work trying to make the surface geometry of the FRP bars look like reinforcing steel, by either ribbing or sand coating the FRP surface. However, no standardized classification of FRP surface deformation patterns is currently available.

FRP bars exhibit different coefficients of thermal expansion (CTE) in the longitudinal and transversal direction. In the longitudinal direction they have lower (even negative) CTEs than concrete and may be eight times higher than concrete’s CTE. In the FRP’s transverse direction, the CTE is governed mostly by the polymer resin matrix (ACI, 2004) and is typically much larger that the CTE of concrete.

2.2.4 Ductility concerns

The same concern arises most times that FRP is proposed as a replacement of steel reinforcement in reinforced concrete; FRP is linear-elastic to failure and is therefore an inherent brittle material. Steel reinforced structures have the ability to deform before failure due to the plastic response of steel reinforcing bars, and at the same time to absorb energy. These characteristics give conventional steel reinforced concrete structures the capability to deform, dissipate energy and provide ample warning of failure; a very attractive capability for any structure, and loosely defined as ductility.

The energy dissipated by a steel-reinforced concrete structure is associated with two main characteristics of the structure, the cracking of the concrete upon loading and the yielding of the steel reinforcement upon further loading (Burgoyne, 2001).

As concluded by Burgoyne (2001), understanding the way the FRP and concrete act together gives the chance to design structures that have the required deformability characteristics, with the attractive properties of FRP as previously discussed.

2.2.5 Economic considerations

Several reputable FRP bar manufacturers have emerged in the last decade or so, producing FRP bars to be used as concrete reinforcement. For FRP bars to be economically viable structural applications, particularly for the comparatively expensive carbon FRPs, they should be used in prestressing applications and not as plain non-prestressed concrete reinforcement, in which cases the FRPs' high strength capacity is not fully exploited.

2.3 Fire Endurance

2.3.1 Philosophy

Fire safety engineering is a multi-disciplinary discipline used to determine the fire safety strategy for a building under fire conditions. Being an extremely complex and rapidly evolving discipline, fire safety engineering considers various factors, from material degradation at high temperatures, to structural integrity, to sprinkler systems. Such a fire strategy is concerned with the protection of life and property from fire, typically with a much larger focus on life safety considerations. Past experience has proved that high temperatures experienced during fire in a building can cause safety or ultimate limit states to be exceeded.

In fires, structural stability and control of fire spread are achieved by providing active and/or passive fire protection (Drysdale, 1998; Buchanan, 2001). In the early stages of a fire, active protection (such as automatic fire sprinklers) provides the necessary means for the fire to be extinguished, before rapid growth of the fire occurs. Even though passive protection will help in the early stages of a fire by minimizing the fire spread, maintaining structural integrity during fire will ensure that there is sufficient means of escape for buildings occupants and for fighting the fire in the later stages of the fire.

Passive fire protection is even more important in those cases in which occupants are unable to escape by their own means (e.g. prisons, hospitals, etc.), or cases in which prolonged fire fighter access to the structure is required. Structural fire engineering deals with specific aspects of passive fire protection, analysing the thermal effects of fires on the building structure.

For traditional reinforced concrete structures, behaviour in fire has been extensively studied and is relatively well understood. Reinforcement property deterioration due to increases of temperature are often the critical factor for reinforced concrete structures, often accompanied by other phenomenon such as concrete cover spalling, concrete degradation, and stresses produced by high thermal gradients (Buchanan, 2001).

Fire endurance requirements for concrete structures are specified in building codes as the ACI (1989), Eurocode 2 (2002) and OGUC (2001). Codes generally present tabulated data in which prescribed times to 'failure' are chosen based on the buildings size, occupancy, fire load density, and these can be a function of member type and dimensions, applied load and fire intensity in the more advanced fire safety codes.

Fiber renforced polymer reinforcing bars are relatively new construction materials which have become increasingly widely used in the last two decades. Structural engineers have become so used to the way steel reinforced concrete is designed that they take for granted the reasons why concrete structures behave the way they do. This is even more harmful in fire design, were prescriptive codes present tabulated data (e.g. member's dimension and concrete cover) which seem to very easy to use but is rarely philosophically or scientifically understood by designers.

2.3.2 Procedures to evaluate fire endurance

In the past, the fire endurance of a particular structural assembly was determined entirely through testing (Lie, 1992). Powerful computers have more recently allowed the development of complex and detailed numerical procedures that can, when suitably validated against the results of carefully conducted tests, accurately predict the behaviour of structural members during a fire. These numerical procedures use detailed information about the thermal and mechanical properties of the members' constituent materials, and have the potential to substantially reduce both the time and expense of fire endurance evaluation.

Simpler, inexpensive test methods to evaluate the fire performance of concrete's compressive and tensile strength, and the reinforcement's tensile and bond strength have been used to determine the thermal and mechanical properties of the members' constituent materials.

2.3.2.1 Steel-reinforced concrete members

Fire endurance tests on a wide range of reinforced concrete members and assemblies have been performed over the last thirty years (Buchanan, 2001). These tests, invariably conducted in standard furnace testing facilities with members subjected to a 'standard' fire, (e.g. E119 (ASTM, 2001) or ISO 834 (ISO, 1999)), have examined a variety of factors and have led to the development of largely prescriptive structural fire design codes for reinforced concrete members. In recent years, the primary purpose in conducting full-scale fire endurance tests has been to validate numerical models, such that parametric studies can subsequently be performed with little additional cost (Khoury, 2000).

2.3.2.2 FRP-reinforced concrete members

Full-scale fire endurance tests on FRP-reinforced concrete members have not been extensively conducted as is the case for steel-reinforced concrete. Fire endurance tests on concrete slabs and beams reinforced with FRP have been previously conducted by Fujisaki et al. (1993), Okamoto et al. (1993), Nakagawa et al. (1993), Tanano et al. (1995), Sakashita (1997), NEFCOM Corporation (1998), Kodur and Baingo (1998), and more recently by Abbasi and Hogg (2006). These studies focused on determining the structural behaviour of the members during fire exposure and under service loads, or on determining the residual strength of members after exposure to fire. Concrete members, with a length of around 3000 mm, were exposed to standard and modified fire curves on one side of the member, for different periods of time.

Carbon, glass, aramid, and carbon/glass hybrid FRP bars were tested in the past studies mentioned above, with unsaturated polyester, epoxy, and vinyl ester matrices. The FRP reinforcements were placed in grids, longitudinal and transversal positions in either regular or prestressed conditions. Deflections, cross-sectional temperatures, and reinforcement temperatures were monitored during these tests.

Different failure modes where observed by the researches of the studies above, but typically involved dramatic increase of deflection, concrete failure in the zone under compressive stress, concrete failure in the zone under tensile stress, and explosive failure of the concrete cover. Reinforcements were heated up to maximum temperatures of 600°C or more, presenting different degradation rates for each type of FRP tested.

When considering the structural performance of FRP reinforced concrete slabs during fire, as compared with steel-reinforced slabs, the situation is significantly complicated by the following factors (Bisby & Kodur, 2007):

1. The deterioration of mechanical properties of FRP reinforcing bars with temperature is not well-known in comparison with steel reinforcement, and may vary significantly depending on the FRPs' fibre type, matrix type, and the presence of any matrix fillers used in the manufacture of the bars.
2. Design of concrete slabs reinforced with FRP reinforcing bars differs from design of concrete slabs with steel reinforcing bars in several key aspects, particularly the assumed failure modes and serviceability criteria. As a result, critical temperatures for FRP bars should thus not necessarily be defined on the same basis as steel reinforcing bars.
3. The deterioration of bond properties for FRP reinforcing bars, which has been shown to be much more severe than the bond deterioration of conventional steel reinforcement at elevated temperatures (Katz et al., 1999), is not well-known and may vary depending on the manufacturing process which the surface is subject to (sand-coated, deformations, smooth).

2.3.3 Bond performance of FRP-reinforced concrete in fire

At both ambient temperature and under fire conditions, the bond of steel reinforcing bars to concrete has not been fully investigated and is not well understood; the scenario is even worse when discussing FRP bars' bond phenomenon at elevated temperature because of the way bond is accomplish by commercially available FRP reinforcing bars (i.e. sand coatings and spiral ribs). In any case, the bond between concrete and steel is considered to be perfect by most structural design codes, even if this is clearly not the case in real structures under fire conditions (Katz & Berman, 2000).

Most of the time, experimental procedures to determinate the capacity of concrete members examine the global behaviour of the concrete member and not much attention is given to how the bond between the reinforcing bar and concrete behaves. A much worse scenario is observed for concrete members under fire conditions, where material deterioration and thermal expansion of both concrete and reinforcing bar occurs at high temperatures, potentially negatively impacting the essential force transfer between the reinforcement and the concrete.

Strain gauges placed at the concrete-reinforcing bar interface and slip measurement at the end of the concrete member have been used in the past to analyse the behaviour of bond between concrete and internal reinforcing bars, this being time-consuming and costly. Pullout tests present an economical and simple solution for the comparative evaluation of bond performance of different types of reinforcing bars and concrete, even though ACI (2003) concluded that the stress conditions encountered in reinforced concrete members differ greatly from those produced in pullout tests.

Pullout testing has been executed in previous research with the objective of determining the bond performance of steel and FRP reinforcing bars under or after high temperatures (Bingöl & Gül, 2009; Abbasi & Hogg, 2005; Katz et al, 1999).

Bingöl and Gül (2009) concluded that, after exposed to high temperatures, bond strength between concrete and ribbed steel bars decreased. This study determined that water cooling the pullout samples, after exposure to fire caused thermal shock due to rapid cooling and sudden temperature differences, and hence caused more severe damage to the concrete residual properties.

Abbasi and Hogg (2005) studied the influence of high temperature with and without long-term exposure of alkaline environments on the durability of GFRP reinforcing bars. They concluded that degradation in bond strength with an increase in temperature obeys a similar relationship irrespective of the prior conditioning of the samples, and the nature of the polymer resin matrix determines the magnitude and rate of degradation of the GFRP reinforcing bar.

Katz et al. (1999) tested different type of FRP reinforcing bar in pullout under similar conditions as the ones in the present study (load-then-heat testing). They concluded that severe reduction in the bond strength as the temperature was raised to 180-200°C.

Considering what others have done in the past to analyze the effects of high temperature in the bond strength between steel and CFRP reinforcing bars, an experimental program was developed to pursue this project’s objectives.

3 EXPERIMENTAL PROCEDURES

3.1 Material Properties

3.1.1 Concrete

The high quality and cost of CFRP tendons require a correspondingly high quality of concrete mixture. A high performance self-consolidating concrete (HPSCC) mixture was design to achieve a 70 MPa compressive strength in cylinders at an age of 28 days.

The self-compacting characteristic of the concrete helps ensure adequate compaction through self-consolidation and facilitate placement of concrete in structures with congested reinforcement and in restricted areas.

3.1.1.1 Mixture

Based on the concrete mixture used in the EMPA study, a high performance concrete mixture was elaborated by using Portland cement, silica fume, fly ash, short polypropylene fibres and superplasticiser as admixtures. Alluvial aggregates were used as filling element.

Figure 3.1: Fresh concrete before casting

3.1.1.1.1 Silica fume

Silica fume, also known as microslica, is a byproduct in the production, on electric furnaces, of silicon and ferrosilicon alloys. For this work, the silica fume constitutes 8% (by weight) of all the cementitious materials (Portland cement, silica fume and fly ash).

The reaction of silica fume in concrete is both chemical and physical. The average silica fume particle is 0.5 micron diameter (Sinclair & Groves, 1986), 100 times smaller than an average cement grain. The ultrafine silica fume particles fill the gaps between the cement grains, providing a finer pore structure. Because of the high surface area of silica fume, water segregation (bleeding) of the concrete is dramatically reduced.

Chemically, silica fume has a very strong pozzolanic reaction to the calcium hydroxide generated by concrete grains throughout the hydration process (Kuennen, 1996). This reaction within concrete results in an increase of strength, increase of elastic modulus and a decrease of ductility of hardened concrete. Also there is an improvement of the resistance to intrusion from a number of factors because more space is filled up.

Past research, which studied the effects of silica fume on the thermal properties of hardened concrete (Xu & Chung, 2000), concluded that the addition of silica fume increases the specific heat and a decreases the thermal conductivity of the hardened concrete. Also, past studies have shown that bond strength between cement paste and various types of reinforcing bars is enhanced by the addition of silica fume (Malhotra & Mehta, 1996).

3.1.1.1.2 Fly ash

Fly ash is a residue from the combustion of ground or powdered coal. In this research, the fly ash constitutes 20% (by weight) of all the cementitious materials.

Practical experience from previous work reported the following observations of the effects of fly ash on fresh concrete (Wesche, 1991):

- Reduction of the water demand of the concrete.
- Improvement of the concrete pumping properties.

- Improvement of workability, compactability, flowability and plasticity of concrete are generally improved.
- The work required for casting and compacting of concrete is reduced, resulting in less risk of surface shrink holes.
- Agglomeration capacity is improved and de-mixing problem is consequently alleviated.
- Reduction of bleeding.

As for the effects of fly ash on hardened concrete, a slower more gradual strength development with potentially higher long-term strength is observed (Lamond, 1983).

3.1.1.1.3 Polypropylene fibres

In this research, Vulkan Harex Polycon HPC 20 fibres were used (see Figure 3.2), which are 20 mm long polypropylene (PP) fibres, with a melting point of 160-170°C and excellent chemical resilience. The addition of PP fibres is of 2kg per m^3 of concrete.

Figure 3.2: Vulkan Harex Polycon HPC 20 fibres

The PP fibres inclusion in the concrete avoid shrinkage cracks (Senthilkumar & Natesan, 2004) and increase the concrete's fire resistance. The increase of concrete's fire resistance is achieved by the ability of the PP fibres to reduce pore pressures of concrete at high temperatures, which arise from the generation of voids and channels for moisture-vapour migration and expanding steam, once the PP fibres vaporise (Khoury, 2008).

3.1.1.1.4 Additive

In order to get the high strength concrete, the water cement ratio was kept at 0.39, and the self compacting properties were achieved by adding 8.5 kg per m^3 of concrete of superplastifier Sika® Viscocrete® Premier.

3.1.1.2 Slump flow test

The attributes of self-consolidating concrete are its filling ability, passing ability and stability. Slump Flow Test C1611 (ASTM, 2009) was designed to measure such attributes. This test is similar to the standard slump test, but with the Abram's cone placed in the inverted orientation (small opening down), and filled in one pouring (no rodding or other consolidation action). The cone is then raised in 3 ± 1 seconds allowing the fluid concrete to flow onto the slump flow board.

Figure 3.3: Performing the Slump Flow Test C1611 (ASTM, 2009)

From the slump flow test, three standardized parameters can be measured: the slump flow, the T_{500} and the visual stability index. All this parameters resulted congruent with the values obtained for concrete in the EMPA study.

3.1.1.2.1 Slump flow

The slump flow is the diameter of the resulting fresh concrete after the cone has been raised up and the concrete stops flowing. The diameter is measured as the average between the greatest diameter and the diameter perpendicular to this direction.

3.1.1.2.2 T_{500}

This is the time it takes for the slump flow to reach 500 mm in diameter, which is relative to the plastic viscosity of the concrete.

3.1.1.2.3 Visual Stability Index (VSI)

The VSI is based on the visual inspection of the slump flow by ranking the concrete on of 0-3, with 0 indicating highly stable self-consolidating concrete and 3 indicating unacceptable self-consolidating concrete.

Figure 3.4: Slump Flow Test visual inspection C1611 (ASTM, 2009)

3.1.2 CFRP tendons

For this research, round pultruded sand-coated CFRP tendons where used. The carbon fibres, aligned longitudinally, are type Tenax UTS with a volume fraction of 62% and the polymer resin matrix is an epoxy type Bakelite 4434. The tendons are made by a pultrusion process (see Figure 3.5), in which the same epoxy was used for the sand coating (silica particles), as shown in Figure 3.6. The tendons nominal tensile strength is 2000 MPa with the elastic modulus being 150 GPa. The tensile stress-strain relation is linear at all stress levels up to the point of failure, without exhibiting any yielding of the material, as shown in Figure 3.8. The ultimate strain is 1.33%. These CFRP tendons have a nominal mass of $123.0\ [g/m]$, 56% of the steel prestressing wire used this same study.

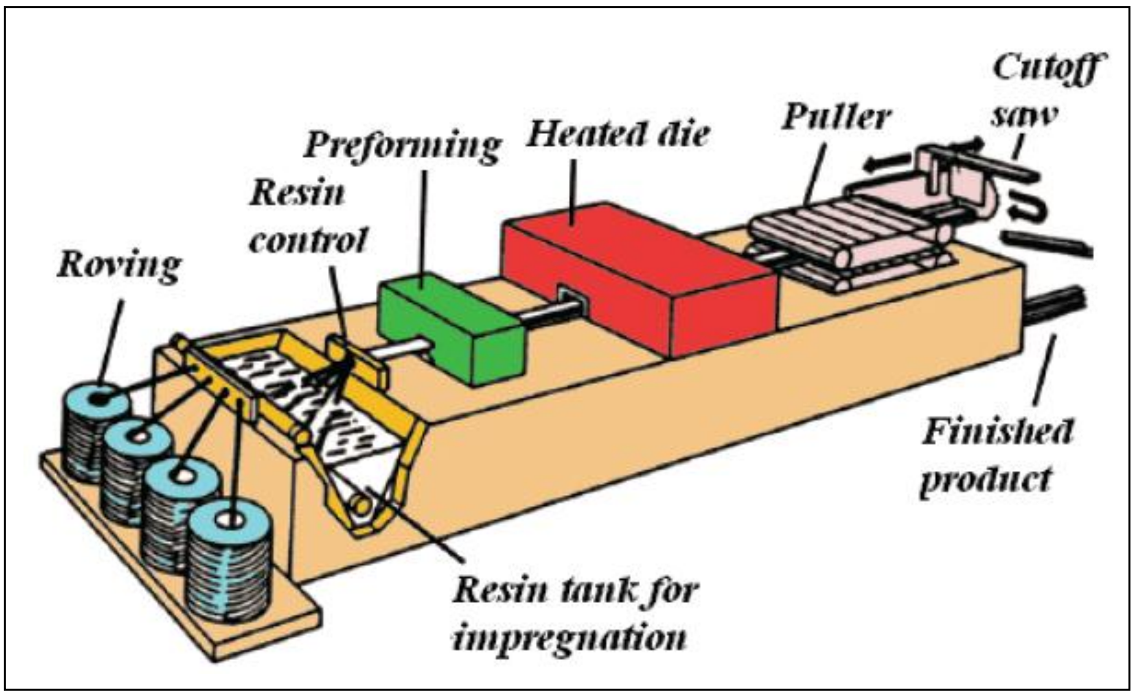

Figure 3.5: Pultrusion process with resin bath impregnation (CNR, 2004)

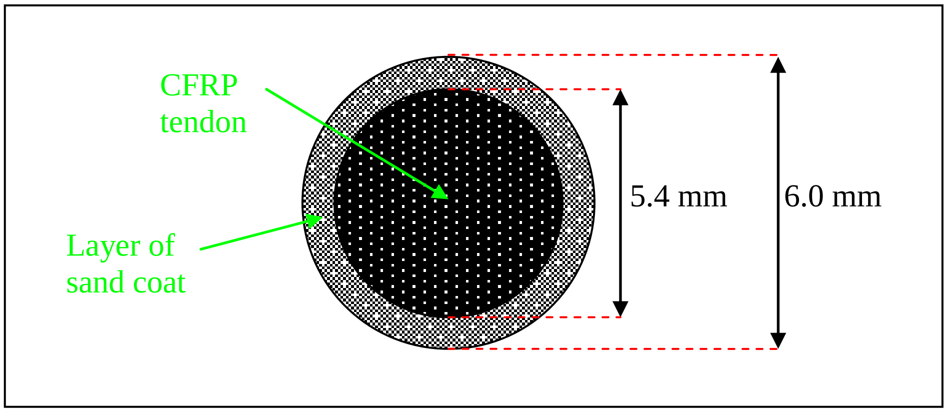

Figure 3.6: CFRP cross sectional area

3.1.2.1 Anchorage

CFRP bars cannot be clamp by the common anchorage systems based on radial compression (wedge action V-notch), like the ones used in steel bars. The carbon fibres crash against each other when a CFRP tendon is compressed in the radial direction. The anchorage system (conical collet and wedges) used to prestress CFRP tendons was optimized (see Figure 3.7) by a previous work performed by Terrasi, Affolter, Barbezat and Bättig (2008). This new anchorage system resulted in a 50% increase in the pretensioning level at on-site applications. The maximum on-site prestress level is now 1200 MPa, still 60% of the design tensile strength of this CFRP tendon, 2000 MPa.

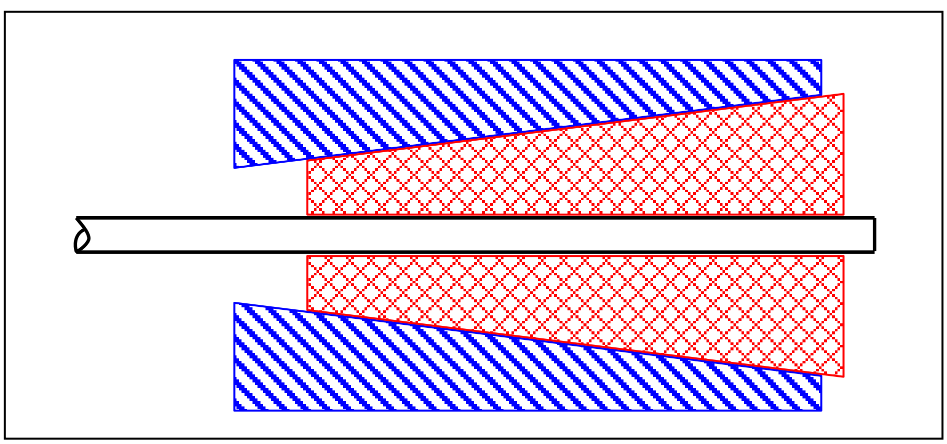

Figure 3.7: Longitudinal cross section of the CFRP anchorage system

3.1.3 Steel prestressing wire

Steel wires, specially produced for prestress applications were also used in this research. The steel prestressing wire was fabricated by NEDRI Spanstaal BV. The steel prestressing wires have a 6 mm nominal diameter and nominal mass of 221 $[g/m]$. The design yield strength is 1592 MPa (0.2% offset) and the ultimate strength is 1770 MPa, with an elastic modulus of 210 GPa. The steel prestressing wire presents a yield strain of 0.76% and an ultimate strain of 5.4%.

In Figure 3.8, a comparison was made between the CFRP tendon and the steel prestressing wire stress-strain curve. A common steel (A63-42H), largely used in reinforced concrete applications in Chile, is also shown, as to take notice of the high strength advantages of both reinforcing bars tested in this study (three times the yield strength of A63-42H).

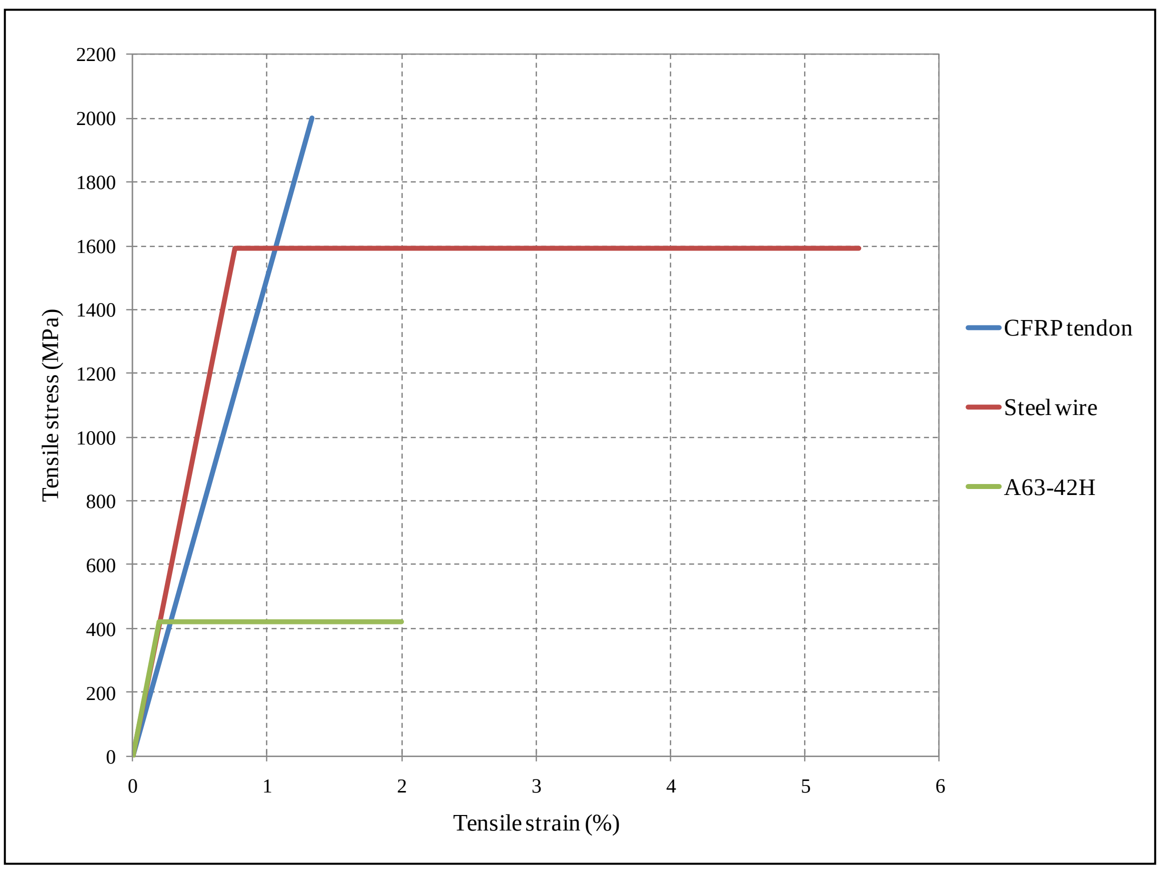

Figure 3.8: Design stress-strain behaviour of CFRP tendon, steel prestressing wire and common steel reinforcement (A63-42H)

3.2 Test Specimens

3.2.1 Pullout test

The pullout samples were designed and casted as concrete cylinders with a diameter of 101.6 mm (4 inches) and a length of 250 mm. The mould was designed in such way that both CFRP tendon and steel prestressing wire were placed vertically and axisymmetrically with the concrete cylinder.

3.2.1.1 Bonded length determination

For the pullout samples the bar was not bonded all along the 250 mm concrete cylinder length. Three requirements defined the length in which the bar was bonded to the concrete:

- Allow to develop the development length, determined by prestress transfer tests performed in the EMPA study.
- Prevent localized failure due to compressive load on the concrete prior to being transferred to the CFRP tendon or steel prestressing wire.
- Prevent that the effect of thermal convection on both ends of the cylinder affected the bonded length.

The prestress transfer tests were performed by EMPA to experimentally asses the prestress development length of CFRP tendons, same as the ones used for this research. In those tests, two prestress HPSCC-plates were produced with a width of 200 mm, a length of 3360 mm and a thickness of 45 mm for test N°1 and 60 mm for test N°2. The plates had no transversal reinforcement. Each of the plates was pretensioned by four CFRP tendons with a horizontal distance of 25 mm from the horizontal edge and 50 mm horizontal distance intra tendons. The prestress level of the experiments was 1200 MPa.

The tests consisted in measuring the surface strains of the two plates immediately after prestress release. The strains at the concrete´s surface were measured by placing strain gauges (type HBM 20 mm / 120Ω) on the concrete surface right above one of the two tendons set in the middle. The distance of the strain gauges from the plate’s end is shown in Table 3.1.

Table 3.1: Distance of the strain gauges from the plate's end

Distance from plate's end (mm)	
Test 1	**Test 2**
20	20
50	50
100	85
150	120
200	160
400	200
	400

The compressive strains increases up to a certain distance from the plates end, and remains constant after that (see Figure 3.9). The distance from which the strain remains constant was labelled l_p. For test N°1, $l_p = 150\ mm$ and for test N°2, $l_p = 160\ mm$.

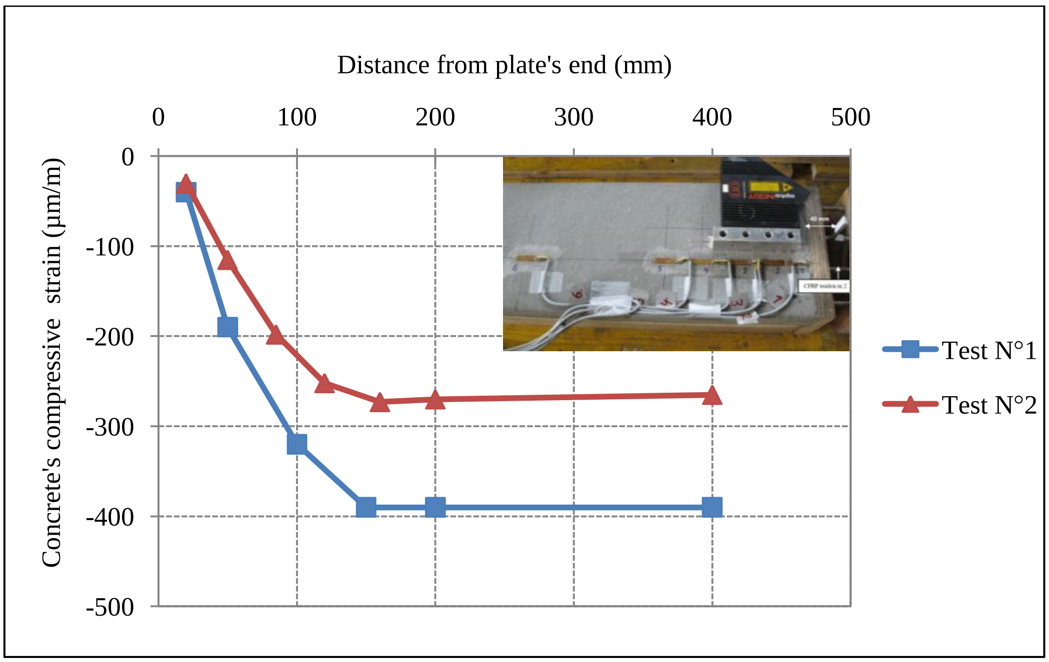

Figure 3.9: Results from prestress transfer tests performed on the EMPA study

From the experimental concrete compression strain profile, an experimental value of the bond development length (L_d) of the HPSCC plates can be estimated. The bond development length can be calculated as shown in Equation (3.1).

$$L_d = l_p - Concrete\ cover \quad (3.1)$$

Table 3.2: Bond development length (L_d) determination

Test	**1**	**2**
Prestress level (MPa)	1200	1200
Cte. compressive strain (mm)	150	160
Concrete cover (mm)	22.5	30.0
L_d (mm)	127.5	130.0

From Table 3.2, it can be seen a consistency between the values of bond development length determined from both tests, in which the thickness of the plates was different. As a safety factor, an embedment length of 160 mm was chosen.

Duct tape was used as a bond breaker at the first 40 mm from the bottom and at the first 50 mm from the top of the cylinders (see Figure 3.10). This way, the 160 mm embedment length lies in the middle of the concrete cylinder, allowing the correct functioning of the three initial requirements.

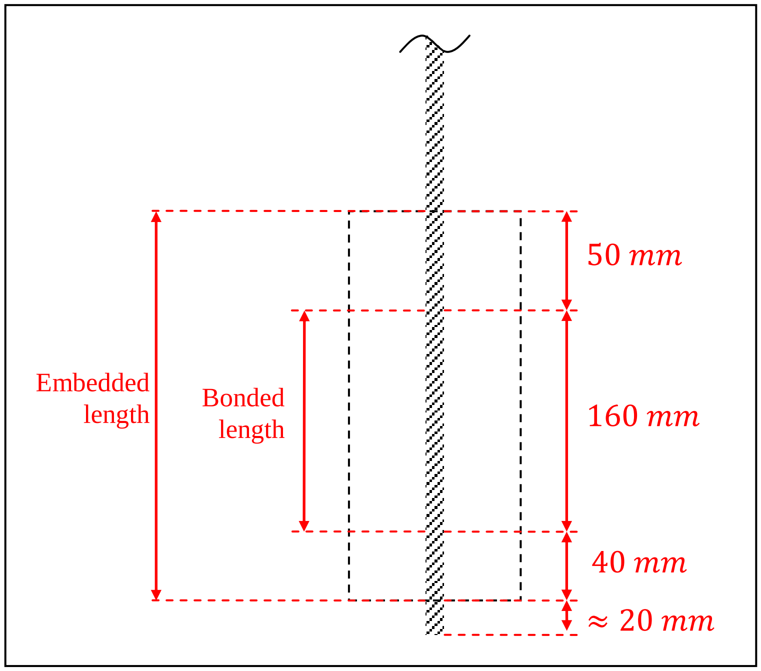

Figure 3.10: Diagram of CFRP pullout test and steel pullout test

3.2.1.2 Temperature recording at the bar

Three thermocouples were fixed to each one of the CFRP tendons and steel prestressing wires at the bottom, middle and top of the bonded length. The thermocouples were bonded to the bonded length by using a common instant adhesive (see Figure 3.11). The effect of the thermocouples on the bond strength is negligible. Once the bars where placed inside the moulds, the thermocouples were placed to go out by the top of the concrete cylinder., keeping them away from the CFRP tendon or steel prestressing wire, as not to affect the bonding. The thermocouples go out of the concrete from the perimeter of the top surface, as shown in Figure 3.15, so the thermocouples are not damaged when executing the pullout tests.

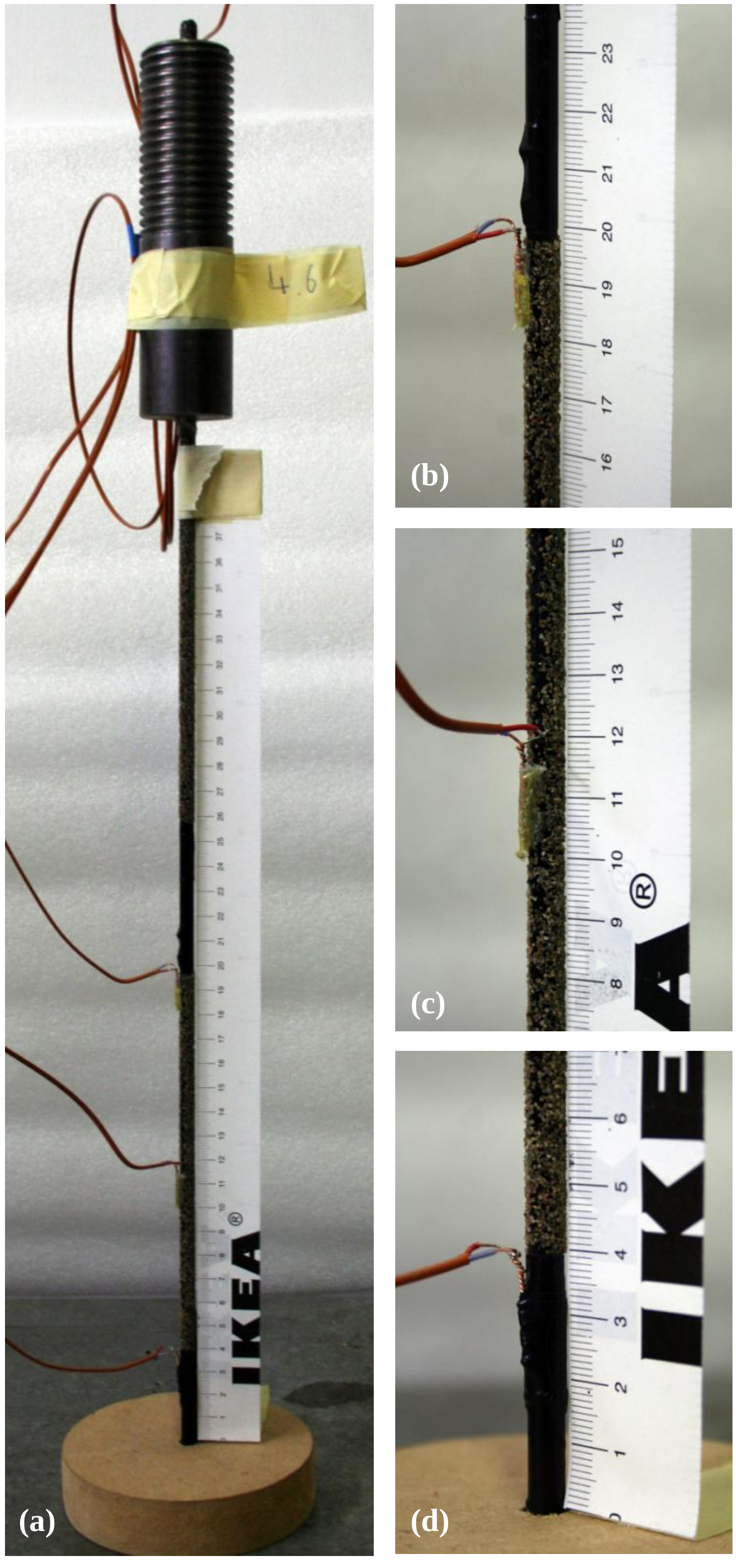

Figure 3.11: Thermocouples distribution **(a)** along the bonded length of a CFRP pullout sample, **(b)** top, **(c)** middle and **(d)** bottom thermocouple

Figure 3.12: Fixing the thermocouples to the pullout samples

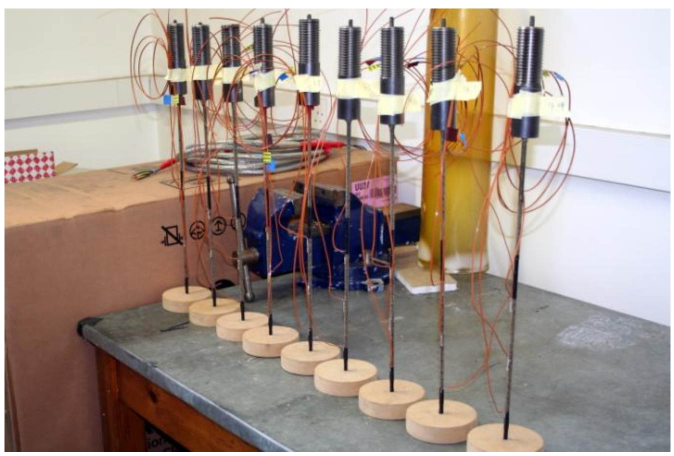

Figure 3.13: CFRP pullout samples set on the mould’s bottom cap

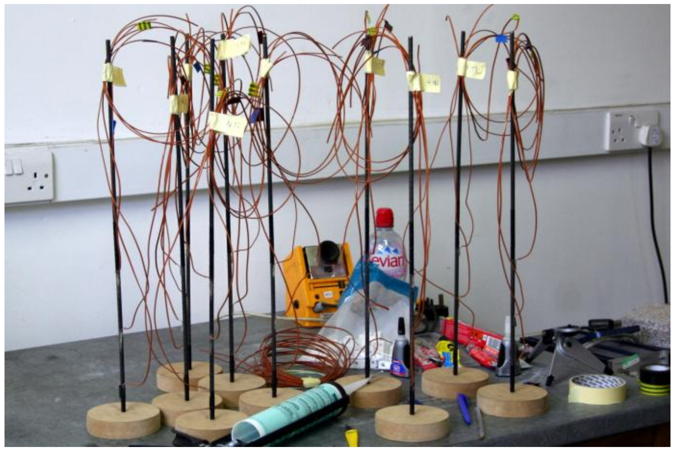

Figure 3.14: Steel pullout samples set on the mould’s bottom cap

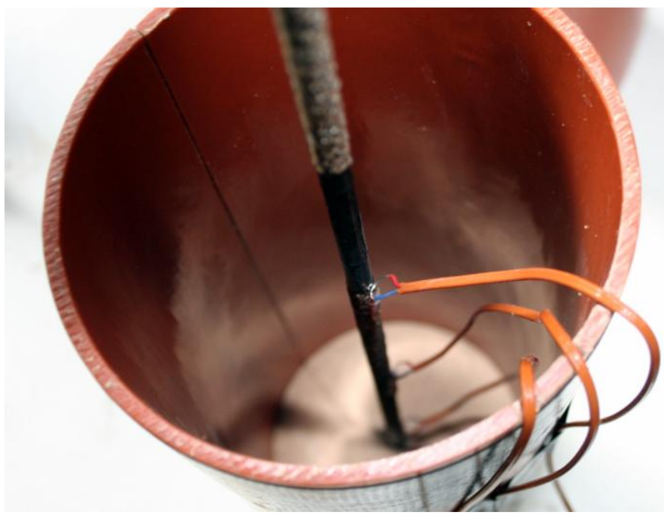

Figure 3.15: Inside look of a CFRP pullout mould

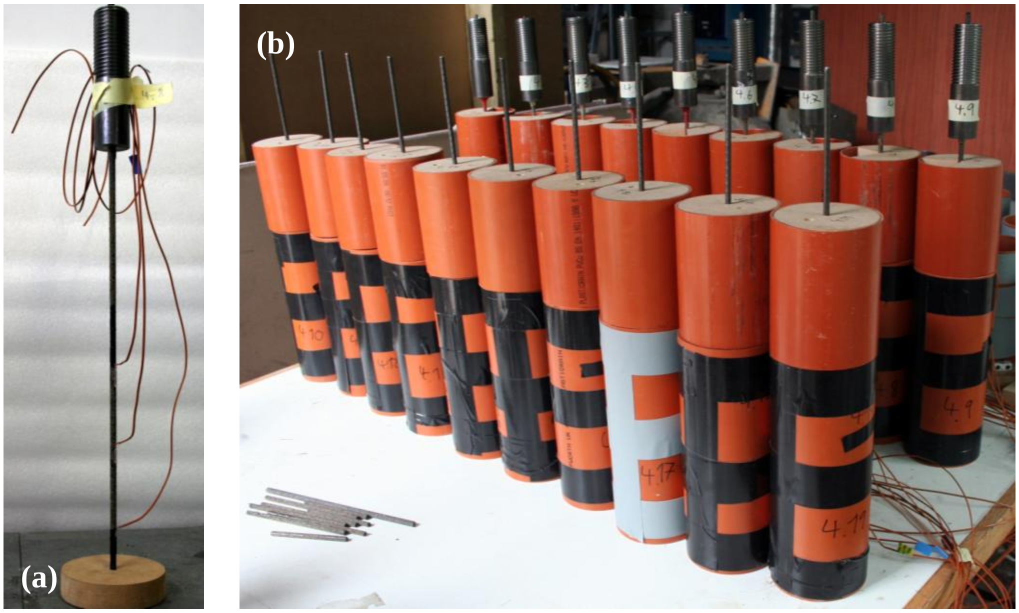

Figure 3.16: (a) CFRP pullout sample fixed to the bottom of the mould and **(b)** all CFRP and steel pullout moulds with top caps on

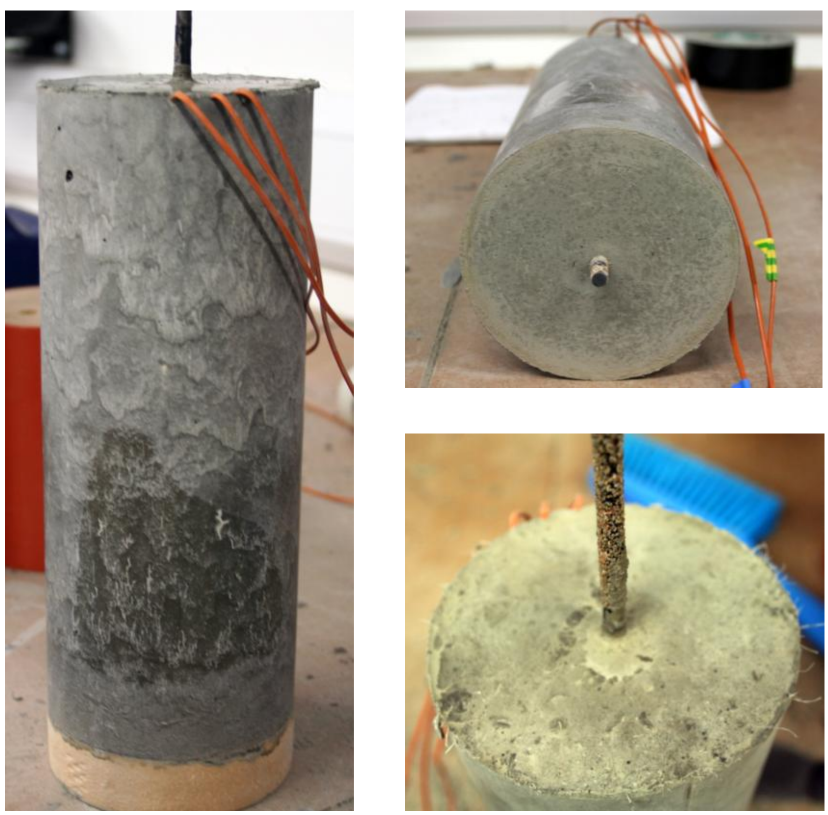

Figure 3.17: CFRP pullout sample after one day of curing

3.2.1.3 Temperature control and recording in the concrete-blanket interface

A heating blanket was used to wrap the pullout samples and apply the required thermal conditions throughout the pullout tests. Even though the blanket's temperature was controlled by a thermocouple place at the blanket-concrete interface, four extra thermocouples were placed to record the blanket-concrete interface temperature.

The four thermocouples at the blanket-concrete interface were placed on opposites sides of the concrete cylinder at the thirds of the length (see Figure 3.18). The blanket-concrete interface temperature is calculated as an average of these four thermocouples.

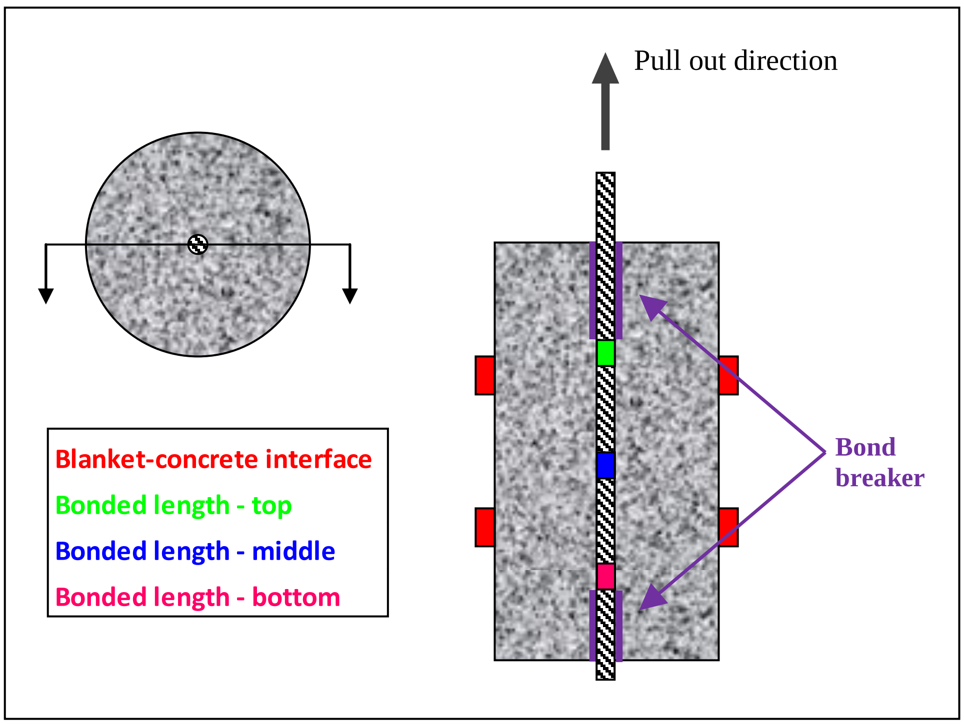

Figure 3.18: Thermocouples distribution on the pullout samples

An insulation layer was setup outside the heating blanket. This insulation was made from a one inch layer of fibre glass and a layer of bubble foil (see Figure 3.19 and Figure 3.20), which works as a protection mechanism for the Instron machine from the heating blanket's high temperature.

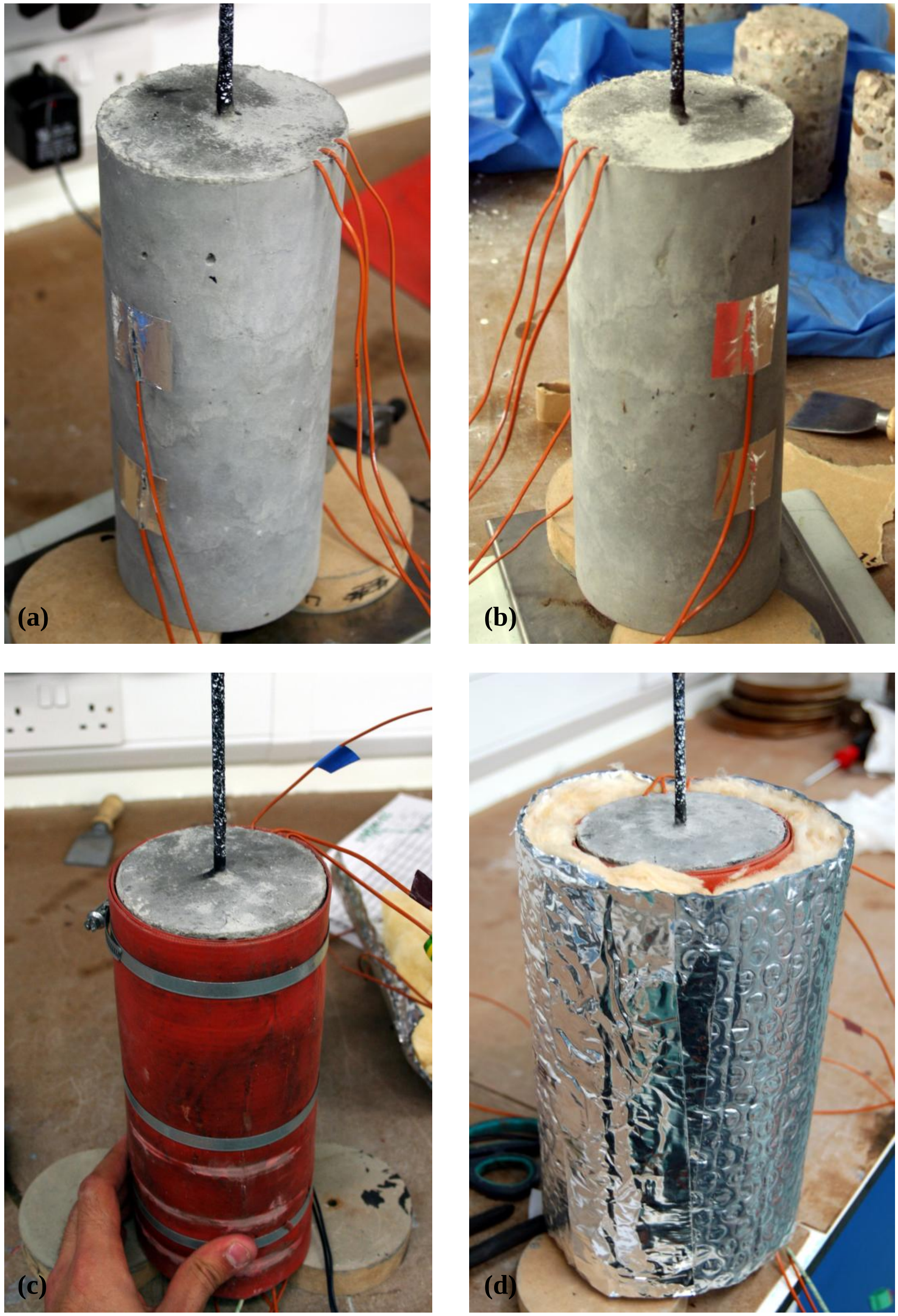

Figure 3.19: Setup of the **(a)** thermocouples placed on the blanket-concrete interface at the pullout samples in one side and **(b)** the other, **(c)** heating blanket wrap around the sample, and **(d)** thermal insulation made from fibre glass and bubble foil insulation

Figure 3.20: Top view of a pullout sample's thermal insulation made from fibre glass and bubble foil insulation

3.2.1.4 Digital image correlation setup

The loaded and free ends were prepared, as shown in Figure 3.21), for digital image correlation analysis (see Section 3.3.6) during pullout tests execution.

Figure 3.21: Preparation of the loaded and free ends for digital image correlation analysis on pullout tests

3.2.1.5 Effects of casting positioning

The bond strength of reinforcing bars is not strictly related to the concrete's compressive and tensile strength, and to the reinforcing bar itself. The casting position plays a significant factor in the ultimate bond strength of the reinforcing bar. For on-site prestress structural element, the reinforcing bar is horizontal and the concrete is poured in by filling the mould. With the bar in the horizontal position, the bond strength is deteriorated by plastic settlement (Valcuende & Parra, 2009), bleeding (Sri Ravindrarajah, Lopez & Reslan, 2002) and trapped air bubbles under the reinforcing bar. The deteriorated bonded zone in horizontally casted concrete members is shown in Figure 3.22. In this research, the casting was done with the reinforcing bar in the vertical position, not allowing for any of the above bond strength deterioration to happen, therefore eliminating extra variables from the present study.

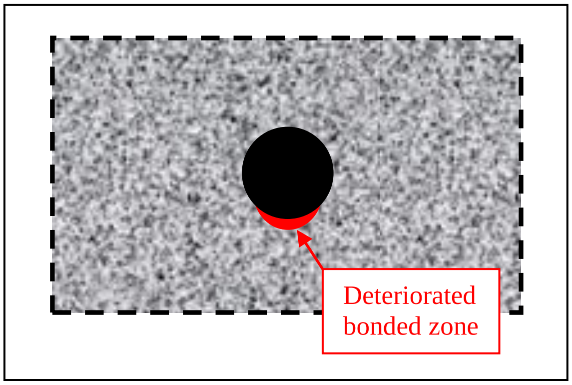

Figure 3.22: Cross sectional area of a deteriorated bonded zone in horizontally casted reinforcing bars (on-site casting)

3.2.2 CFRP Dynamic Mechanical Analysis

The samples needed to run the Dynamic Mechanical Analysis (DMA) where extracted from a CFRP tendon, same as the ones used for the pullout samples. This was done by cutting an 18 mm long rectangular section (4.5 x 3 mm) out of a CFRP tendon, as shown in Figure 3.23.

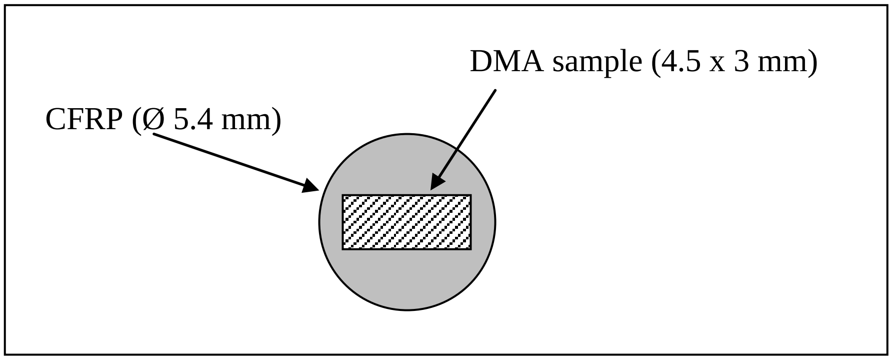

Figure 3.23: Cross sectional area of a typical DMA sample cut from a CFRP tendon

3.2.3 Concrete compressive strength test

The compressive strength test samples are concrete cylinders with a diameter of 100 mm and a length of 200 mm.

3.2.3.1 Digital image correlation setup

The cylinders were prepared for digital image correlation analysis (see Section 3.3.6) during compressive strength tests execution by painting their surface, as shown in Figure 3.24.

Figure 3.24: Compressive strength test sample preparation for digital image correlation analysis

3.2.4 Splitting tensile strength test

The splitting tensile strength test samples are concrete cylinders with a diameter of 100 mm and a length of 200 mm.

3.2.4.1 Digital image correlation setup

The cylinders were prepared for digital image correlation analysis (see Section 3.3.6) during splitting tensile strength tests execution by painting their surface, as shown in Figure 3.25.

Figure 3.25: Splitting tensile strength test sample preparation for digital image correlation analysis

3.2.5 Concrete thermal conductivity test

In this test, concrete's thermal resistance was measured at a thermal steady state. This is not a very good approach in concrete because of the transient phenomenon occurring as concrete heats up: steam migration caused by the heated concrete's water content, melting of the polypropylene fibres and the deterioration of the concrete crystals. This test was used as a first approach to determinate the thermal properties of concrete.

The machine used for this test is the C-Matic guarded heat flow meter (see Section 3.3.9) which works by placing a sample between two plates controlled at different temperatures, resulting in a flow of heat from the hotter to the colder plate.

The samples were cast into small moulds specially fabricated for this research. The machine requires a cylindrical sample of the material with a diameter of 50 mm and a thickness of 20 mm, as the one shown in Figure 3.26. A thin uniform layer of heat sink compound is applied to both surfaces of the test sample, in order to allow a uniform heat flow on the surfaces.

Figure 3.26: Typical concrete sample used for C- Matic guarded heat flow meter

The casting process of the different concrete specimens used during this study is shown in Figure 3.27, Figure 3.28, Figure 3.29 and Figure 3.30.

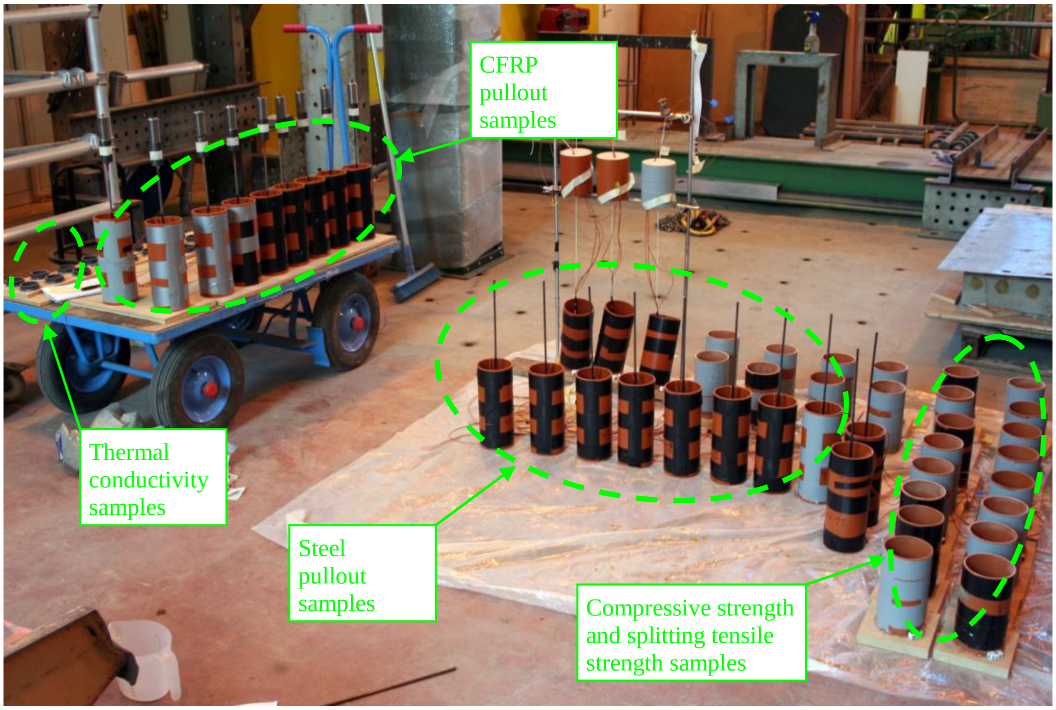

Figure 3.27: Setup of concrete moulds before pouring of concrete

Figure 3.28: CFRP pullout samples right after casting

Figure 3.29: Steel pullout, compressive strength and splitting tensile strength samples right after casting

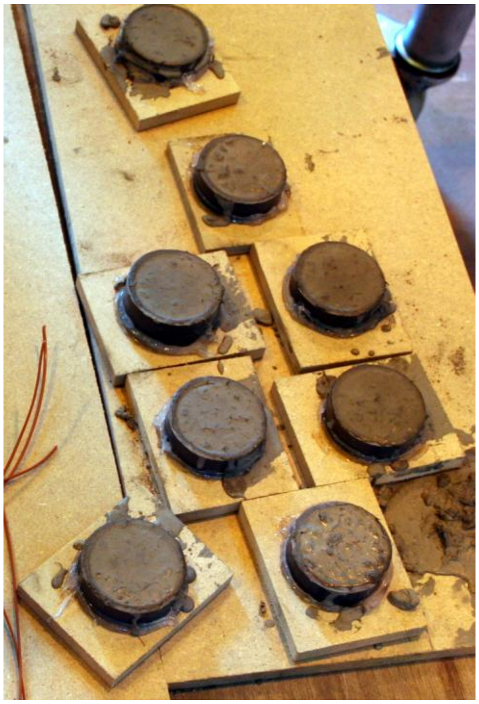

Figure 3.30: Thermal conductivity samples right after casting

3.3 Testing Equipment and Data Acquisition Systems

The equipments used to execute the mechanical and thermal conditions for each test, and the techniques employed to measure and record temperature, slip, strain and others are an important aspect of this experimental research, and are described in the following sections.

3.3.1 Instron 3369 Dual Column Tabletop Universal Testing Systems

The Instron materials testing machine seats at The Crichton Laboratory, located within King's Buildings Campus at the University of Edinburgh. It was used to run pullout tests and steel prestressing wire tensile strength tests.

On its original setup, the machine works on displacement control, but is also capable of sustaining the load over time (load control mode), condition needed for the pullout tests. This testing system works for both tension and compression applications, in which the top crosshead moves up or down. For the pullout tests, a frame was designed and constructed as shown on Figure 3.31. The load cell was placed on the top crosshead and had a capacity of 50 kN. The data acquisition rate of the machine was set at 10 Hz.

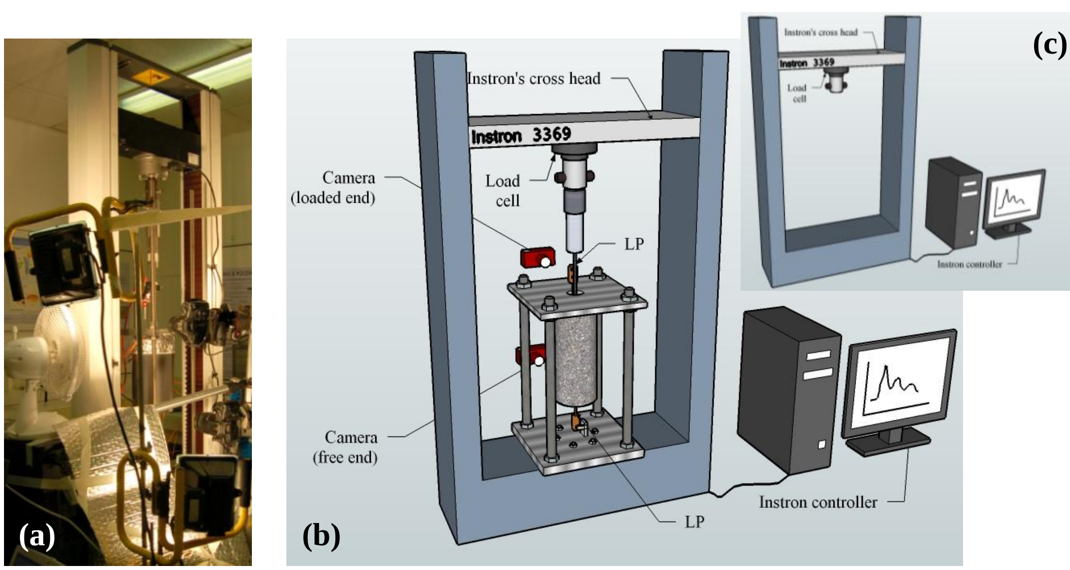

Figure 3.31: (a) Photo of the pullout's test setup, and schematic of the Instron 3369 machine **(b)** with the pullout test frame installed and **(c)** without the pullout test frame

3.3.2 Heating blanket

A heating blanket was used to wrap the pullout sample. The blanket was an ΩOmega® blanket made of silicone rubber (see Figure 3.32), capable of being mounted on a curved surface, like the 2” radius of the pullout samples (concrete cylinder).

The heating blanket has a maximum exposure temperature of 190°C. The blanket temperature is controlled by an external control device which monitors the blanket’s temperature by a thermocouple placed at the blanket-concrete interface.

Figure 3.32: Pullout sample wrapped with the heating blanket

3.3.3 T type thermocouples

A thermocouple is a sensor for measuring temperature with high accuracy and repeatability. It consists in two wires made of different metals joined at two points. Due to thermoelectric effect, if the junctions are at different temperatures, voltage is generated, which is approximately a linear function for a wide range of temperature differences. One of the junctions (cold junction) is kept at a known reference temperature, and the other junction (hot junction) is used to measure the temperature of interest.

The thermocouples were used in every pullout test by placing them at the blanket-concrete interface and at three points along the bar's bonded length (top, middle and bottom), as shown in Section 3.2.1.3.

For this research, T type thermocouples were used because of its high accuracy and sensitivity at the required temperature range. Another key aspect of T type thermocouples is their tolerance to environments with high humidity, as the one found inside concrete. T type thermocouples have accuracy between 0.5 and 0.8°C at temperatures below 200°C (IEC, 1982).

3.3.4 Linear potentiometers

A linear potentiometer (LP) measures displacements and is used in the pullout tests to measure the slip at the loaded and free ends.

3.3.5 Vishay StrainSmart 7000

This is a high performance data acquisition equipment with a measurement accuracy of $\pm 0.05\%$ of full scale. It was used to record the data measured by the thermocouples and LPs during pullout tests. The instrument was set to record at 10 Hz.

3.3.6 Digital image correlation analysis

Digital image correlation (DIC) analysis is a novel technique, used in this study to measure the slip in pullout tests, strains in concrete compressive strength tests and crack opening in concrete splitting tests. This analysis was performed with GeoPIV, which is a digital image correlation software developed specifically for measuring displacement/strains of solids (White & Take, 2002).

DIC works by taking digital images of the specimen from which displacements or strains aimed to be measured. The surface from which displacements are meant to be measured was prepared for an optimum analysis by painting it with black spray paint. Once dry, a random pattern of white spots, identifiable by the computational analysis, was painted.

The images were taken every five or ten seconds during testing, using an 8 Megapixels resolution Canon Digital Rebel camera. Regions of interest (patches) were defined for the first image and then tracked for each subsequent image over a defined surrounding region (search zone). The patches were 64x64 pixels when measuring strains in concrete compressive strength tests, and 32x32 pixels when measuring slips in pullout tests and crack opening in concrete splitting tests (see Figure 3.33 for a typical patch).

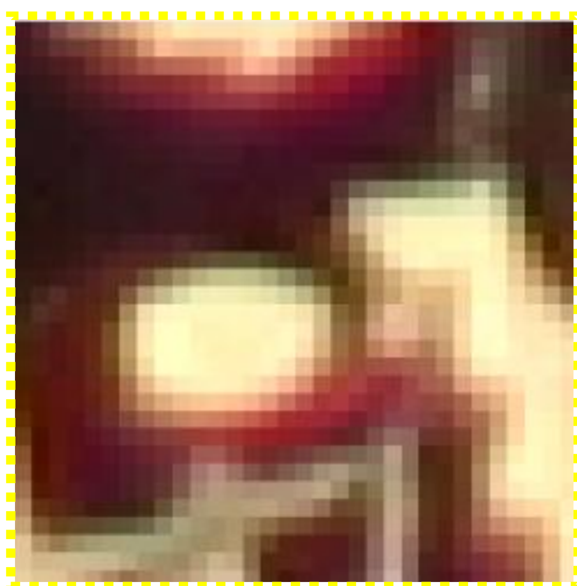

Figure 3.33: Typical patch from digital image correlation analysis

In pullout tests and concrete splitting tensile strength tests, a ruler was placed at the same plane of the region of analysis, in order to determine the pixels/mm ratio of the digital image. Also three patches are placed over the ruler's numbers in order to identify any false displacement (noise) that could come from the camera or the analysis itself. Typical distribution of patches, with the patch in yellow and the patch name in red are shown in Figure 3.34.

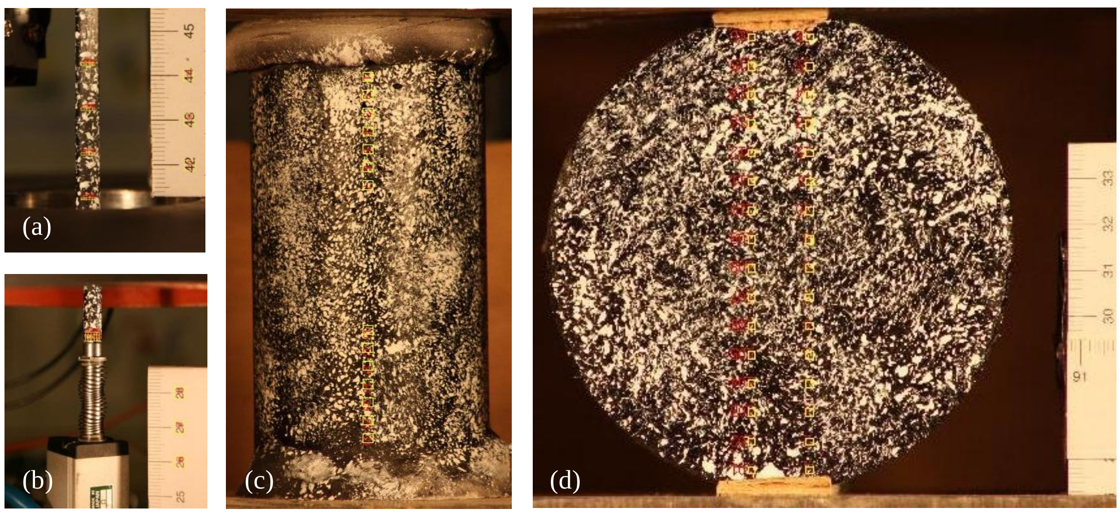

Figure 3.34: Digital image correlation analysis typical patch distribution in a **(a)** pullout test's loaded end, **(b)** pullout test's free end, **(c)** concrete compressive strength tests, **(d)** concrete splitting tensile strength tests

3.3.7 Tritec 2000 Dynamic Mechanical Analyser

The Tritec 2000 Dynamic Mechanical Analyser (DMA) is used to measure the stiffness and damping characteristics of a material with respect to temperature (see Figure 3.35). This is achieved by applying a small sinusoidal stress to the sample and measuring the resulting displacement. The sample is mounted in an environmental chamber, with a temperature range between -150 and 400°C.

The applied stresses are in the elastic range, so as not to alter the material being analysed. With the analysis, storage modulus, loss modulus and $\tan\delta$ are determined as a function of temperature, from which the glass transition temperature (T_g) of a polymeric material can be calculated.

Storage modulus is defined as the elastic response of the material to deformation, while the loss modulus is the viscous response to deformation. The $\tan\delta$ value can be interpreted as the ability of the material to dissipate energy, calculated as the ratio between loss modulus and storage modulus.

The value of $\tan\delta$, also called the loss tangent or damping factor, is one of the key parameters in dynamic mechanical testing, since it is known to increase during transitions between different deformational mechanisms (Li, Lee-Sullivan & Thring, 2000).

There are several techniques to determine T_g by DMA:

- Peak on $\tan\delta$ curve
- Peak on loss modulus curve
- Half height of storage modulus curve
- Onset of storage modulus curve

The transition between glassy and rubbery behaviour in polymers is due to the markedly increased ability of polymer molecules to slide and rotate relative to each other as temperature increases through a certain range (Findley, Lai & Onaran, 1976). From the mechanical point of view, this transition manifests in a reduction of stiffness and in the ability to reversibly deform without fracture.

DMA is a great tool to determinate the mechanical behaviour of a polymeric material below, through and above glass transition temperature. Another instrument widely used to define glass transition temperature is the Differential Scanning Calorimeter (DSC), which basically calculates the glass transition temperature by measuring the heat absorbed or given off from a sample as a function of temperature (ASTM, 2003). DMA and DSC measure different processes and therefore, the T_g determination can have as much as a 25 degree difference. DMA was used to determine the T_g in the present study.

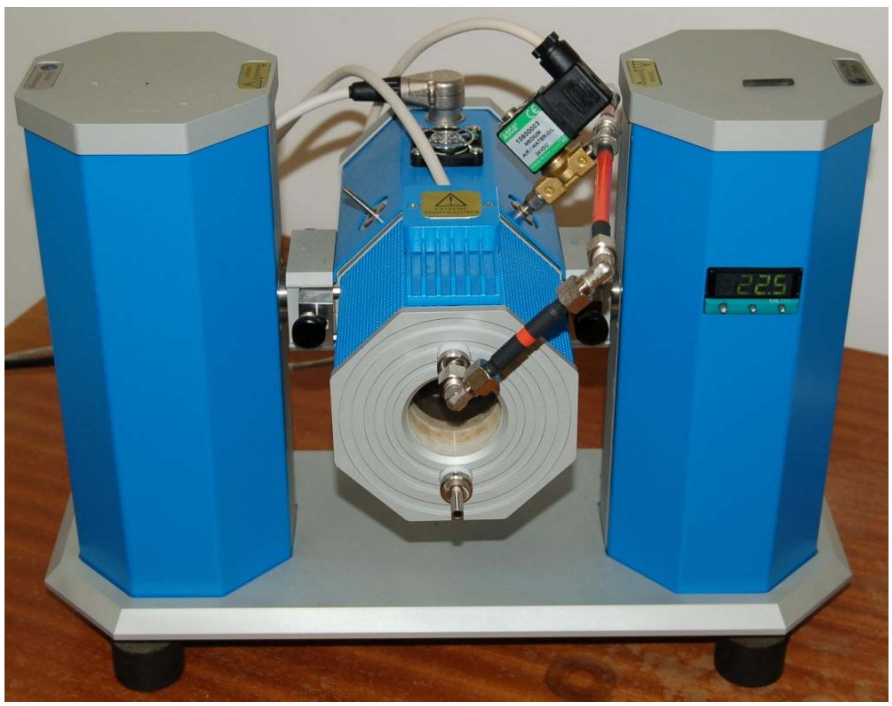

Figure 3.35: Tritec 2000 DMA

3.3.8 Avery universal testing machine

The Avery machine is seated at The Structures Laboratory, located within King's Buildings Campus at the University of Edinburgh. It was used to run concrete compressive strength tests and concrete splitting tensile strength tests (see Figure 3.36).

It works on displacement control and the loading rate is set by kN/min, ideal for both types of tests for which the machine was employed. Both tests were complemented with digital image correlation analysis in order to obtain the compressive strain and crack opening in concrete compressive strength tests and concrete splitting tensile strength tests, respectively.

Figure 3.36: Avery universal testing machine

3.3.9 C-Matic guarded heat flow meter

The C-Matic machine (see Figure 3.38) is used to measure thermal conductivity of solid materials by a guarded heat flow meter method. A test sample is placed between two plates at different controlled temperatures, resulting in a flow of heat from the hotter to the colder plate, as shown in Figure 3.37. The amount of heat is measured with a thin heat flux transducer attached to one of the temperature controlled plates. Surrounding the sample is a cylindrical guard heater maintained at or near the mean sample temperature, to minimize lateral heat transfer. The overall temperature difference between the two surfaces in contact with the sample is measured with built-in thermocouples.

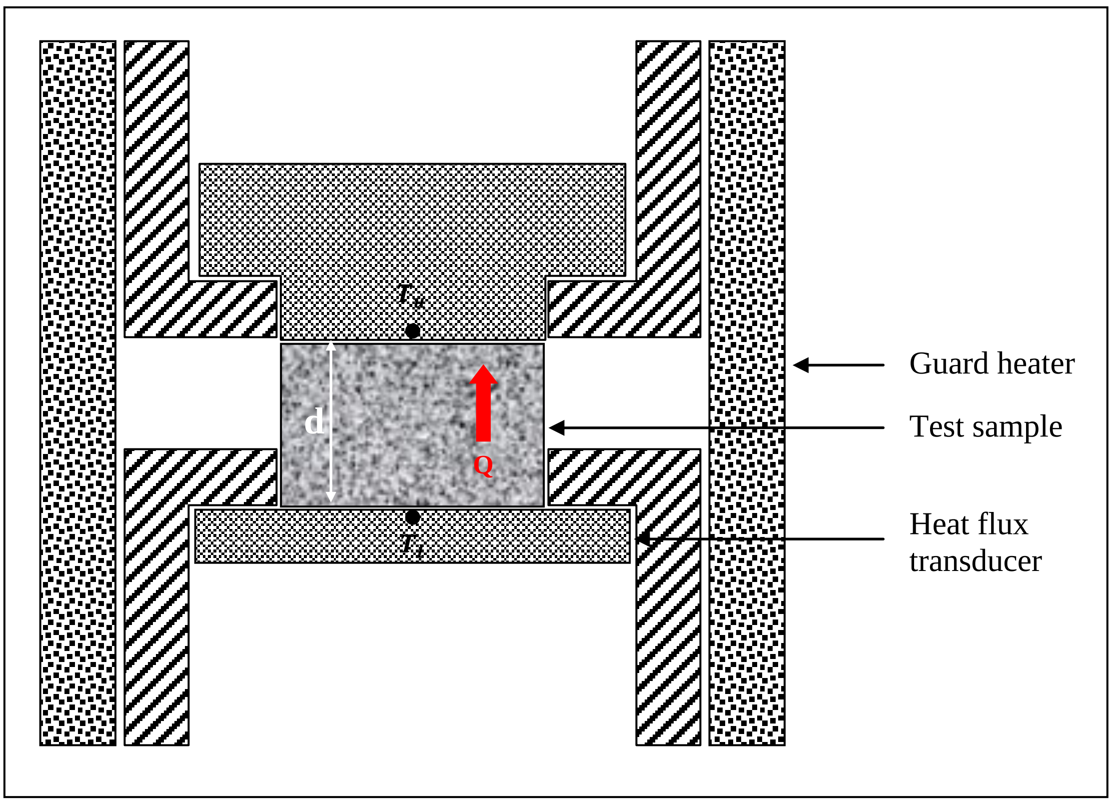

Figure 3.37: Schematic diagram of C-Matic test section

At thermal equilibrium (steady state), the Fourier heat flow equation applied to the test stack becomes as shown in Equation (3.2).

$$R_s = N \cdot \left(\frac{T_l - T_u}{Q}\right) - R_o \tag{3.2}$$

Where:

$R_s = sample\ thermal\ resistance$

$N = proportionality\ constant$

$T_l = lower\ surface\ temperature$

$T_u = upper\ surface\ temperature$

$Q = heat\ flux\ transducer\ output$

$R_o = contact\ thermal\ resistance$

And the material thermal conductivity is defined as shown in Equation (3.3).

$$\lambda = \frac{d}{R_s} \tag{3.3}$$

Where:

$\lambda = sample\ thermal\ conductivity$

$d = sample\ thickness$

The values of N and R_o are dependent parameters and are determined by calibrating the C-Matic machine at each temperature level using samples with known thermal conductivity. To calibrate the machine Vespel SP1 and Pyrex 7740 samples were used, and the calibration was executed for a mean sample temperatures of 76, 114 and 155°C. It should be mention again that the calibrated values of N and R_o are only valid in this specific C-Matic machine, as properties would differ from one machine to another. The parameters obtained are summarized in Table 3.3.

Table 3.3: C-Matic calibration dependent parameters

Sample Temperature [°C]	N [*10]	R_o [(m^2K/W) *10^4)]
76	1.7275	17.6580
114	1.7647	19.2010
155	1.7820	18.2260

Figure 3.38: C-Matic guarded heat flow meter

3.4 Testing Program

The testing program was designed to examine the bond performance of CFRP tendon and steel prestressing wire with high performance self-consolidating concrete (HPSCC) at elevated temperatures. The pullout test was the main experiment in this research, although other tests were performed to determine various properties of CFRP tendon, steel prestressing wire and HPSCC. In Figure 3.39, the tests for each material are shown.

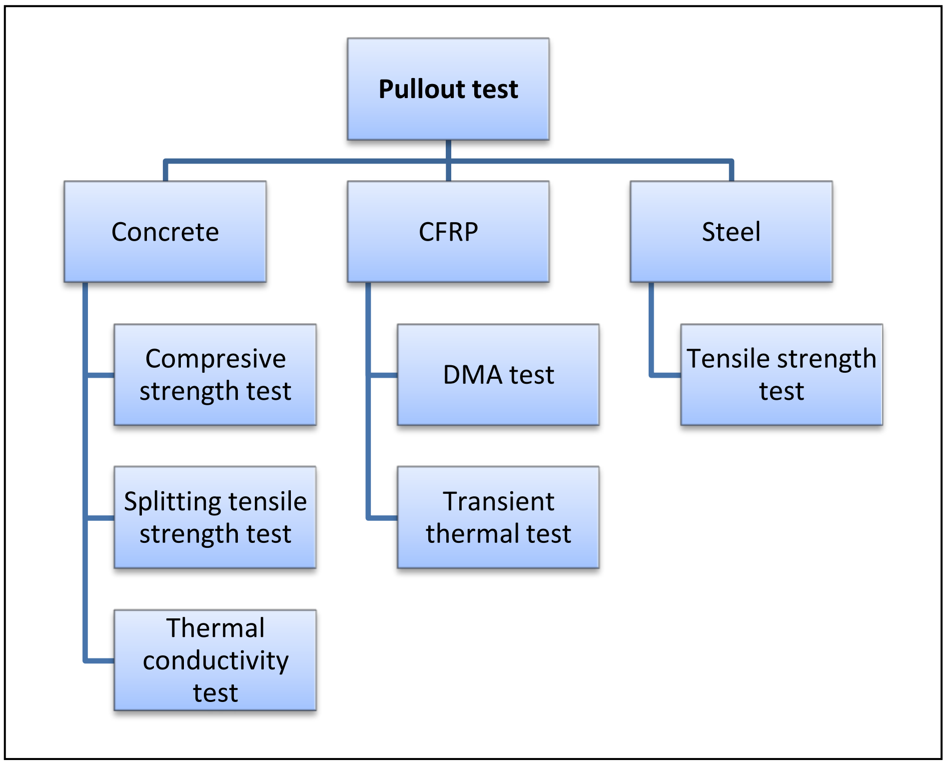

Figure 3.39: Schematic diagram of the experimental research

3.4.1 Pullout test

Although stress conditions encountered in reinforced concrete members differ greatly from those produced in pullout tests (ACI, 2003), this type of test has been widely adopted in the assessment of bond performance between concrete and steel reinforcing bars. The reason for this is that pullout tests offer an economical and simple solution for the comparative evaluation of bond performance.

Past research performed on the bond performance of fibre reinforced polymer (FRP) and steel reinforcing bars at high temperatures has been done, in most cases, by heating a pullout sample and then testing it in pull-out (or pull-in) up to failure (Bingol & Gul, 2009; Abbasi & Hogg, 2005). This is not representative of what happens in real fire conditions, where materials are heated as they maintain at least a certain level of sustained static loads. Furthermore, in prestressed bonded concrete members there is considerable bond strength requirement throughout the structural element’s whole lifetime in order to maintain the required prestressing forces.

Real fire conditions present a different phenomenon from the test of heating and then pulling the bar out of the concrete, especially for CFRP reinforcing bars in which the epoxy present on the bars’ surface might undergo significant creep under sustained load at elevated temperature (Bakis 2008).

If pull out is executed after the concrete is heated up, a bond strength value is obtained for a certain temperature. This is essentially opposite to what happens if pullout is applied at a certain sustained bond stress (below the failure bond stress) and the sample is heated up until failure occurs. In this case, a temperature value is obtained for a given bond stress. This second scenario is much more representative of the state of stress within a real FRP prestressed structural element during a fire.

3.4.1.1 Experimental setup

The pullout test setup is shown in Figure 3.40. Pullout arrangements used by previous researchers, previously mentioned, were carefully studied to determine the most appropriate setup for the experiments. Special consideration was given to the accuracy of the measurements of bar slip at both the loaded and free ends of the specimens. At the loaded end, the elastic deformation of the un-bonded length of the bar was subtracted from the measured slip, as explained in Section 3.4.1.3 and shown in Figure 3.49. The displacement of the bars was measured against the frame’s reference plates (see Figure 3.40).

At the free end, the un-bonded length of the bar is not subject to any stress, which means that no mechanical deformation of the bar occurs.

At both ends of the bonded length, the slip was measured by two systems: linear potentiometers (LP's) and digital image correlation analysis (see Figure 3.43). The recorded data, from both systems, was compared against each other, with very good results, as shown in Section 3.4.1.3.

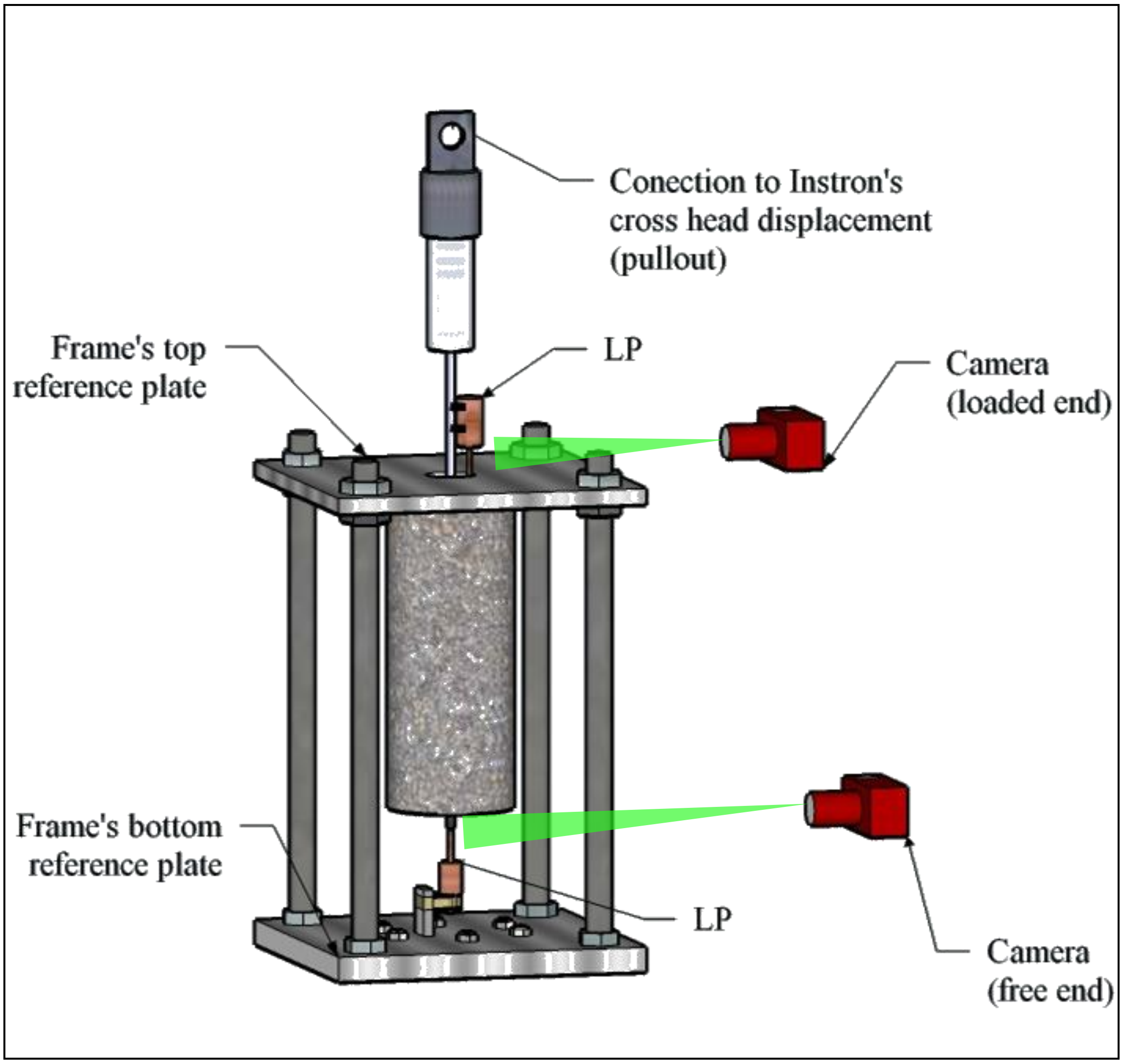

Figure 3.40: Schematic of the pullout test experimental configuration

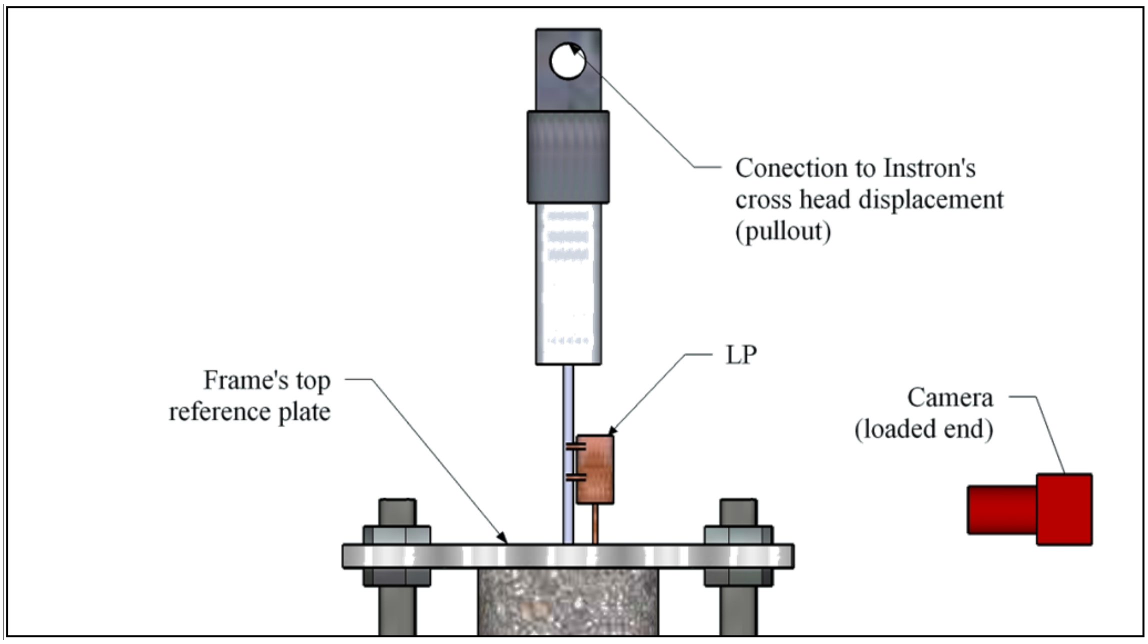

Figure 3.41: Schematic of the loaded end instrumentation

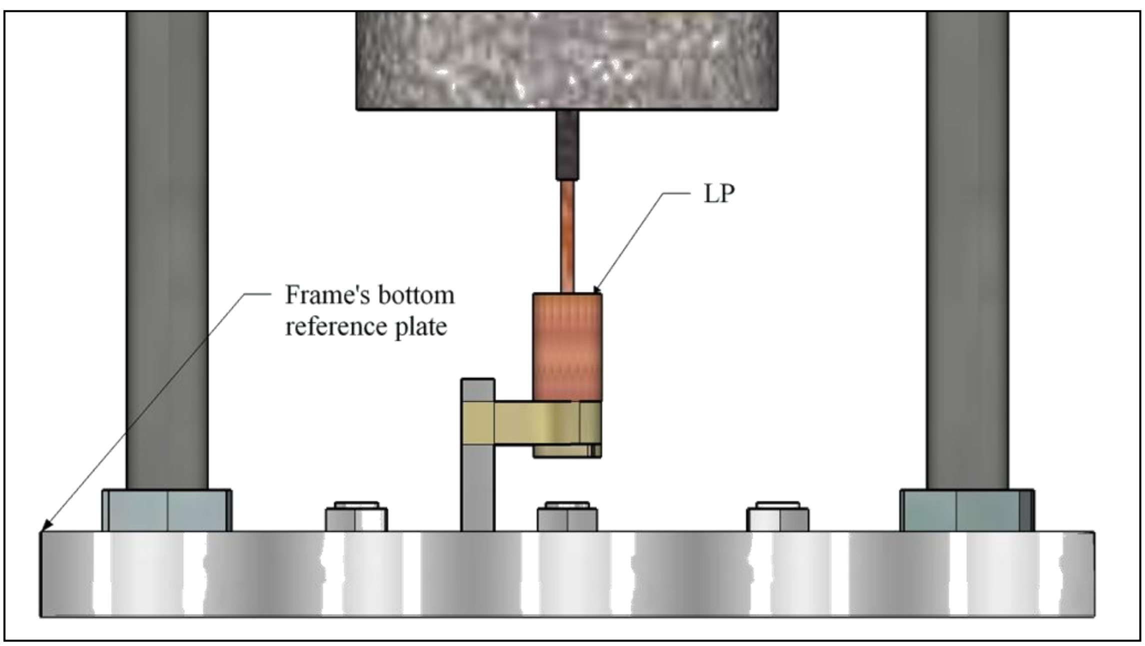

Figure 3.42: Schematic of the free end instrumentation

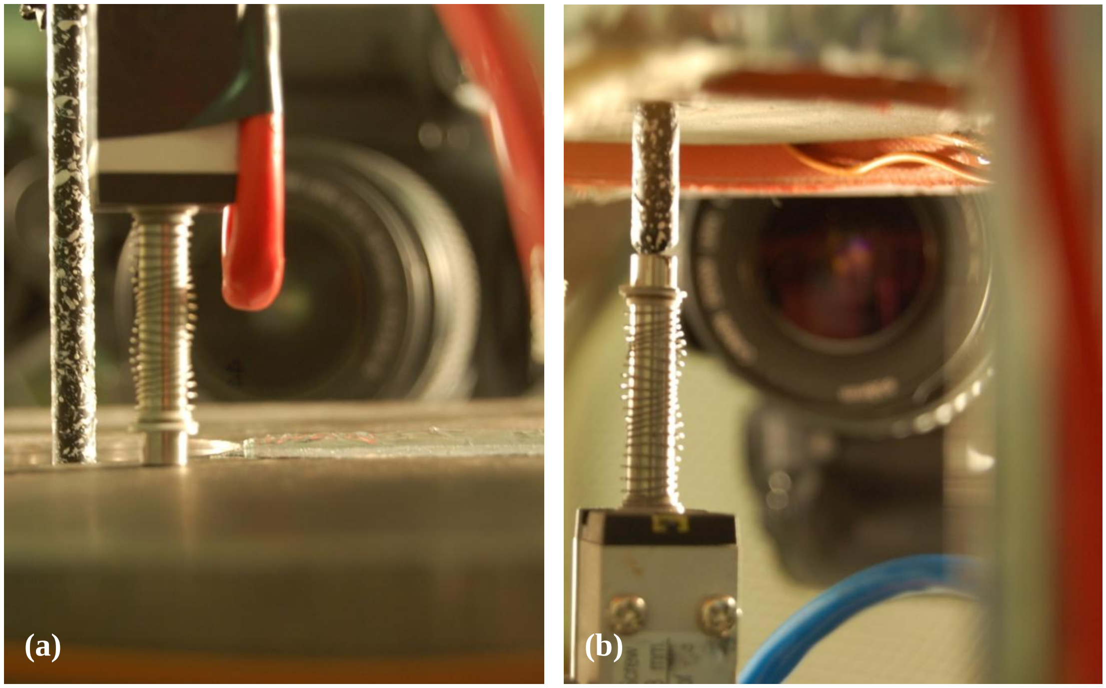

Figure 3.43: Photos of the LP's and cameras used to measure slip at **(a)** loaded end and **(b)** free end

After preparing the pullout sample as described in Section 3.2.1, the sample was placed on the frame which was fixed to the test table of the Instron materials testing machine. For the CFRP pullout tests, the sample was clamped on the loaded end by the specially fabricated potted resin anchorage (see Section 3.1.2.1). For the steel pullout tests the clamping was made with standard wedge-action V-notch Instron grips. After the sample was placed in the frame, the T-type thermocouples and LP's were connected to the Vishay StrainSmart 7000 data logger. This process was repeated for each one of the eighteen pullout samples.

3.4.1.2 Test procedure

The experiments were conducted at The Crichton Laboratory, located within King's Buildings Campus at the University of Edinburgh. A total of eighteen specimens were tested, nine with CFRP tendon and nine with steel prestressing wire. Two types of pullout test were performed:

- RPOT (Regular Pull-Out Test): the specimen was loaded at room temperature at a constant loaded end displacement rate until pullout occurred.
- PHPOT (Prestress and then Heated Pull-Out Test): the specimen was loaded at room temperature to a prescribed load under a load control mode, and then the specimen was heated, maintaining the load constant until pullout occurred.

3.4.1.2.1 Loading rate

The loading rate applied during PHPOTs was determined from the Canadian Standards Association document for the design of concrete buildings with FRP reinforcement (CSA, 2002), which states that for a pullout test done on FRP reinforcement, the loading shall be applied at a tensile stress rate between 250 and 500 MPa/min. A rate of 300 MPa/min was selected for the pullout tests with CFRP tendons. The bond stress rate was calculated as follows:

$$\tau'_{CFRP} = \frac{P'_{CFRP}}{\pi \cdot D_{Coat} \cdot L} \tag{3.4}$$

$$\tau'_{CFRP} = \frac{\sigma'_{CFRP} \cdot \pi \cdot D_{CFRP}^2}{4 \cdot \pi \cdot D_{Coat} \cdot L} \tag{3.5}$$

$$\tau'_{CFRP} = \frac{\sigma'_{CFRP} \cdot D_{CFRP}^2}{4 \cdot D_{Coat} \cdot L} \tag{3.6}$$

$$\tau'_{CFRP} = \frac{\left(300\ {}^{MPa}/_{min}\right) \cdot (5.4\, mm)^2}{4 \cdot (6\, mm) \cdot (160\, mm)} \tag{3.7}$$

$$\tau'_{CFRP} = 2.28\ \left[\frac{MPa}{min}\right] \tag{3.8}$$

Because the Instron machine operates under displacement control, the displacement rate of the crosshead had to be calculated in order to apply the required bond stress rate. Before doing this, the elastic modulus of the system had to be estimated; in theory, this is the summation of the reciprocal of the reinforcing bar's modulus of elasticity, the clamping system slipping, the testing frame's elasticity, and the slipping at the beginning of the bonded length (see Figure 3.44).

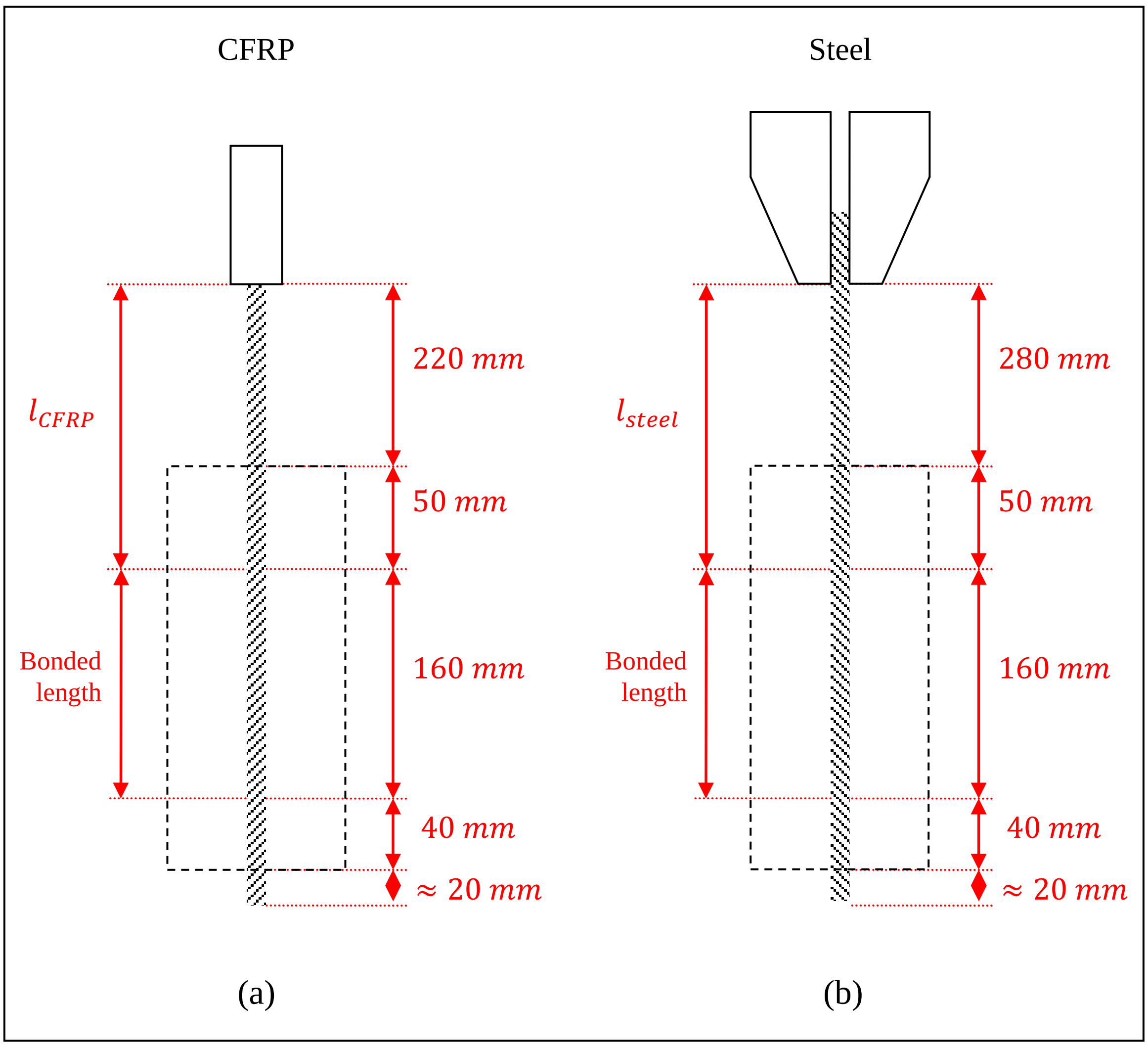

Figure 3.44: Diagram of **(a)** CFRP pullout test and **(b)** steel pullout test

The system's elastic modulus was calculated from the first pullout test of both materials, CFRP (CFRP_AT_e1) and steel (Steel_AT_e1), and then used as the elastic modulus of the system to calculate the displacement rate of the Instron´s crosshead for the remaining samples with the same reinforcing bar.

For samples CFRP_AT_e1 and Steel_AT_e1, the displacement rate of the crosshead was set at 1.27 ${}^{mm}/_{min}$ (Wilson et al., 2002), and the elastic modulus (E^*) was estimated as shown in Equation (3.9), on the linear range of the test.

$$E^*_{CFRP} = \frac{\sigma'_{CFRP}}{\varepsilon'^*_{CFRP}} \qquad E^*_{steel} = \frac{\sigma'_{steel}}{\varepsilon'^*_{steel}} \tag{3.9}$$

It is well understood that the gauge lengths l_{CFRP} and l_{steel} are not the gauge lengths of the systems, but the gauge lengths only of the un-bonded lengths of the bars on the loaded end, from the clamping system till the beginning of the bonded length. Because this distance is the same for every sample on CFRP and steel pullout sample, once the system's elastic modulus was estimated for the first sample, this value was used to calculate the displacement rate of the crosshead of every other pullout samples that had the same reinforcing bar.

$$E^*_{CFRP} = \sigma'_{CFRP} \cdot \frac{l_{CFRP}}{\delta'^*_{CFRP}} \qquad E^*_{steel} = \sigma'_{steel} \cdot \frac{l_{steel}}{\delta'^*_{steel}} \tag{3.10}$$

$$\rightarrow \quad \delta'^*_{CFRP} = \frac{\sigma'_{CFRP} \cdot l_{CFRP}}{E^*_{CFRP}} \qquad \rightarrow \quad \delta'^*_{steel} = \frac{\sigma'_{steel} \cdot l_{steel}}{E^*_{steel}} \tag{3.11}$$

For both CFRP tendons and steel prestressing wire pullout tests, the rate at which the bond stress was applied on the CFRP-concrete interface and the steel-concrete interface was the same. The CFRP tensile strength is attributed to the carbon fibres aligned longitudinally along the tendon; the tendon has an outer resin-rich layer which acts to adhere the sand coating for enhanced bond, but which does not contribute significantly to the CFRP's axial strength or stiffness. This is why the tensile stress was considered to be only distributed over the 5.4 mm diameter central cross sectional area and the bond stress on the CFRP-concrete interface was assumed to be distributed through the 6.0 mm diameter perimeter, as shown in Figure 3.45(a).

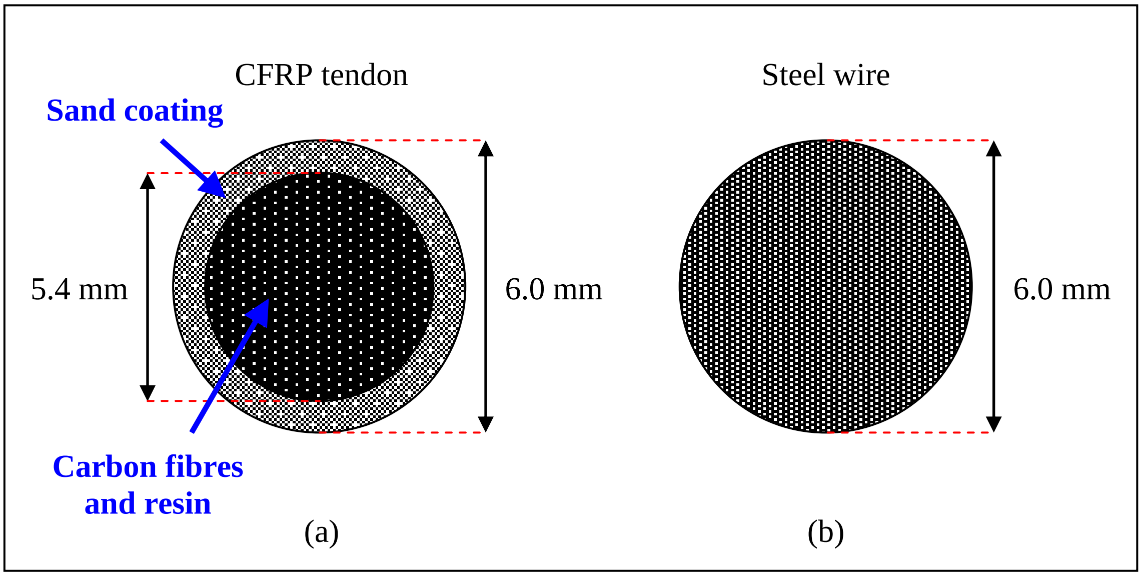

Figure 3.45: Cross sectional area of **(a)** CFRP tendons and **(b)** steel prestressing wire

Given the condition that bond stress rate on both types of reinforcing bars should be the same in order to make a fair comparison of the relative performance of each type of prestressing material; the desired tensile stress rate on the steel pullout tests was calculated as follows:

$$\tau'_{\mathrm{CFRP}} = \tau'_{\mathrm{steel}} \tag{3.12}$$

$$\frac{\mathrm{P}'_{\mathrm{CFRP}}}{\pi \cdot D_{Coat} \cdot L} = \frac{\mathrm{P}'_{\mathrm{steel}}}{\pi \cdot D_{Steel} \cdot L} \tag{3.13}$$

$$\frac{P'_{CFRP}}{D_{Coat}} = \frac{P'_{Steel}}{D_{Steel}} \tag{3.14}$$

$$\frac{\sigma'_{\mathrm{CFRP}} \cdot \pi \cdot D^2_{CFRP}}{D_{Coat}} = \frac{\sigma'_{\mathrm{steel}} \cdot \pi \cdot D^2_{Steel}}{D_{Steel}} \tag{3.15}$$

$$\frac{\sigma'_{\mathrm{CFRP}} \cdot D^2_{CFRP}}{D_{Coat}} = \sigma'_{\mathrm{steel}} \cdot D_{Steel} \tag{3.16}$$

Now, the tensile stress rate for steel pullout tests was determined as follows:

$$\sigma'_{\text{steel}} = \frac{\sigma'_{\text{CFRP}} \cdot D_{CFRP}^2}{D_{Coat} \cdot D_{Steel}} \tag{3.17}$$

$$\rightarrow \quad \sigma'_{\text{steel}} = \frac{300\ \left[{}^{\text{MPa}}/_{\text{min}}\right] \cdot (5.4\ [mm])^2}{6\ [mm] \cdot 6\ [mm]} \tag{3.18}$$

$$\rightarrow \quad \sigma'_{\text{steel}} = 248.80\ \left[\frac{\text{MPa}}{\text{min}}\right] \tag{3.19}$$

3.4.1.2.2 Heating rate

Before starting the pullout tests, the average temperature of the heating blanket, measured with four thermocouples at the blanket-concrete interface, was determinate to be approximately two degrees higher than the temperature at midway of the bonded length. This was seen on all eighteen pullout tests.

In PHPOTs, the heat controller was turned on exactly 15 minutes from the moment in which the Vishay StrainSmart 7000 data logger started recording, at a target set temperature of 180°C. The average temperature rise at the blanket-concrete interface was initially at a rate of about 24 °C/min, until 140°C, when the temperature rise continued to increase at a progressively slower rate until is reached 180°C. The three thermocouples at the concrete-reinforcing bar interface followed the rise in temperature by three minutes, with an initial rate of about 5 °C/min until minute 30, at which point the increase in temperature of these three thermocouples became logarithmic; affected by convection conditions at top and bottom of the cylinder, and by the temperature dependant thermal properties of concrete.

For those experiments in which the bond did not fail as the temperature was rising, at minute 152 the temperature at the heating blanket was increased up to 185°C, and after five minutes the temperature at the bar followed the rise in temperature.

A typical plot of the average temperature rise of the four thermocouples at the blanket-concrete interface, and of the three thermocouples along the bonded length of the reinforcing bar is shown in Figure 3.46.

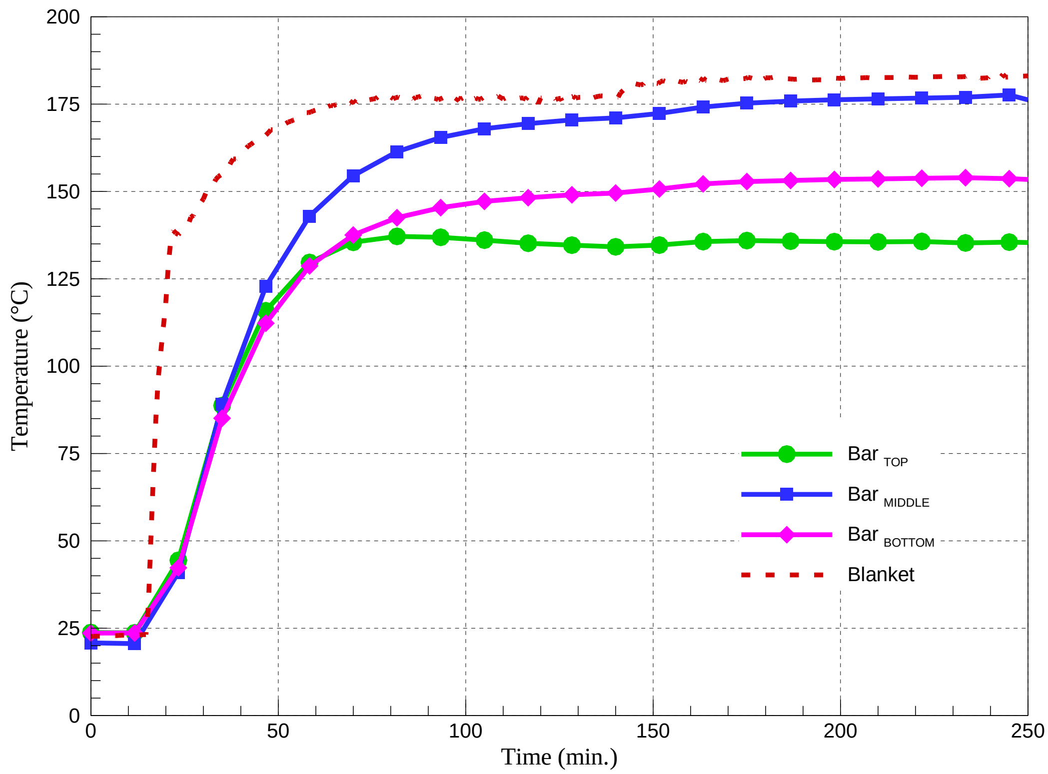

Figure 3.46: Typical temperature evolution during a pullout test (specimen CFRP_15%)

In structural fire engineering, prescriptive codes give design procedures based around standard fires and standard fire tests such as the E119 (ASTM, 2001) or ISO 834 (ISO, 1999). However, performance-based codes allow designers to consider the impact of “real” fires by using parametric fires or advanced numerical fire modelling to determine the temperatures within a fire compartment in a building.

Even though the available codes prescribe standard fires, these are implemented in furnaces across the world, which have different heat transfer conditions. It’s worth mentioning that there are not two furnaces with identical heat transfer conditions, meaning that standard fires reproduced in different furnaces most likely will not give the same heat input to an identical tested sample. In the pullout tests carried out for this research, the heat input was applied directly to the concrete using a silicone rubber heating blanket. This gave better defined heat transfer condition during the pullout testing, even if it cannot be considered as wholly representative of a typical standard fire resistance test.

The concrete surface temperature for a PHPOT compared with the E119 (ASTM, 2001) and ISO 834 (ISO, 1999) standard fires, is shown in Figure 3.47. Because of the heating blanket's limitations, its maximum temperature was 185°C, much lower than the temperatures described by any of the available standard fire curves. But as mentioned before, standard fire temperatures are applied by placing the sample inside a furnace (radiation and convection effect) and in this research the temperature was applied directly by using a heating blanket (only conduction effect). The heating blanket is actually a reasonable representation of the temperature within a concrete member at a depth of about 25 mm.

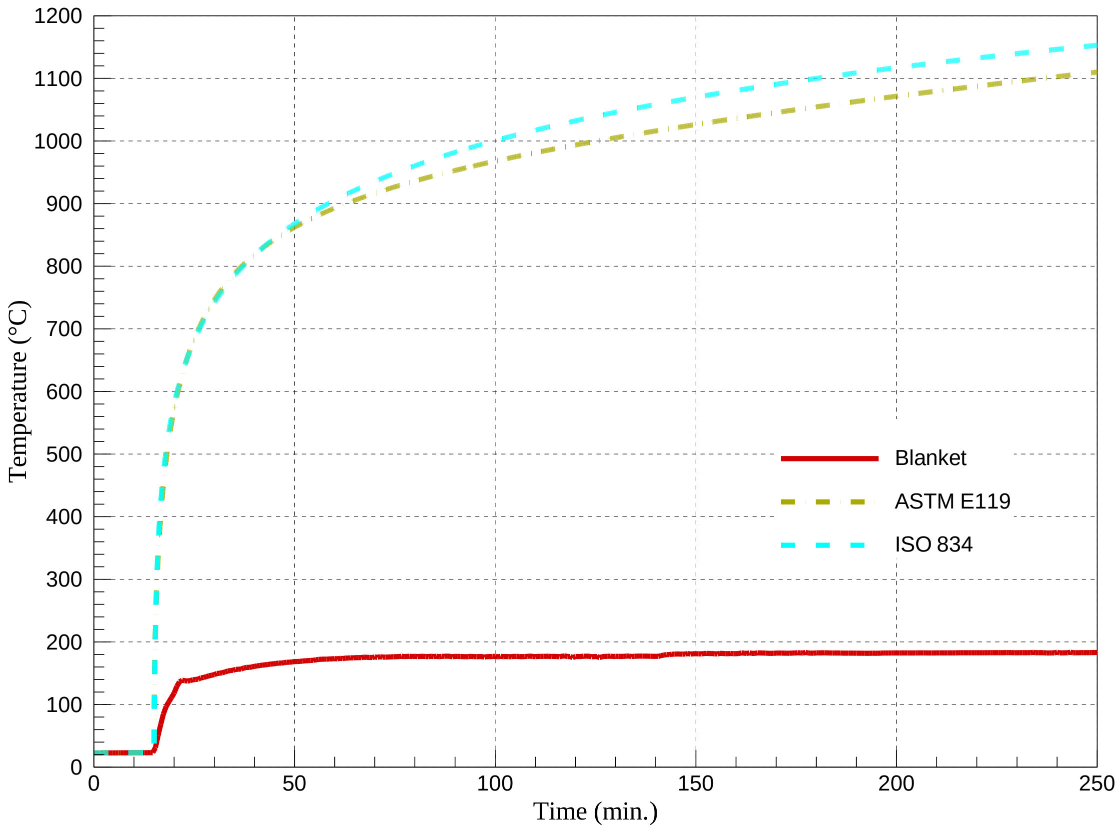

Figure 3.47: Typical concrete surface temperature in a PHPOT (specimen CFRP_15%), compared against ambient temperatures specified in standard fire curves E119 (ASTM, 2001) and ISO 834 (ISO, 1999)

3.4.1.3 Digital image correlation analysis

A unique digital image correlation analysis was chosen to measure the reinforcement slip during the pullout tests, in addition to the use of the linear potentiometers (LP's). At the free end the reinforcing bar does not experience any strain below the bonded length. This is why three groups of five 32x32 pixel patches were distributed as shown in Figure 3.48. This distribution was performed to get the average displacement from each group and check the consistency of the group's average displacement. The slip was then calculated as the average displacement from these three groups of patches.

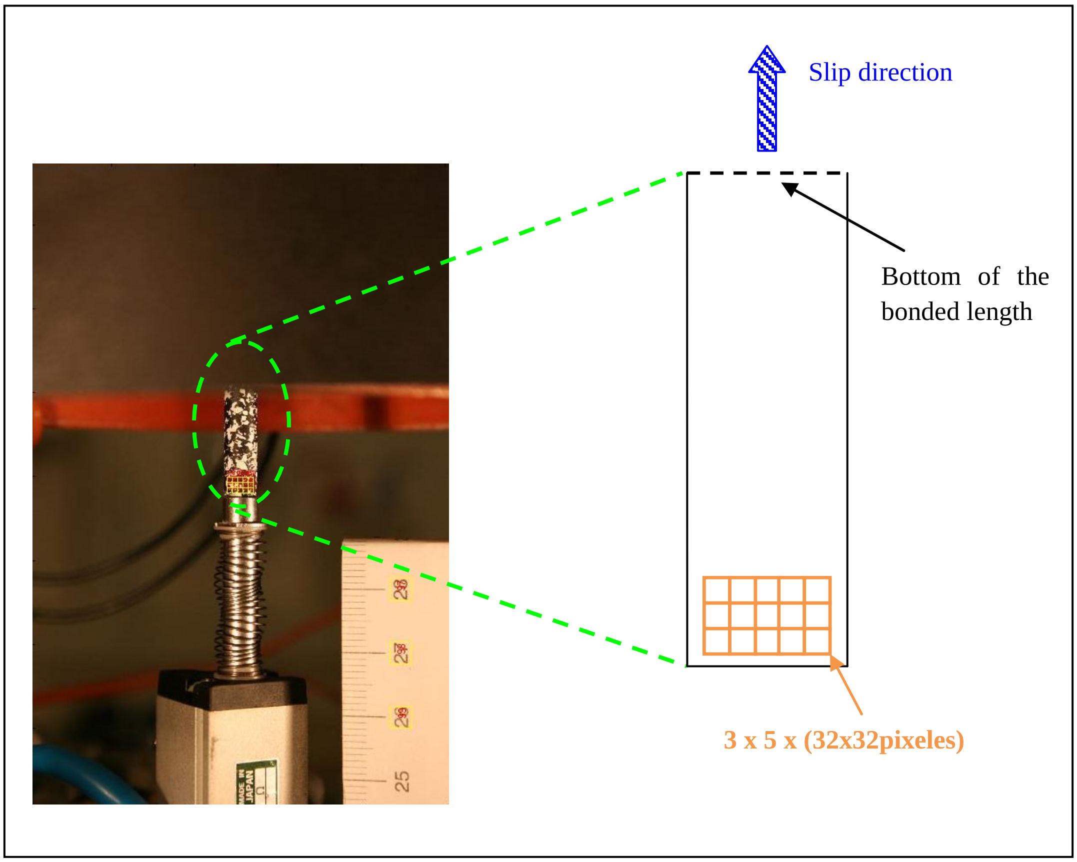

Figure 3.48: Patch distribution for image correlation analysis performed at the free end of the pullout tests

At the loaded end four groups of five 32x32 pixel patches were set along the bar's length, to determine the consistency of the measured elastic strain in the reinforcing bar, as shown in Figure 3.49.

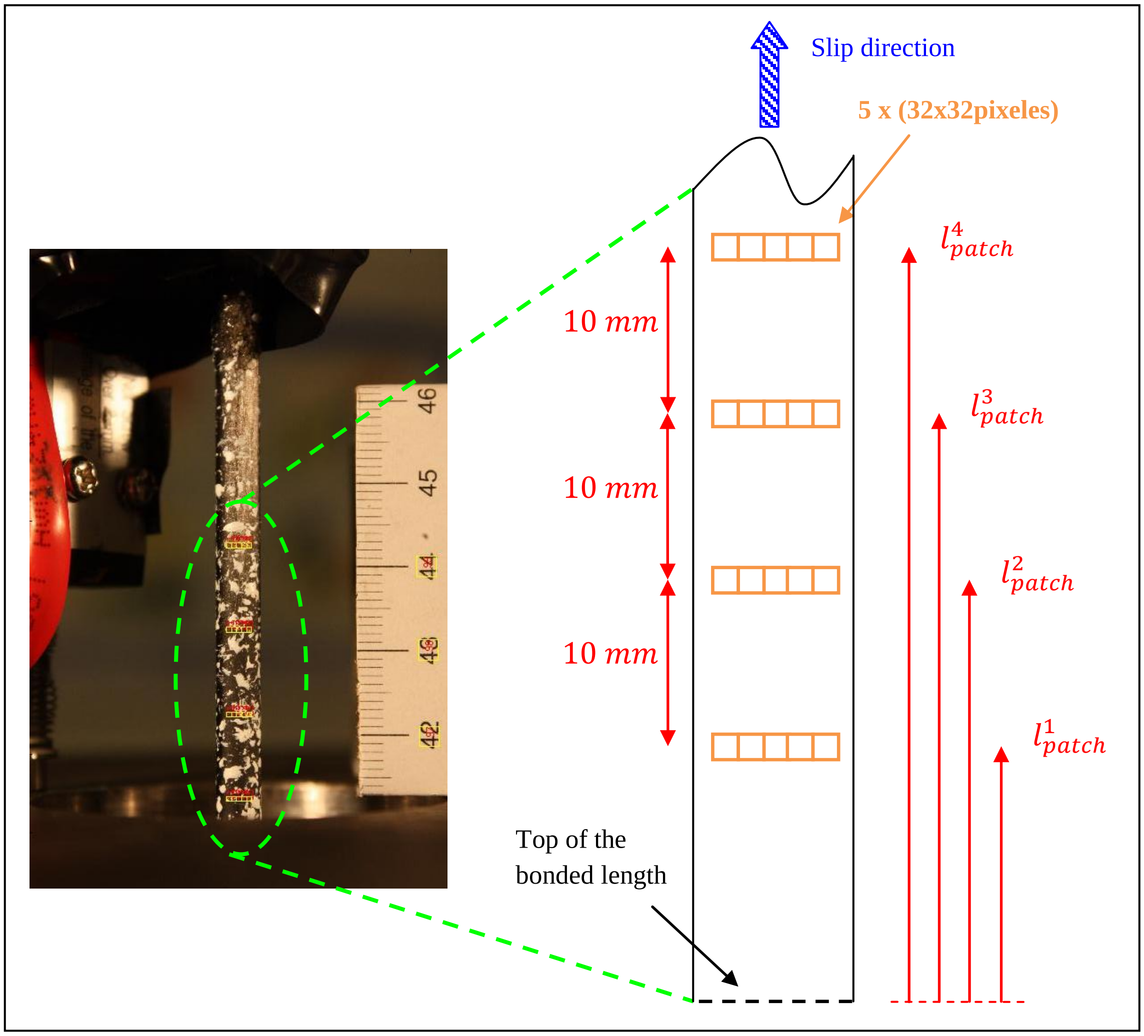

Figure 3.49: Patch distribution and gauge length for image correlation analysis performed at the loaded end of the pullout tests

At the loaded end, the elastic elongation of the bar was considered and subtracted from the average displacement of each group of patches, and the bar slip was calculated for each group of patches as follows:

$$Slip = \delta_{measured}^{i} - \delta_{elongation}^{i} \tag{3.20}$$

With:

$$\delta^i_{elongation} = \frac{\sigma_{FRP} \cdot l^i_{patch}}{E_{FRP}} \quad or \quad \delta^i_{elongation} = \frac{\sigma_{steel} \cdot l^i_{patch}}{E_{steel}} \qquad (3.21)$$

Where l^i_{patch} is the distance between the top of the bonded length and the ith group of patches. This was performed separately for each of the four groups of patches and the data were compared against each other, with very good agreement (see Figure 3.50).

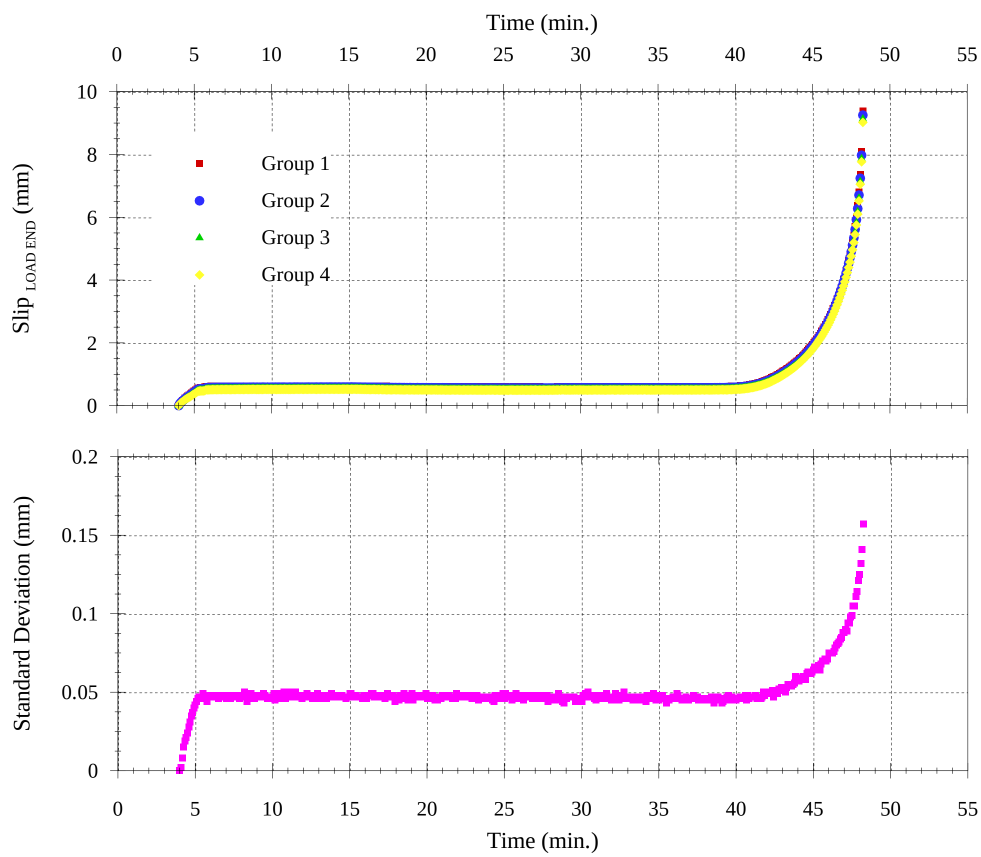

Figure 3.50: Digital image correlation analysis performed at the loaded end, showing individual plots for each patch group (specimen CFRP_60%)

Even better consistency was accomplished by performing a similar comparison of the data from the free end of the specimen, as shown on Figure 3.51.

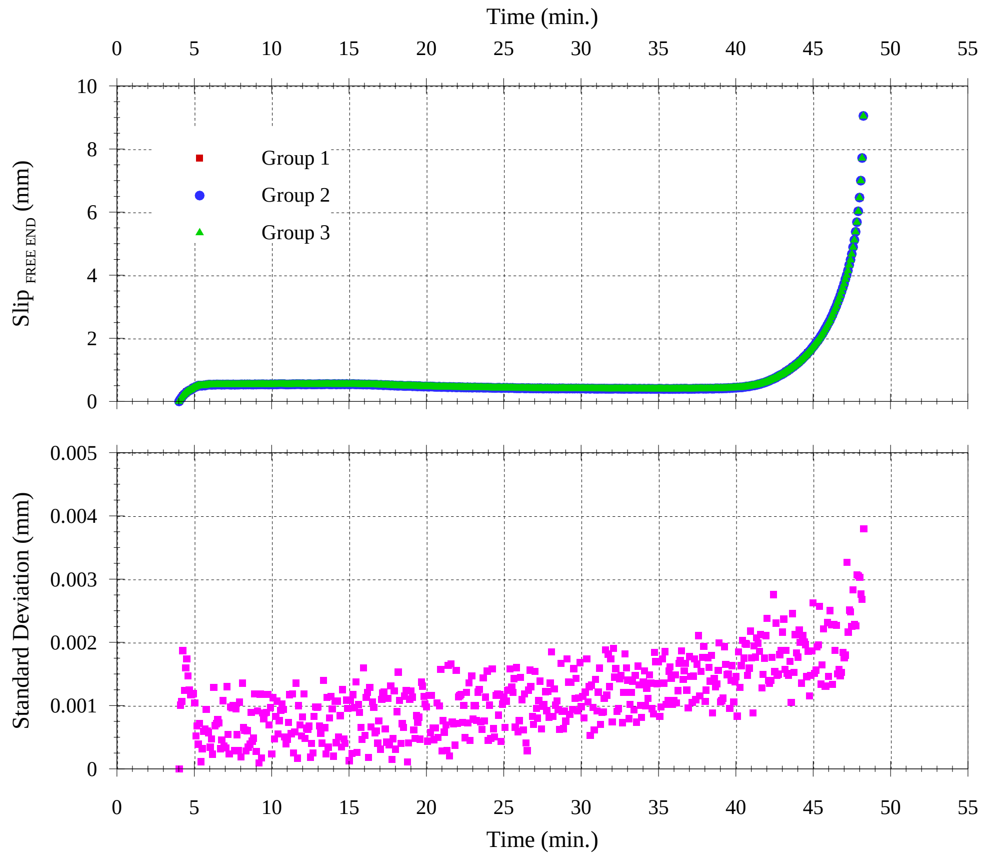

Figure 3.51: Digital image correlation analysis performed at the free end showing individual plots for each patch group (Specimen CFRP_60%)

The low standard deviation was observed in every digital image correlation analysis performed at the loaded and free end of the pullout tests.

In order to validate the measurements performed using the digital image correlation analysis, the measurements were compared with the data obtained from the linear potentiometers (LP's). This was performed for the slip at the loaded end (see Figure 3.52) and free end (see Figure 3.53), resulting in excellent agreement.

The low standard deviation values allow the digital image correlation analysis to be used to measure the slip at the loaded and free end in the pullout tests. Similar standard deviation values were found for all of the pullout tests.

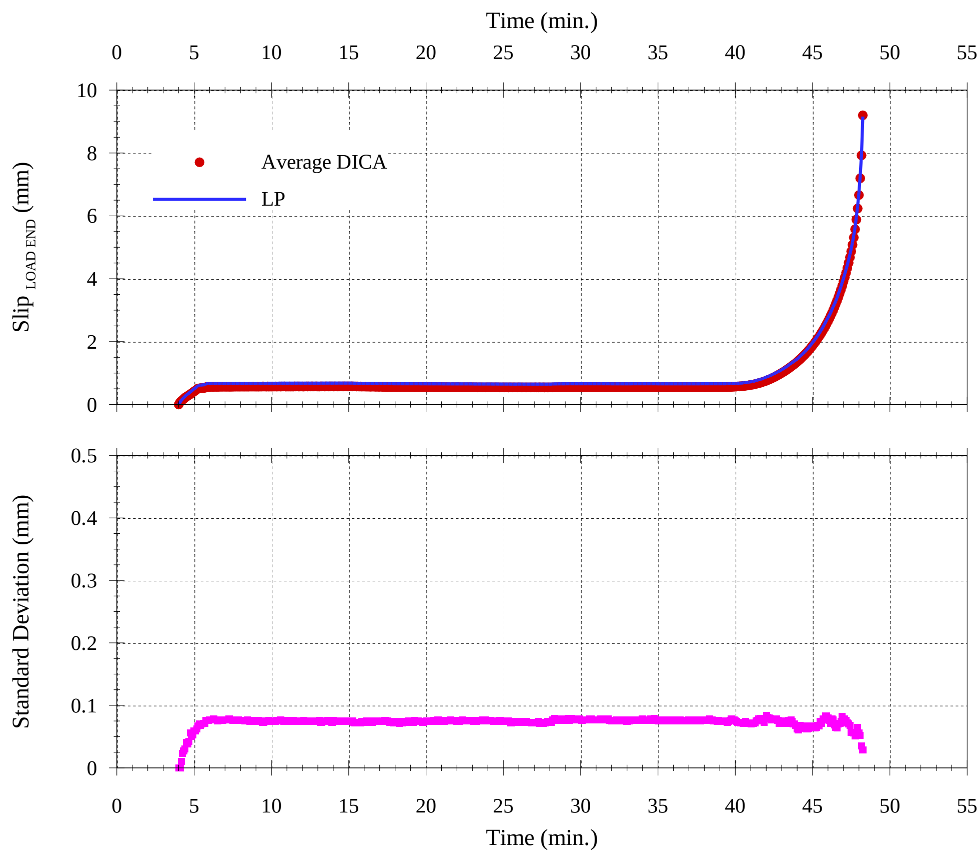

Figure 3.52: Comparisons of digital image correlation analysis (DICA) with the linear potentiometers slip measurements taken at the loaded end (Specimen CFRP_60%)

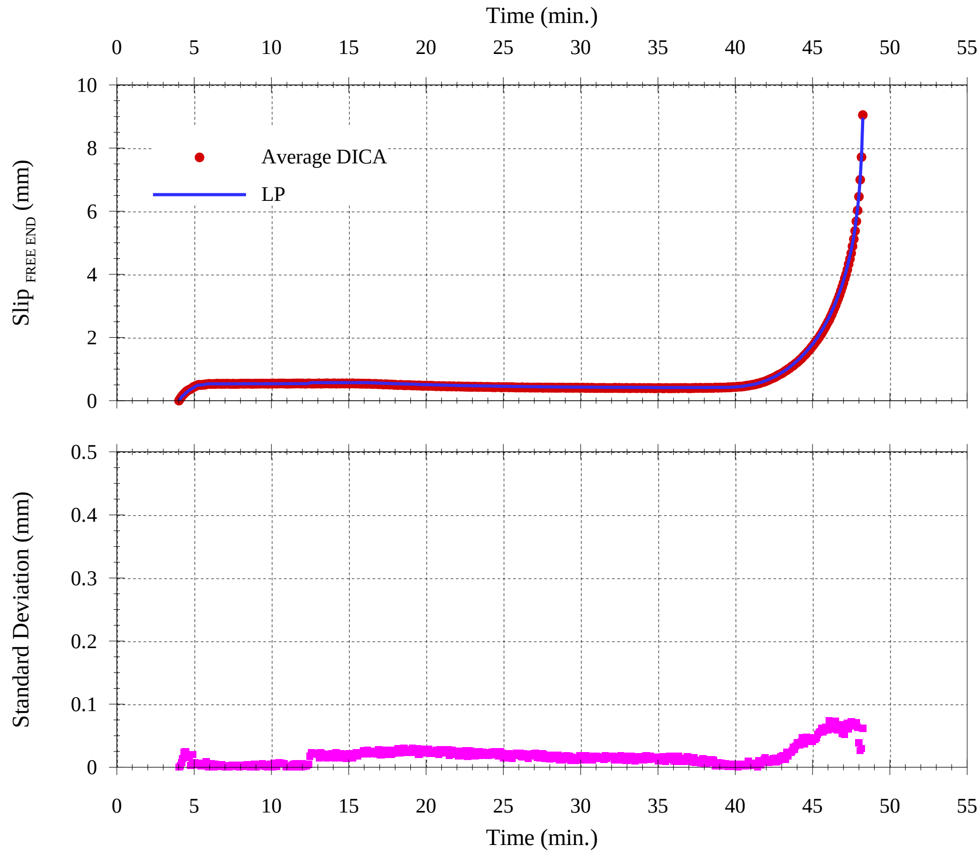

Figure 3.53: Comparisons of digital image correlation analysis (DICA) with the linear potentiometers slip measurements taken at the free end (Specimen CFRP_60%)

While analysing the data from the digital image correlation analysis, the linear potentiometers were always on the image sight. This way, the images were used to determinate the reason for any unexpected slip measured by any of the measurement systems.

3.4.1.4 Test matrix

For both CFRP and steel, two samples were first tested in the RPOT mode. The prestress level of the PHPOTs performed on the following seven samples of each reinforcing bar type was determined as a percentage of the failure loads obtained from the RPOTs, as shown in Equation (3.22). A summary of the pullout tests, and the prestress levels of each PHPOT, is given in Table 3.4.

$$Prestress\ Load_{\ PHPOT} = \frac{Prestress\ Level}{100} \times Failure\ Load_{\ RPOT} \quad (3.22)$$

Table 3.4: Test matrix of pullout tests

Test label	Embedded bar	Type of test	Presstress level
CFRP_AT_e1	CFRP	RPOT	-
CFRP_AT_e2	CFRP	RPOT	-
CFRP_15%	CFRP	PHPOT	15%
CFRP_30%	CFRP	PHPOT	30%
CFRP_38%	CFRP	PHPOT	38%
CFRP_45%	CFRP	PHPOT	45%
CFRP_53%	CFRP	PHPOT	53%
CFRP_60%	CFRP	PHPOT	60%
CFRP_68%	CFRP	PHPOT	68%
Steel_AT_e1	Steel	RPOT	-
Steel_AT_e2	Steel	RPOT	-
Steel_37%_e1	Steel	PHPOT	37%
Steel_37%_e2	Steel	PHPOT	37%
Steel_46%_e1	Steel	PHPOT	46%
Steel_46%_e2	Steel	PHPOT	46%
Steel_55%_e1	Steel	PHPOT	55%
Steel_55%_e2	Steel	PHPOT	55%
Steel_55%_e3	Steel	PHPOT	55%

During RPOTs, the data logger started recording data from the LP's at minute 0 (zero). At minute 2, the cameras started taking photos of both ends in sync, every five seconds. At minute 4, the Instron machine started pulling the bar until failure of the bond occurred.

During PHPOTs, the data logger started recording data from the LP's and thermocouples at minute 0 (zero). At minute 2, the cameras started taking photos of both ends in sync, every five seconds. At minute 4, the Instron machine started pulling the bar until the desired load level was reached. At minute 15, the heating blanket was turned on at a target set temperature 180°C.

For PHPOTs in which the bond did not failed with as temperature increased, at minute 152 the blanket temperature was set to a slightly higher target temperature of 185°C. If, with the further increase in temperature, the bond still did not fail, at minute 233 the Instron was set to pullout at a crosshead displacement rate of about $0.22\ {}^{mm}/_{min}$, until failure occurred.

3.4.2 CFRP transient thermal tensile test

For this test, a new materials testing machine at Queen’s University in Kingston, Canada was used and the tests were performed by Dr. Luke Bisby of the University of Edinburgh in collaboration with Dr. Mark Green of Queen’s University. The test was performed to determine the effects of elevated temperature on the specific strength of the CFRP tendons used in the current study.

3.4.2.1 Test procedure

A series of nine transient high temperature tensile tests was performed on the CFRP tendons at sustained stress levels between 800 MPa and 1200 MPa (a realistic stress range for pretensioning applications). The tendons were stressed to sustained loads of approximately 800, 1000, or 1200 MPa and then heated, at 10°C/min, to failure. The anchorages were protected from high temperature, as shown in Figure 3.54.

Figure 3.54: Testing equipment for transient high temperature tensile tests

3.4.2.2 Test matrix

Three specimens were tested for each service stress, 800 MPa, 1000 MPa and 1200 MPa, as shown in Table 3.5.

Table 3.5: Test matrix of CFRP tendons transient thermal tensile test

Test	**Tensile Stress (MPa)**	**Number of specimens tested**
CFRP_800MPa	800	3
CFRP_1000MPa	1000	3
CFRP_1200MPa	1200	3

3.4.3 CFRP Dynamic Mechanical Analysis

Dynamic Mechanical Analysis (DMA) is used to determine changes in the mechanical properties of materials as a function of temperature. Glass transition temperature can also be measured by running this analysis. This analysis works by measuring stress and strain during sinusoidal flexure loading of the sample on elastic range of the CFRP tendon, as the temperature of the sample increases at a given rate.

On this research, CFRP samples, as described in Section 3.2.2, were subjected to DMA. Instead of using a constant increase of temperature, the ramp in temperature was build up from data recorded in the pullout tests. The temperature measured on the bar on each one of the seven CFRP PHPOTs was averaged to generate the heat ramp for the DMA tests. Because the CFRP_68% test failed before the heating blanket was switched on, that test was not considered to calculate the DMA heat ramp.

Because the tendon's temperature was measured by three thermocouples located at the top, middle and bottom of the bonded length, the temperature from the thermocouples was interpolated by a Lagrange polynomial and the area under the curve is then divided by the bonded length to calculate the mean temperature. The calculations are graphically explained in Figure 3.55.

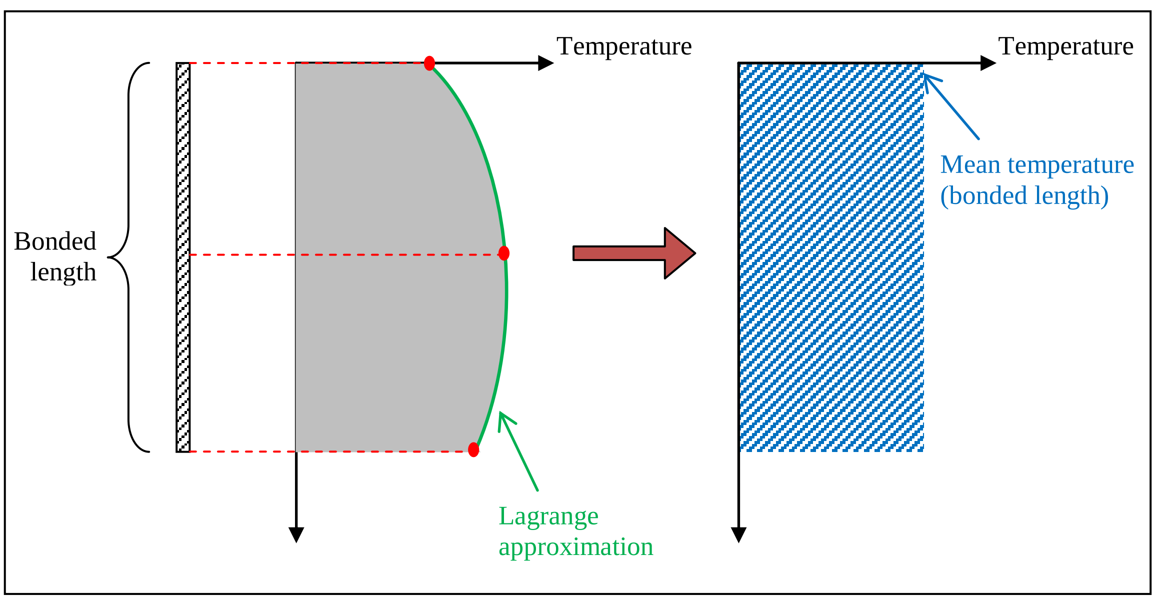

Figure 3.55: Diagram of Lagrange polynomial approximation into a mean bonded length temperature

This temperature is used as the bar temperature, for both CFRP and steel pullout tests, for results display, and also used as an input in the heat ramp of the sample used in the DMA analysis.

$$\begin{matrix} Mean\ bonded \\ length\ temperature \end{matrix} = \frac{\int Lagrange\ polynomial}{Bonded\ length} \qquad (3.23)$$

The bar temperature over time, in the six tests, is shown in Figure 3.56 and the ramp for DMA analysis was calculated as the average of this six tests.

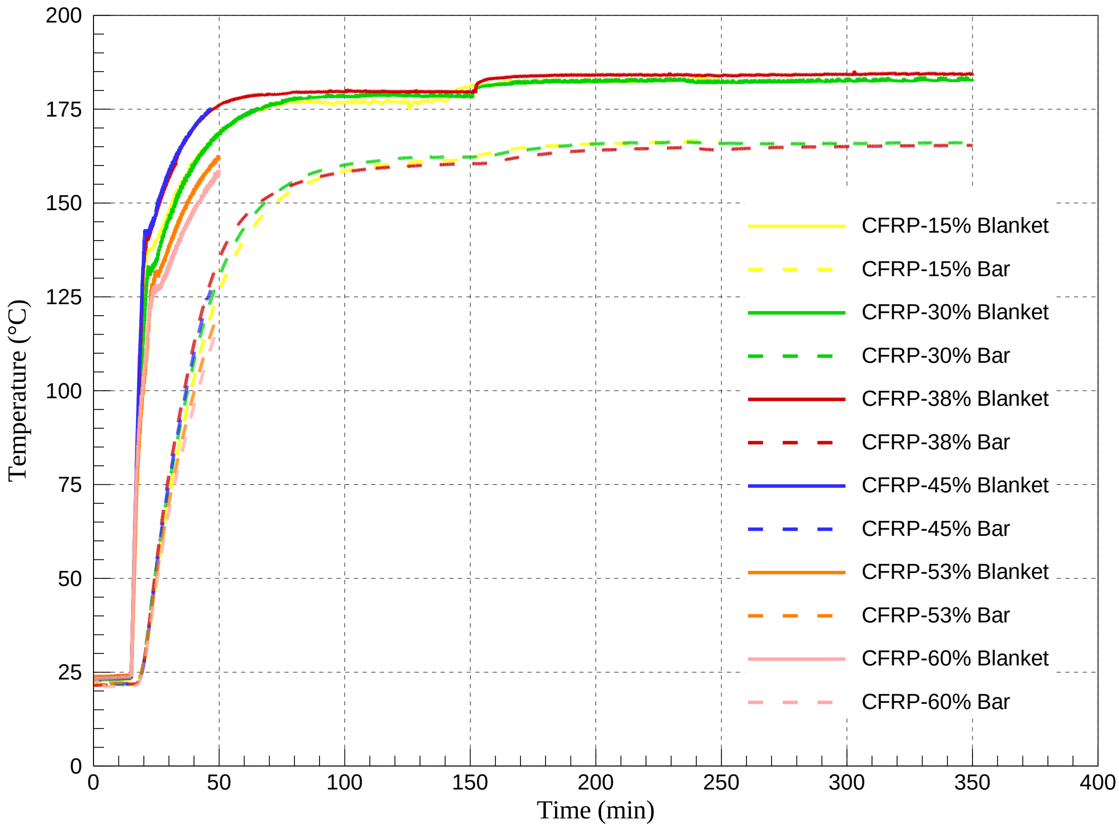

Figure 3.56: Average temperature of the heating blanket and mean bonded length temperature evolution during six pullout tests used to build up the DMA temperature ramp

3.4.3.1 Test procedure

The experiments were conducted at The Materials Laboratory, located within King's Buildings Campus at the University of Edinburgh.

Carbon fibres don't suffer considerable deterioration under 600°C (Schwartz, 2002), which makes the carbon fibre deterioration, through the DMA test, marginal. This is why this test setup only measures the changes in the mechanical properties of the epoxy.

The span between the supports is 15 mm and the rate of loading was determinate in order to allow a deflection of 20 microns. The sample is placed and tested as shown in the images below, Figure 3.57.

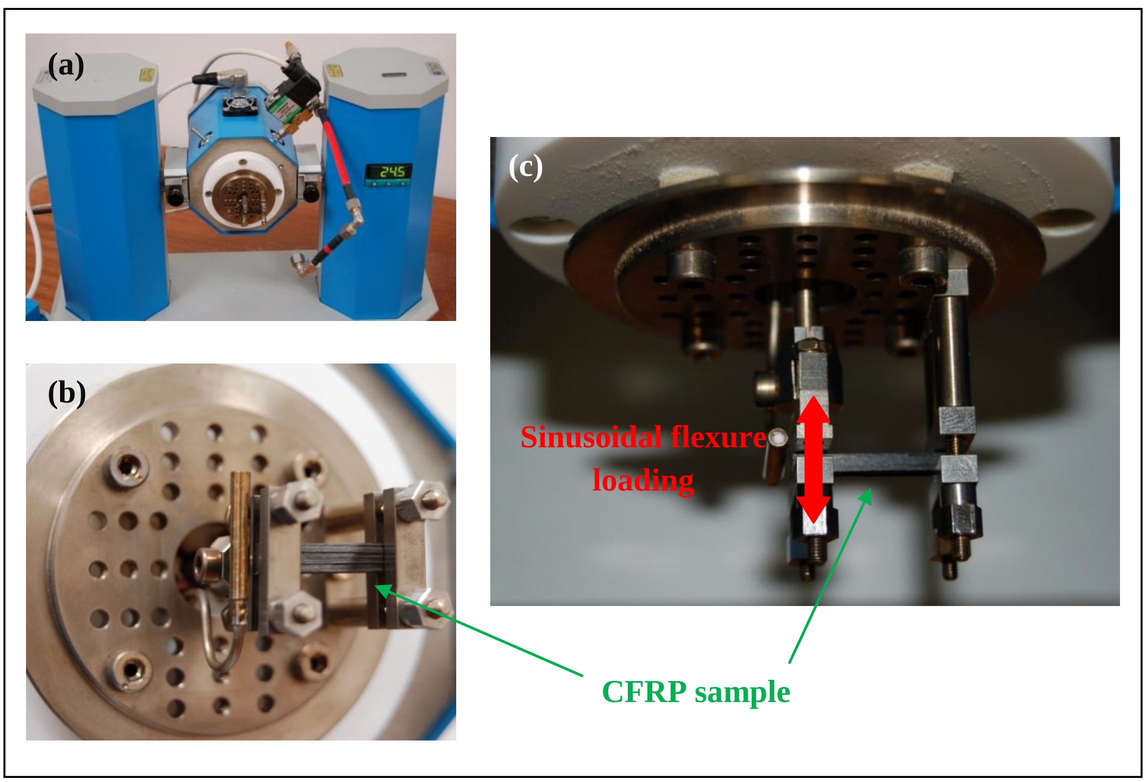

Figure 3.57: Images of **(a)** Tritec 2000 DMA machine, **(b)** CFRP sample mounting for single cantilever bending and **(c)** sinusoidal flexure loading of the CFRP sample.

3.4.3.2 Test matrix

In some samples, the test was executed twice, as summarized in Table 3.6. This was performed to check if additional curing occurred during the first test, implying that the CFRP's epoxy was not fully cured. When running the DMA analysis for a second time, the glass transition temperature moved up to a higher temperature, which meant that cure took place during the first run of the test.

Table 3.6: Test matrix of DMA tests on CFRP samples

Test	Heat Ramp	Loading condition
DMA_1.1 DMA_1.2	Extracted from the pullout tests average	Single cantilever bending Sinusoidal flexure
DMA_2.1 DMA_2.2		
DMA_3.1 DMA_3.2	3 °C/min	
DMA_4		
DMA_5		

3.4.4 EMPA large scale fire tests

Seven large scale fire tests were performed on CFRP prestressed HPSCC slabs in a floor furnace at EMPA laboratories (Swiss Federal Laboratories for Material Testing and Research). The fire endurance tests were conducted in accordance with the ISO 834 (ISO, 1999). Figure 3.58 shows schematics of the specimens and test setup.

Initial scoping tests performed on small scale slabs (Terrasi, 2010) indicated that loss of bond between the FRP tendons and the concrete was a governing factor in determining the fire resistance of the CFRP prestressed slabs. Bond failure occurred at bond line temperatures near the glass transition temperature of the CFRP's epoxy matrix (Tg = 148°C for these CFRP tendons). Thus, the testing programme included slabs with unheated overhangs (of varying length) at each end to provide a cold anchorage region during fire testing. The smallest anchorage length (160 mm) represented the room temperature prestress development length for a tendon stress of 1200 MPa, as determined from previous testing presented in Section 3.2.1.1. The slab thickness, and hence the cover to the reinforcement, varied between 45 mm and 75 mm. The 100 MPa compressive strength concrete incorporated 2 kg/m3 of short polypropylene (PP) fibers and had a high moisture content at the time of testing (4.4-4.8%). The load in the central span corresponded to a typical service load condition (Terrasi, 2007). One slab used 6 mm Ø cold-drawn steel prestressing wire stressed to 1200 MPa.

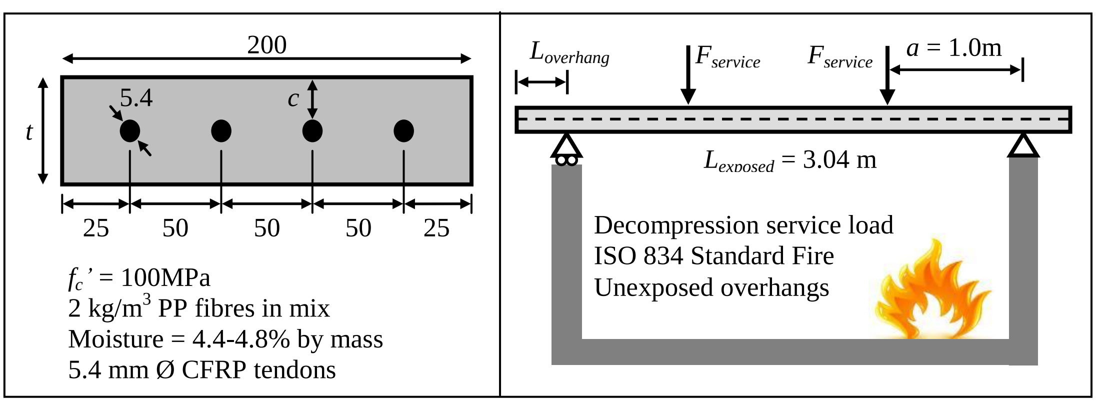

Figure 3.58: Details of fire test specimens and fire test setup.

3.4.5 Concrete compressive strength test

This test was performed to determine the compressive strength of the cylindrical concrete specimens made from the same batch of concrete as the pullout specimens. Results from these tests are presented in Appendix A.

3.4.5.1 Test matrix

To determine the development of the compressive strength of the concrete with time, compressive tests were repeated at 7, 14, 28, 49 (date of the first pullout tests) and 84 (date of the last pullout tests) days.

Table 3.7: Test matrix of concrete compressive strength tests

Test	Concrete's age (days)	Number of specimens tested
HPSCC_7d_c	7	3
HPSCC_14d_c	14	3
HPSCC_28d_c	28	3
HPSCC_49d_c	49	3
HPSCC_84d_c	84	3

3.4.5.2 Test procedure

The experiments were conducted at The Structures Laboratory, located within King's Buildings Campus at the University of Edinburgh.

Each test was performed according to ASTM (2003b). This method is based on the application of a compressive axial load to a concrete cylinder at a constant rate until failure occurs. For each test, the specimen was placed in an Avery compressive testing frame, making sure that the side of the cylinder was prepared for digital image correlation analysis, as described in Section 3.2.3.1, and was facing a digital camera. A second digital camera was placed facing the Avery machine's load display (see Figure 3.59) in order to correlate the images and obtain the applied load at which each photo was taken.

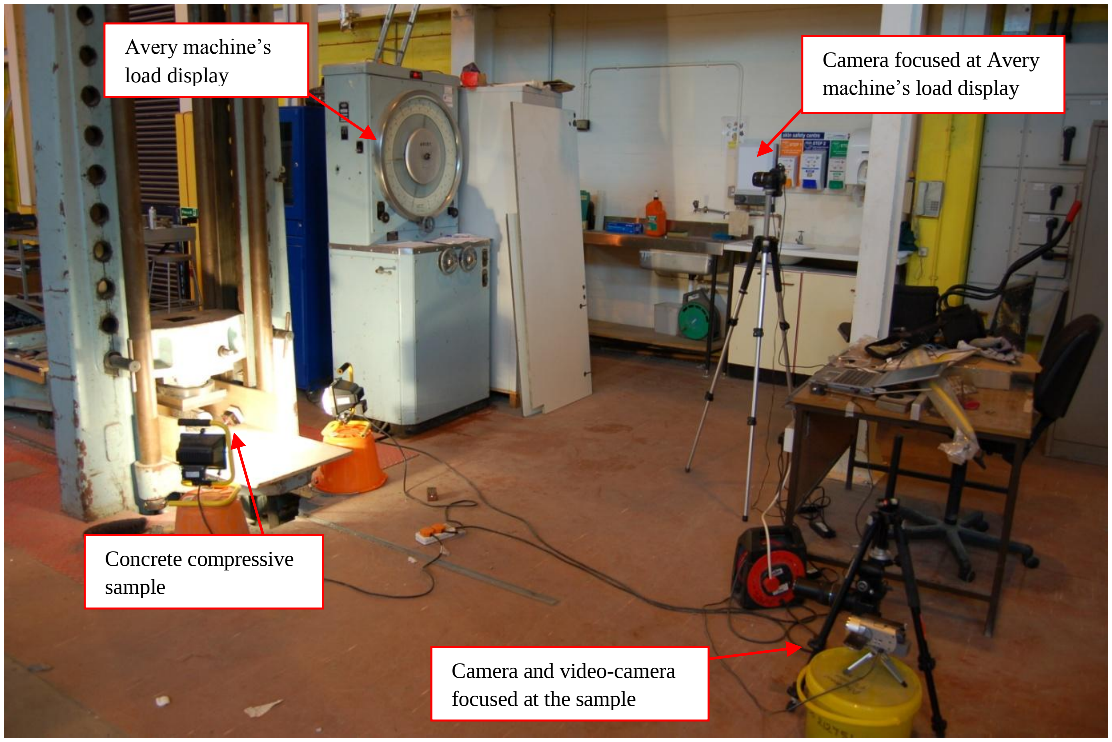

Figure 3.59: Camera setup for image correlation analysis performed on concrete compressive strength and splitting tensile strength tests

After each compressive strength test was executed, the sample was weighted and left inside an oven for a minimum of seven days. This way, the water content of each sample was determined at the moment it was tested.

3.4.5.3 Loading rate

ASTM (2003b) indicates that the sample should be loaded at a rate of 15 MPa/min. The Avery machine operates by setting the loading rate in kN/min; this value is calculated as follows:

$$Loading\ rate = 15\ \left[\frac{MPa}{min}\right] \times Cross\ sectional\ area \tag{3.24}$$

$$= 15\left[\frac{{}^{N}/_{mm^2}}{min}\right] \times \left[\pi \cdot \frac{(4 \cdot 25.4\ [mm])^2}{4}\right] \tag{3.25}$$

$$= 121.6\ \left[\frac{KN}{min}\right] \approx 120\ \left[\frac{KN}{min}\right] \tag{3.26}$$

3.4.5.4 Digital image correlation analysis

This analysis was performed to determine the strain in the concrete as it was being subjected to compressive stresses. The modulus of elasticity was also obtained from this analysis.

Pixels patches were set along the concrete sample's length in pairs in order to measure the strains in concrete using different gauge lengths (see Figure 3.60 and Table 3.8). This is one of the key advantages of using the image correlation analysis in experiments, as opposed to conventional instrumentation typically used in such experiments. The digital images can be used for further analysis in order to obtain an essentially infinite combination of strain gauges anywhere on the sample within the plane of the image.

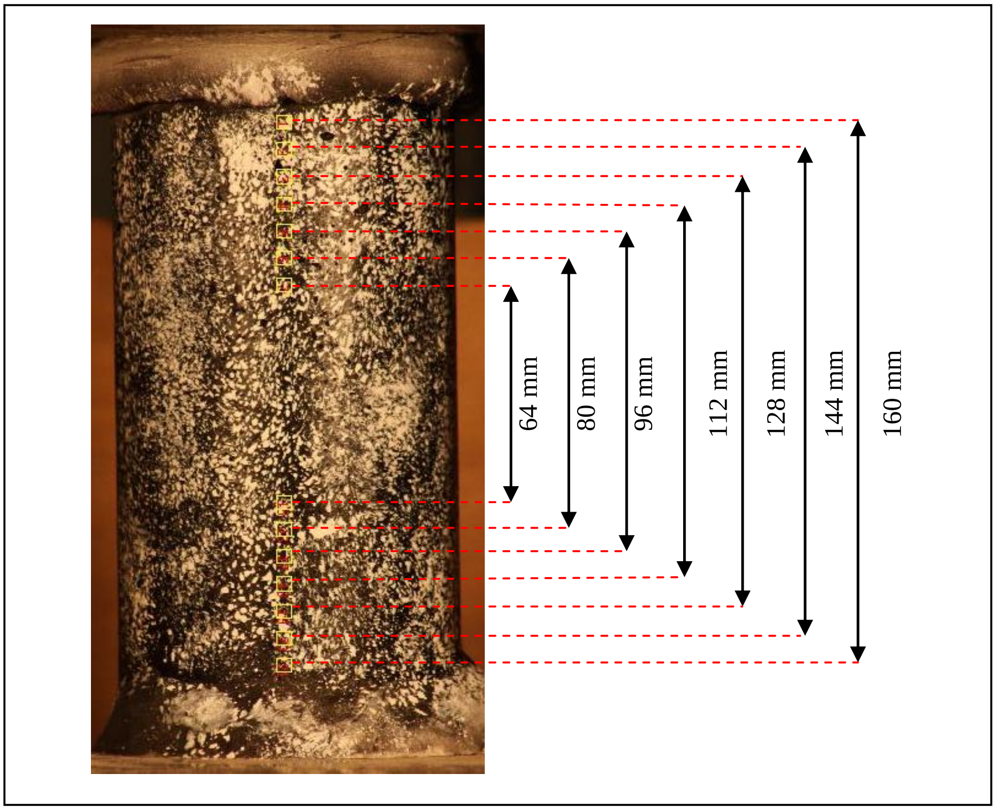

Figure 3.60: Patch distribution and gauge lengths used in the image correlation analysis performed for the compressive strength tests

Table 3.8: Label and gauge length used in the image correlation analysis performed for the compressive strength tests

Pixel patch couple	Optical strain gauge	
	(pixels)	(mm)
C1	2560	160
C2	2304	144
C3	2048	128
C4	1792	112
C5	1536	96
C6	1280	80
C7	1024	64

3.4.5.5 Results of a typical test

An analysis of all seven gauge lengths shown in Figure 3.60 was performed for each compressive strength experiment, and a typical result is shown in Figure 3.61. It can be seen that the consistency between the strains measured with the optical technique at different gauge lengths has a maximum standard deviation of about 100 μm.

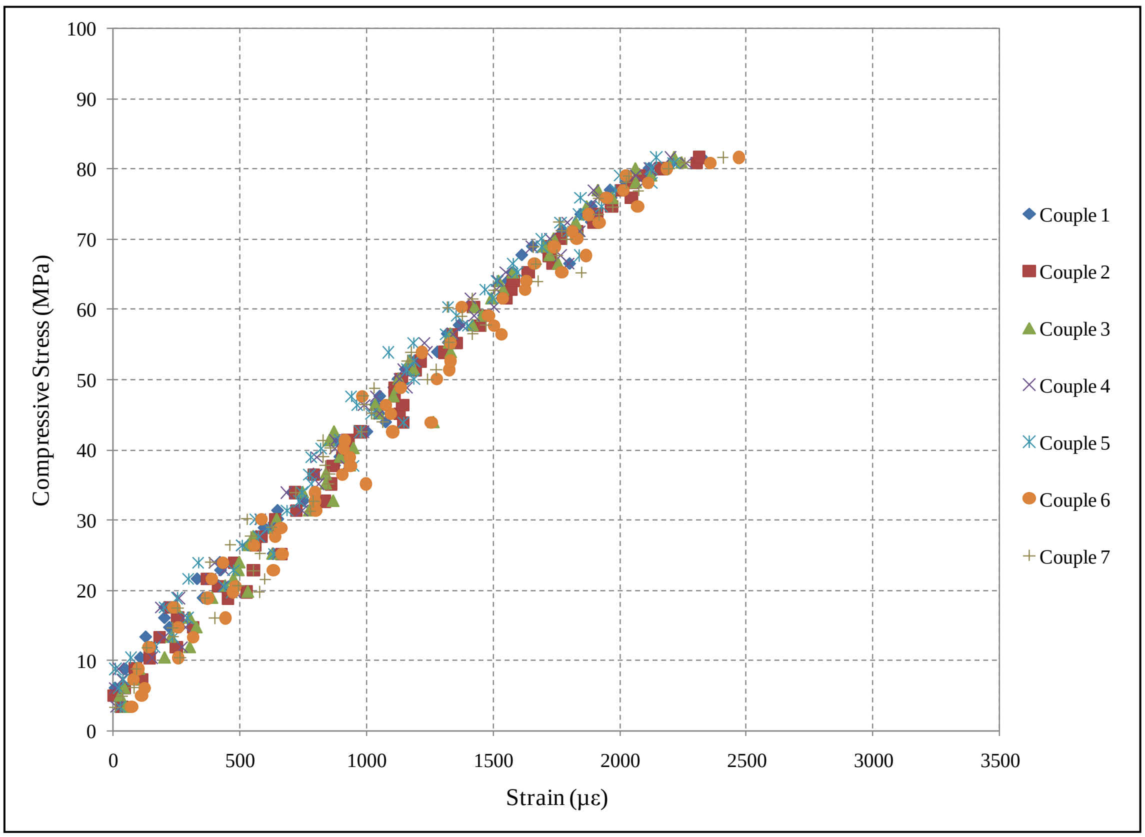

Figure 3.61: Typical applied stress versus axial strain curve determined by digital image correlation analysis performed on a compressive strength test of a concrete cylinder (Test HPSCC_84d_c3)

The modulus of elasticity was calculated from the average strain of the seven gauge lengths. A straight line which fits the average experimental data by the least squares linear regression method was calculated, as shown in Figure 3.62. The slope of such linear approximation is considered to be the modulus of elasticity of the concrete sample. ASTM (2002) states that the modulus of elasticity of concrete is to be measured in the range of strains between 50 µm and the strain produced by 40% of the ultimate load. The average strain has an uncertainty smaller than $8e^{-9}$ on every test.

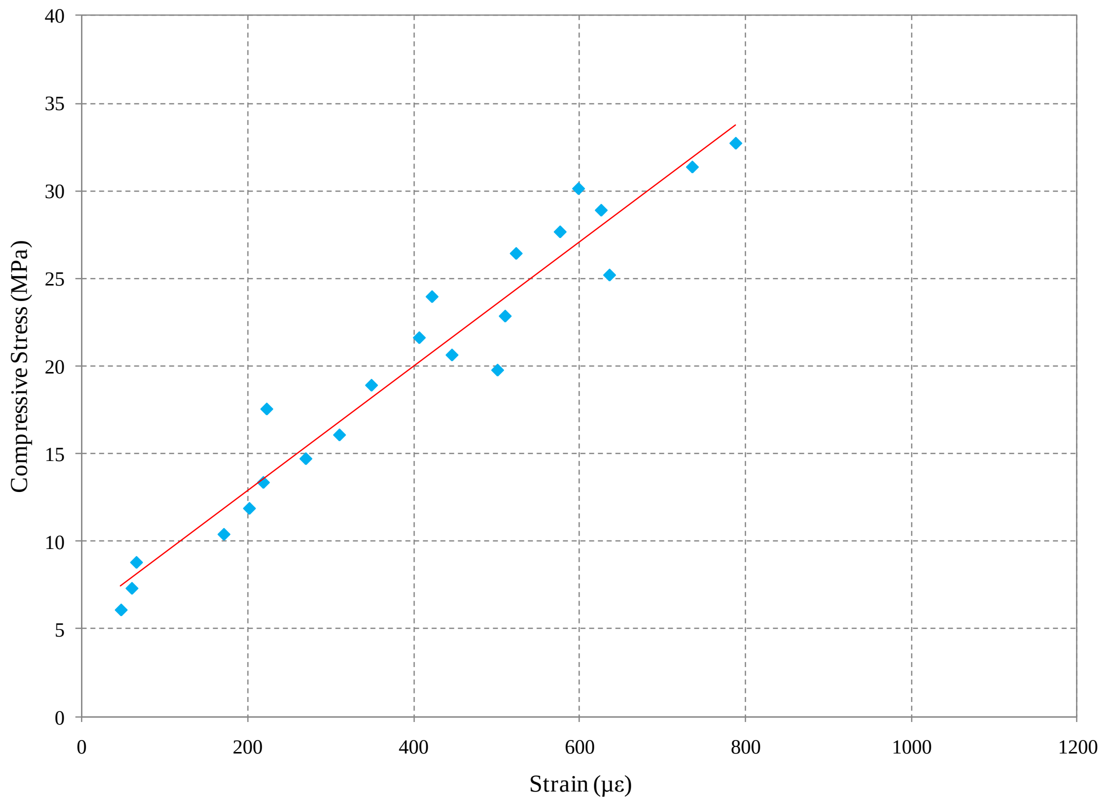

Figure 3.62: Typical modulus of elasticity determination by digital image correlation analysis performed on compressive strength test of a concrete cylinder (Test HPSCC_84d_c3)

3.4.6 Concrete splitting tensile strength test

This test was performed to determine the splitting tensile strength of the cylindrical concrete specimens made from the same batch of concrete as pullout specimens. Results from these tests are presented in Appendix B.

3.4.6.1 Test matrix

The tensile strength of the concrete is a fundamental input in predicting the crack generation due to thermal incompatibility between CFRP tendons and concrete (see Section 6.2). The concrete splitting tensile strength tests were executed at 28 and 84 days (date of the last pullout test), as summarized in Table 3.9.

Table 3.9: Test matrix of concrete splitting tensile strength tests

Test	Concrete's age (days)	Number of specimens tested
HPSCC_28d_st	28	3
HPSCC_84d_st	84	3

3.4.6.2 Test procedure

The experiments were conducted at The Structures Laboratory at the University of Edinburgh. Each test was performed according to ASTM (2004).

3.4.6.3 Loading rate

A formula for computing the horizontal tensile stress distribution across the vertical diameter for the splitting tensile tests was obtained based on the theory of linear elasticity developed by Chen and Chen (1976), with the parameters defined in Figure 3.63.

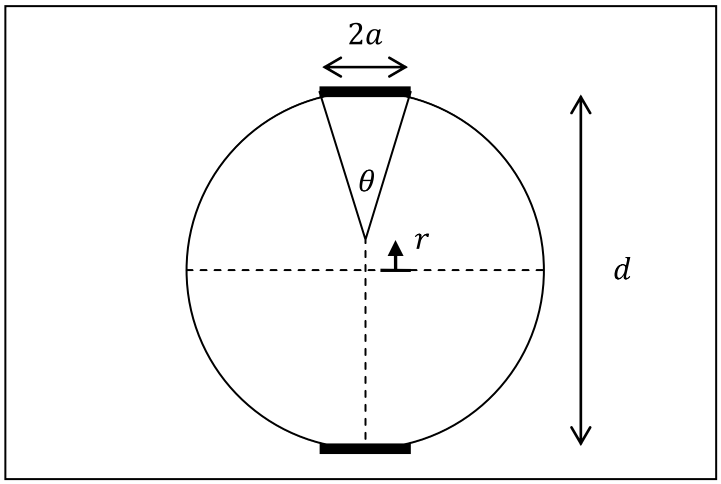

Figure 3.63: Schematics of a concrete splitting tensile strength test

Where:

$d = 101.6\,mm$ $\quad(cylinder's\ nominal\ diameter)$

$l = 200\,mm$ $\quad(cylinder's\ nominal\ length)$

$2a = 23.74\,mm$ $\quad(bearing\ strips\ width\ according\ to\ ASTM\ standard)$

The horizontal tensile stress distribution across the vertical diameter is:

$$\sigma(\theta) = \frac{2 \cdot P}{\pi \cdot l \cdot d} \cdot \left[1 - \frac{d}{4 \cdot a}(\theta - \sin\theta)\right] \tag{3.27}$$

At the centre of the cylinder, the value of θ is:

$$\theta(r = 0\,mm) = 4 \cdot \frac{a}{d} = 0.4674\,rad \tag{3.28}$$

The horizontal tensile stress at the centre of the cylinder is:

$$\sigma(\theta = 0.4674\,rad) = \sigma(r = 0\,mm) = \frac{2 \cdot P}{\pi \cdot l \cdot d} \cdot 0.9640 \tag{3.29}$$

ASTM (2004) calculates the maximum horizontal tensile stress on a splitting tensile strength test as follows (assuming $\theta = 0$ at the centre of the cylinder):

$$\sigma_0^{ASTM} = \frac{2 \cdot P}{\pi \cdot l \cdot d} \tag{3.30}$$

The suggested calculation of the maximum horizontal tensile stress indicated in the ASTM (2004) overestimates the value by 3.6%.

$$1 - \frac{\sigma(\theta = 0.4674\, rad)}{\sigma_0^{ASTM}} = 1 - 0.964 = 0.036\ \ (3.6\%) \tag{3.31}$$

The specimens were loaded at a rate of $\dot{\sigma}(r = 0\, mm) = 1.15\, \left[{}^{MPa}/_{min}\right]$. As previously noted, the Avery machine that was used for these tests operates by setting the rate of the load P at kN/min. Again, with the formula obtained by the theory of linear elasticity, the loading rate is calculated.

$$\dot{P} = \frac{\dot{\sigma}(r = 0\, mm) \cdot \pi \cdot l \cdot d}{2 \cdot 0.9640} = 36705.37 \frac{N}{min} \approx 35 \frac{KN}{min} \tag{3.32}$$

3.4.6.4 Digital image correlation analysis

This analysis was performed in order to verify another application area for the unique image correlation analysis technique. The objective was to measure the crack opening across the vertical diameter as the sample failed. In order to do this, the sample was prepared by texturizing the surface with paint, as mentioned in Section 3.2.4.1.

For this analysis, pairs of patches were set on both sides of the crack across the vertical diameter, the pixels patch pairs were labelled and the distance from the centre (r) is shown in Table 3.10. Patches lined up in groups of two, were 256 pixels away from each other, as shown in Figure 3.64. The resolution achieved in this experiment was $20.60\, {}^{px}/_{mm}$. Since once the crack opens up the zone next to the crack is not subject to any stress, the relative displacement between patches is equivalent to the size of the crack on the vertical diameter.

Table 3.10: Labels and vertical positions of the pixel patches used in the image correlation analysis performed on tensile splitting strength tests.

Couples	r (pixels)	r (mm)
Couple 1	960	46.6
Couple 2	832	40.4
Couple 3	704	34.2
Couple 4	576	28.0
Couple 5	448	21.7
Couple 6	320	15.5
Couple 7	192	9.3
Couple 8	64	3.1
Couple 9	64	-3.1
Couple 10	192	-9.3
Couple 11	320	-15.5
Couple 12	448	-21.7
Couple 13	576	-28.0
Couple 14	704	-34.2
Couple 15	832	-40.4
Couple 16	960	-46.6

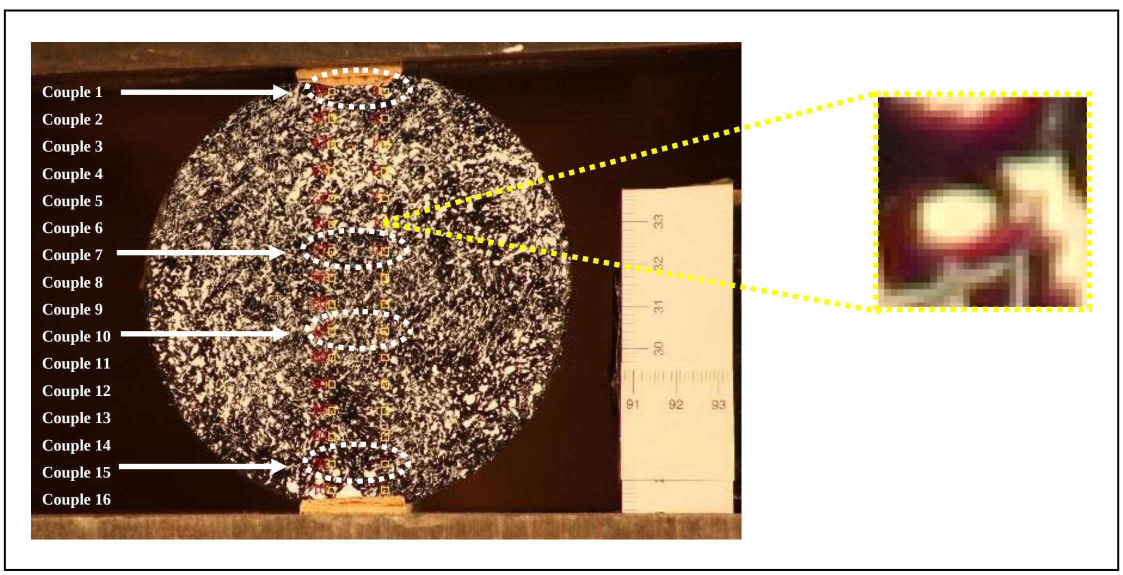

Figure 3.64: Patch distribution used in the image correlation analysis performed on splitting tensile strength tests

3.4.6.5 Results of a typical test

From the analysis performed with the digital image correlation technique, the relative displacement between patches across the vertical diameter was plotted, as shown in Figure 3.65. Each curve represents a moment in time (a load level). The maximum horizontal tensile stress calculated at the centre of the cylinder at a given load level is labelled in the legend. After the crack across the vertical diameter is first generated, the load capacity of the sample keeps on increasing but because of the crack, no horizontal tensile stress takes place across the vertical diameter. For the concrete splitting tensile strength test, ASTM (2004) indicates that the sample must be loaded up till the maximum load capacity is achieved.

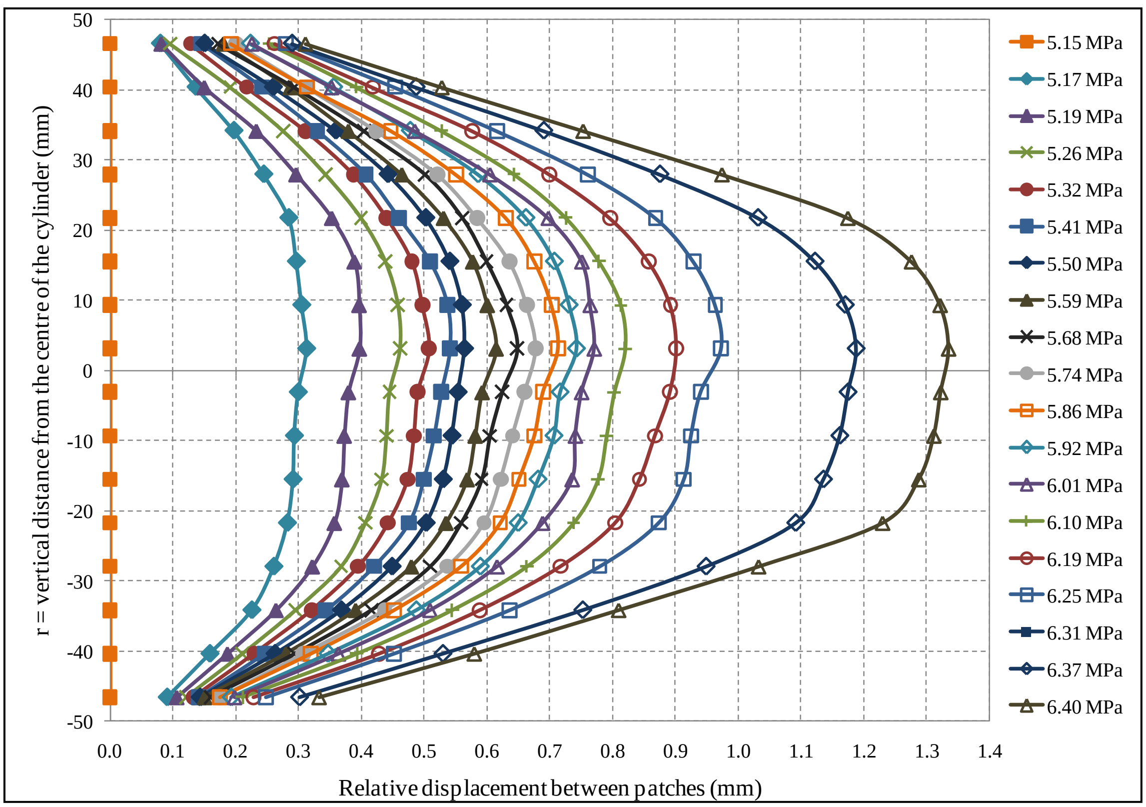

Figure 3.65: Relative displacement between patches in a concrete splitting tensile strength test (HPSCC_84d_st3), for different horizontal tensile stresses at the centre of the cylinder

It should be recalled that the photos were taken every five seconds. In Figure 3.65, when the horizontal tensile stress at the centre of the cylinder was 5.15 MPa, no significant relative displacement was measured. In the subsequent image, when the calculated horizontal tensile stress at the centre of the cylinder was 5.17 MPa, significant relative displacement was measured between patches.

Test HPSCC_84d_st3 showed no significant relative displacement up until the horizontal stress at the centre of the cylinder was 5.17 MPa, load level at which a crack opened up across the vertical diameter. The sample kept on increasing its load capacity as the crack kept on opening, and failed at a calculated maximum horizontal tensile stress of 6.40 MPa.

The results from the digital image correlation analysis performed in concrete splitting tensile strength tests can also be displayed as shown in Figure 3.66, in which the maximum calculated horizontal tensile stress is plotted against the measured relative displacement between patches across the vertical diameter.

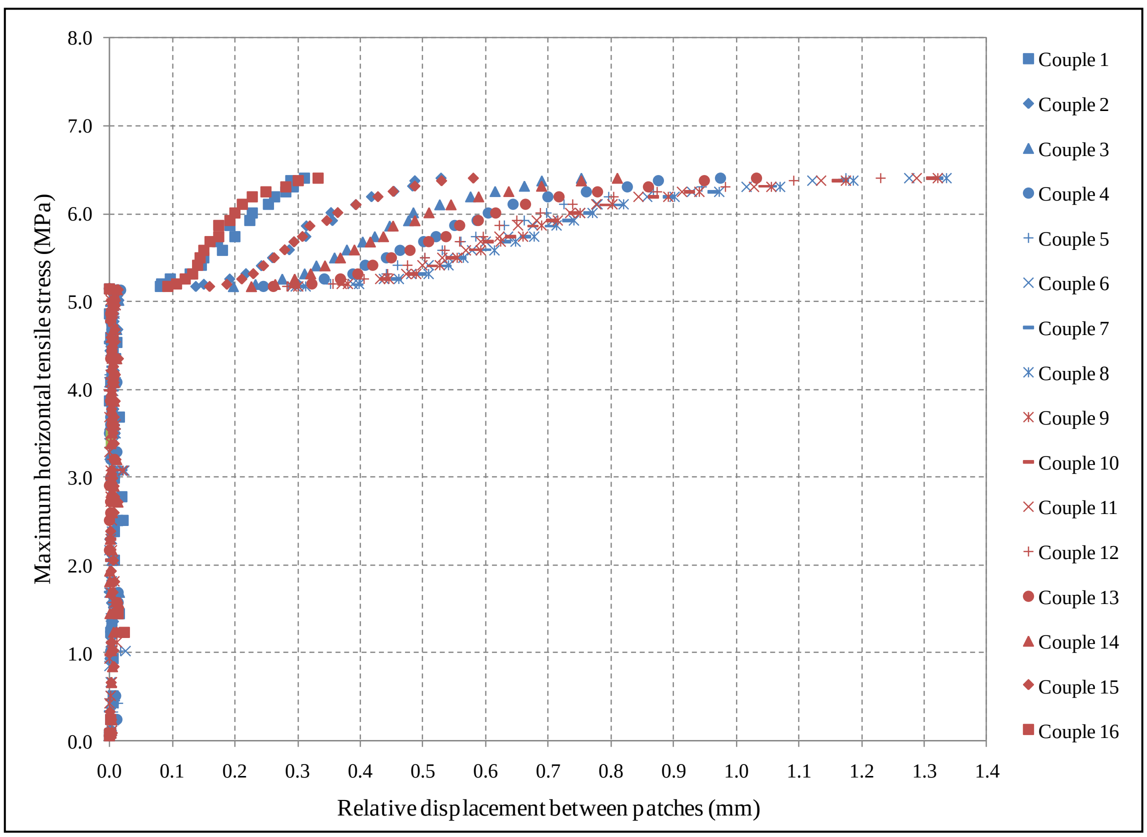

Figure 3.66: Relative displacement between patches in a concrete splitting tensile strength test (HPSCC_84d_st3), for different couple of patches

Figure 3.67 shows a zoom-in from the load level at which the crack across the vertical diameter is first generated. The concrete sample keeps on increasing its load capacity in the splitting tensile strength test setup.

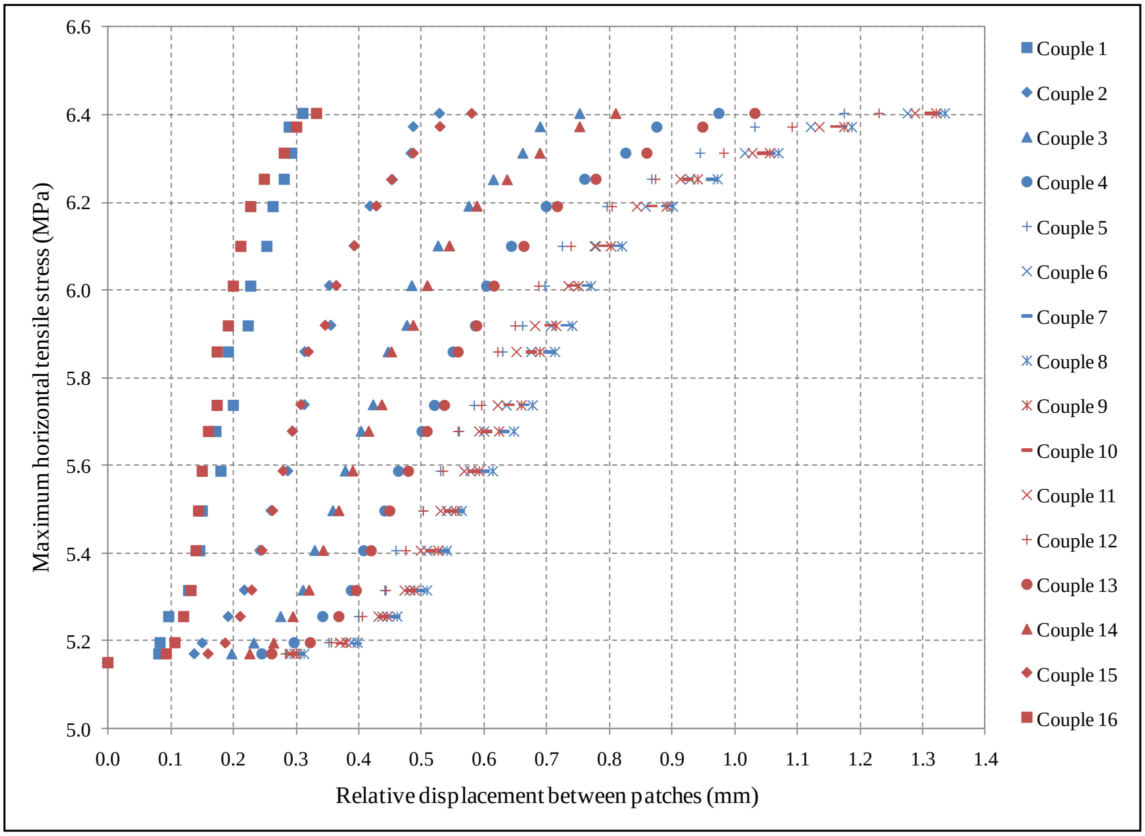

Figure 3.67: Zoom-in of the relative displacement between patches in a concrete splitting tensile strength test (HPSCC_84d_st3) after first vertical crack, for different couple of patches

This is a very interesting result which has not, to the knowledge of the author, been reported in the literature. This may be a consequence of the small polypropylene fibres that were incorporated into the concrete mixture, as mentioned in Section 3.1.1.1.3.

The fact that the crack does not open uniformly all the way through the vertical diameter, is partly the effect of horizontal compression immediately beneath the points where the load is applied; which does not allow the crack to fully develop across the vertical diameter. This is verified below by using the expressions for the horizontal stresses.

At the transition between compression and tension, the stress equals zero, $\sigma(\theta) = 0$. Then, the value of r at which this happens is calculated as follows:

$$0 = \frac{2 \cdot P}{\pi \cdot l \cdot d} \cdot \left[1 - \frac{d}{4 \cdot a}(\theta - \sin\theta)\right] \tag{3.33}$$

$$0 = 1 - \frac{d}{4 \cdot a}(\theta - \sin\theta) \tag{3.34}$$

$$\rightarrow \frac{4 \cdot a}{d} = \theta - \sin\theta \tag{3.35}$$

Equation (3.36) can be written as $f(x) = 0$.

$$f_{st}(x) = \frac{4 \cdot a}{d} - \theta + \sin\theta \tag{3.36}$$

With:

$$d = 101.6\,mm \qquad l = 200\,mm \qquad a = 23.74\,mm$$

By using the Newton-Raphson method, an approximation of θ is calculated.

$$\theta_{n+1} = \theta_n - \frac{f(x)}{f'(x)} \tag{3.37}$$

The result is:

$$\theta = 1.46\,rad \tag{3.38}$$

$$r(\theta = 1.46\,rad) = 36.29\,mm \tag{3.39}$$

The resulting distribution of the horizontal stress is shown in Figure 3.68. It is verified that under the point of application of the load there are horizontal compressive stresses, which is consistent with the observed length of the vertical crack.

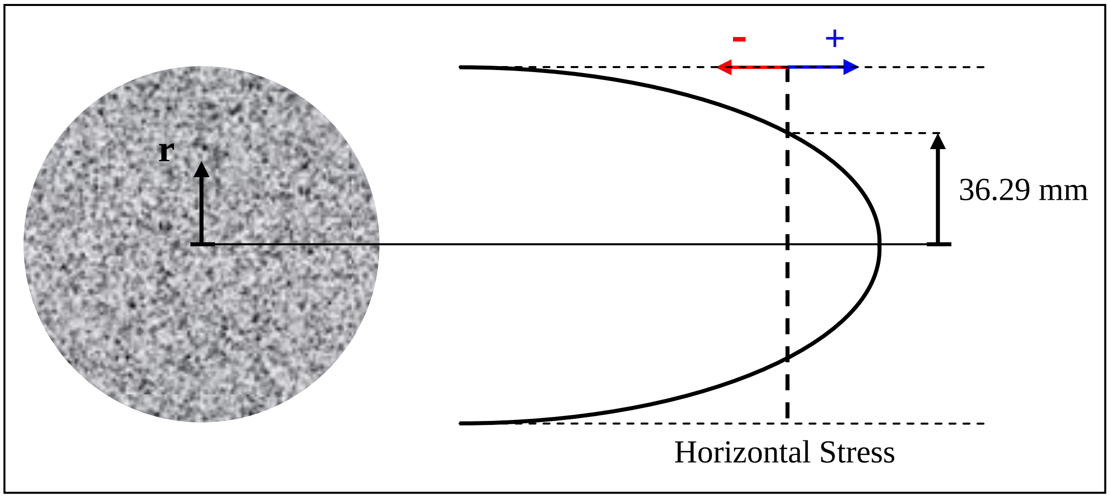

Figure 3.68: Theoretical horizontal stress distribution across the vertical diameter during a concrete splitting tensile strength test

Past research available in the literature, performed on high strength concrete, proposed a correlation between the splitting tensile strength and the compressive strength at all ages (Choi & Yuan, 2004), given be Equation (3.40).

$$f_{st}^{Choi} = 0.55 \cdot (f_c{}')^{0.5} \tag{3.40}$$

Other research determined a relationship between splitting tensile strength, compressive strength and concrete age (Zain, Mahmud, Ilham & Faizal, 2002), given by Equation (3.41).

$$f_{st}^{Zain} = 0.59 \cdot \sqrt{f_c{}'} \cdot \left(\frac{t}{t_{28}}\right)^{0.04} \tag{3.41}$$

Studies have also been performed to determinate a correlation between the splitting tensile strength and the direct tensile strength, given be Equation (3.42). For this study, a new approach was used to measure concrete's direct tensile strength (Ghaffar, Chaundhry & Kamran Ali, 2005).

$$f_t^{Ghaffar} = 0.66 \cdot f_{st} \tag{3.42}$$

This last correlation is of great interest to the results found using digital image correlation analysis. It is expected to find out that the stress at which the crack first initiates, identified by the digital image correlation analysis, is the actual tensile strength of the concrete. For this reason the stress at which the crack first initiates should be a value much closer to the strength determinate by a direct tensile strength test, not performed in this study for its complexity. Further studies should be made in this area to identify a possible influence of the PP fibres in the analysis performed on the concrete's splitting tensile strength tests.

The analysis performed in this study was only possible with the help of digital image correlation analysis, and is an interesting area for future research. In this research, two considerations were taken in order to calculate the splitting tensile strength of concrete:

- The actual value of θ is used to calculate the maximum horizontal tensile stress, and not the approximation $\theta = 0$ used by the ASTM (2004) which overestimates the maximum horizontal tensile stress by 3.6% (see Section 3.4.6.3).

- The maximum horizontal tensile stress is considered to be reached when the crack first initiates (load level identified using the digital image correlation analysis). This value was found to be 17-28% from the maximum horizontal tensile stress measured on the splitting tensile strength tests.

3.4.7 Concrete thermal conductivity test

The thermal conductivity of concrete has been highly studied in past research (Lie, 1992). Because the concrete mix used for this research has silica fume, fly ash and polypropylene fibres, which are admixtures not commonly used in past studies of concrete's thermal properties, a value of thermal conductivity was determinate with the C-Matic machine.

Past research has shown that thermal properties of concrete vary widely with temperature (Lie, 1992). The test executed on the C-Matic machine works on steady state, therefore it doesn't take into account the transient temperature dependant changes going on concrete as it heats up (vapour pressure of capillarity and gel water, decomposition of cement hydration products, collapse of filling aggregate, and melting of the PP fibres). This is why the thermal properties experimentally calculated for this study are complemented with data obtained from past literature (Lie, 1992). A heat transfer finite element model of the pullout test is also build, and the value of thermal conductivity and specific heat are calibrated by complementing the experimental data with the experimental data from past literature.

3.4.7.1 Test procedure

The experiments were conducted at The Rushbrook Fire Laboratory, located within King's Buildings Campus at the University of Edinburgh. Results from these tests are presented in Appendix C.

The C-Matic machine was calibrated to determine thermal conductivity of any sample, with the sample's mean temperature at 76, 114 and 155°C. A total of six samples were tested, two at each calibrated temperature. Before testing each sample, a thin uniform layer of the heat sink compound was applied to both surfaces of the sample. The sample was then placed in the sample holder, inside the Teflon rim, and the test was executed. The sample temperature was set to the temperature at which the thermal conductivity was to be determinate, and the temperature of the sample increased at a given rate which maintains relatively the same for every test at that same temperature. The variation of temperature of the tested samples at the three mean temperature levels is shown in Figure 3.69.

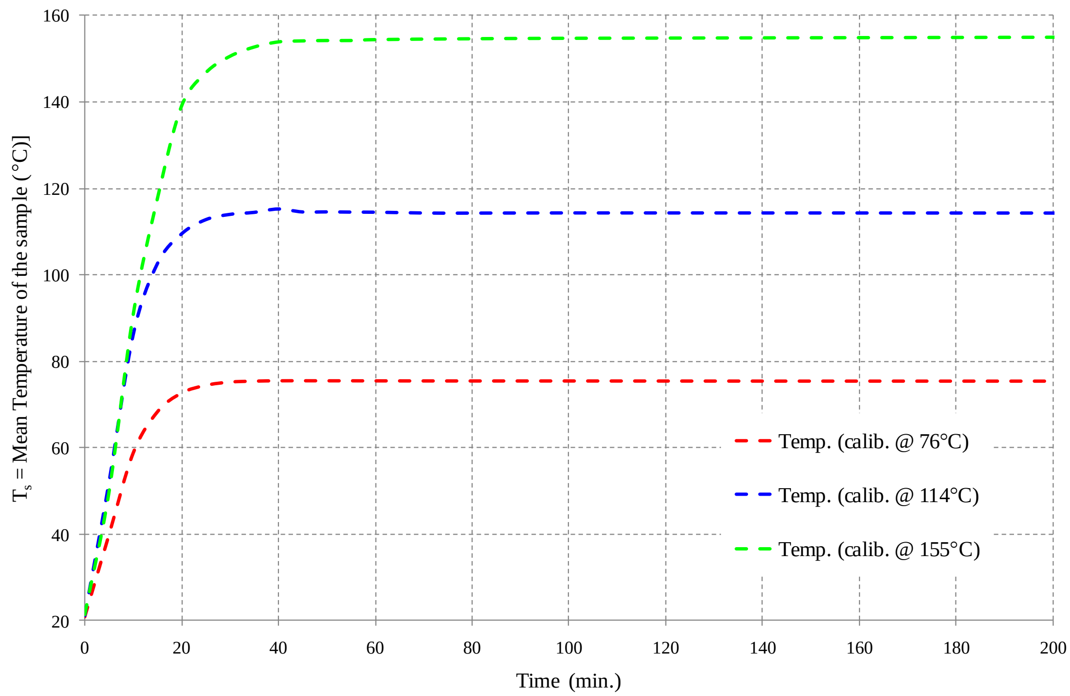

Figure 3.69: Typical variation in the mean temperature of a sample on a C-Matic thermal conductivity test

3.4.7.2 Test matrix

Table 3.11: Samples tested to determine the thermal conductivity of concrete

Test	Sample temperature at TC determination (°C)	Heating ramp (°C/min)
T1 @ 76°C T2 @ 76°C	76	4
T1 @ 114°C T2 @ 114°C	114	7
T1 @ 155°C T2 @ 155°C	155	8

3.4.8 Steel tensile strength test

The experiments were conducted at The Crichton Laboratory, located within King's Buildings Campus at the University of Edinburgh. The objective of this tests is to determinate the stress-strain curve of the steel prestressing wire used in this research. Results from these tests are presented in Appendix D.

3.4.8.1 Test procedure

Three 20 mm long steel prestressing wire samples were tested in the test was executed on the Instron machine. The three specimens were tested till failure, identifying yield strength and ultimate strength, according to ASTM (2003c).

The Instron machine is equipped with wedge grips which cause an slipping of the sample as the test is executed. Because of the slipping of the sample, the tensile strain of the sample cannot be calculated from the Instron’s crosshead displacement. For this reason the stress-strain plot cannot be determined.

3.4.8.2 Test matrix

Table 3.12: Test matrix of steel tensile strength tests

Test	Instron's crosshead displacement rate (mm/min)
Steel_tensile_1	0.89
Steel_tensile_2	0.89
Steel_tensile_3	0.89

4 EXPERIMENTAL RESULTS

4.1 Pullout Test

RPOTs and PHPOTs, described in Section 3.4.1, were the primary experiments performed for this research. The analysis of the data of these tests required synchronisation of the data obtained from the thermocouples, the Instron's controller and the digital image correlation analysis. The results for each test are displayed in four separate plots (a, b, c and d) which display the development of the each parameter over time.

(a) Heating blanket and reinforcing bar (CFRP tendon or steel prestressing wire) temperature, calculated as described in Sections 3.2.1.3 and 3.4.3 [°C].

(b) Average bond stress assuming uniform bond stress distribution along the bonded length [MPa].

(c) Slip of the loaded and free ends measured with the digital image correlation analysis technique, as described in Section 3.4.1.3 [mm].

(d) The difference between loaded end slip and free end slip [mm].

4.1.1 CFRP_AT_e1

This was a RPOT done on a CFRP pullout sample. This sample was pulled out until failure of the bond interface occurred. At minute 4, the Instron machine was set to start the pullout at a bond stress rate of 0.71 MPa/min, as shown in Figure 4.4(b).

The heating blanket was not set on this sample. Nonetheless the thermocouples were placed on the CFRP tendon's surface and at the cylinders surface, as described in Sections 3.2.1.2 and 3.2.1.3, respectively. This was executed to have precisely the same conditions as for the PHPOTs. The temperature at the concrete's surface and at the tendon were 24°C and 21°C, respectively (see Figure 4.1(a)).

The failure of the bond interface is clearly visible at minute 11.6, where a sudden drop of the bond stress occurs (see Figure 4.1(b)) along with a rapid increase in the slip rate of both ends (see Figure 4.1(c)). The maximum bond stress was 5.34 MPa and immediately after failure it dropped to 4.80 MPa. As the configuration of the test, which was performed under a displacement-control mode in the RPOT case, allows for the pullout to continue after failure and the free end of the CFRP tendon enter into the already failed bonded length interface. After the tendon kept on slipping the sample exhibited a residual bond strength which tended to about 4.09 MPa, as shown in Figure 4.1(b).

The slip at both ends kept increasing, at almost the same rate, as shown in Figure 4.1(c). In Figure 4.1(d), the difference between the loaded and the free end slip over time is shown.

At the loaded end, slip is calculated by subtracting the elasticity of the un-bonded part of the tendon, as described in Section 3.4.1.3. For this, the theoretical elastic modulus of the CFRP tendon (150 GPa) was used. The value of the difference between the loaded and the free end slip drops below zero as the loading occurs at minute 4. This happens because at the loading stage there is an accommodation of the testing frame described in 3.3.1 and 3.4.1.1, which leads to a lower modulus of elasticity than the one used to subtract the elasticity of the un-bonded length at the loaded end. This phenomenon repeats in the other pullout tests.

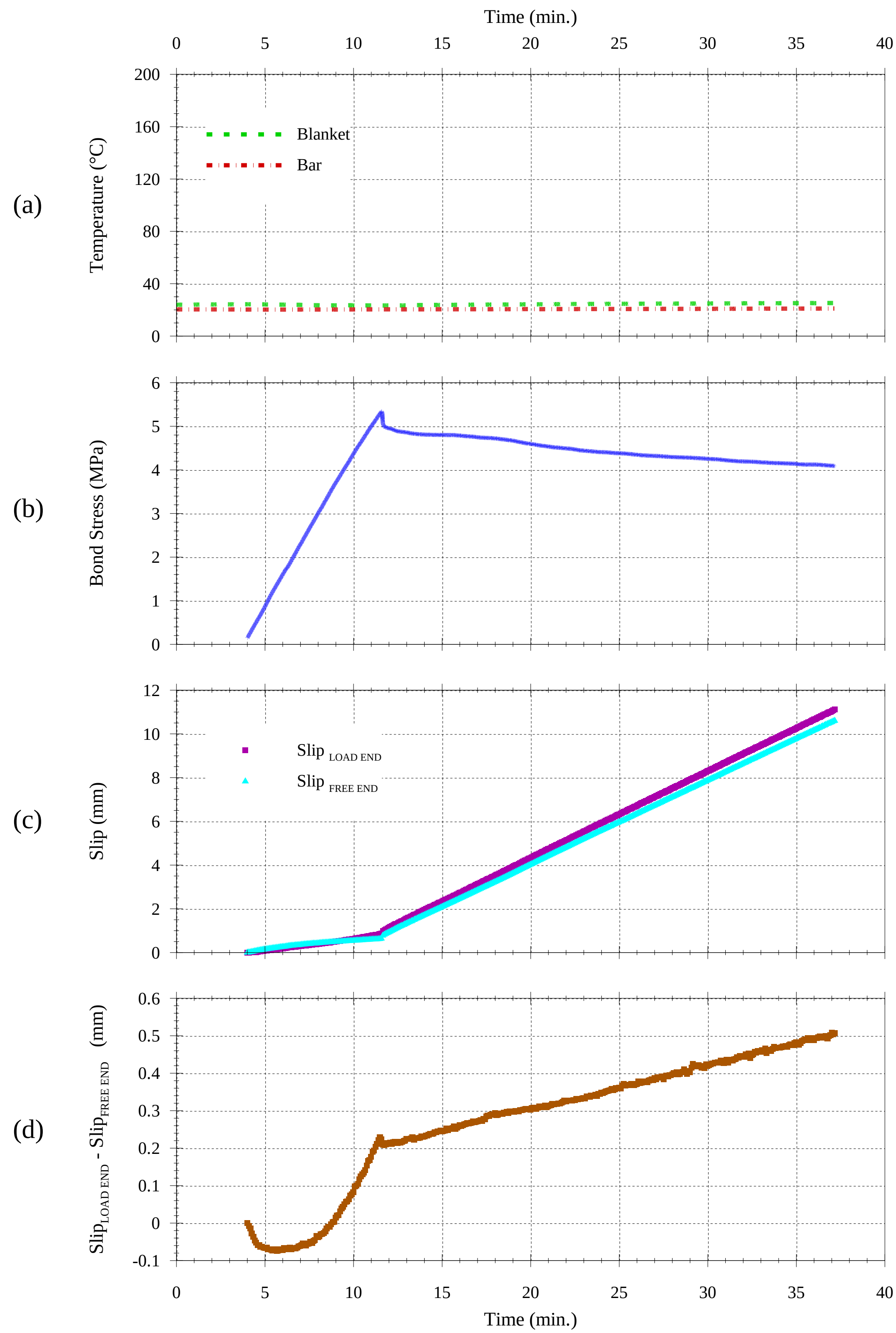

Figure 4.1: Experimental data for CFRP_AT_e1

Right before failure occurs, Figure 4.1(d) shows a rapid increase in the difference between loaded and free end slip. A zoom-in at the moment in which failure occurs, reveals that before failure there is an increase in the rate at the loaded end slip, as shown in Figure 4.2.

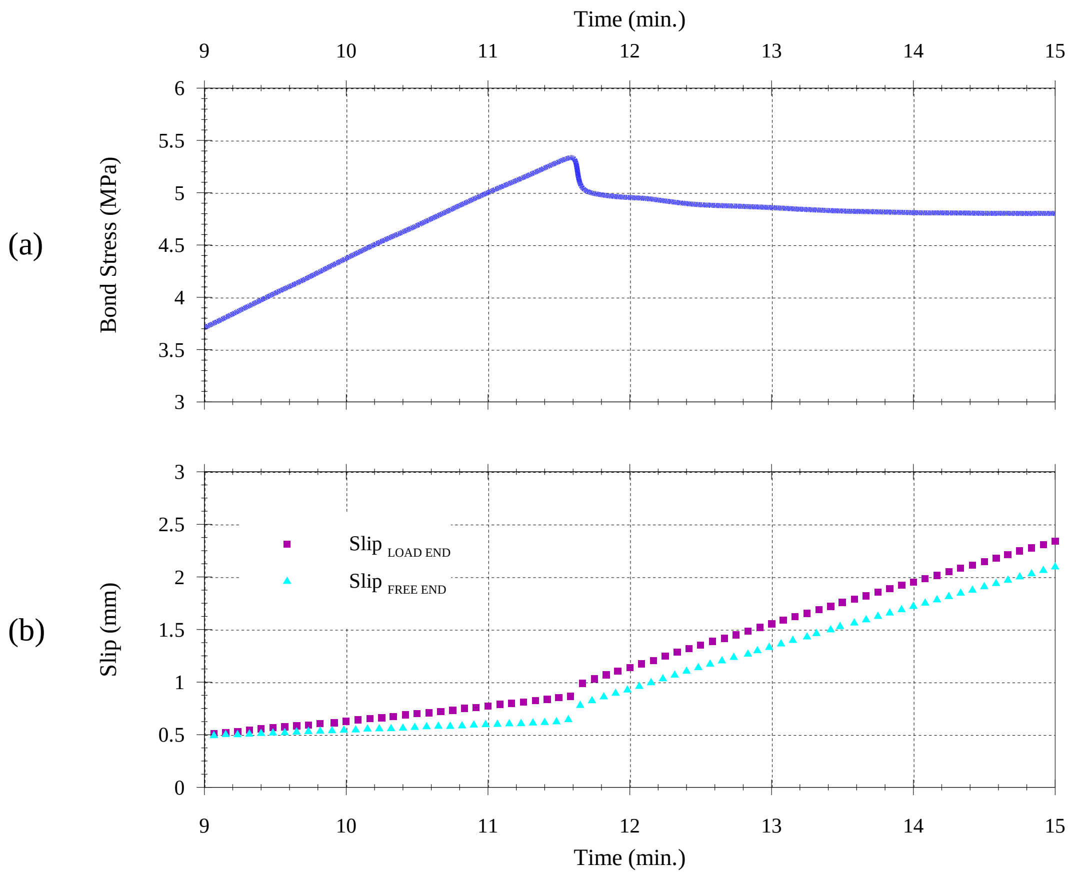

Figure 4.2: Zoom-in of the development of bond stress and slip at failure for CFRP_AT_e1

The objective of this test was to determine the bond strength of the pullout sample, at ambient temperature. The most typical way in which pullout tests are displayed is by plotting the results in a bond stress versus slip plot (see Figure 4.3).

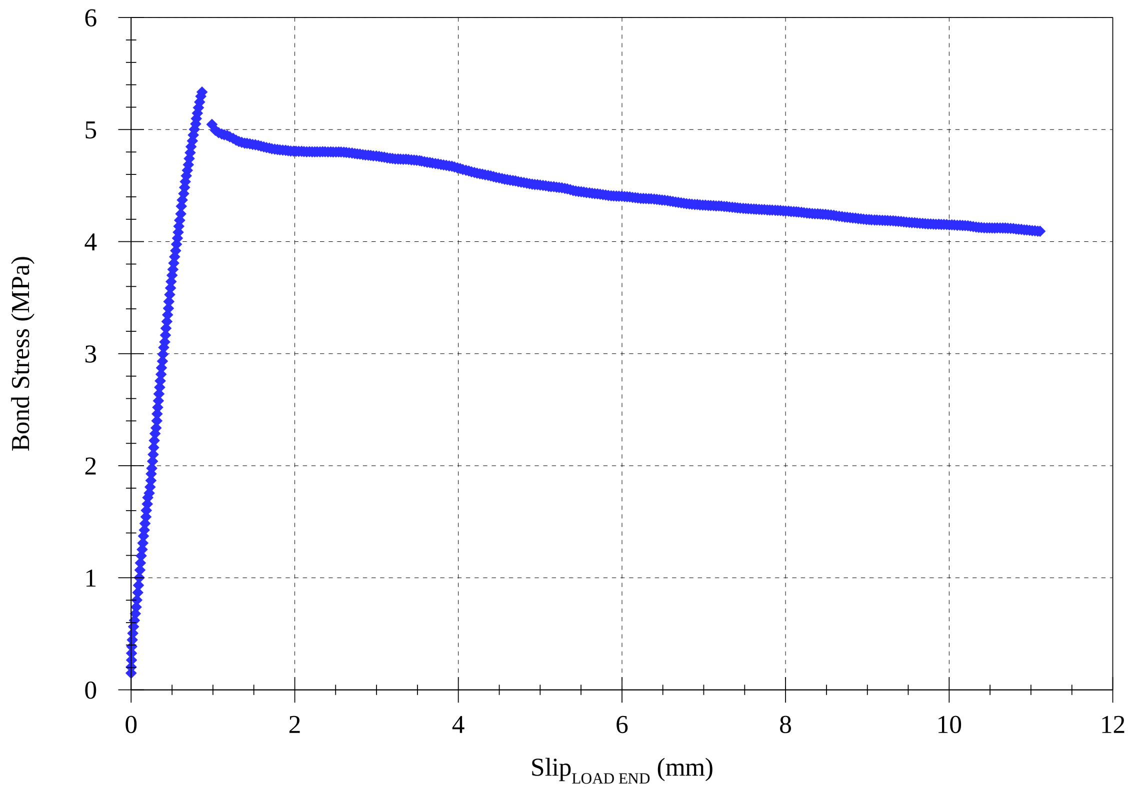

Figure 4.3: Bond stress versus loaded end slip for CFRP_AT_e1

4.1.2 CFRP_AT_e2

This was a second RPOT done on a CFRP pullout sample. This sample was pulled out until failure of the bond interface occurred. At minute 4, the Instron machine was set to start the pullout at a bond stress rate of 4.96 MPa/min, as shown in Figure 4.4(b). For this second RPOT done on the CFRP tendons the pullout rate was increased seven times from that applied in the CFRP_AT_e1 test. This was executed to check if a variation in the loading rate had an impact on the bond strength at ambient temperature.

Again, the heating blanket was not set on this sample, but thermocouples were placed on the CFRP tendon’s surface and at the cylinders surface. Again, this was executed in order to have the same conditions as for the PHPOTs. The temperature at the concrete’s surface and at the tendon were 24°C and 20°C, respectively (see Figure 4.4(a)).

The failure of the bond interface is clearly visible at minute 4.9, in which a sudden drop of the bond stress occurs (see Figure 4.4(b)) along with a rapid increase in the slip rate of both ends (see Figure 4.4(c)). The maximum bond stress was 4.42 MPa and immediately after failure it dropped to 3.95 MPa. After failure, the tendon kept slipping and the sample exhibited a residual bond strength which tended to 2.90 MPa, as shown in Figure 4.4(b).

The slip in both ends kept on increasing, at almost the same rate, as shown in Figure 4.4(c). In Figure 4.4(d), the difference between the loaded and the free end slip over time is shown, and dropped below zero at the loading stage, as it also happened in CFRP_AT_e1 and discussed in Section 4.1.1.

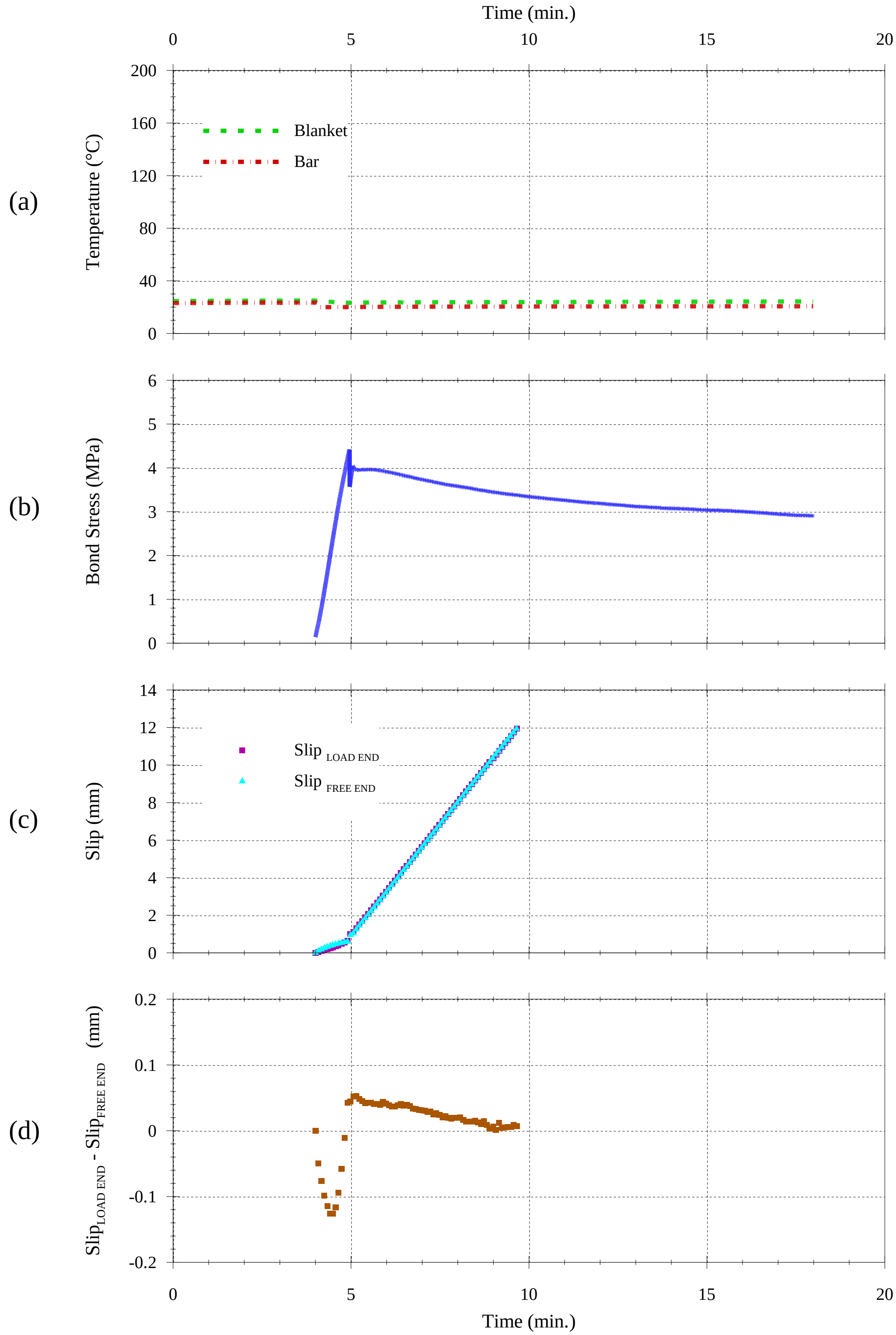

Figure 4.4: Experimental data for CFRP_AT_e2

Right before failure occurred, Figure 4.4(d) showed a rapid increase in the difference between loaded and free end slip. Again, a zoom-in at the moment in which failure occurred, reveals that before failure there was an increase in the rate at the loaded end slip, as shown in Figure 4.5.

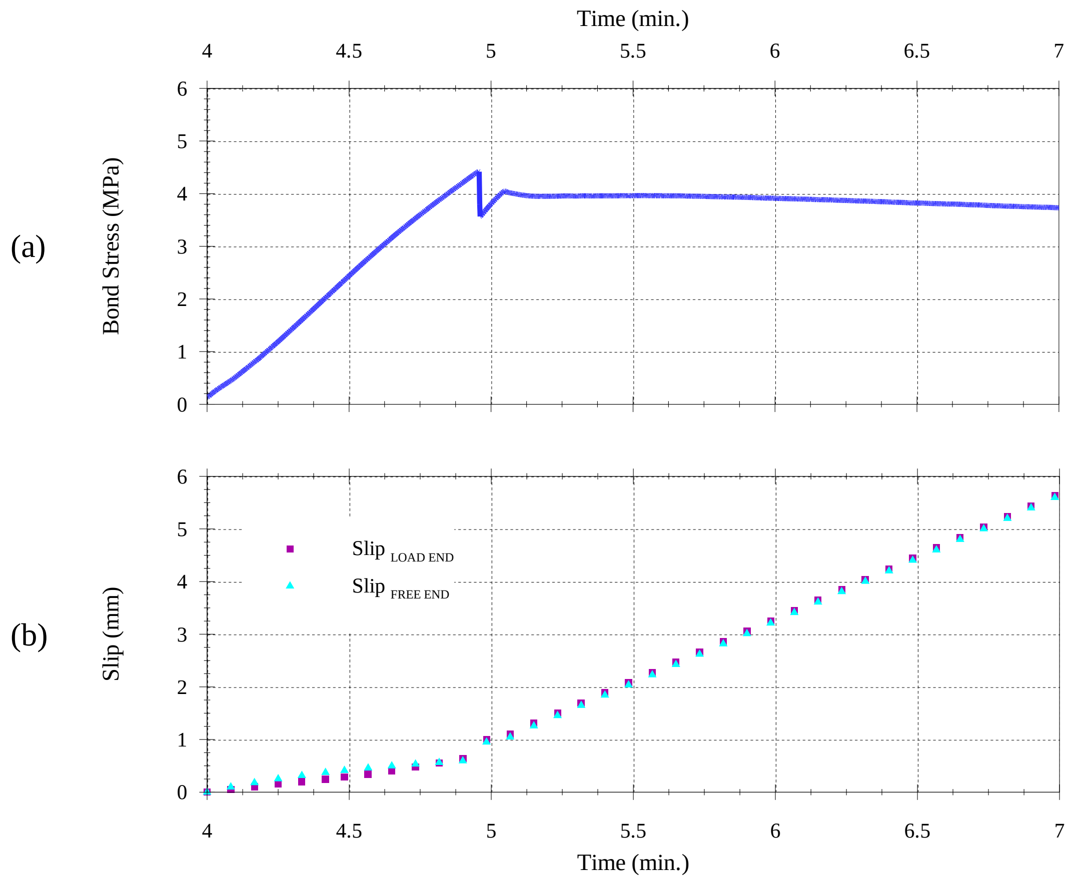

Figure 4.5: Zoom-in of the development of bond stress and slip at failure for CFRP_AT_e2

The objective of this test was to determine the bond strength of the pullout sample, at ambient temperature under a higher loading rate. A bond stress versus slip plot is given in Figure 4.6.

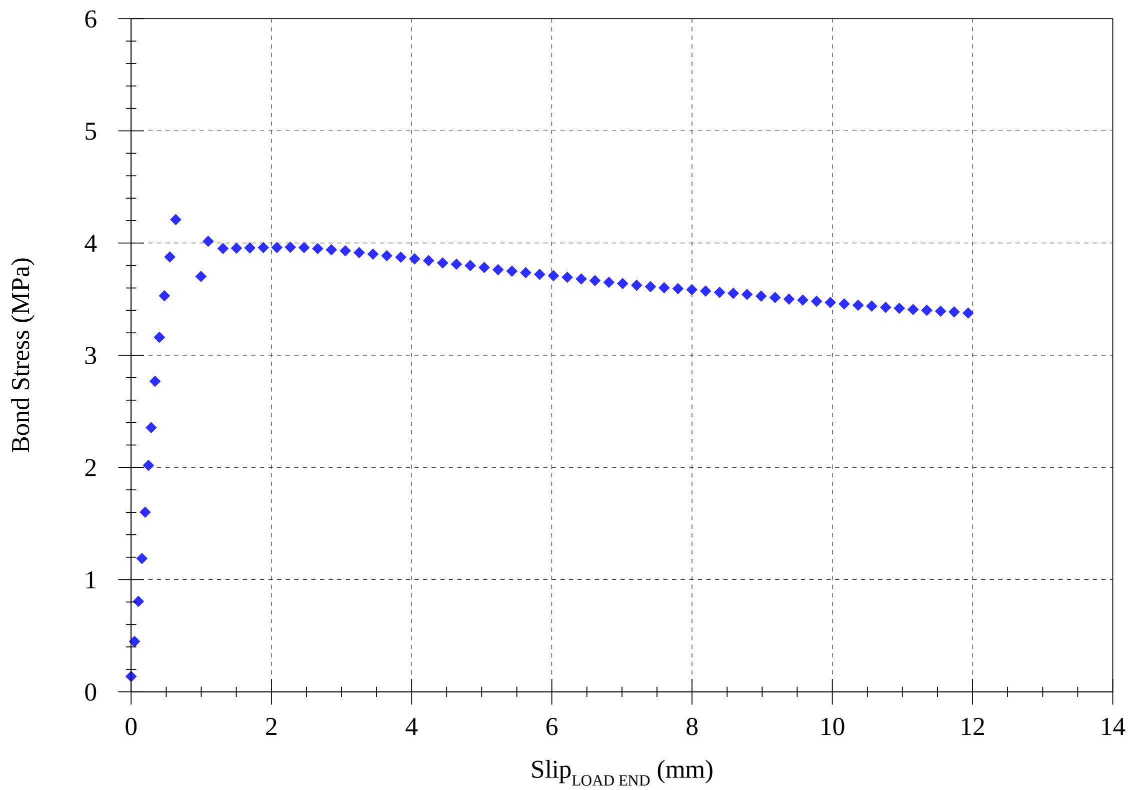

Figure 4.6: Bond stress versus loaded end slip for CFRP_AT_e2

4.1.3 CFRP_15%

This was a PHPOT done on a CFRP pullout sample. This sample was stressed up to 15% (0.74 MPa) of the average bond strength capacity measured on the two RPOTs done on the CFRP pullout samples (CFRP_AT_e1 and CFRP_AT_e2). The same loading and heating rate were executed in this test, as for every other PHPOT. The pullout began at minute 4 (see Figure 4.7(b)) and the heating blanket was turned on at minute 15, with the tendon's temperature beginning its rise at minute 18 (see Figure 4.7(a)). The Instron machine was configured to pullout from the tendon at a bond stress rate of 2.64 MPa/min during the initial loading phase of the tests up until the required sustained load was reached.

In this test, failure did not occur as the temperature of the tendon increased. The heating rate developed as described in Section 3.4.1.2.2. The tendon reached a steady state temperature at 161°C and then, at minute 141, the heating blanket temperature was increased and the tendon reached a steady state temperature of 166°C, as shown in Figure 4.7(a).

At minute 212, after not having any signs of failure, with the tendon at a steady temperature of 166°C, the Instron machine was configured to pullout until failure occurred at a bond stress rate of 0.52 MPa/min. Failure occurred at about minute 219.5 with a rapid increase of the slip at both ends, as shown in Figure 4.7(c). The maximum average bond stress was 3.89 MPa, with the tendon's temperature at 166°C, and immediately after failure it dropped to 3.43 MPa. After failure, the tendon kept slipping and the sample exhibited a residual bond strength which tended to 2.26 MPa, as shown in Figure 4.7(b).

At the moment of failure there was a sudden drop of the difference between the loaded and the free end slip, as shown in Figure 4.7(d).

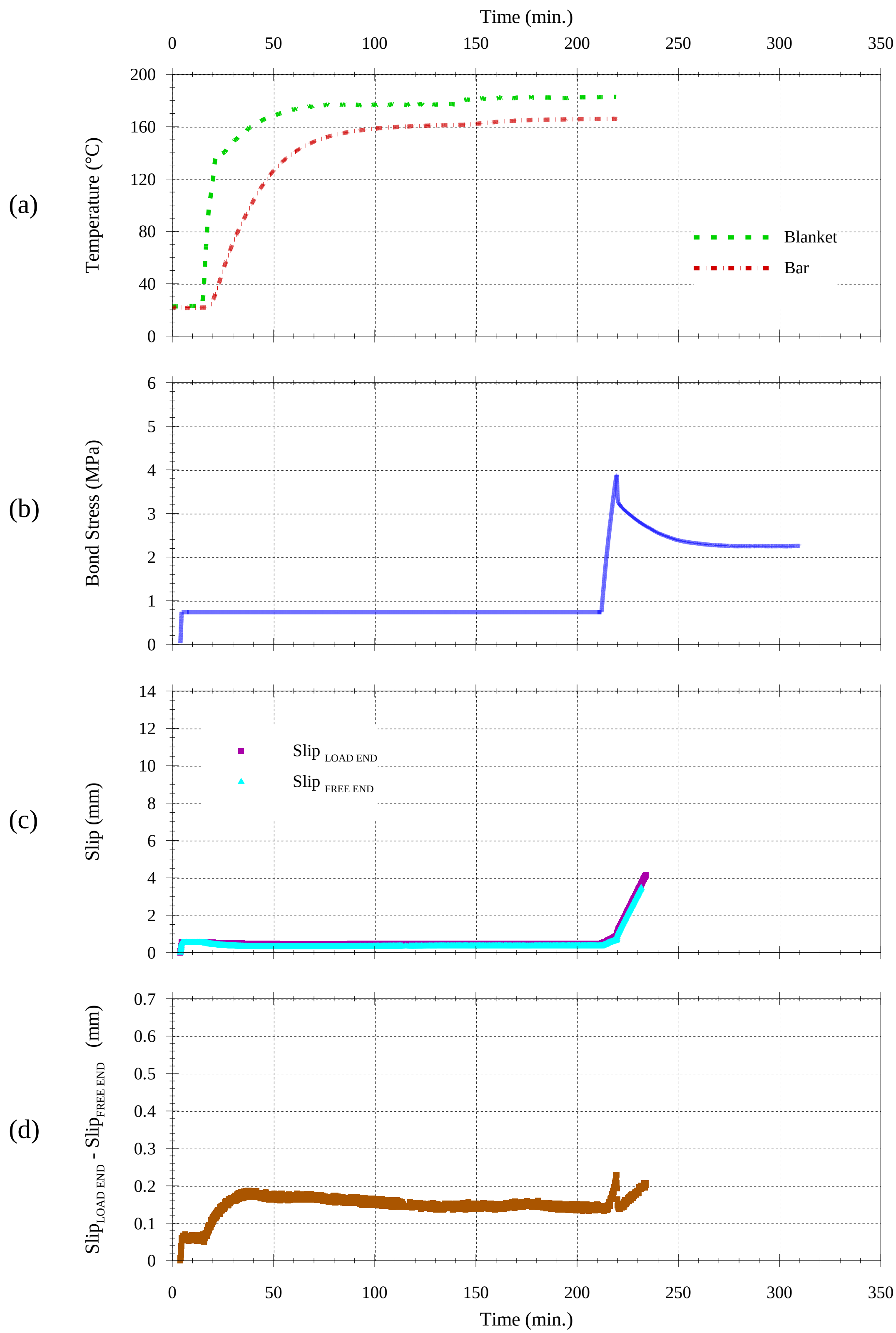

Figure 4.7: Experimental data for CFRP_15%

Figure 4.8 illustrates a zoom-in of the experimental data at the moment at which failure occurred. At this moment the tendon's temperature was at a steady state of 166°C, with the heating blanket at 182°C, as shown in Figure 4.8(a). Every parameter was steady up until minute 212, at which further loading was applied in order to produce a bond failure of the sample.

The average bond stress was steady at 0.74 MPa up until minute 212 at which point it started increasing at rate of 0.52 MPa/min. Bond stress increased until minute 219.5 at which point a maximum bond stress of 3.89 MPa was achieved, as shown in Figure 4.8(b). A sudden drop of the bond stress occurred and it dropped to 3.30 MPa at the moment of failure. A residual bond strength of 2.26 MPa was measured as the tendon kept slipping.

Slip at both ends remained steady, and started increasing as further pullout began. Both ends started slipping at the same time (minute 212) with a more pronounced increase at the loaded end, up until minute 219.5 at which point a relatively large slip occurred, as shown in Figure 4.8(c). At this point (bond failure), the difference between the loaded and the free end slip dropped, as shown in Figure 4.8(d).

After failure, both slip readings kept increasing at a constant rate, which was slightly larger at the loaded end. This causes the difference between the loaded and the free end slip to increase at a constant rate, after failure occurred, as shown in Figure 4.7(d).

(a)

(b)

(c)

(d)

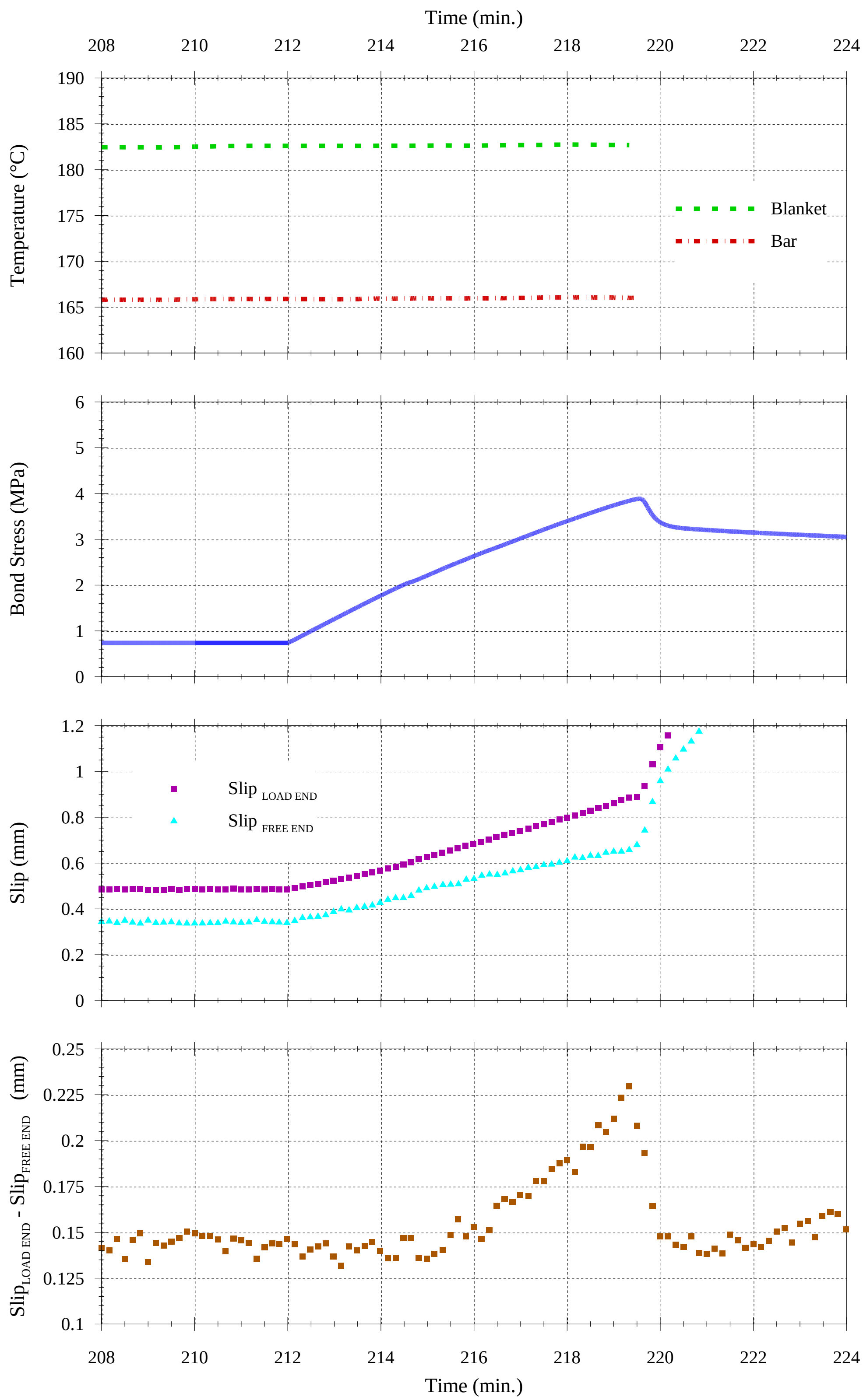

Figure 4.8: Zoom-in of the failure for CFRP_15%

Pullout tests are commonly display by bond stress versus slip plots (see Figure 4.9), which work reasonably well when presenting the data from a RPOT. For PHPOTs however, a bar temperature versus loaded end slip plot is more instructive (see Figure 4.10) because in these tests the objective is to determine the failure temperature of the bond for a given average bond stress.

In Figure 4.9, 3.89 MPa was the maximum average bond stress achieved. After failure there was a sudden drop of the bond stress until 3.30 MPa and then a constant trend toward the residual bond strength of 2.26 MPa as the tendon kept on slipping. In this test, the image correlation analysis was able to measure slips only up to a 4 mm slip, and that's why Figure 4.9 does not display the final residual strength, as shown in Figure 4.7(b).

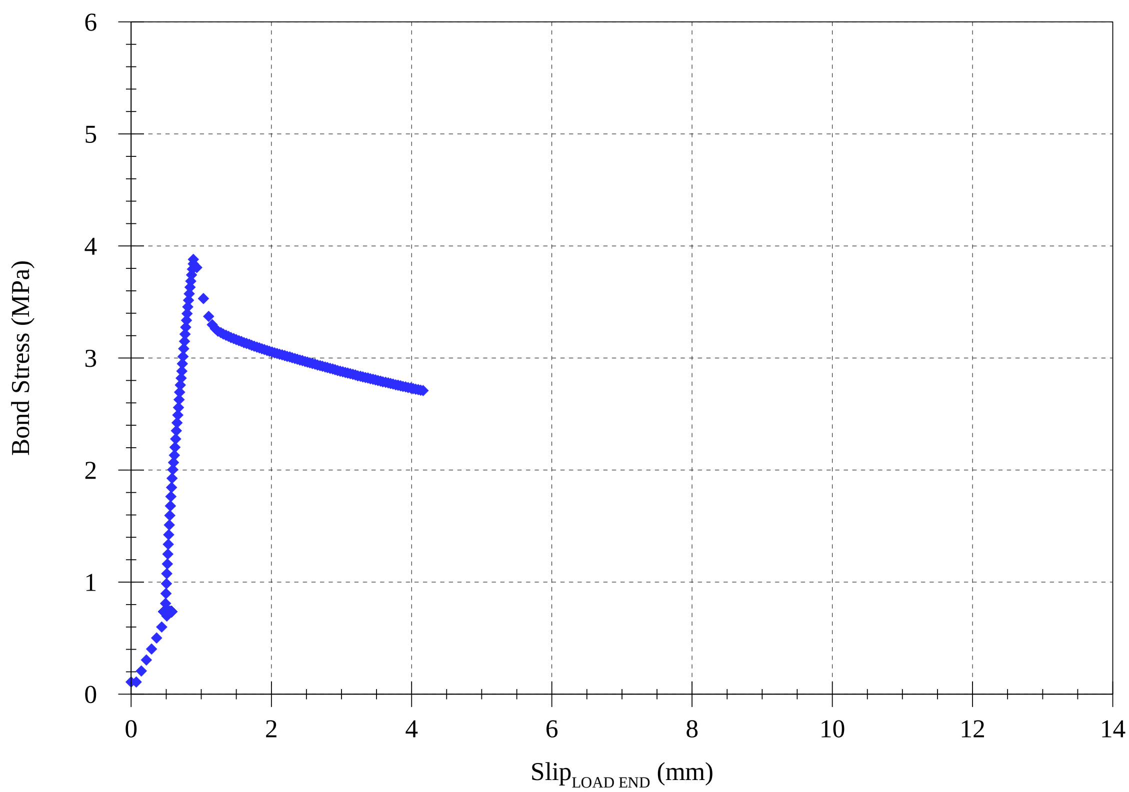

Figure 4.9: Bond stress versus loaded end slip for CFRP_15%

In this test, the bond interface did not fail as expected (it was assumed that the bond would fail as the tendon's temperature increased), but it failed as the load was increased with the tendon at a temperature of 166°C, and an initial average bond stress of 0.74 MPa. Nonetheless, Figure 4.10 is instructive to display that the failure occurred at a tendon's temperature of 164°C.

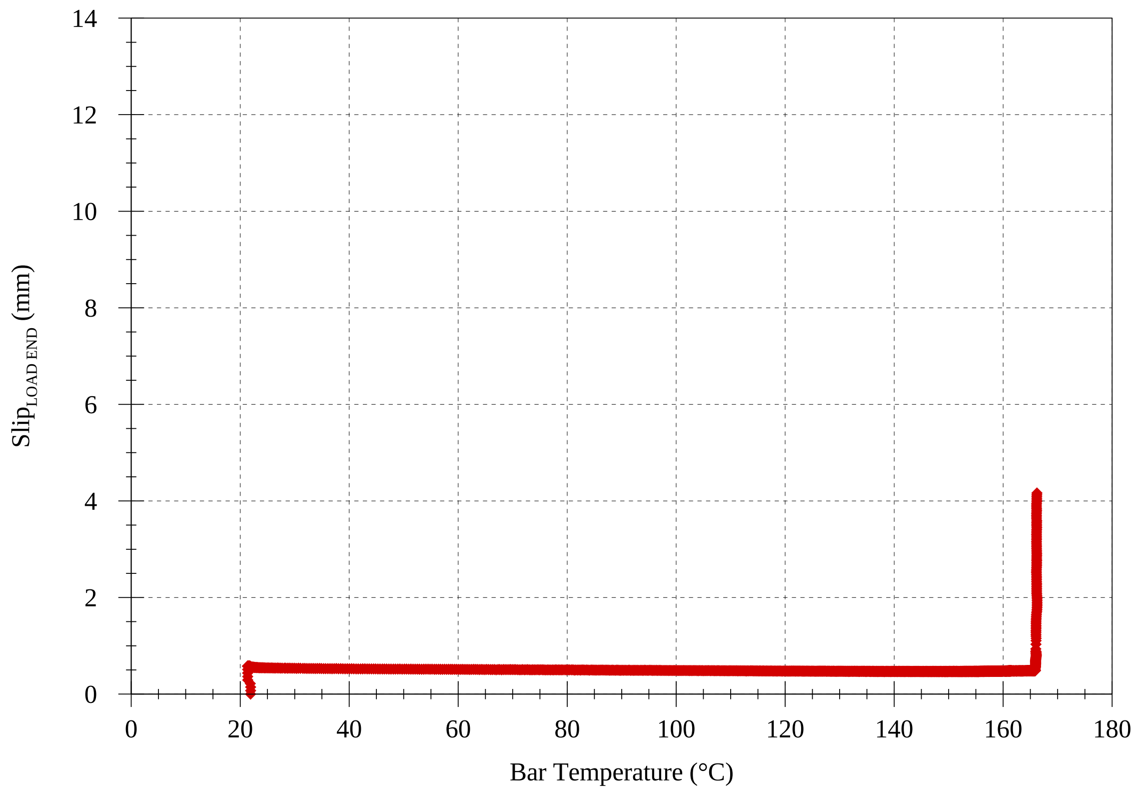

Figure 4.10: Bar temperature versus loaded end slip for CFRP_15%

After the heating blanket was turned on at minute 15, the average bond stress remained constant over time while the difference between the loaded and the free end slip increased, as shown in Figure 4.7(d). A zoom-in of the slip readings (see Figure 4.11) reveals that the increase of the slip difference after minute 15 is a result of the decrease of the slip readings at both ends, with a more pronounced drop of the free end slip.

This decrease in both slips is not a result of the loaded end slipping towards the inside of the concrete cylinder, nor the free end slipping away of it; the opposite to what should happen in a pullout test of this type. This phenomenon is a result of the concrete cylinder and CFRP tendon combined thermal expansion as explained in Section 5.4.

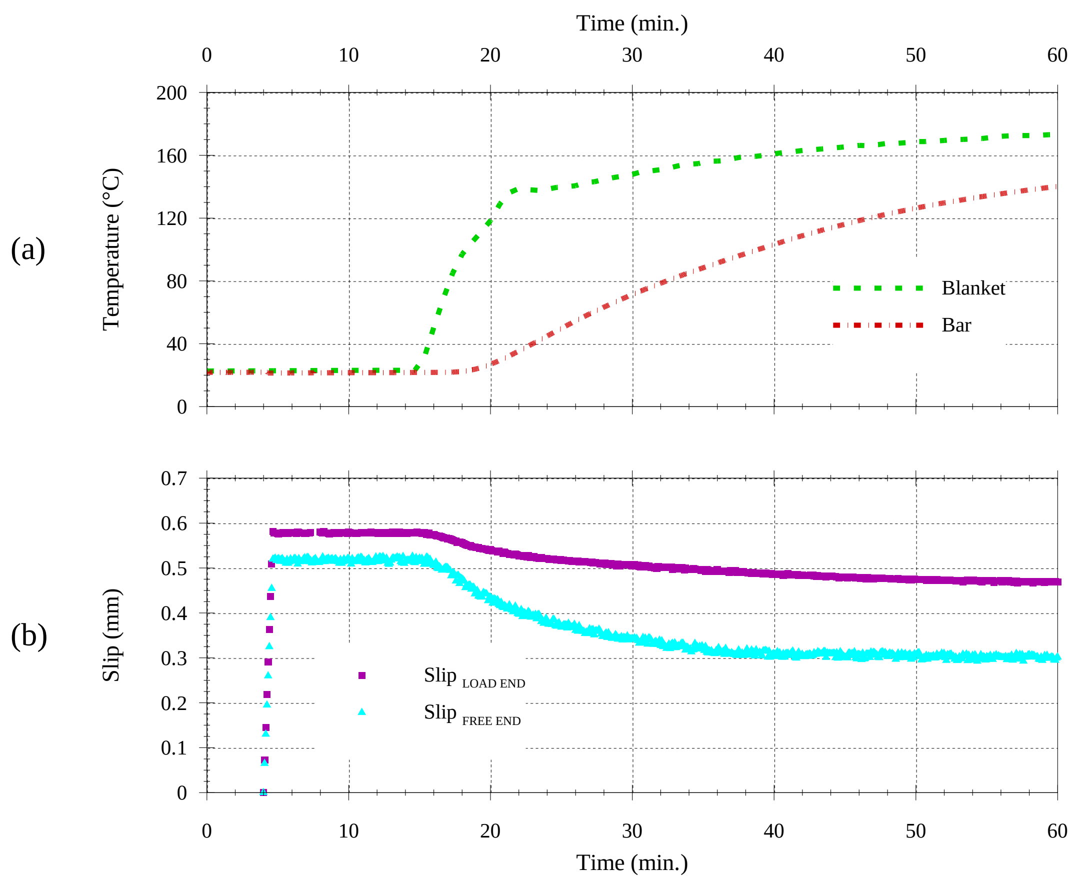

Figure 4.11: Zoom-in of temperature and slip for CFRP_15%

4.1.4 CFRP_30%

This was a PHPOT done on a CFRP pullout sample. This sample was stressed up to 30% (1.47 MPa) of the average bond strength capacity measured from the two RPOTs done on the CFRP pullout samples (CFRP_AT_e1 and CFRP_AT_e2). The same loading and heating rate were executed in this test as for every other PHPOT. The pullout began at minute 4 (see Figure 4.12(b)) and the heating blanket was turned on at minute 15, with the tendon's temperature beginning its rise at minute 18 (see Figure 4.12(a)). The Instron machine was configured to pullout from the tendon at a bond stress rate of 2.43 MPa/min during the initial loading phase of the tests up until the required sustained load was reached.

Again, failure did not occur as the temperature of the tendon increased. The heating rate developed as described in Section 3.4.1.2.2. The tendon reached a steady state temperature at 162°C and then, at minute 151, the heating blanket temperature was increased and the tendon reached a steady state temperature of 166°C, as shown in Figure 4.12(a).

At minute 232, after not showing any signs of failure, with the tendon at a steady temperature of 166°C, the Instron machine was configured to pullout until failure occurred at a bond stress rate of 0.48 MPa/min. Failure occurred at about minute 240 with a rapid increase of the slip at both ends, as shown in Figure 4.12(c). The maximum average bond stress was 5.07 MPa, with the tendon's temperature at 166°C, and immediately after failure it dropped to 4.12 MPa. After failure, the tendon kept slipping and the sample exhibited a residual bond strength which tended to 2.21 MPa, as shown in Figure 4.12(b).

At the moment of failure there was a sudden drop of the difference between the loaded and the free end slip, as shown in Figure 4.12(d).

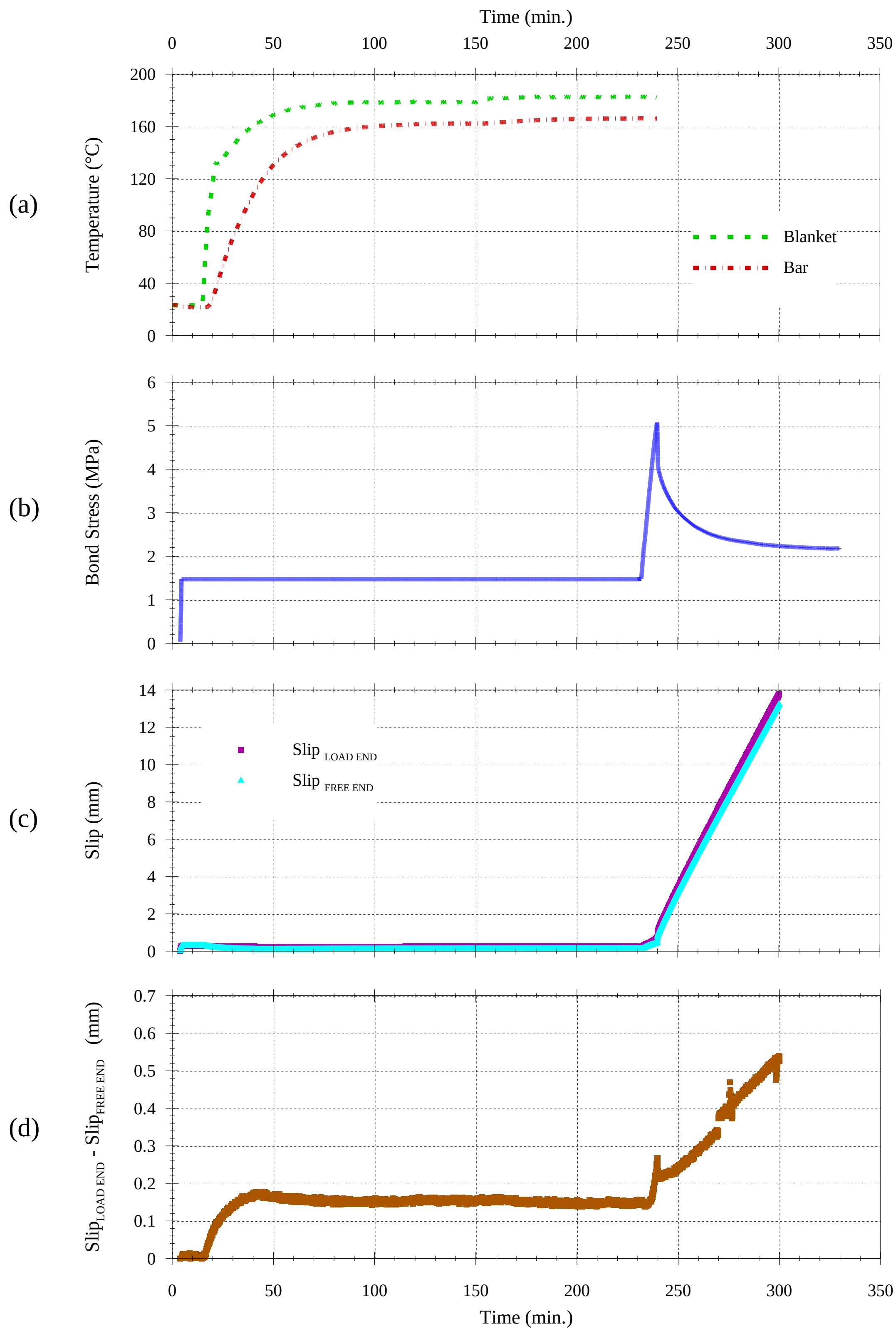

Figure 4.12: Experimental data for CFRP_30%

Figure 4.13 illustrates a zoom-in of the experimental data at the moment at which failure occurred. At this moment the tendon was at a steady state temperature of 166°C, with the heating blanket at 182°C, as shown in Figure 4.13(a). Every parameter was steady up until minute 232, at which point additional load was applied to produce bond failure of the sample.

The average bond stress was steady at 1.47 MPa, up until minute 232 at which point it started increasing at rate of 0.48 MPa/min. Bond stress increased until minute 240 at which point the maximum bond stress of 5.07 MPa was achieved, as shown in Figure 4.13(b). A sudden drop of the bond stress then occurred and it dropped to 4.12 MPa at the moment of failure. A residual bond strength of 2.21 MPa was measured as the tendon kept slipping.

Slip at both ends remained steady and started increasing as the load was increased. Both ends started slipping at the same time (minute 232) with a more pronounced increase at the loaded end, up until minute 240 at which point a relatively large slip occurred, as shown in Figure 4.13(c). At this point (bond failure), the difference between the loaded and the free end slip dropped, as shown in Figure 4.13(d).

After failure, both slip readings kept increasing at a constant rate, which was slightly larger at the loaded end. This causes the difference between the loaded and the free end slip to increase at a constant rate, after failure occurred, as shown in Figure 4.12(d).

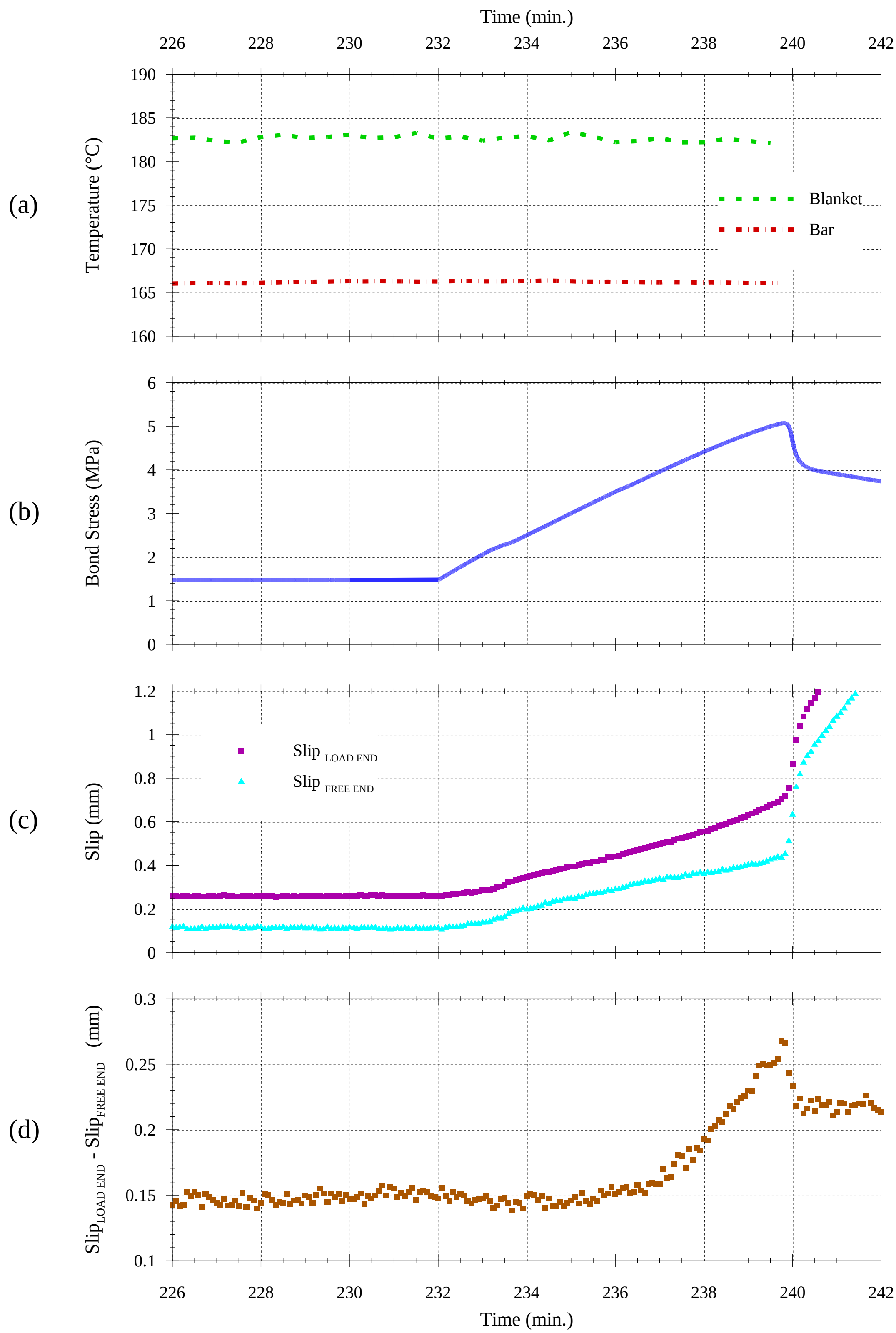

Figure 4.13: Zoom-in of the failure for CFRP_30%

In Figure 4.14, 5.07 MPa was the maximum average bond stress observed. After failure there was a sudden drop of the average bond stress to 4.21 MPa and it then tended to a residual bond strength of 2.21 MPa as the tendon kept on slipping.

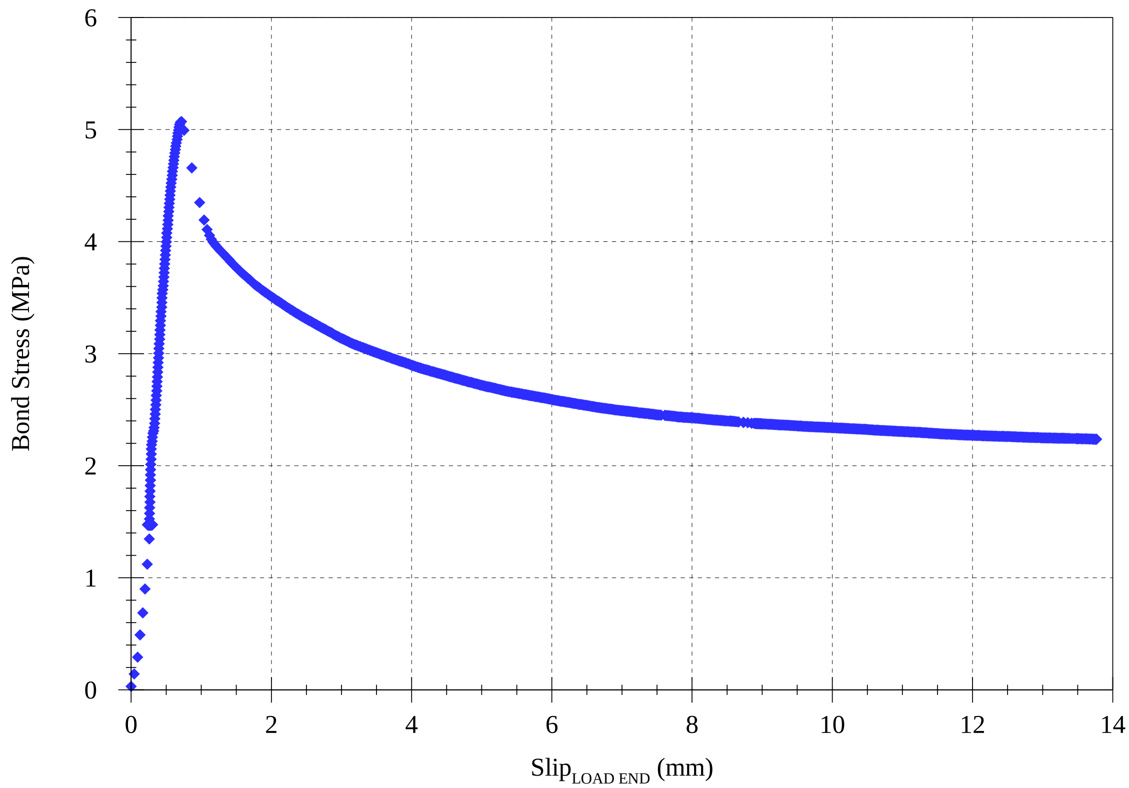

Figure 4.14: Bond stress versus loaded end slip for CFRP_30%

Again, in this test the bond interface did not fail as expected, during the heating phase. It failed only as the load was increased with the tendon at a temperature of 166°C, with an initial bond stress of 1.47 MPa. Nonetheless, Figure 4.15 is instructive to display that the failure occurred at a tendon's temperature of 166°C.

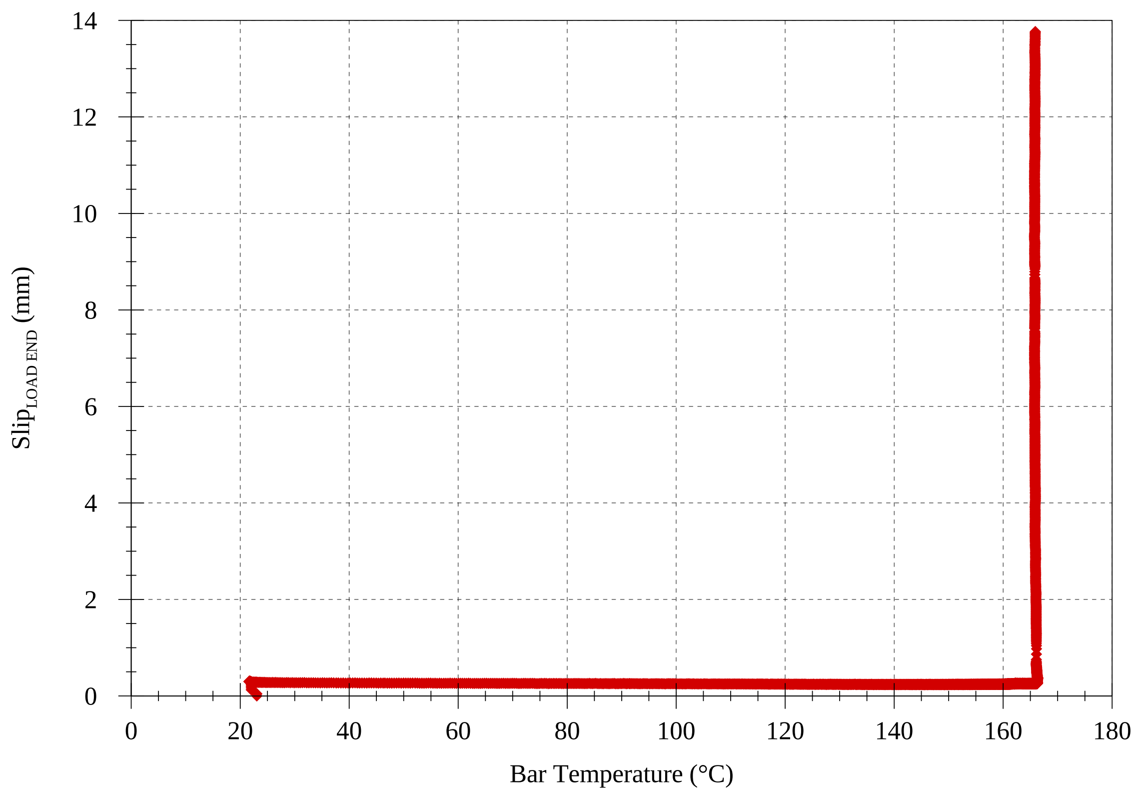

Figure 4.15: Bar temperature versus loaded end slip for CFRP_30%

After the heating blanket was turned on at minute 15, the average bond stress remained constant over time while the difference between the loaded and the free end slip increased, as shown in Figure 4.12(d). A zoom-in of the slip readings (see Figure 4.16) reveals that the increase of the slip difference after minute 15 is a result of the decrease of the slip readings at both ends, with a more pronounced drop of the free end slip.

This phenomenon is a result of the concrete cylinder and CFRP tendon combined thermal expansion as noted and explained in Section 5.4.

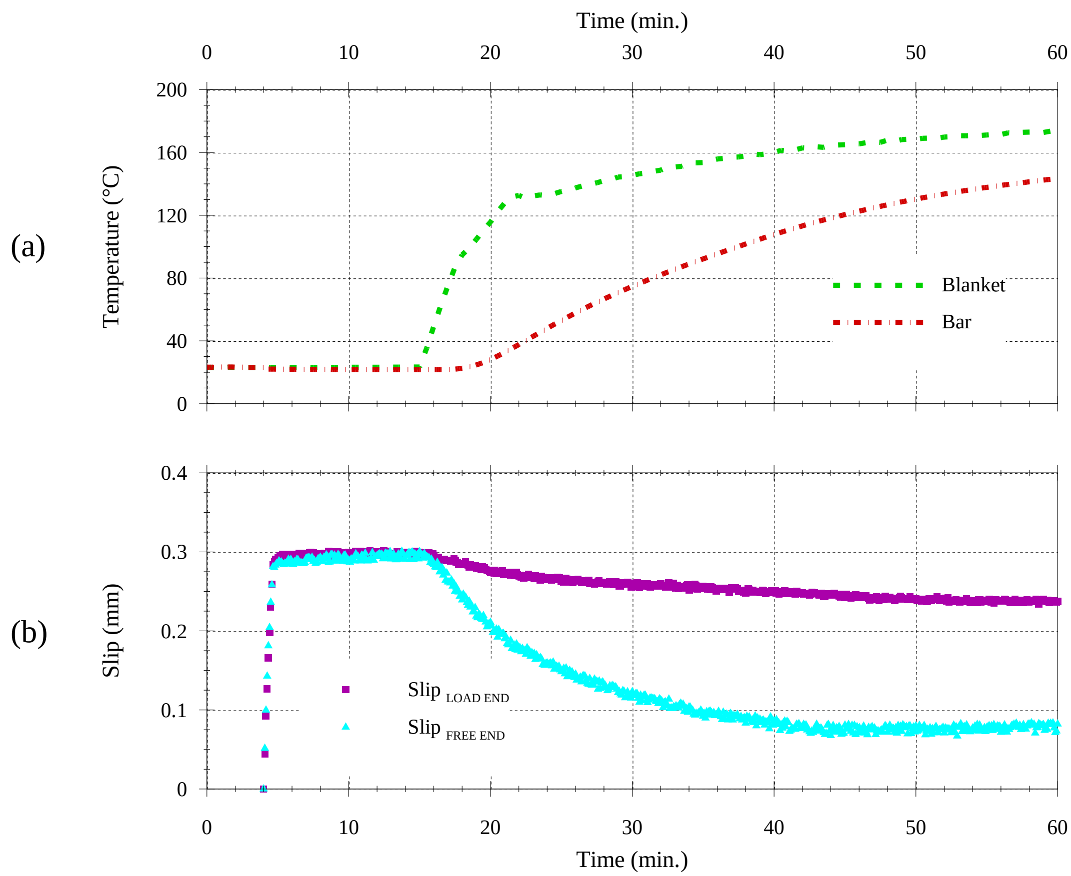

Figure 4.16: Zoom-in of temperature and slip for CFRP_30%

4.1.5 CFRP_38%

This was a PHPOT done on a CFRP pullout sample. This sample was stressed up to 38% (1.84 MPa) of the average bond strength capacity measured from the two RPOTs done on the CFRP pullout samples (CFRP_AT_e1 and CFRP_AT_e2). The same loading and heating rate were executed in this test as for every other PHPOT. The pullout began at minute 4 (see Figure 4.17(b)) and the heating blanket was turned on at minute 15, with the tendon's temperature beginning its rise at minute 18 (see Figure 4.17(a)). The Instron machine was configured to pullout from the tendon at a bond stress rate of 2.36 MPa/min during the initial loading phase of the tests up until the required sustained load was reached.

Again, failure did not occur as the temperature of the tendon increased. The heating rate developed as described in Section 3.4.1.2.2. The tendon reached a steady state temperature at 160°C and then, at minute 152, the heating blanket temperature was increased and the tendon reached a steady state temperature of 164°C, as shown in Figure 4.17(a).

At minute 233, after not showing any signs of failure, with the tendon at a steady temperature of 164°C, the Instron machine was configured to pullout until failure occurred at a bond stress rate of 0.45 MPa/min. Failure occurred at about minute 238.5 with a rapid increase of the slip at both ends, as shown in Figure 4.17(c). The maximum average bond stress was 4.33 MPa, with the tendon's temperature at 164°C, and immediately after failure it dropped to 3.82 MPa. After failure, the tendon kept slipping and the sample exhibited a residual bond strength which tended to 2.29 MPa, as shown in Figure 4.17(b).

At the moment of failure there was a sudden drop of the difference between the loaded and the free end slip, as shown in Figure 4.17(d).

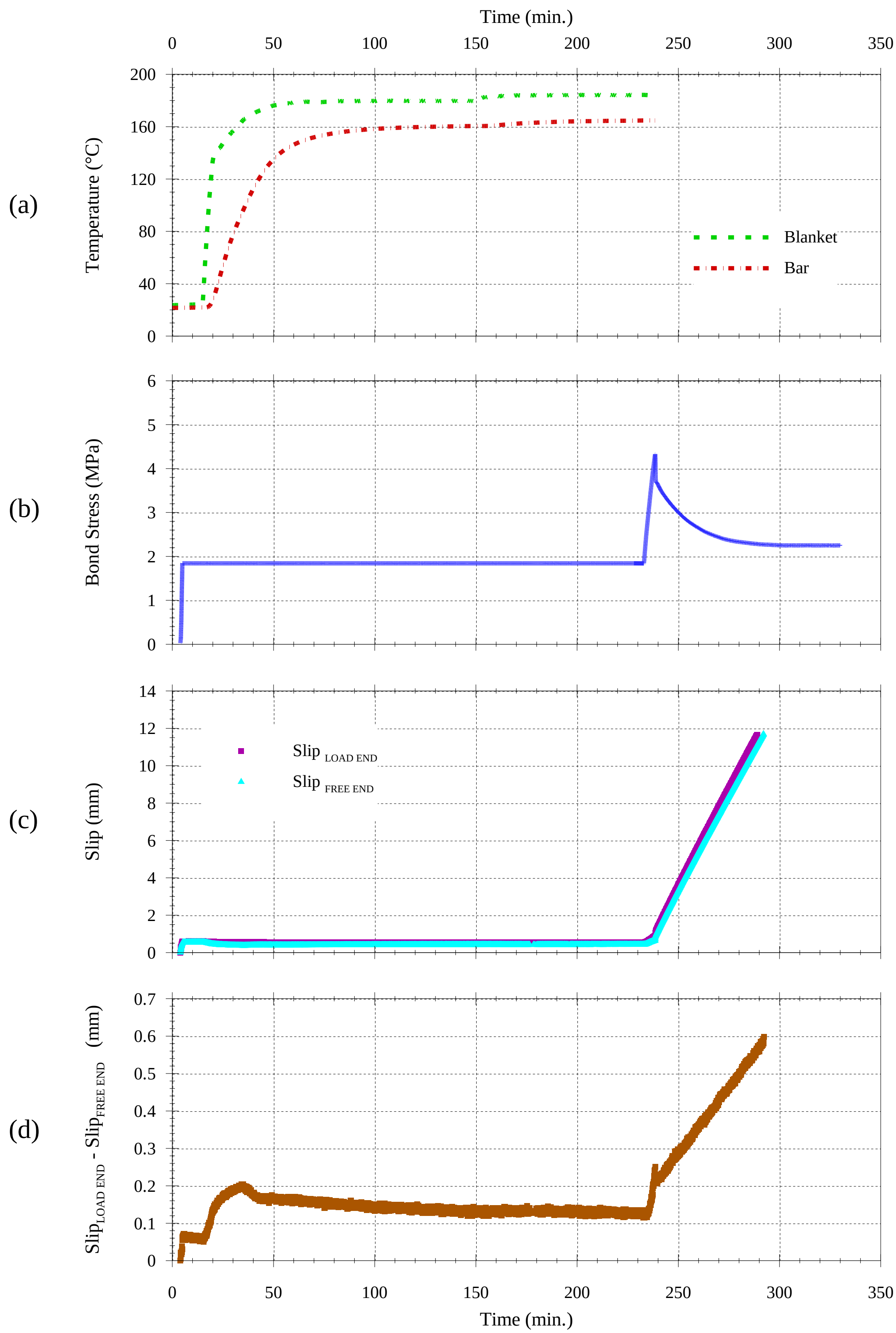

Figure 4.17: Experimental data for CFRP_38%

Figure 4.18 illustrates a zoom-in of the experimental data at the moment at which failure occurred. At this moment the tendon was at a steady state temperature of 164°C, with the heating blanket at 185°C, as shown in Figure 4.18(a). Every parameter was steady up until minute 233, at which point additional load was applied to produce bond failure of the sample.

The average bond stress was steady at 1.84 MPa, up until minute 233 at which point it started increasing at rate of 0.45 MPa/min. Bond stress increased until minute 238.5 at which point the maximum bond stress of 4.33 MPa was achieved, as shown in Figure 4.18(b). A sudden drop of the bond stress then occurred and it dropped to 3.82 MPa at the moment of failure. A residual bond strength of 2.29 MPa was measured as the tendon kept slipping.

Slip at both ends remained steady and started increasing as the load was increased. Both ends started slipping at the same time (minute 233) with a more pronounced increase at the loaded end, up until minute 238.5 at which point a relatively large slip occurred, as shown in Figure 4.18(c). At this point (bond failure), the difference between the loaded and the free end slip dropped, as shown in Figure 4.18(d).

After failure, both slip readings kept increasing at a constant rate, which was slightly larger at the loaded end. This causes the difference between the loaded and the free end slip to increase at a constant rate, after failure occurred, as shown in Figure 4.17(d).

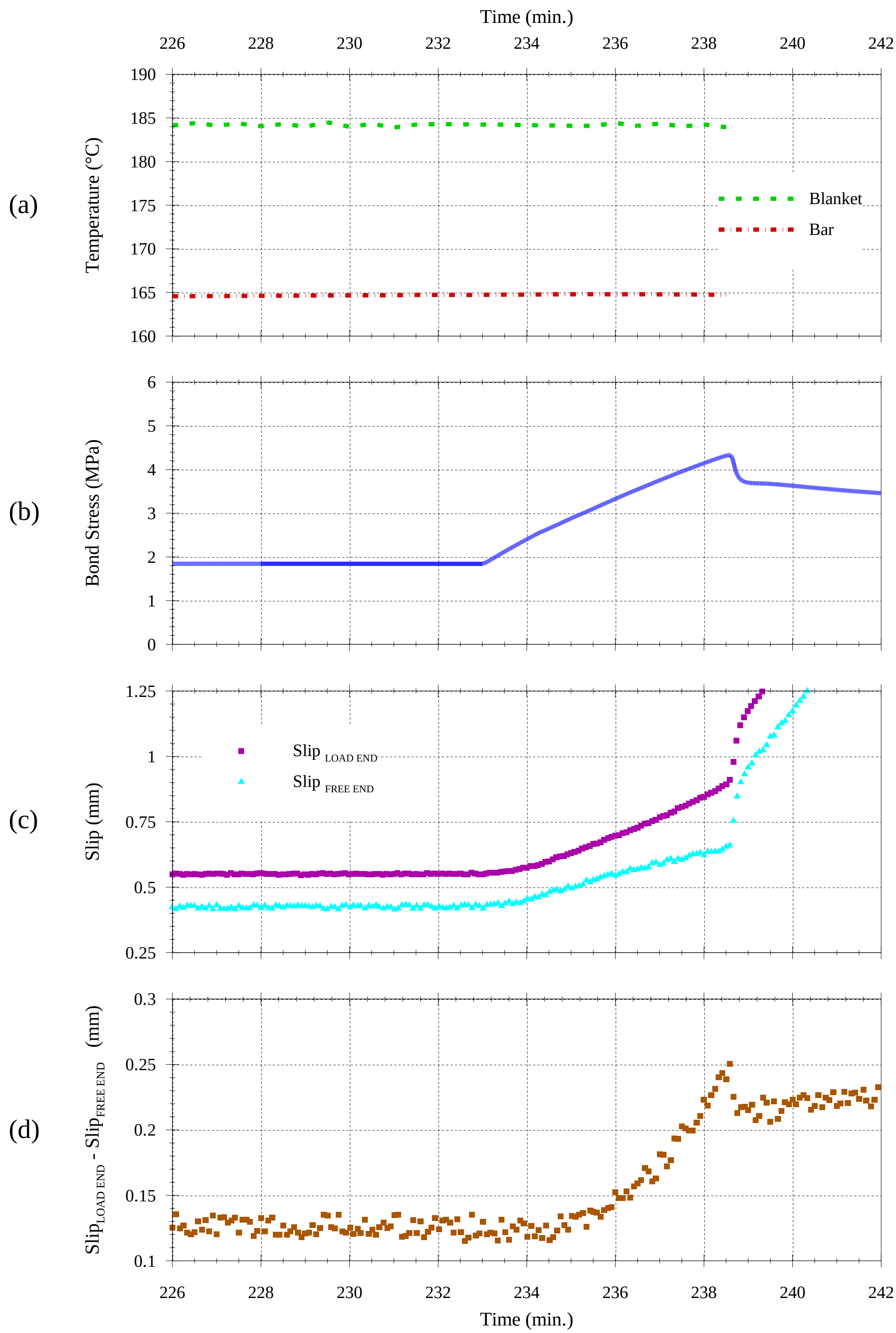

Figure 4.18: Zoom-in of the failure for CFRP_38%

In Figure 4.19, 4.33 MPa was the maximum average bond stress observed. After failure there was a sudden drop of the average bond stress to 3.82 MPa and it then tended to a residual bond strength of 2.29 MPa as the tendon kept on slipping.

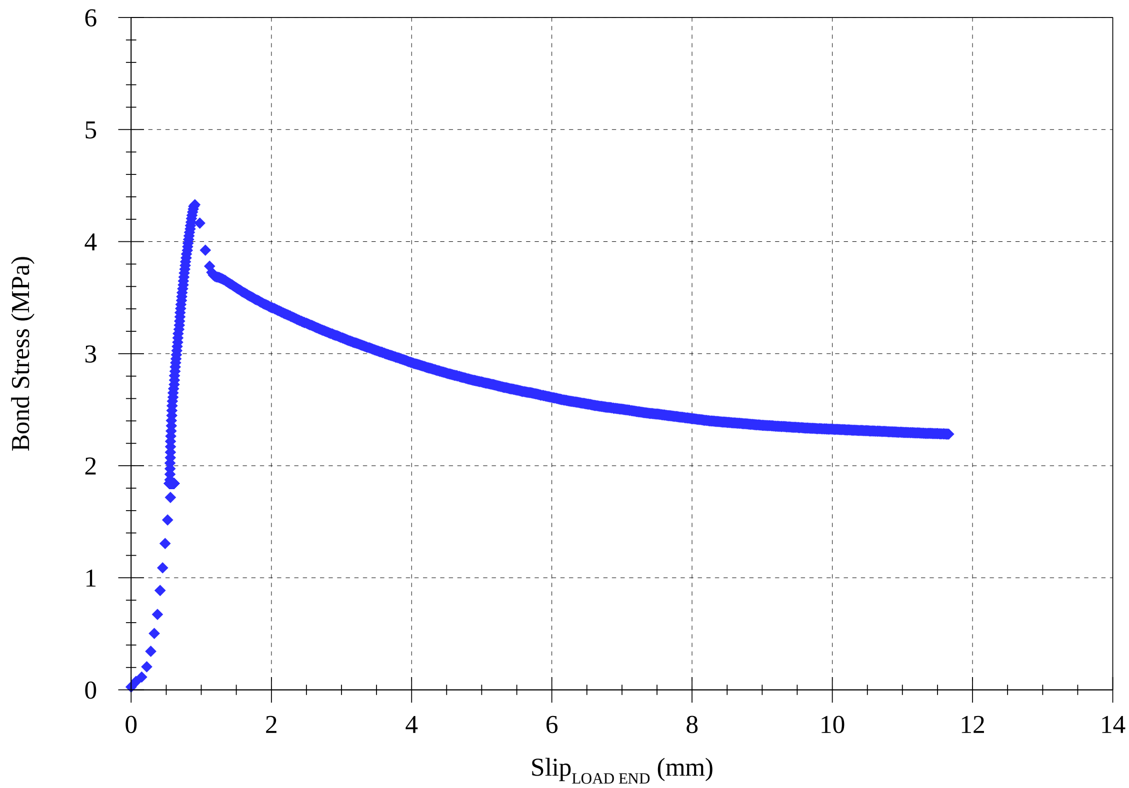

Figure 4.19: Bond stress versus loaded end slip for CFRP_38%

Again, in this test the bond interface did not fail as expected, during the heating phase. It failed only as the load was increased with the tendon at a temperature of 164°C, with an initial bond stress of 1.84 MPa. Nonetheless, Figure 4.20 is instructive to display that the failure occurred at a tendon's temperature of 164°C.

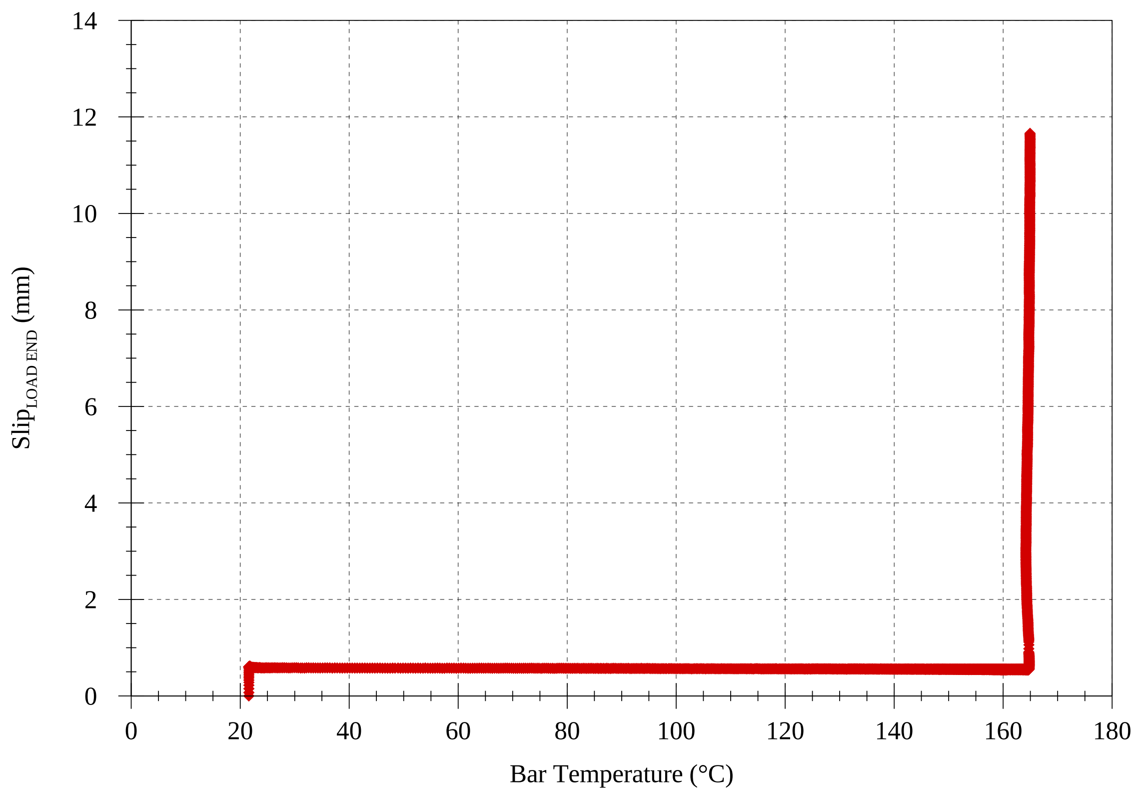

Figure 4.20: Bar temperature versus loaded end slip for CFRP_38%

After the heating blanket was turned on at minute 15, the average bond stress remained constant over time while the difference between the loaded and the free end slip increased, as shown in Figure 4.17(d). A zoom-in of the slip readings (see Figure 4.21) reveals that the increase of the slip difference after minute 15 is a result of the decrease of the slip readings at both ends, with a more pronounced drop of the free end slip.

This phenomenon is a result of the concrete cylinder and CFRP tendon combined thermal expansion as noted and explained in Section 5.4.

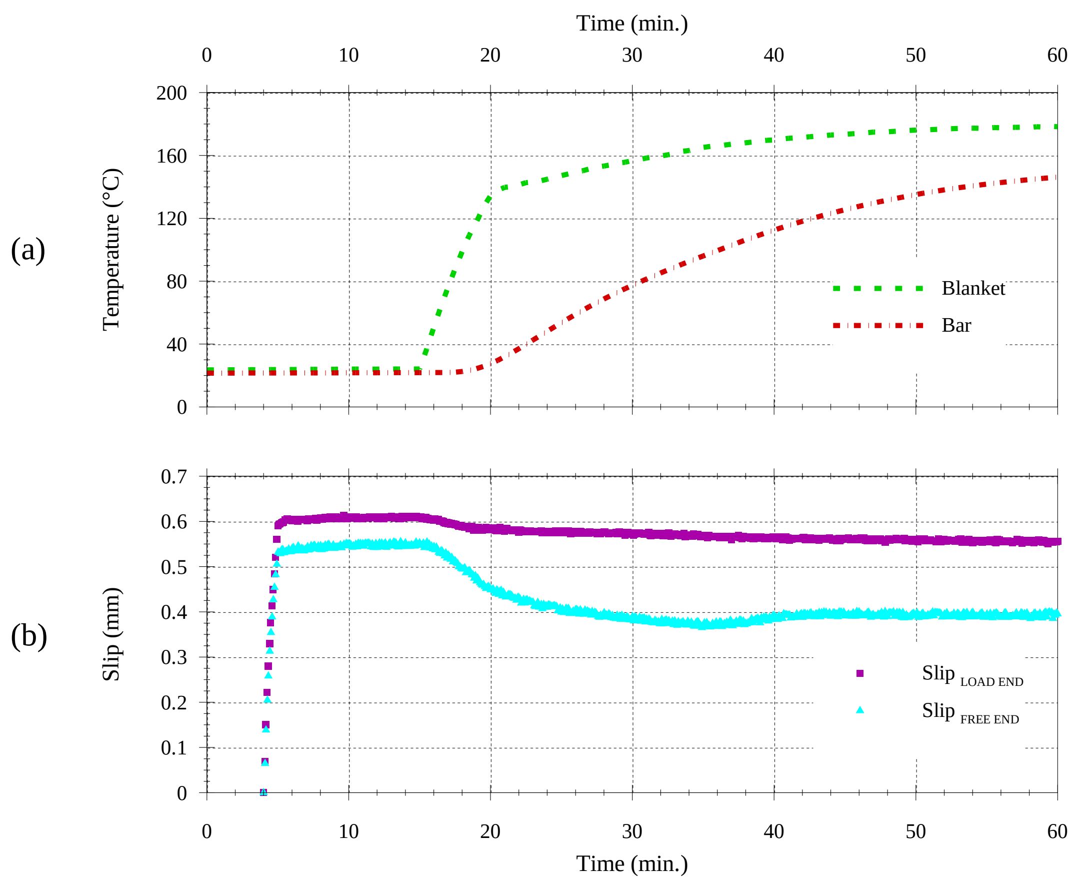

Figure 4.21: Zoom-in of temperature and slip for CFRP_38%

4.1.6 CFRP_45%

This was a PHPOT done on a CFRP pullout sample. This sample was stressed up to 45% (2.21 MPa) of the average bond strength capacity measured from the two RPOTs done on the CFRP pullout samples (CFRP_AT_e1 and CFRP_AT_e2). The same loading and heating rate were executed in this test as for every other PHPOT. The pullout began at minute 4 (see Figure 4.22(b)) and the heating blanket was turned on at minute 15, with the tendon’s temperature beginning its rise at minute 18 (see Figure 4.22(a)). The Instron machine was configured to pullout from the tendon at a bond stress rate of 2.33 MPa/min during the initial loading phase of the tests up until the required sustained load was reached.

The results from this test, unlike the previously described tests, turned out to be as expected for the PHPOTs, and failure did occur under sustained bond stress as the temperature of the tendon was increasing. The heating rate developed as described in Section 3.4.1.2.2. The sample was kept at a steady stress level until failure occurred, as showed in Figure 4.22(b).

Figure 4.22(d), shows the difference between the loaded and the free end slip. At the initial loading stage the value dropped below zero, as it also happened in CFRP_AT_e1 and described in Section 4.1.1. After minute 15, the value increased as a result of the combined thermal expansion of the concrete cylinder and the CFRP tendon, a phenomenon which is further discussed analysed in Section 5.4.

Figure 4.22(d) also defines the moment at which failure occurred. At minute 36, with the tendon at 97°C, the difference between the loaded end and the free end slips started decreasing as a result of slip at the free end (signifying bond failure). This went on until minute 39.5, with the tendon at 109°C and the heating blanket at 169°C, at which point the slip difference started rising as a result of considerable slip at both ends of the bonded length, always at a bigger rate at the loaded end, until total pullout occurred (at minute 45 with the tendon at 123°C) and the bond strength dropped to zero. At the end of the test, slip at both ends rapidly increased, as shown in Figure 4.22(c), because of the Instron´s attempt to keep the bond stress at the predetermined level (2.21 MPa) in a load-control mode.

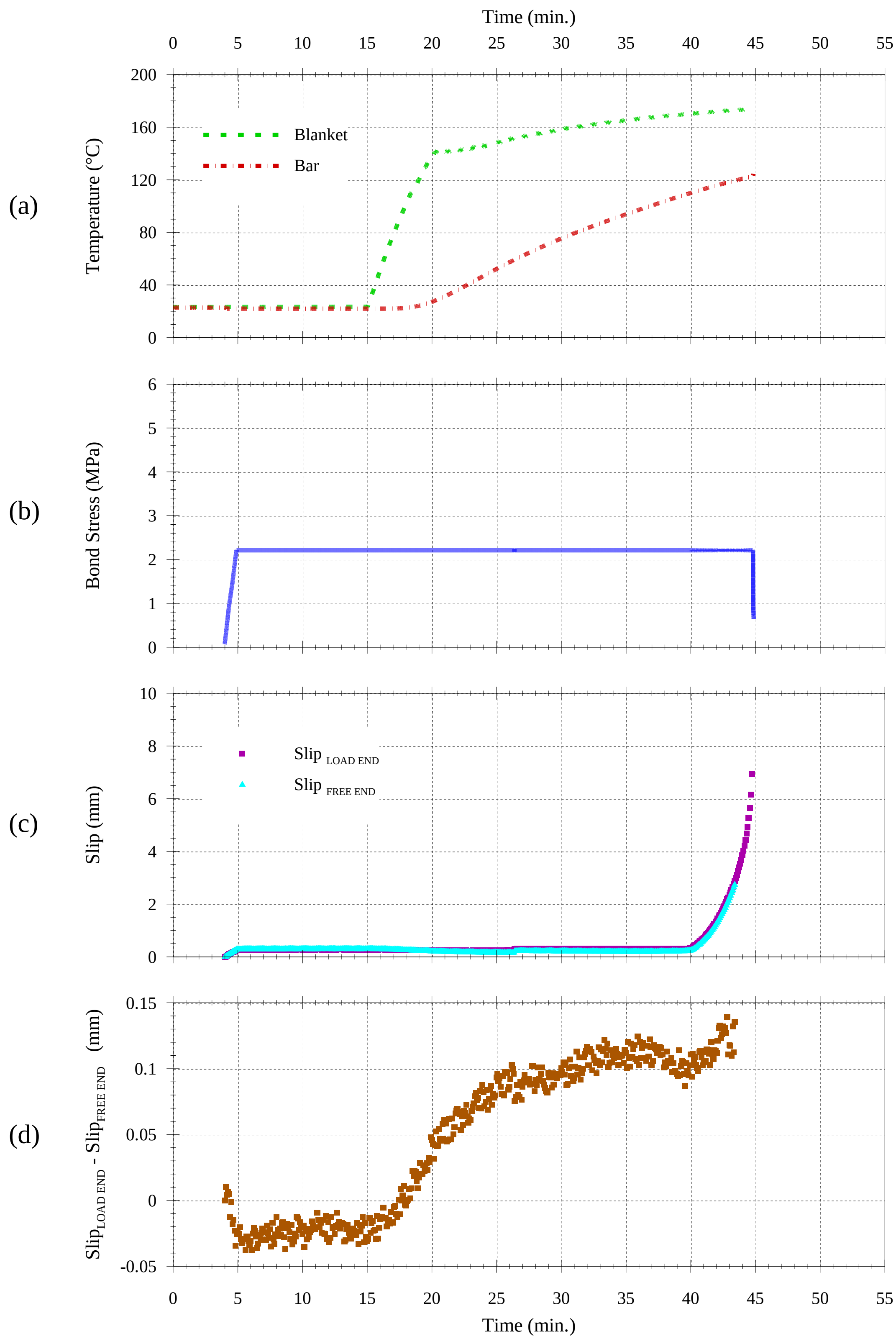

Figure 4.22: Experimental data for CFRP_45%

In this test it was not easy to precisely define the bond failure temperature. Figure 4.23 is a zoom-in of the moment at which failure initiated. From this graph it is possible to define the moment at which considerable slip started at the free end (minute 36 with the tendon at 97°C) and afterwards started at the loaded end (minute 39.5 with the tendon at 109°C) at a much higher rate. These observations were corroborated by the information obtained from Figure 4.22(d).

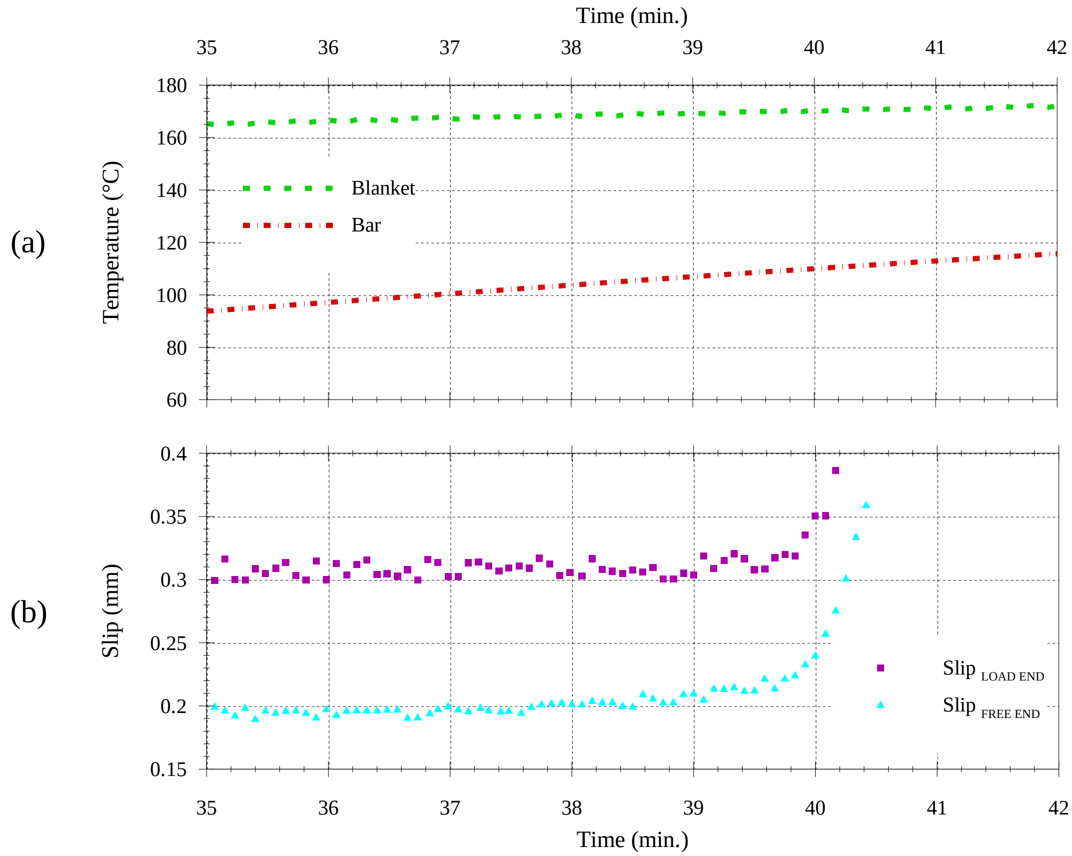

Figure 4.23: Zoom-in of the development of temperature and slip at failure for CFRP_45%

The CFRP tendon's bond failure temperature was about 109°C when the bond stress was sustained at 2.21 MPa, as instructively shown in Figure 4.24.

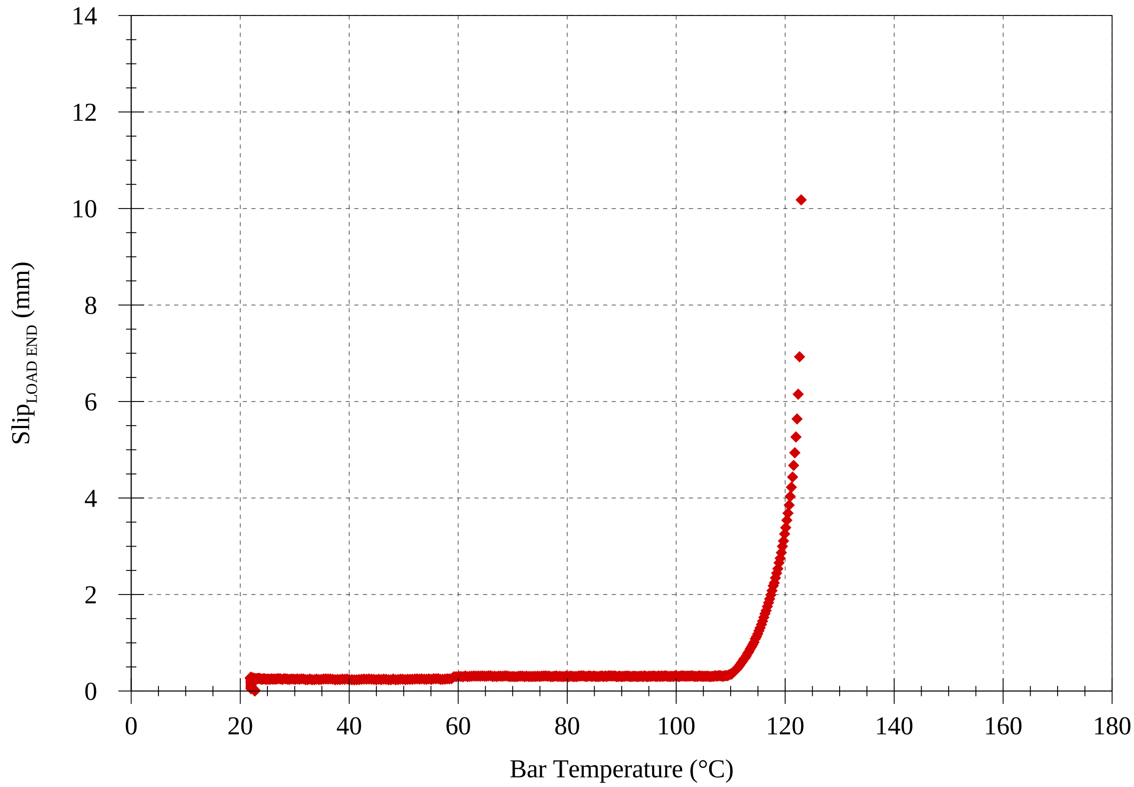

Figure 4.24: Bar temperature versus loaded end slip for CFRP_45%

As failure occurred, the Instron machine tried to keep the average bond stress at the predetermined sustained level (2.21 MPa) in load-control testing mode; this is the reason why the bond stress suddenly dropped and the slip accelerated rapidly toward failure. At this high slip, the slip measurement systems were unable to continue measuring. This is why the residual bond strength relative to the Instron’s crosshead displacement was determined (see Figure 4.25), rather than relative to the loaded end slip. The residual bond stress tended to a value of only 0.65 MPa.

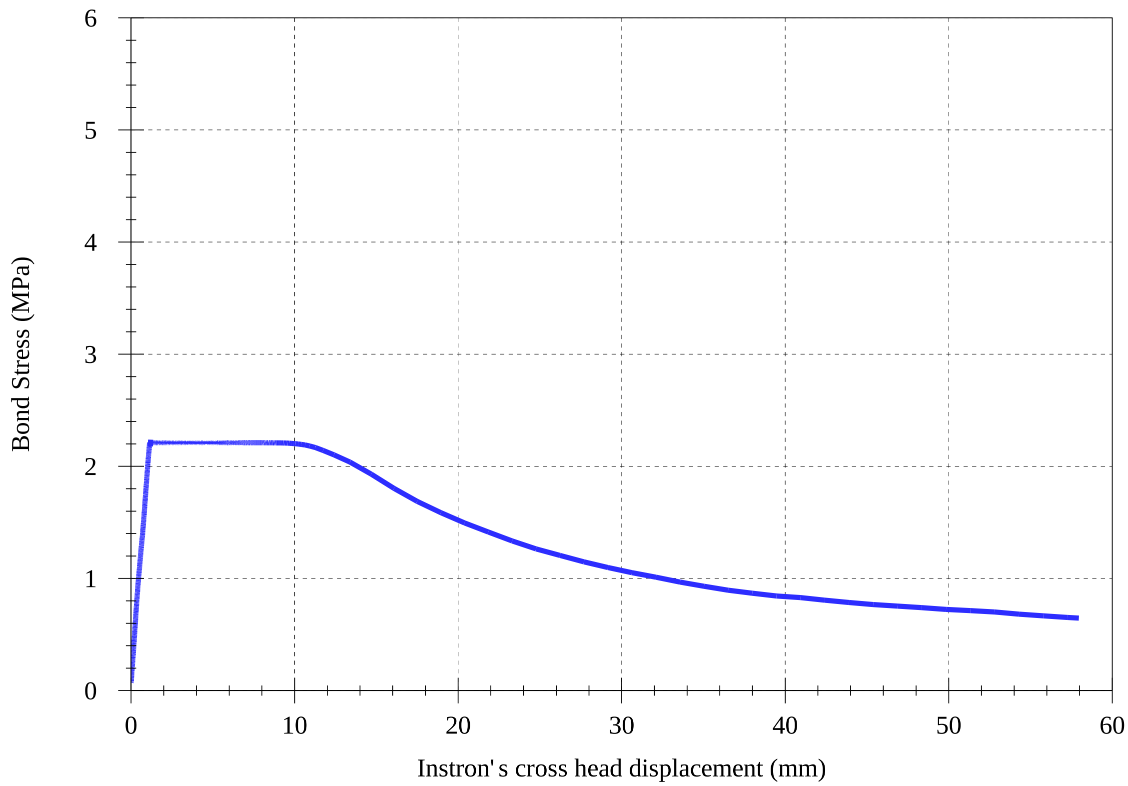

Figure 4.25: Bond stress versus Instron’s crosshead displacement for CFRP_45%

After the heating blanket was turned on at minute 15, the average bond stress remained constant over time while the difference between the loaded and the free end slip increased, as shown in Figure 4.22(d). A zoom-in of the slip readings (see Figure 4.26) reveals that the increase of the slip difference after minute 15 is a result of the decrease of the slip readings at both ends, with a more pronounced drop of the free end slip.

This phenomenon is a result of the concrete cylinder and CFRP tendon combined thermal expansion as noted and explained in Section 5.4.

A local failure was observed at minute 26, which was expressed as a sudden jump in the slip measurements, which are measured every 5 seconds with the digital image correlation system, at both ends. An almost imperceptible variation was observed in the bond stress measurement at that time.

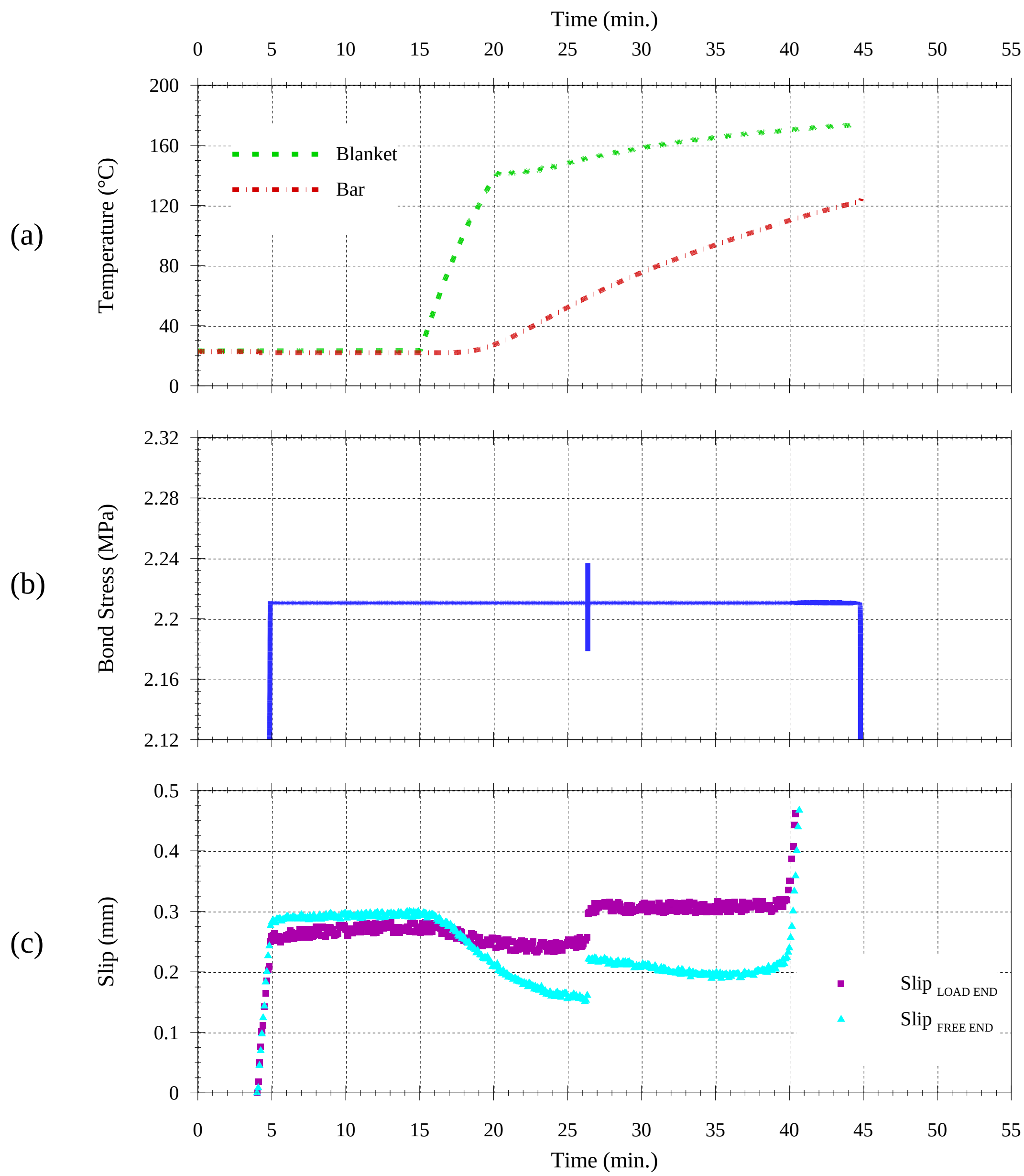

Figure 4.26: Zoom-in of temperature, bond stress and slip for CFRP_45%

4.1.7 CFRP_53%

This was a PHPOT done on a CFRP pullout sample. This sample was stressed up to 53% (2.58 MPa) of the average bond strength capacity measured from the two RPOTs done on the CFRP pullout samples (CFRP_AT_e1 and CFRP_AT_e2). The same loading and heating rate were executed in this test as for every other PHPOT. The pullout began at minute 4 (see Figure 4.27(b)) and the heating blanket was turned on at minute 15, with the tendon's temperature beginning its rise at minute 18 (see Figure 4.27(a)). The Instron machine was configured to pullout from the tendon at a bond stress rate of 3.23 MPa/min during the initial loading phase of the tests up until the required sustained load was reached.

The results from this test turned out to be as expected for the PHPOTs; failure occurred under sustained bond stress as the temperature of the tendon was increasing. The heating rate developed as described in Section 3.4.1.2.2. The sample was kept at a steady stress level until failure occurred, as showed in Figure 4.27(b).

Figure 4.27(d), shows the difference between the loaded and the free end slip. At the initial loading stage the value dropped below zero, as it also happened in CFRP_AT_e1 and described in Section 4.1.1. After minute 15, the value increased as a result of the combined thermal expansion of the concrete cylinder and the CFRP tendon, a phenomenon which is further discussed analysed in Section 5.4.

Figure 4.27(d) also defines the moment at which failure occurred. At minute 35, with the tendon at 86°C, the difference between the loaded end and the free end slips started decreasing as a result of slip at the free end (signifying bond failure). This went on until minute 41, with the tendon at 102°C and the heating blanket at 155°C, at which point the slip difference started rising as a result of considerable slip at both ends of the bonded length, always at a bigger rate at the loaded end, until total pullout occurred (at minute 51 with the tendon at 123°C) and the bond strength dropped to zero. At the end of the test, slip at both ends rapidly increased, as shown in Figure 4.27(c), because of the Instron´s attempt to keep the bond stress at the predetermined level (2.58 MPa) in a load-control mode.

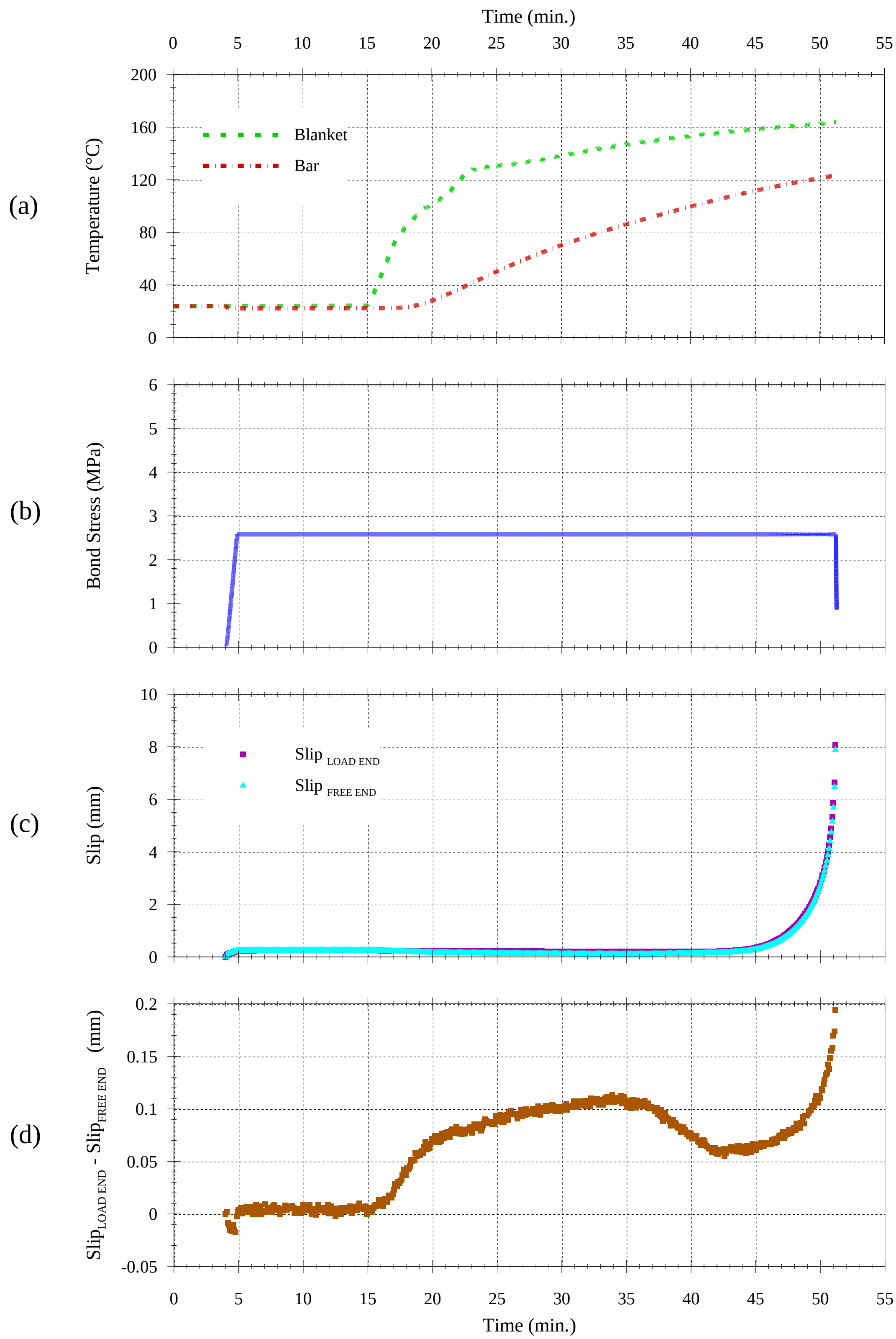

Figure 4.27: Experimental data for CFRP_53%

As for the previous test, it was not easy to precisely define the bond failure temperature. Figure 4.28 is a zoom-in of the moment at which failure initiated. From this graph it is possible to define the moment at which considerable slip starts at the free end (minute 35 with the tendon at 86°C) and afterwards starts at the loaded end (minute 41 with the tendon at 102°C) at a much higher rate. These observations were corroborated by the information obtained from Figure 4.27(d).

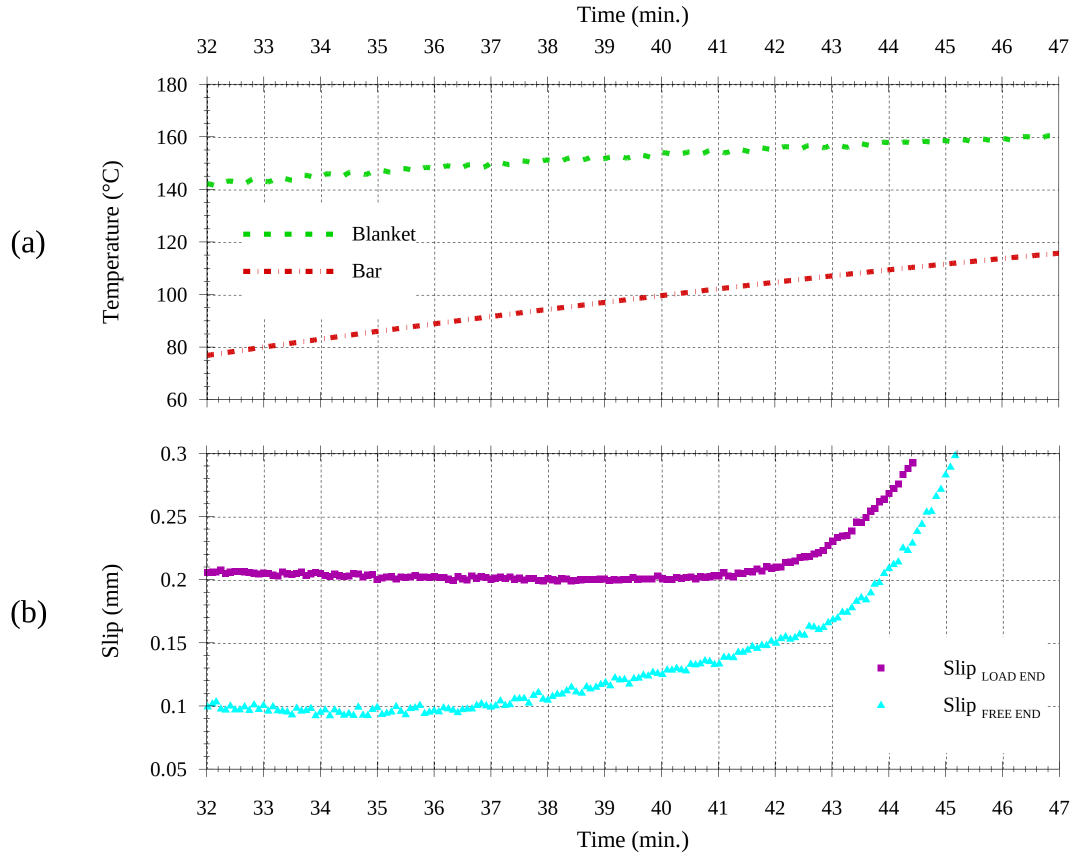

Figure 4.28: Zoom-in of the development of temperature and slip at failure for CFRP_53%

The CFRP tendon's bond failure temperature was about 102°C when the bond stress was sustained at 2.58 MPa, as instructively shown in Figure 4.29.

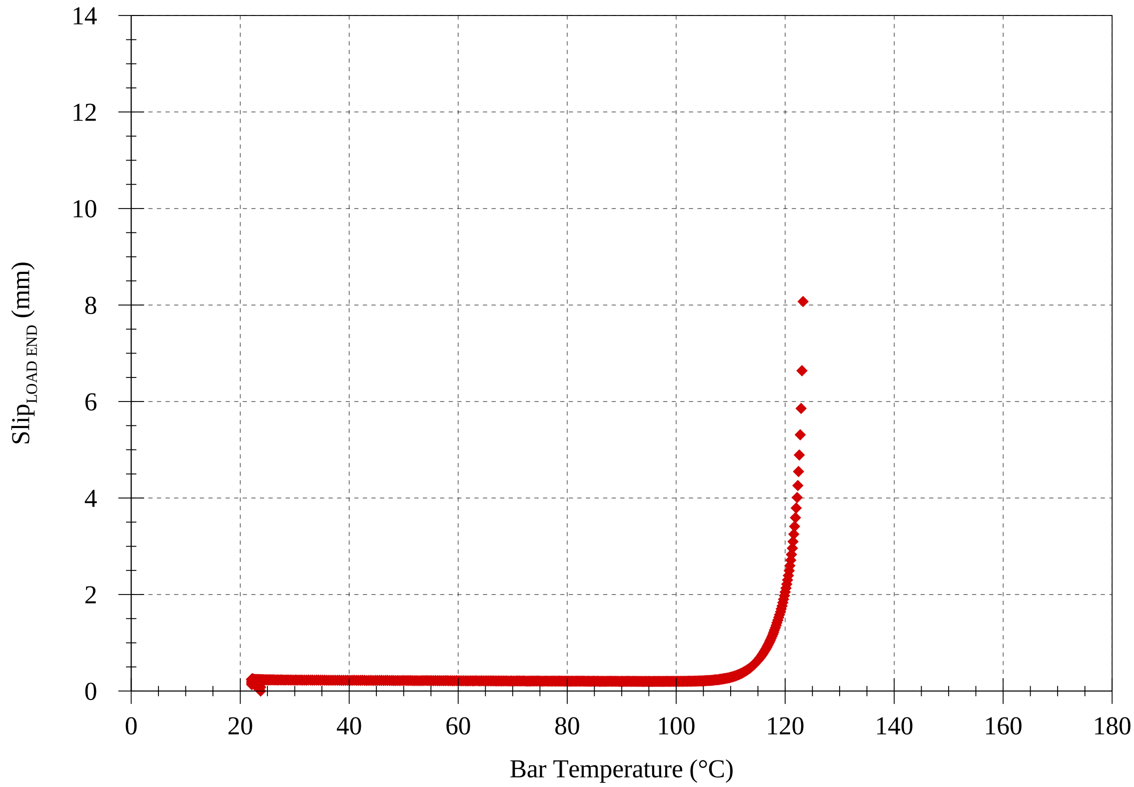

Figure 4.29: Bar temperature versus loaded end slip for CFRP_53%

As failure occurred, the Instron machine tried to keep the average bond stress at the predetermined sustained level (2.58 MPa) in load-control testing mode; this is the reason why the bond stress suddenly dropped and the slip accelerated rapidly toward failure. As for the previous test, at this high slip, the slip measurement systems were unable to continue measuring. This is why the residual bond strength relative to the Instron's crosshead displacement was determined (see Figure 4.30), rather than relative to the loaded end slip. The residual bond stress tended to a value of only 0.89 MPa.

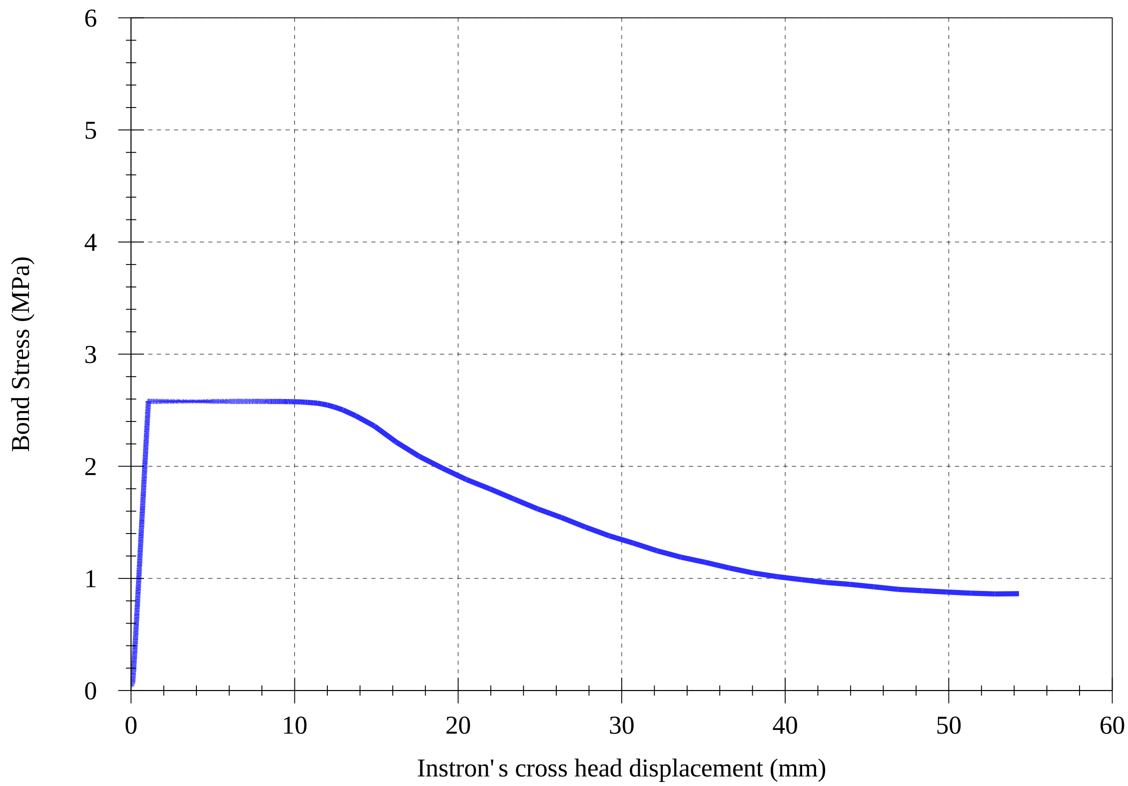

Figure 4.30: Bond stress versus Instron's crosshead displacement for CFRP_53%

After the heating blanket was turned on at minute 15, the average bond stress remained constant over time while the difference between the loaded and the free end slip increased, as shown in Figure 4.27(d). A zoom-in of the slip readings (see Figure 4.31) reveals that the increase of the slip difference after minute 15 is a result of the decrease of the slip readings at both ends, with a more pronounced drop of the free end slip.

This phenomenon is a result of the concrete cylinder and CFRP tendon combined thermal expansion as noted and explained in Section 5.4.

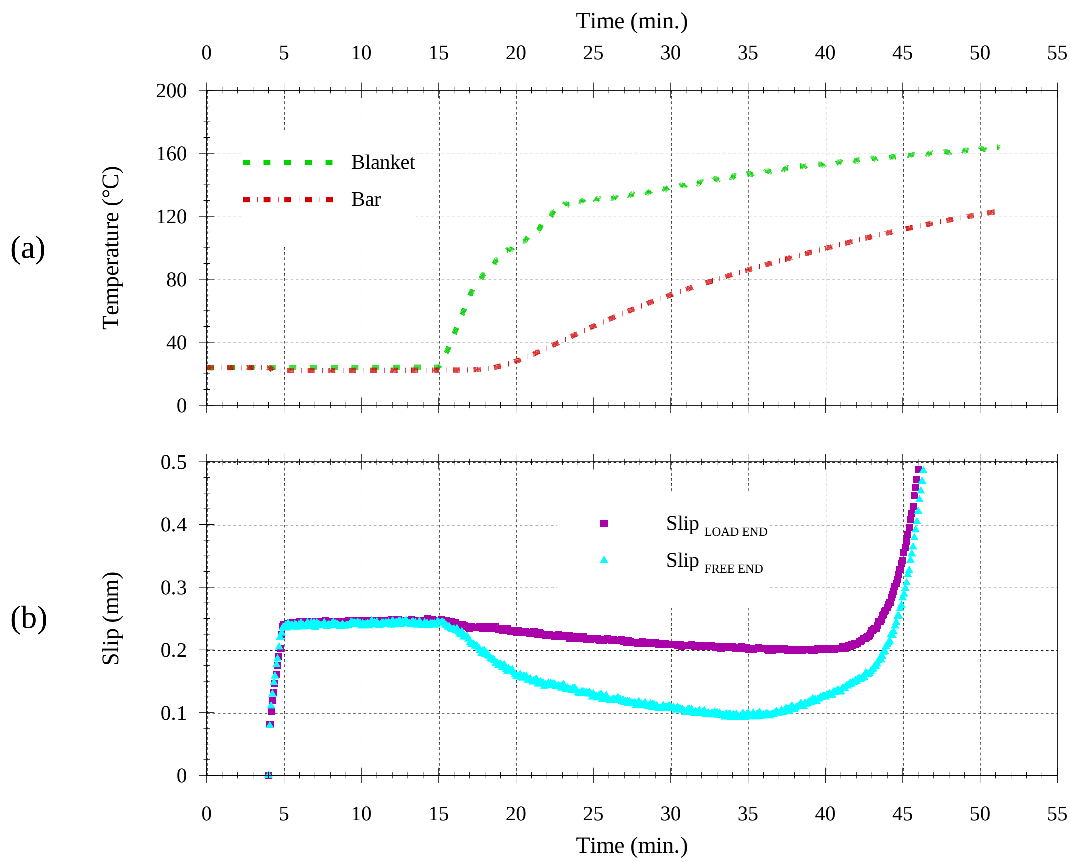

Figure 4.31: Zoom-in of temperature and slip for CFRP_53%

4.1.8 CFRP_60%

This was a PHPOT done on a CFRP pullout sample. This sample was stressed up to 60% (2.95 MPa) of the average bond strength capacity measured from the two RPOTs done on the CFRP pullout samples (CFRP_AT_e1 and CFRP_AT_e2). The same loading and heating rate were executed in this test as for every other PHPOT. The pullout began at minute 4 (see Figure 4.32(b)) and the heating blanket was turned on at minute 15, with the tendon's temperature beginning its rise at minute 18 (see Figure 4.32(a)). The Instron machine was configured to pullout from the tendon at a bond stress rate of 2.71 MPa/min during the initial loading phase of the tests up until the required sustained load was reached.

The results from this test turned out to be as expected for the PHPOTs; failure occurred under sustained bond stress as the temperature of the tendon was increasing. The heating rate developed as described in Section 3.4.1.2.2. The sample was kept at a steady stress level until failure occurred, as showed in Figure 4.32(b).

Figure 4.32(d), shows the difference between the loaded and the free end slip. At the initial loading stage the value dropped below zero, as it also happened in CFRP_AT_e1 and described in Section 4.1.1. After minute 15, the value increased as a result of the combined thermal expansion of the concrete cylinder and the CFRP tendon, a phenomenon which is further discussed analysed in Section 5.4.

Figure 4.32(d) also defines the moment at which failure occurred. At minute 36, with the tendon at 86°C, the difference between the loaded end and the free end slips started decreasing as a result of slip at the free end (signifying bond failure). This went on until minute 39, with the tendon at 95°C and the heating blanket at 155°C, at which point the slip difference started rising as a result of considerable slip at both ends of the bonded length, always at a bigger rate at the loaded end, until total pullout occurred (at minute 48 with the tendon at 114°C) and the bond strength dropped to zero. At the end of the test, slip at both ends rapidly increased, as shown in Figure 4.32(c), because of the Instron´s attempt to keep the bond stress at the predetermined level (2.95 MPa) in a load-control mode.

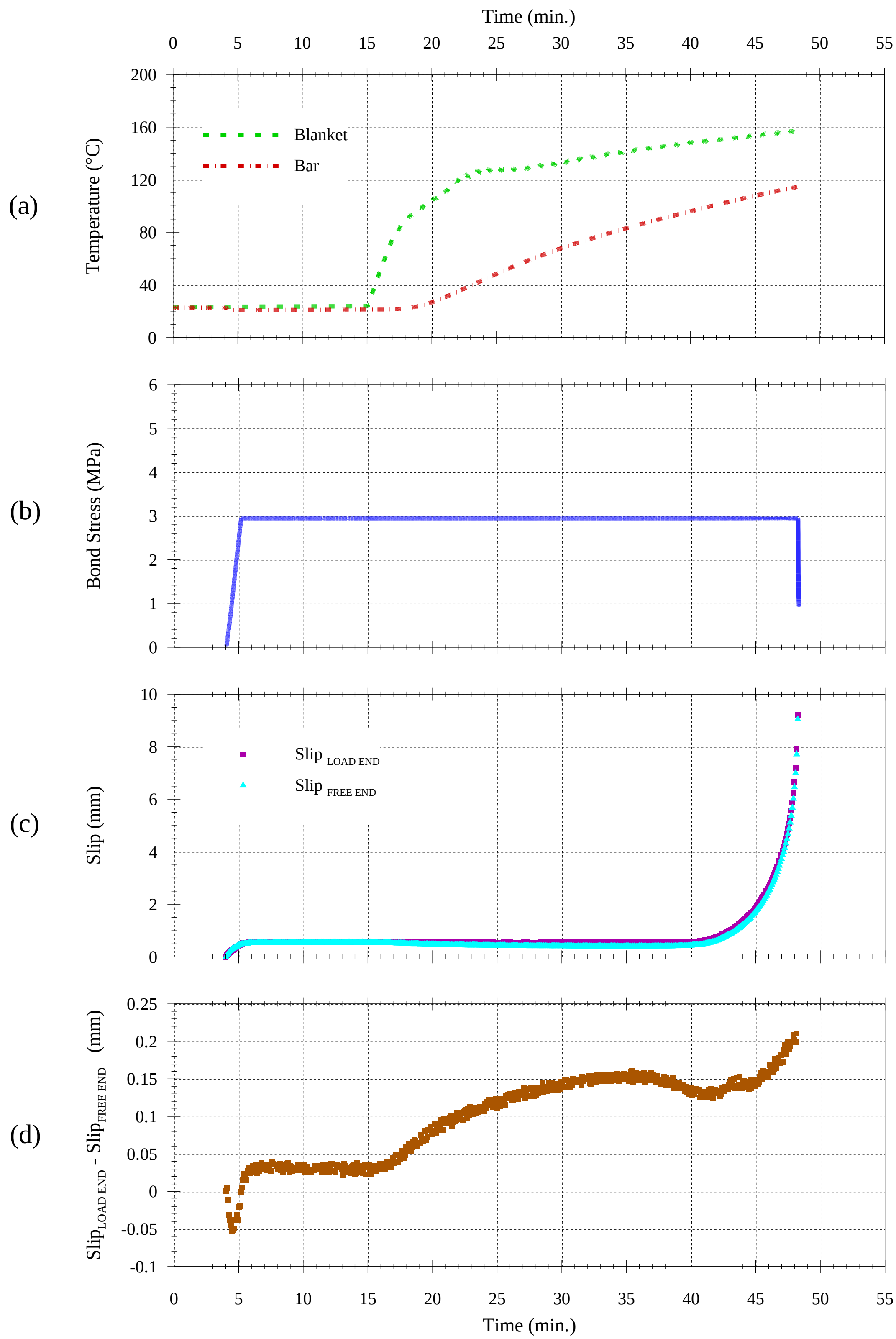

Figure 4.32: Experimental data for CFRP_60%

As for the previous test, it was not easy to precisely define the bond failure temperature. Figure 4.33 is a zoom-in of the moment at which failure initiated. From this graph it is possible to define the moment at which considerable slip starts at the free end (minute 36 with the tendon at 86°C) and afterwards starts at the loaded end (minute 39 with the tendon at 95°C) at a much higher rate. These observations were corroborated by the information obtained from Figure 4.32(d).

(a)

(b)

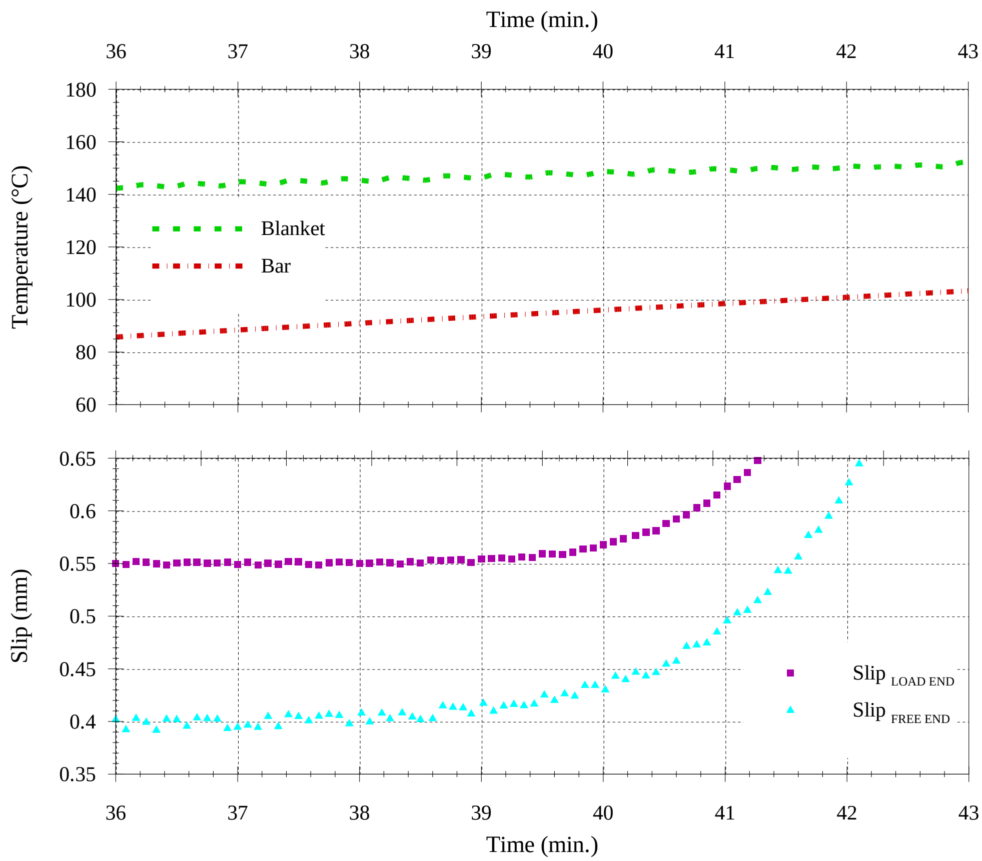

Figure 4.33: Zoom-in of the development of temperature and slip at failure for CFRP_60%

The CFRP tendon's bond failure temperature was about 95°C when the bond stress was sustained at 2.95 MPa, as instructively shown in Figure 4.34.

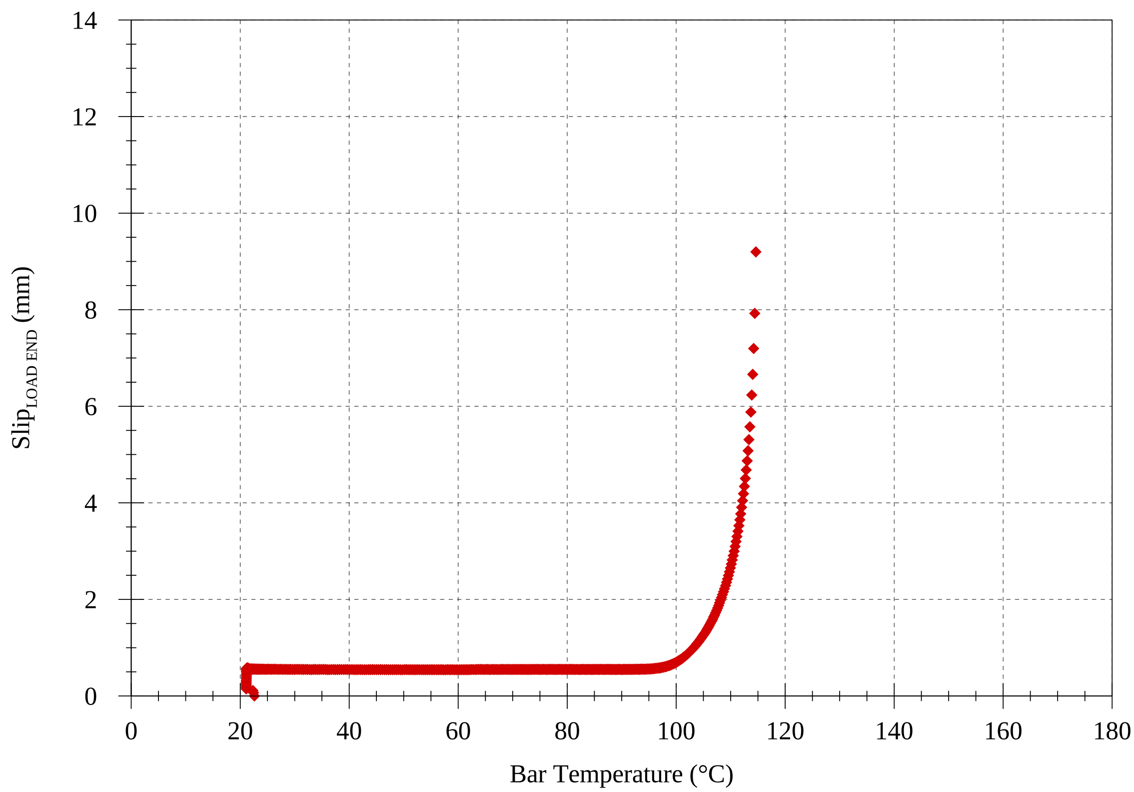

Figure 4.34: Bar temperature versus loaded end slip for CFRP_60%

As failure occurred, the Instron machine tried to keep the average bond stress at the predetermined sustained level (2.95 MPa) in load-control testing mode; this is the reason why the bond stress suddenly dropped and the slip accelerated rapidly toward failure. As for the previous test, at this high slip, the slip measurement systems were unable to continue measuring. This is why the residual bond strength relative to the Instron's crosshead displacement was determined (see Figure 4.35), rather than relative to the loaded end slip. The residual bond stress tended to a value of only 0.92 MPa.

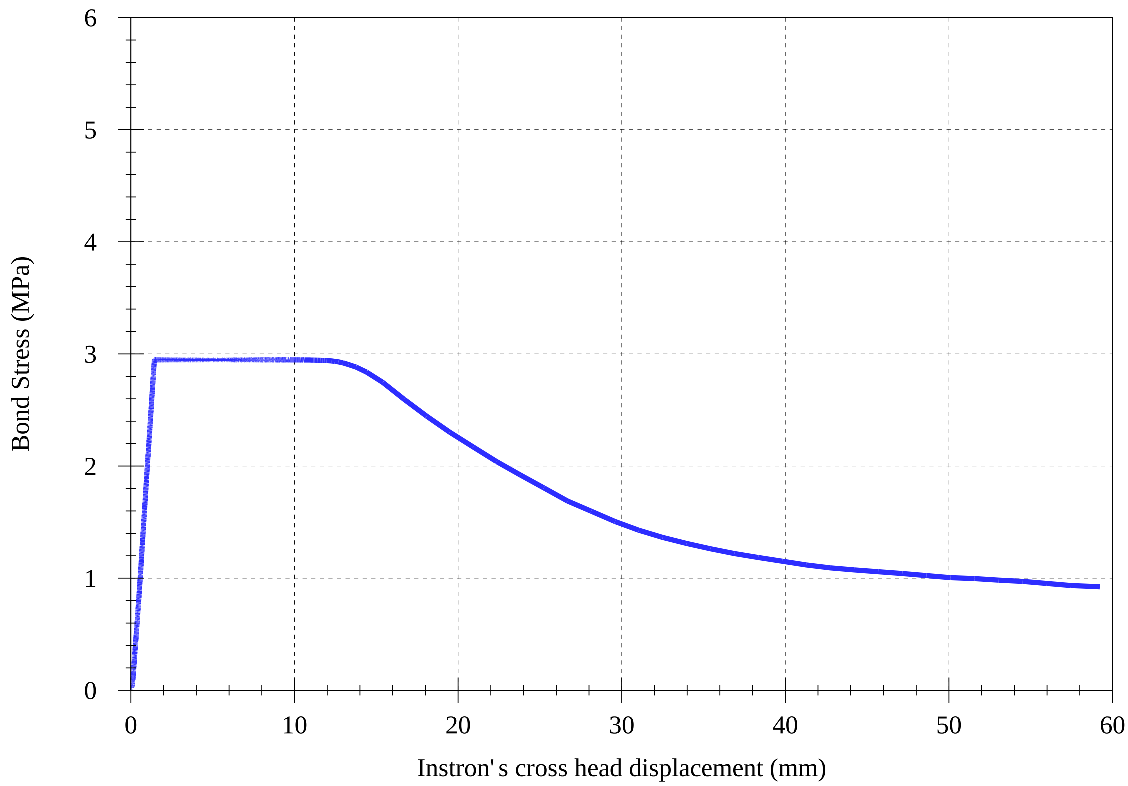

Figure 4.35: Bond stress versus Instron's crosshead displacement for CFRP_60%

After the heating blanket was turned on at minute 15, the average bond stress remained constant over time while the difference between the loaded and the free end slip increased, as shown in Figure 4.32(d). A zoom-in of the slip readings (see Figure 4.36) reveals that the increase of the slip difference after minute 15 is a result of the decrease of the slip readings at both ends, with a more pronounced drop of the free end slip.

This phenomenon is a result of the concrete cylinder and CFRP tendon combined thermal expansion as noted and explained in Section 5.4.

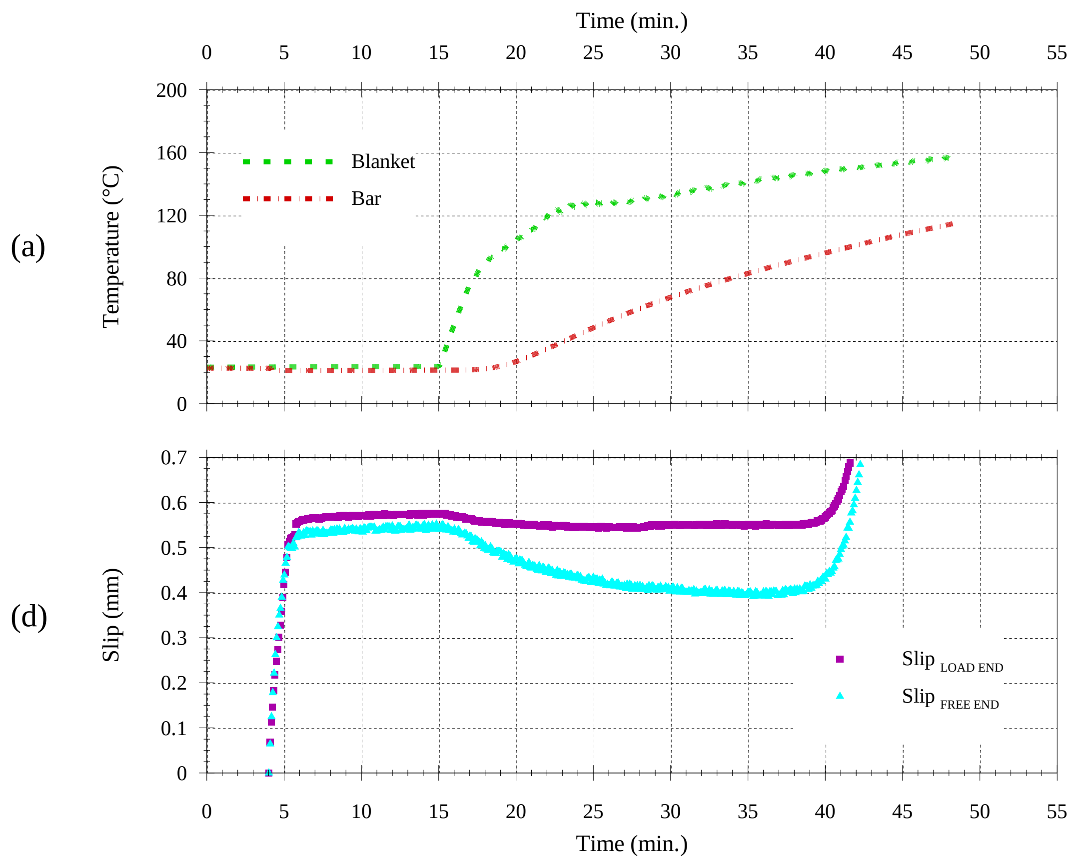

Figure 4.36: Zoom-in of temperature and slip for CFRP_60%

4.1.9 CFRP_68%

This was a PHPOT done on a CFRP pullout sample. This sample was stressed up to 68% (3.32 MPa) of the average bond strength capacity measured from the two RPOTs done on the CFRP pullout samples (CFRP_AT_e1 and CFRP_AT_e2). The same loading and heating rate were executed in this test as for every other PHPOT. The pullout began at minute 4 (see Figure 4.37(b)) and the heating blanket was turned on at minute 15, with the tendon's temperature beginning its rise at minute 18 (see Figure 4.37(a)). The Instron machine was configured to pullout from the tendon at a bond stress rate of 2.78 MPa/min during the initial loading phase of the tests up until the required sustained load was reached.

In this test, failure occurred before the temperature of the tendon started increasing. The results from this test were different from the proposed PHPOT. The sample was kept at a steady stress level and bond failure occurred suddenly, at minute 22, before the tendon's temperature started rising, as shown in Figure 4.37(a). Thus, 3.32 MPa (68% of the ambient temperature bond strength) could be considered as the sustained average bond stress level which cannot be kept steady over the period of time necessary to run a PHPOT. At failure the tendon's and concrete's surface temperature were at 21°C and 76°C respectively. This failure could also be the result of the slip produced by the concrete's temperature increase. This phenomenon is noted and explained in Section 5.4.

Because this test ended earlier than expected, Figure 4.37(c) and Figure 4.37(d) only display useful data from the initial loading stage. At the initial loading stage the value dropped below zero, as it also happened in CFRP_AT_e1 and described in Section 4.1.1.

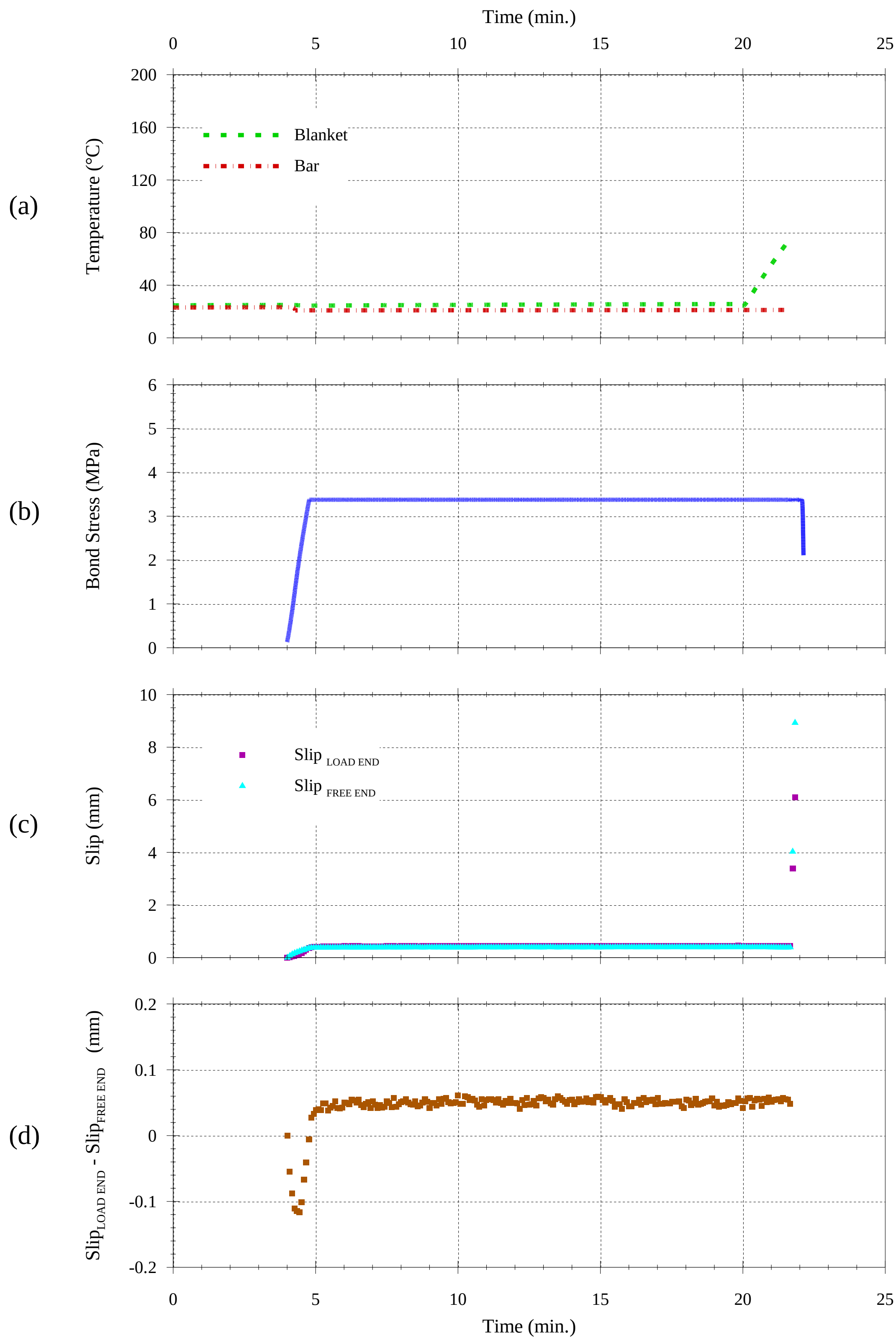

Figure 4.37: Experimental data for CFRP_68%

As failure occurred, the Instron machine tried to keep the average bond stress at the predetermined sustained level (3.32 MPa) in load-control testing mode; this is the reason why the bond stress suddenly dropped and the slip accelerated rapidly toward failure. As for the previous test, at this high slip, the slip measurement systems were unable to continue measuring. This is why the residual bond strength relative to the Instron's crosshead displacement was determined (see Figure 4.38), rather than relative to the loaded end slip. Because the failure mode was extremely sudden, the bond residual strength does not reach a steady value.

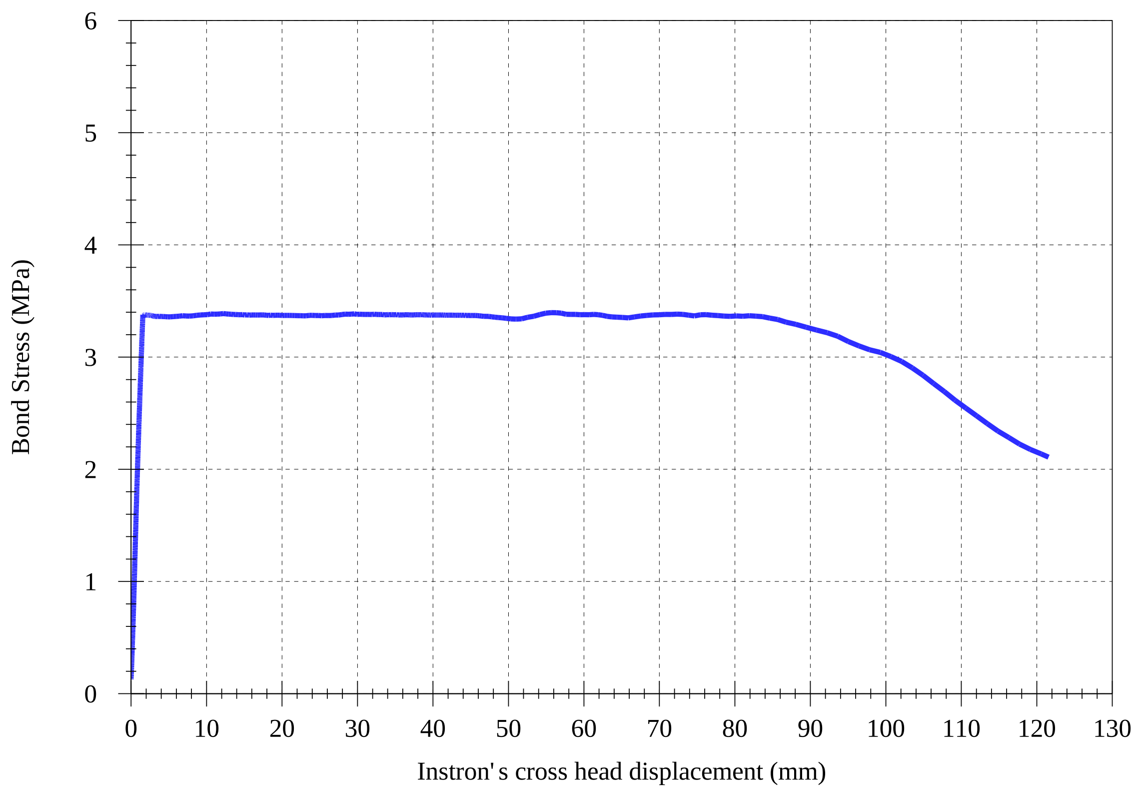

Figure 4.38: Bond stress versus Instron's crosshead displacement for CFRP_68%

After the heating blanket was turned on at minute 20, less than two minutes passed before sudden bond failure. Before bond failure, at minute 21, both slips started decreasing very slightly, with a more pronounced drop at the free end, as shown in Figure 4.39(b).

This phenomenon is a result of the concrete cylinder and CFRP tendon combined thermal expansion as noted and explained in Section 5.4. As mentioned before, the slip produced by the increase in temperature could be the result of the bond failure occurring earlier than expected.

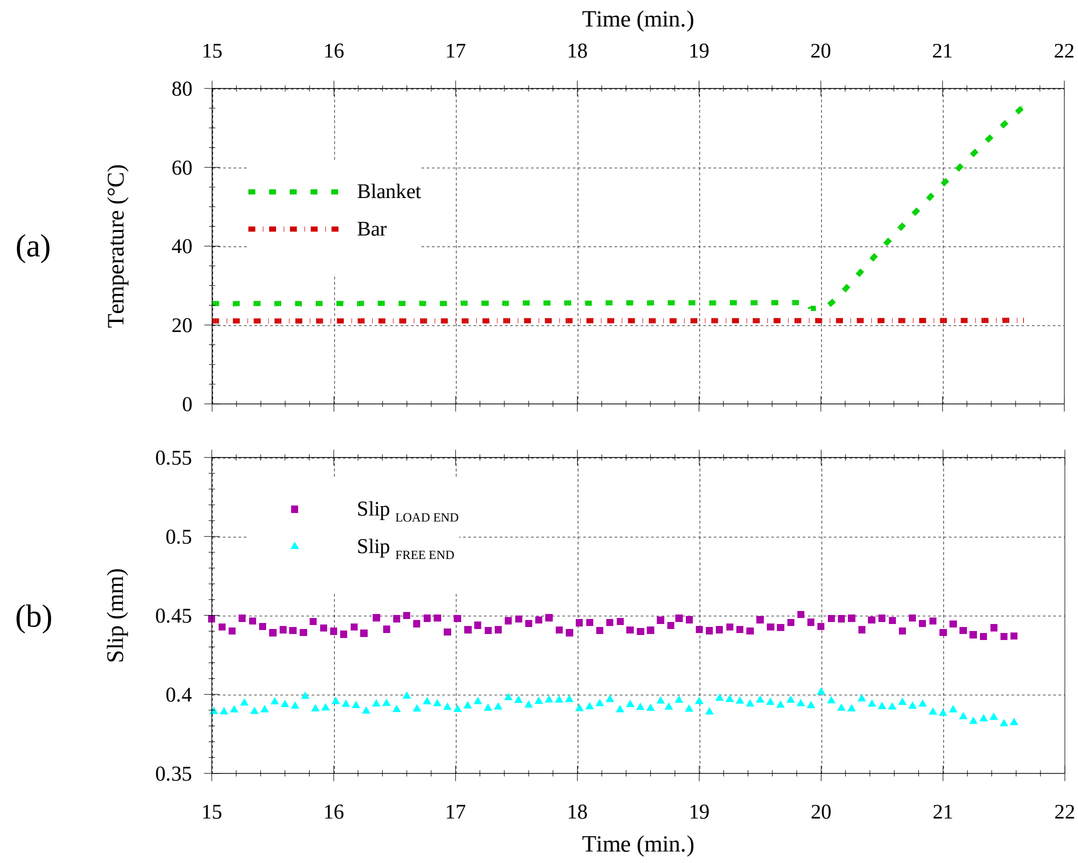

Figure 4.39: Zoom-in of temperature and slip for CFRP_68%

4.1.10 Steel_AT_e1

This was a RPOT done on a steel pullout sample. This sample was intended to be pulled out until failure of the bond interface occurred. At minute 4, the Instron machine was set to start the pullout at a bond stress rate of 3.27 MPa/min, as shown in Figure 4.40(b).

As for the CFRP RPOTs, the heating blanket was not set on this sample, but thermocouples were placed on the CFRP tendon’s surface and at the cylinders surface. This was executed in order to have the same conditions as for the PHPOTs. The temperature at the concrete’s surface and at the tendon were 24°C and 22°C, respectively (see Figure 4.40(a)).

At the loaded end, slip is calculated by subtracting the elasticity of the un-bonded part of the tendon, as described in Section 3.4.1.3. For this, the theoretical elastic modulus of the steel prestressing wire (210 GPa) was used.

This RPOT did not fail as expected. In this test, the bond strength of the steel prestressing wire was actually greater than the tensile capacity of the wire. The steel prestressing wire yielded and eventually failed in tension at the loaded end, thus preventing observation of the entire bond behaviour. The data obtained from this test is only interesting in terms of comparison against the CFRP tendons up to the minute 8, at which point the elastic behaviour of the steel prestressing wire ended. After minute 8, plastic deformation began and because the pullout was executed at a constant cross displacement rate (mm/min) the bond stress rate drastically decreased, as shown in Figure 4.40(b). The subtraction of the elasticity at the un-bonded length of the loaded end, which considers elastic deformation of the steel prestressing wire, was no longer valid. For these reasons, the information in Figure 4.40(c) and Figure 4.40(d) is only useful until minute 8.

From this test is can be concluded that the average bond strength of the steel sample was larger than 16.63 MPa at 22°C.

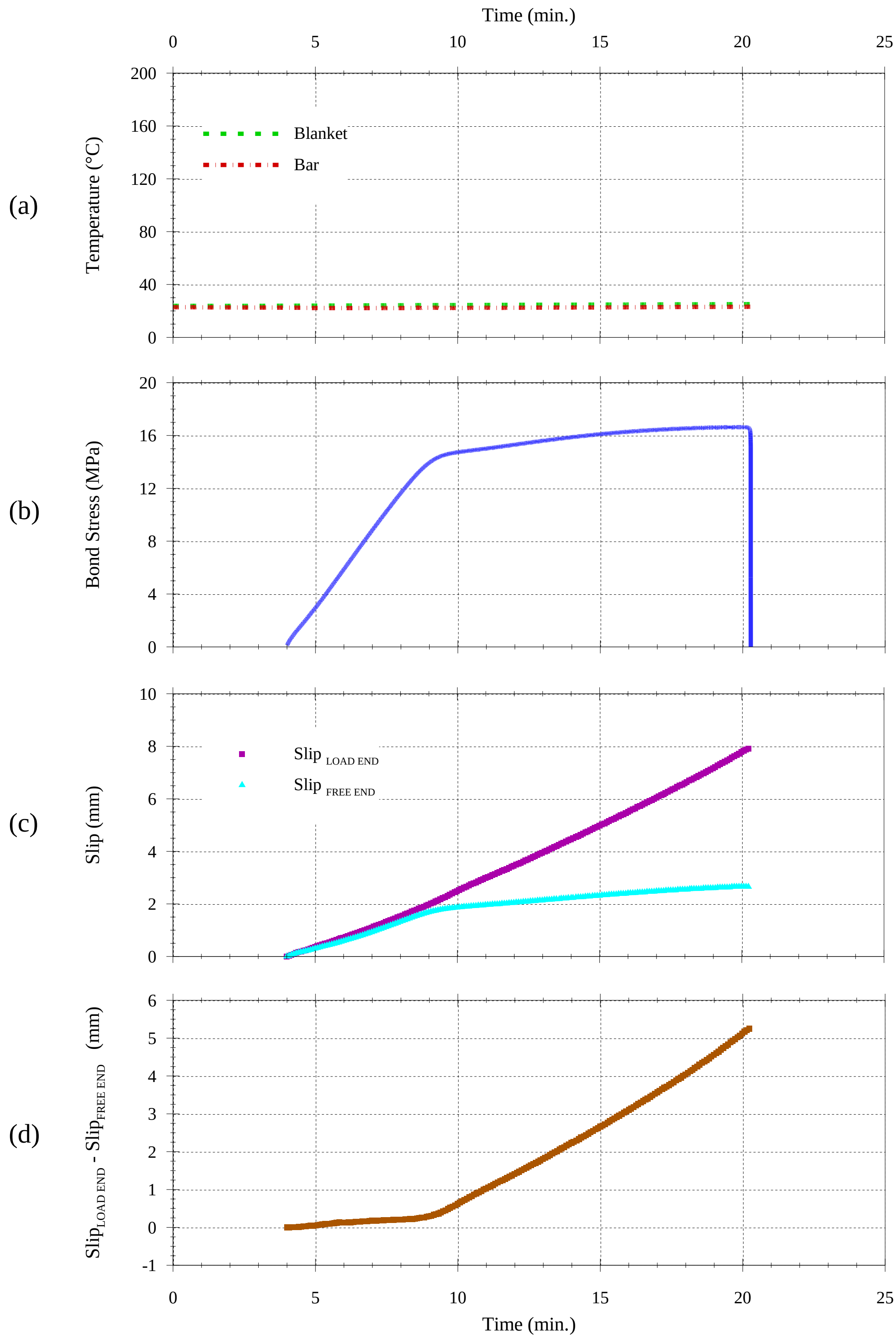

Figure 4.40: Experimental data for Steel_AT_e1

Figure 4.41 displays the period during the test at which the steel prestressing wire deformed elastically. The yield strength is well defined in Figure 4.41(a). The slip rate increased at the loaded end and decreased at the free end; this is the effect of the steel's plastic deformation.

(a)

(b)

(c)

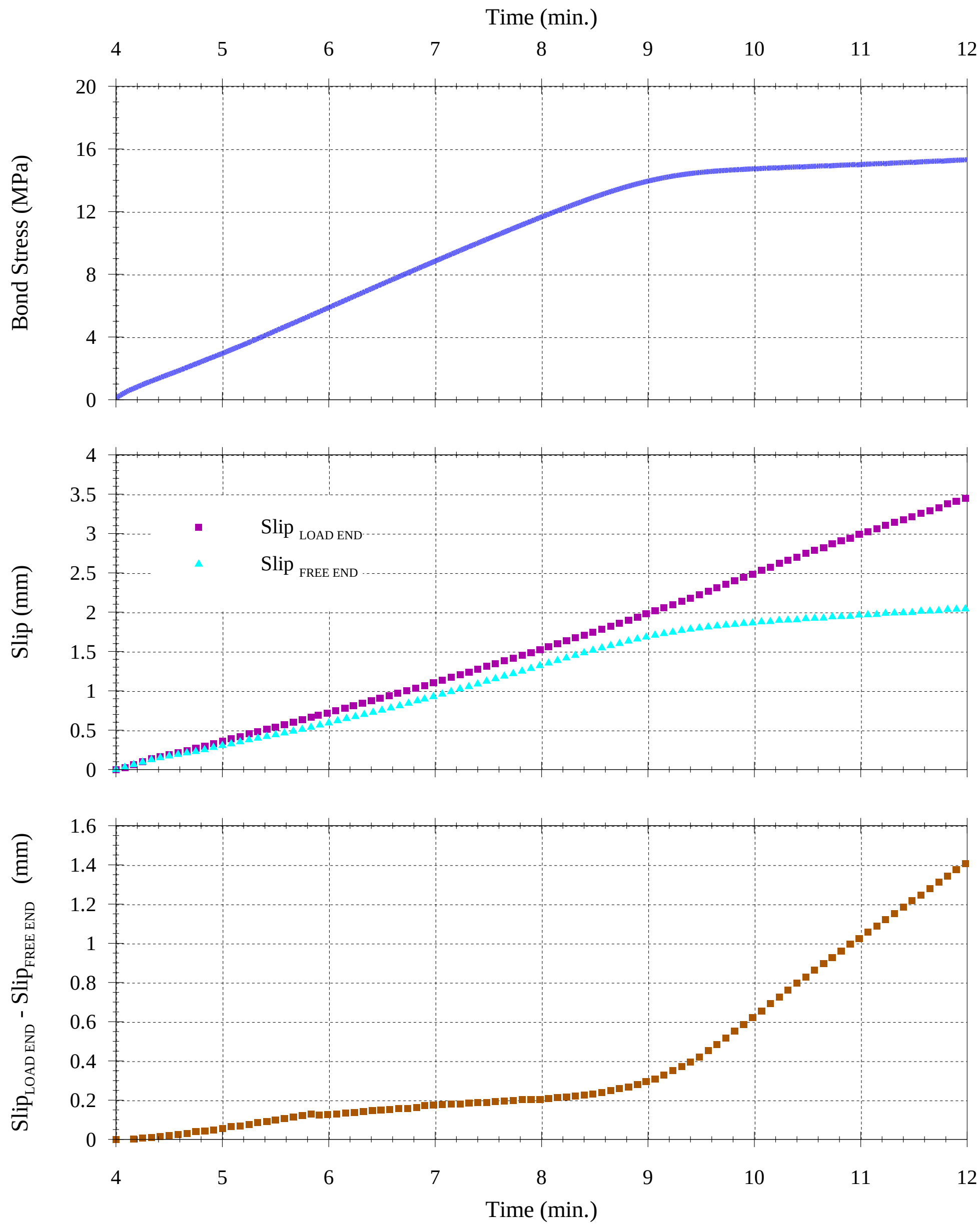

Figure 4.41: Zoom-in for Steel_AT_e1 at steel's elastic behaviour

The objective of this test was to determine the bond strength of the pullout sample at ambient temperature. The typical way in which pullout tests are displayed is by plotting the results in a bond stress versus slip plots (see Figure 4.42). It should be recalled that failure occurred at the wire's tensile strength capacity, which is why this plot looks more like a stress versus strain curve from a tensile strength test than a classical load-slip response.

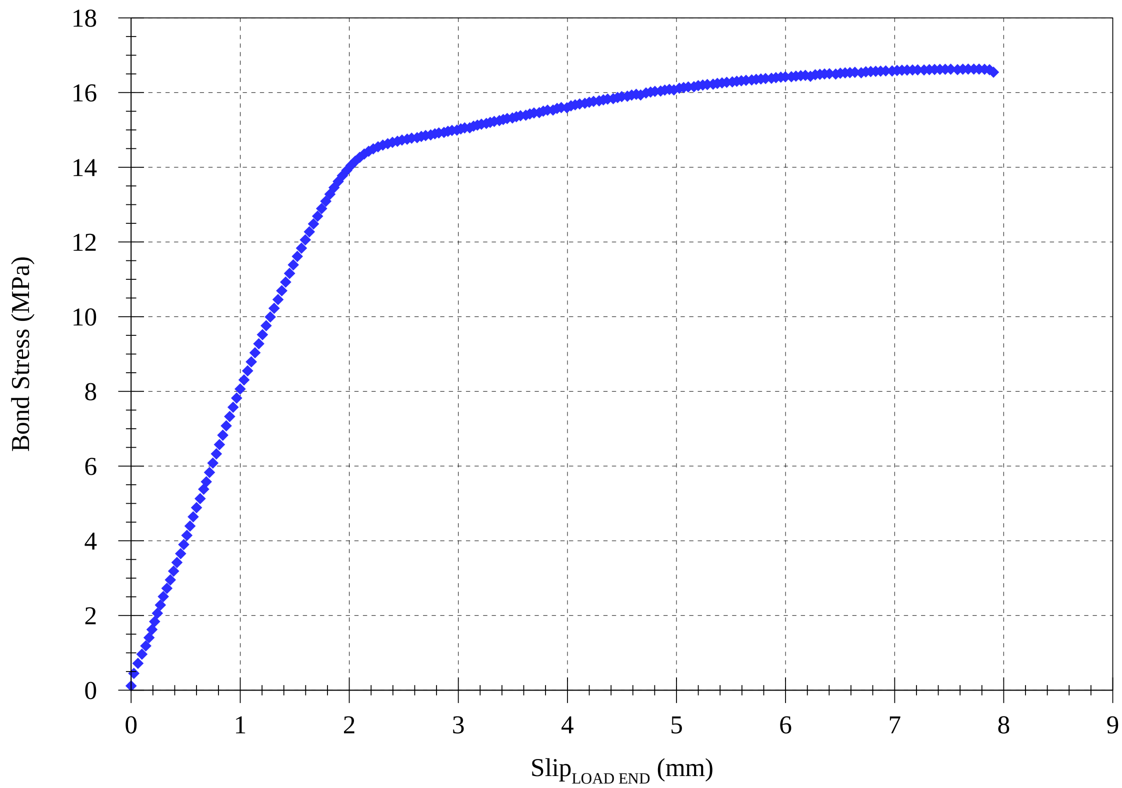

Figure 4.42: Bond stress versus loaded end slip for Steel_AT_e1 (on tensile strength failure)

4.1.11 Steel_AT_e2

This was a second RPOT done on a steel pullout sample. This sample was intended to be pulled out until failure of the bond interface occurred. At minute 4, the Instron machine was set to start the pullout at a bond stress rate of 2.71 MPa/min, as shown in Figure 4.43(b).

As for the CFRP RPOTs, the heating blanket was not set on this sample, but thermocouples were placed on the CFRP tendon’s surface and at the cylinders surface. This was executed in order to have the same conditions as for the PHPOTs. The temperature at the concrete’s surface and at the tendon were 24°C and 22°C, respectively (see Figure 4.43(a)).

This RPOT did not fail as expected, but responded in a similar fashion to the test described above. Again, the bond strength of the steel prestressing wire was actually greater than the tensile capacity of the wire. The steel prestressing wire yielded and eventually failed in tension at the loaded end, thus preventing observation of the entire bond behaviour. After minute 8.5, plastic deformation began and because the pullout was executed at a constant cross displacement rate (mm/min) the bond stress rate drastically decreased, as shown in Figure 4.43(b). As in Steel_AT_e1, the subtraction of the elasticity at the un-bonded length of the loaded end was no longer valid. For these reasons, the information in Figure 4.43(c) and Figure 4.43(d) is only useful until minute 8.5.

From this test is can be concluded that the average bond strength of the steel sample was larger than 16.61 MPa at 22°C.

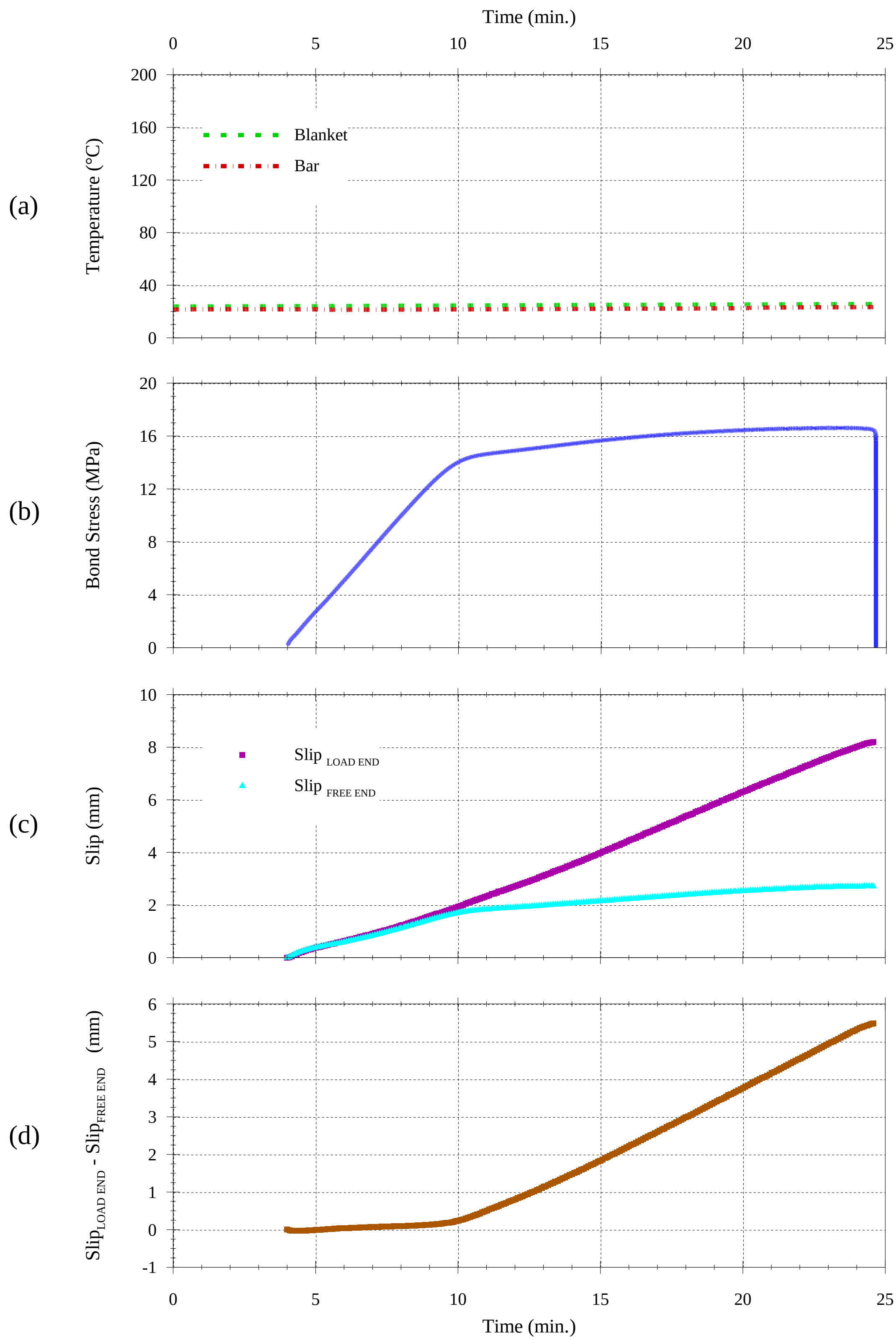

Figure 4.43: Experimental data for Steel_AT_e2

Figure 4.44 displays the period during the test at which the steel prestressing wire deformed elastically, from which similar conclusions can be drawn as for Steel_AT_e1.

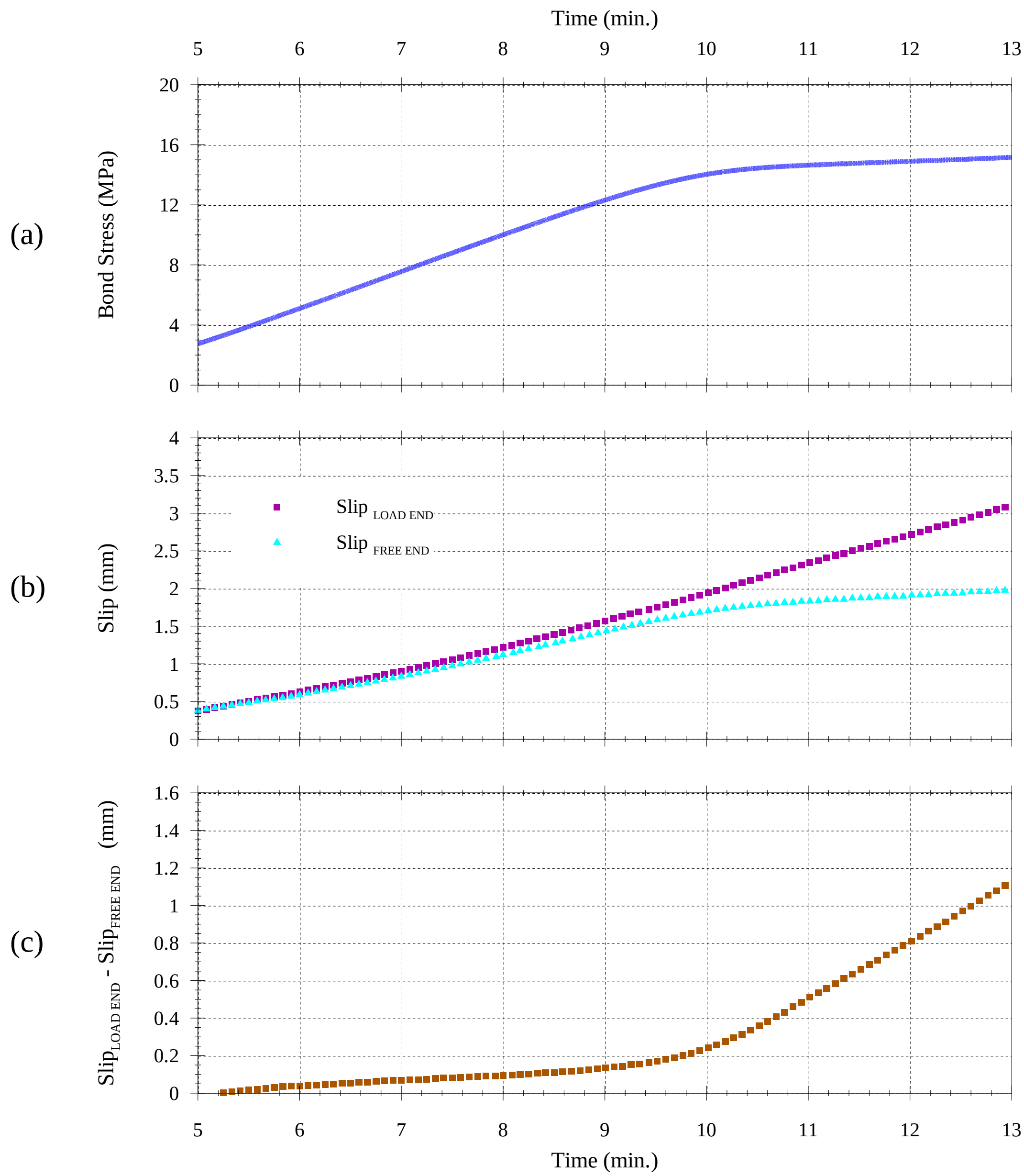

Figure 4.44: Zoom-in for Steel_AT_e2 at steel's elastic behaviour

Figure 4.45 displays a bond stress versus slip plot. Again this looks more like a stress versus strain curve from a tensile strength test due to the observed tensile rupture failure mode.

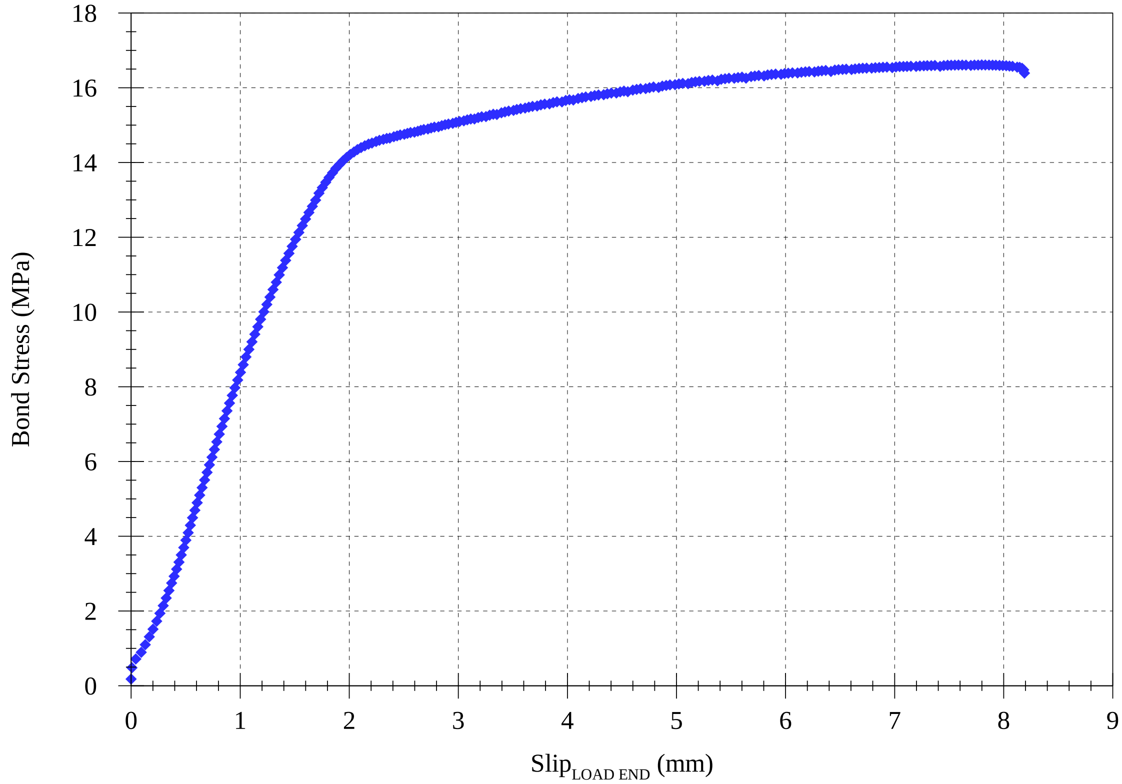

Figure 4.45: Bond stress versus loaded end slip for Steel_AT_e2 (on tensile strength failure)

4.1.12 Steel_37%_e1

This was a PHPOT done on a steel pullout sample. This sample was stressed up to 37% (6.07 MPa) of the tensile strength capacity measured on the two RPOTs done on the steel pullout samples (Steel_AT_e1 and Steel_AT_e2), because this RPOTs failed at the wire's tensile strength (not at the bond interface). The same loading and heating rate were executed in this test, as for every other PHPOT. The pullout began at minute 4 (see Figure 4.46(b)) and the heating blanket was turned on at minute 15, with the wire's temperature beginning its rise at minute 18 (see Figure 4.46(a)). The Instron machine was configured to pullout from the wire at a bond stress rate of 2.72 MPa/min during the initial loading phase of the tests up until the required sustained load was reached.

In this test, failure did not occur as the temperature of the wire increased. The heating rate developed as described in Section 3.4.1.2.2. The wire reached a steady state temperature at 160°C and then, at minute 152, the heating blanket temperature was increased and the wire reached a steady state temperature of 164°C, as shown in Figure 4.46(a).

At minute 233, after not having any signs of failure, with the wire at a steady temperature of 164°C, the Instron machine was configured to pullout until failure occurred at a bond stress rate of 0.42 MPa/min. Failure occurred at about minute 248 with a rapid increase of the slip at both ends, as shown in Figure 4.46(c). The maximum average bond stress was 11.78 MPa, with the wire's temperature at 164°C, and immediately after failure it dropped to zero bond strength capacity. After failure, slip continued and the residual bond strength evolved into an oscillating curve, shown in Figure 4.46(b). This phenomenon is analysed in Section 4.1.12.1.

At the moment of failure there was a sudden drop of the difference between the loaded and the free end slip, as shown in Figure 4.46(d).

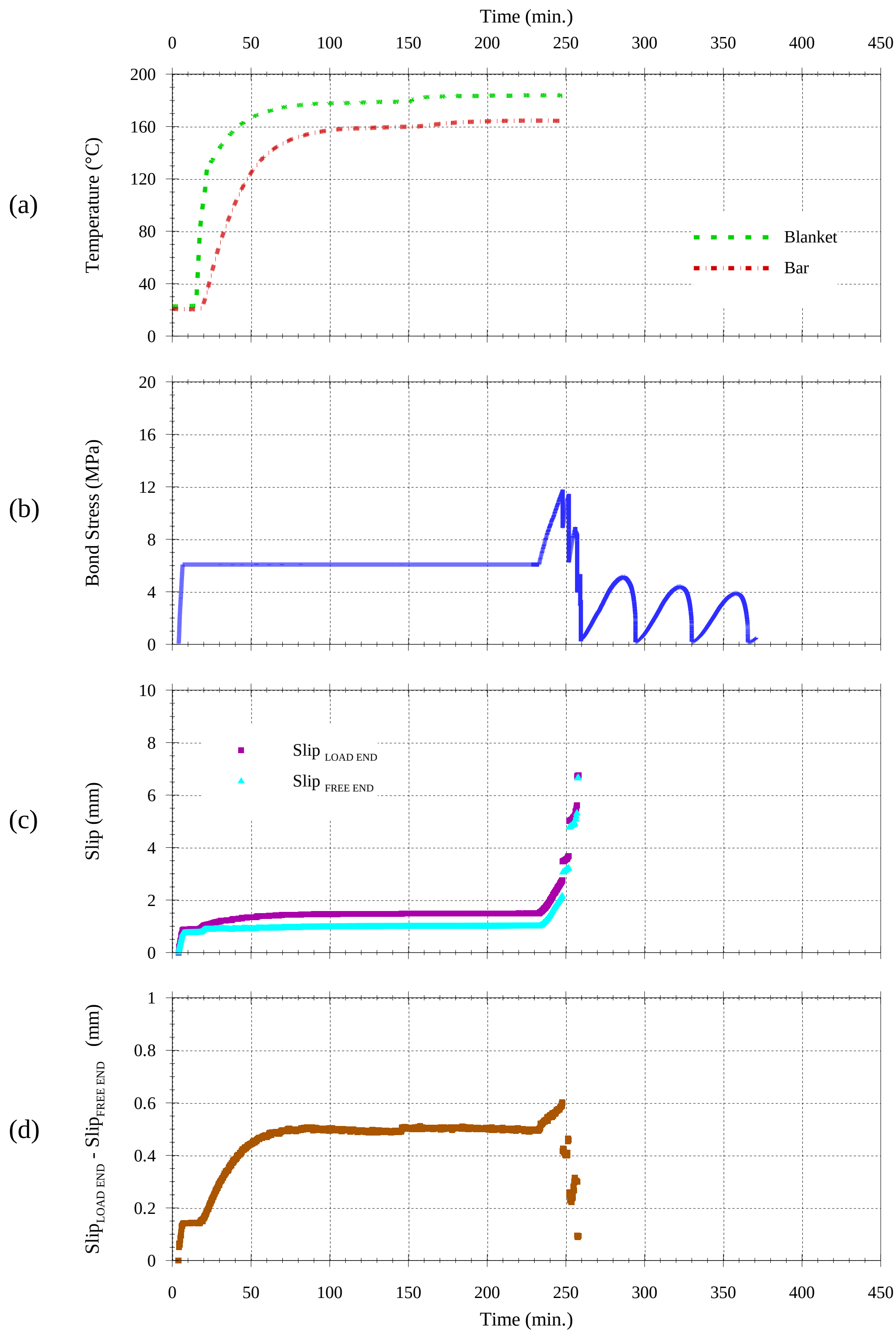

Figure 4.46: Experimental data for Steel_37%_e1

Figure 4.47 illustrates a zoom-in of the experimental data at the moment at which failure occurred. At this moment the wire's temperature was at a steady state of 164°C, with the heating blanket at 184°C, as shown in Figure 4.47(a). Every parameter was steady up until minute 233, at which further loading was applied in order to produce a bond failure of the sample.

The average bond stress was steady at 6.07 MPa up until minute 233 at which point it started increasing at rate of 0.42 MPa/min. Bond stress increased until minute 248 at which point a maximum bond stress of 11.78 MPa was achieved, as shown in Figure 4.47(b), and dropped to zero bond stress capacity at minute 260.

Slip at both ends remained steady, and started increasing as further pullout began. Both ends started slipping at the same time (minute 233) with a more pronounced increase at the loaded end, up until minute 248 at which point a relatively large slip occurred, as shown in Figure 4.47(c). At this point (bond failure), the difference between the loaded and the free end slip dropped, as shown in Figure 4.47(d).

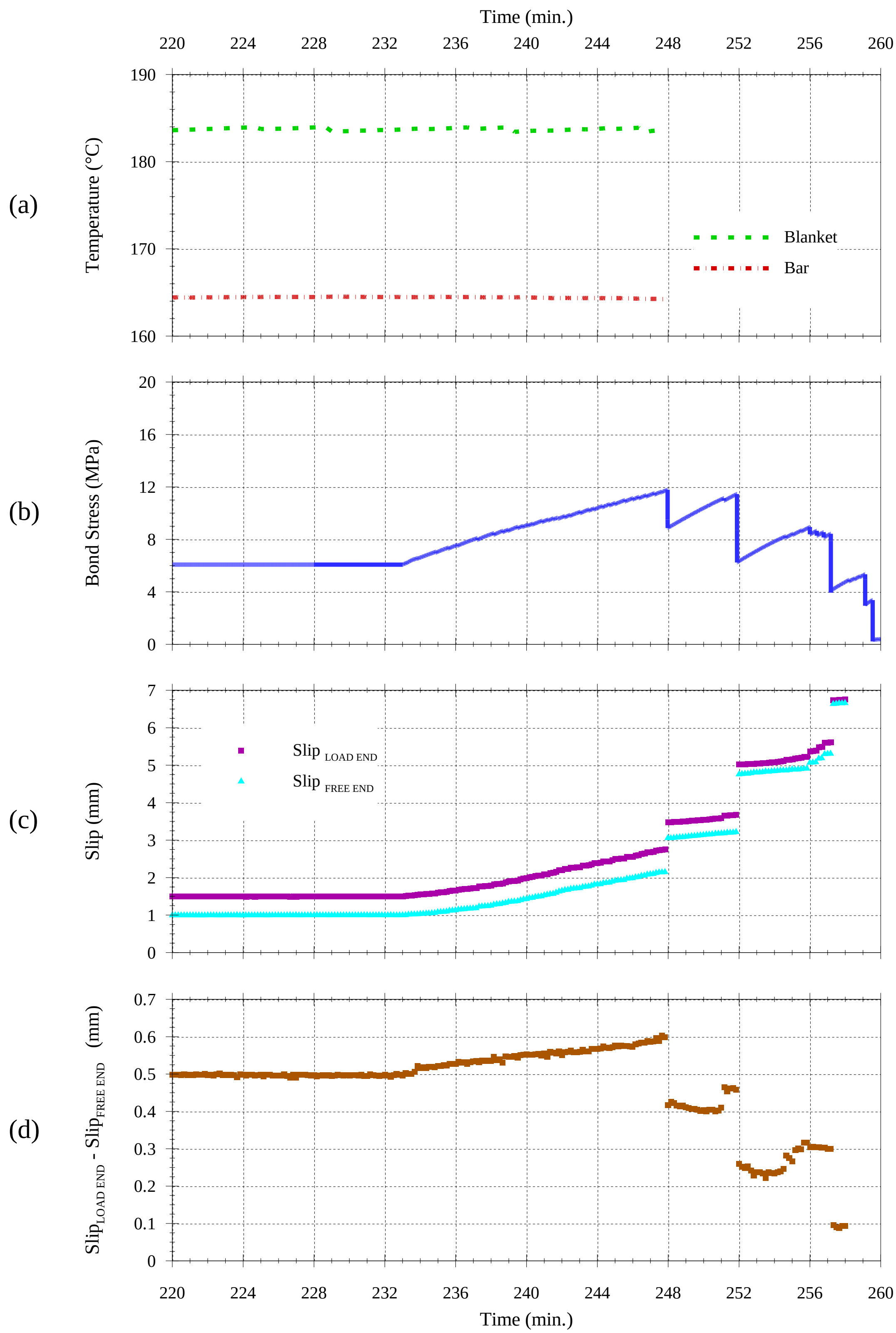

Figure 4.47: Zoom-in at failure for Steel_37%_e1

In Figure 4.48, 11.78 MPa was the maximum average bond stress observed. After failure there were local failures which occurred at the bond interface up until the bond stress capacity dropped to zero. The digital image correlation analysis used to measure the slip measured until a maximum slip of 7 mm.

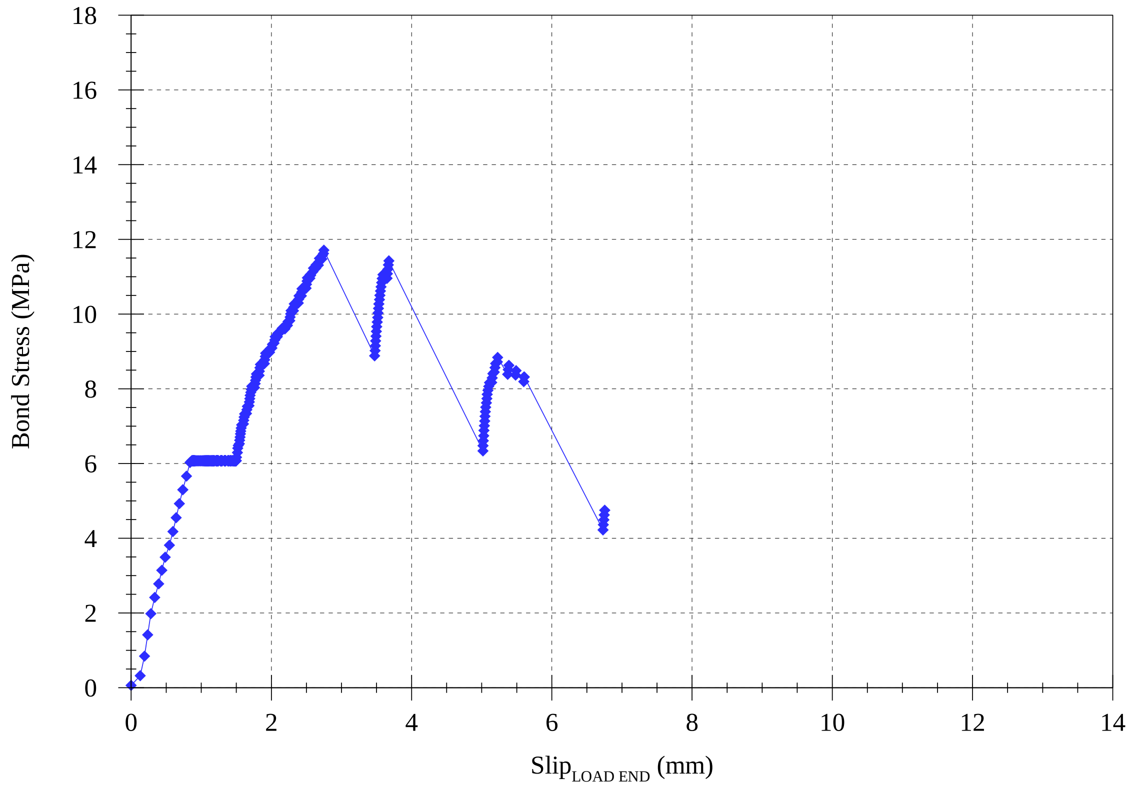

Figure 4.48: Bond stress versus loaded end slip for Steel_37%_e1

In this test, the bond interface did not fail as expected (it was assumed that the bond would fail as the tendon's temperature increased), but it failed as the load was increased with the tendon at a temperature of 164°C, and an initial average bond stress of 6.07 MPa. Nonetheless, Figure 4.49 is instructive to display that the failure occurred at a tendon's temperature of 164°C.

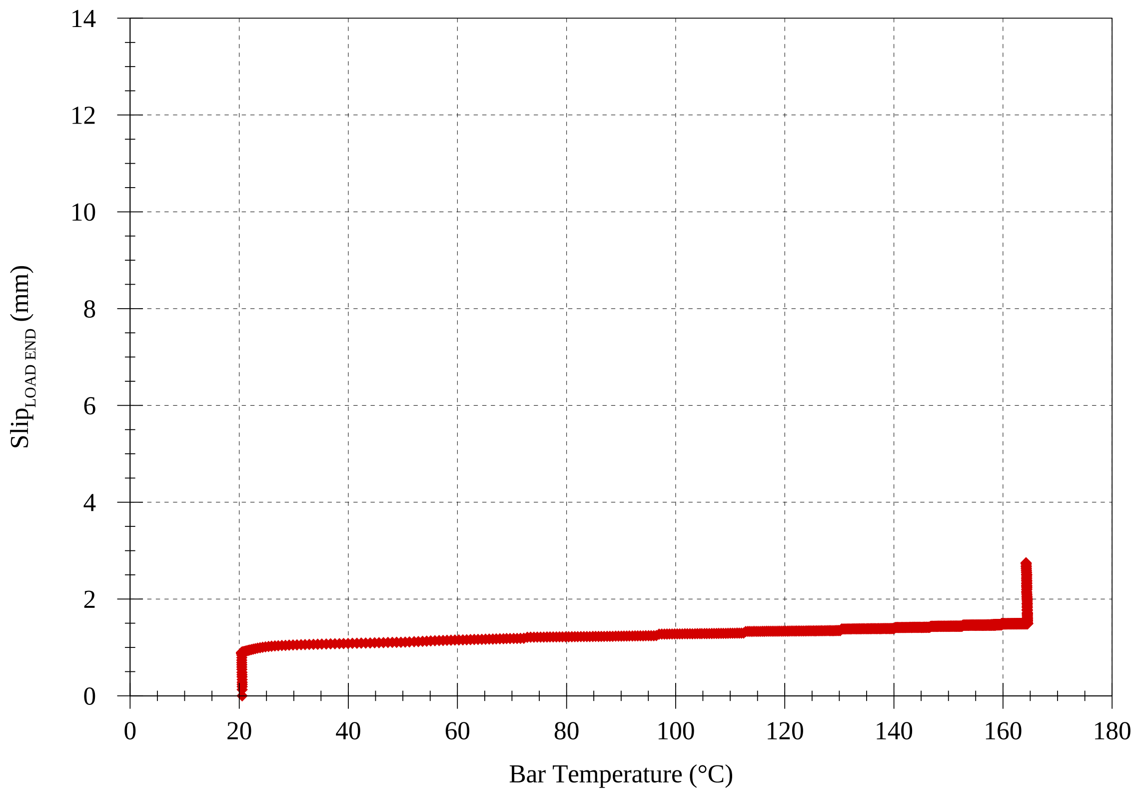

Figure 4.49: Bar temperature versus loaded end slip for Steel_37%_e1

After the heating blanket was turned on at minute 15, the average bond stress remained constant over time while the difference between the loaded and the free end slip increased, as shown in Figure 4.46(d). A zoom-in of the slip readings (see Figure 4.50) reveals that the increase of the slip difference after minute 15 is a result of the increase of the slip readings at both ends, with a more pronounced rise of the free end slip.

This increase in both slips is not a result of the loaded end slipping away the inside of the concrete cylinder, nor the free end slipping towards of it; what should happen in a pullout test of this type. This phenomenon is a result of the concrete cylinder and steel prestressing wire combined thermal expansion as explained in Section 5.4.

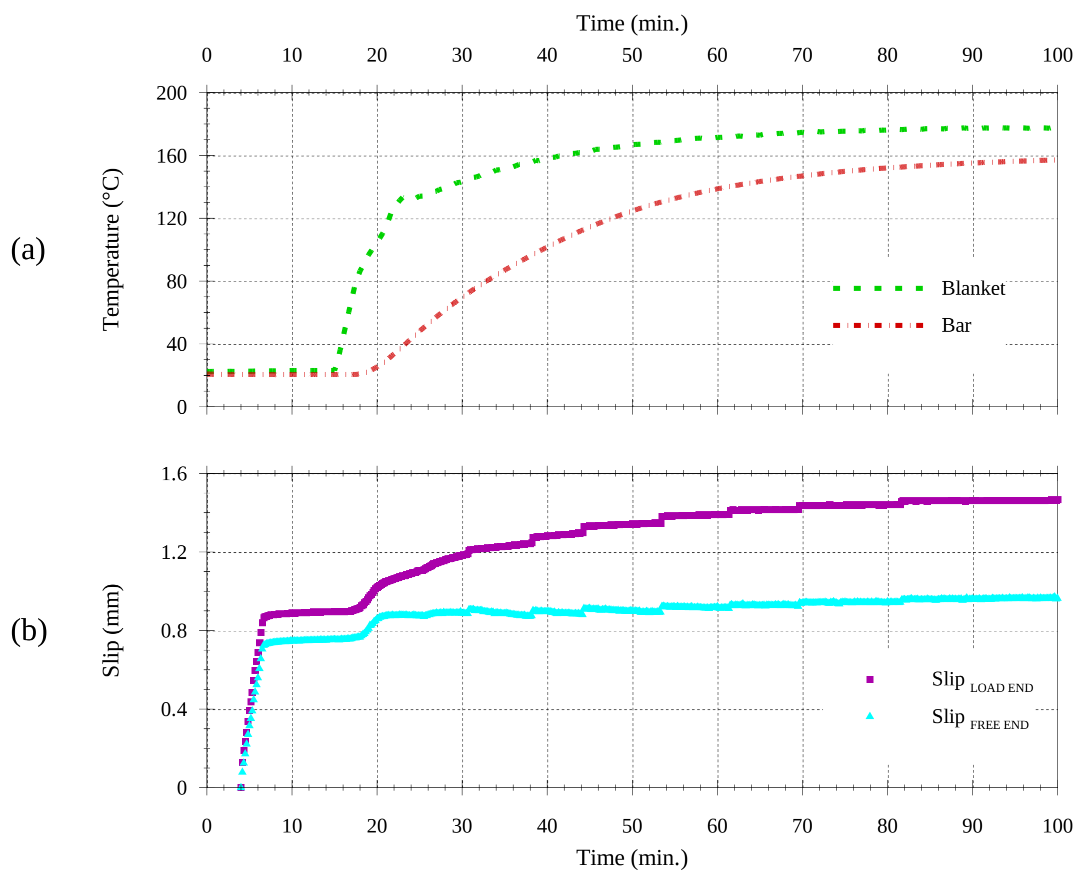

Figure 4.50: Zoom-in of temperature and slip for Steel_37%_e1

4.1.12.1 Oscillating residual pullout capacity

A typical bond failure of a steel prestressing wire pullout test is shown in Figure 4.51. After the maximum bond stress occurs, the bond stress capacity of the sample drops down to zero, as also shown in Figure 4.46(b). As the configuration of the test allows for the pullout to continue after failure, the free end of the steel prestressing wire keeps on slipping into the already failed bonded length interface. The bond stress versus time plot evolves into an oscillating curve, generated from the wire's ribs slipping along the already failed bonded length. The residual bond strength of the sample could be defined as the maximum value of ever cycle, as shown in Figure 4.51. As the free end slips into the sample, on each cycle there is a decrease of the residual bond strength, occasioned by the wire's ribs crushing the steel-concrete interface as the steel prestressing wire slips along the already failed bonded length.

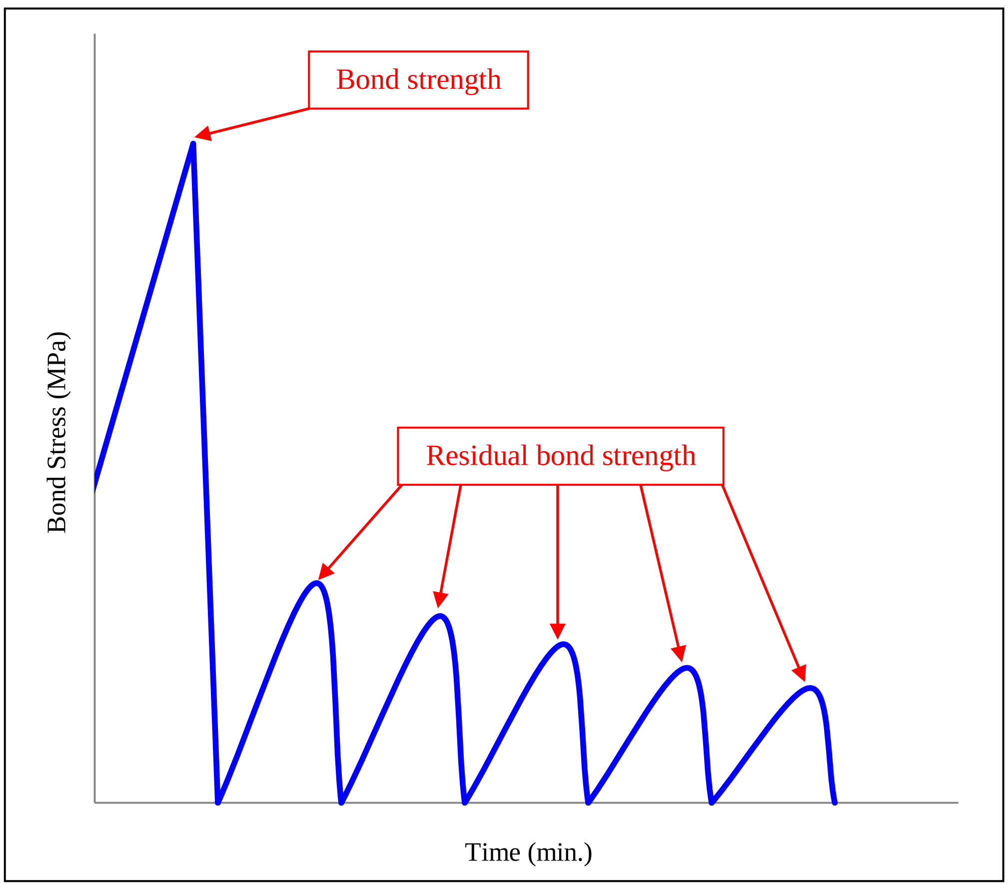

Figure 4.51: Simplified bond failure conditions (maximum and residual bond strength) for steel prestressing wire pullout tests

4.1.13 Steel_37%_e2

This was a PHPOT done on a steel pullout sample. This sample was stressed up to 37% (6.07 MPa) of the tensile strength capacity measured on the two RPOTs done on the steel pullout samples (Steel_AT_e1 and Steel_AT_e2), because this RPOTs failed at the wire's tensile strength (not at the bond interface). The same loading and heating rate were executed in this test, as for every other PHPOT. The pullout began at minute 4 (see Figure 4.52(b)) and the heating blanket was turned on at minute 15, with the wire's temperature beginning its rise at minute 18 (see Figure 4.52(a)). The Instron machine was configured to pullout from the wire at a bond stress rate of 2.58 MPa/min during the initial loading phase of the tests up until the required sustained load was reached.

Again, failure did not occur as the temperature of the wire increased. The heating rate developed as described in Section 3.4.1.2.2. The wire reached a steady state temperature at 156°C and then, at minute 152, the heating blanket temperature was increased and the wire reached a steady state temperature of 160°C, as shown in Figure 4.52(a).

At minute 233, after not having any signs of failure, with the wire at a steady temperature of 160°C, the Instron machine was configured to pullout until failure occurred at a bond stress rate of 0.44 MPa/min. Failure occurred at about minute 248 with a rapid increase of the slip at both ends, as shown in Figure 4.52(c). What seems to be like a local failure of the bond interface occurred about minute 248 with a drop of one third of the average bond stress which then kept on rising up to a maximum average bond stress of 13.45 MPa, with the wire's temperature at 160°C, and immediately after failure it dropped to zero bond strength capacity. After failure, slip continued and the residual bond strength evolved into an oscillating curve, shown in Figure 4.52(b). This phenomenon is analysed in Section 4.1.12.1.

At the moment of failure there was a sudden drop of the difference between the loaded and the free end slip, as shown in Figure 4.52(d).

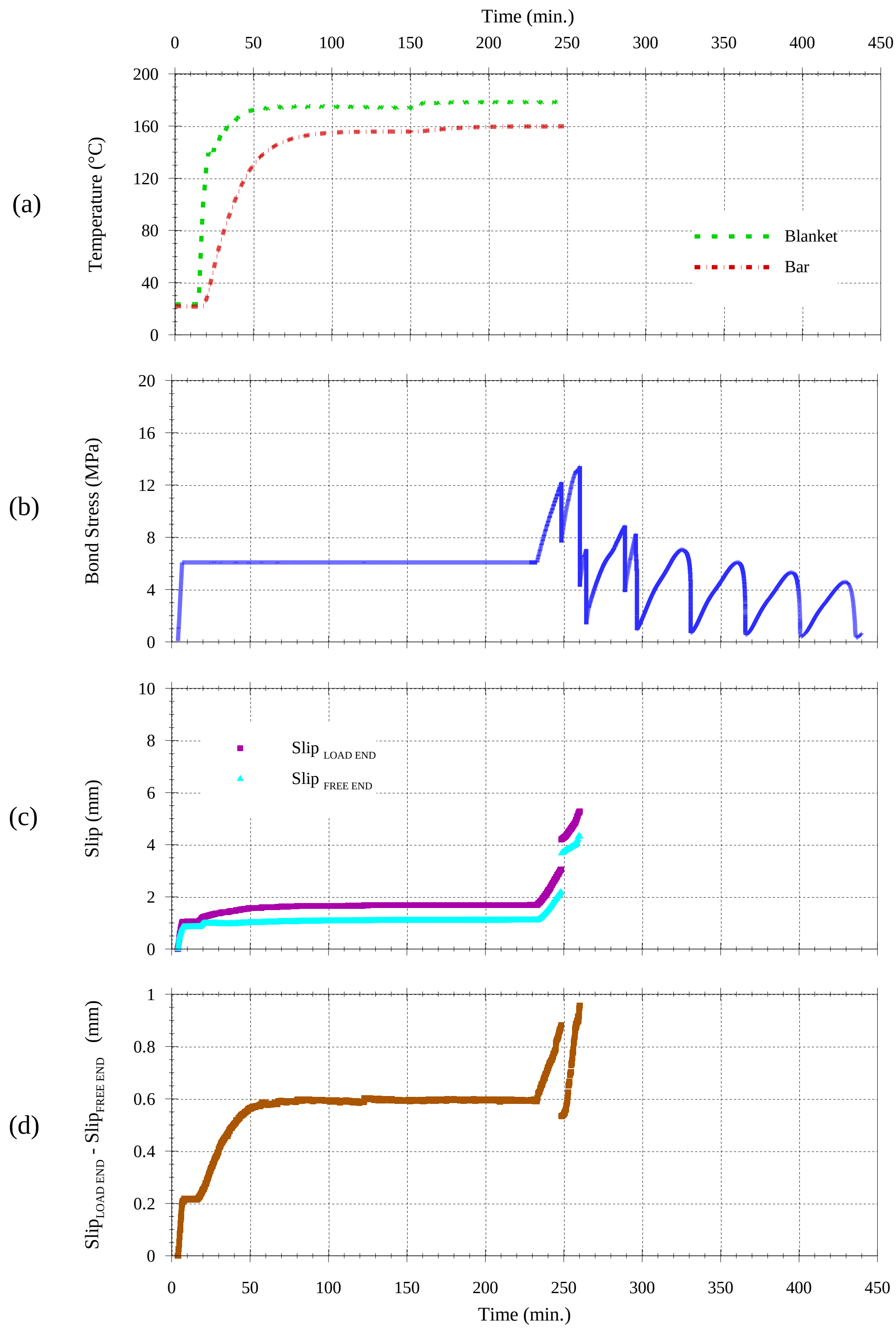

Figure 4.52: Experimental data for Steel_37%_e2

Figure 4.53 illustrates a zoom-in of the experimental data at the moment at which failure occurred. At this moment the wire’s temperature was at a steady state of 160°C, with the heating blanket at 178°C, as shown in Figure 4.53(a). Every parameter was steady up until minute 233, at which further loading was applied in order to produce a bond failure of the sample.

The average bond stress was steady at 6.07 MPa up until minute 233 at which point it started increasing at rate of 0.44 MPa/min. Bond stress increased until minute 248 at which point a maximum bond stress of 13.45 MPa was achieved, as shown in Figure 4.53(b), and dropped to zero bond stress capacity at minute 264.

Slip at both ends remained steady, and started increasing as further pullout began. Both ends started slipping at the same time (minute 233) with a more pronounced increase at the loaded end, up until minute 248 at which point a relatively large slip occurred, as shown in Figure 4.53(c). At this point (bond failure), the difference between the loaded and the free end slip dropped, as shown in Figure 4.53(d).

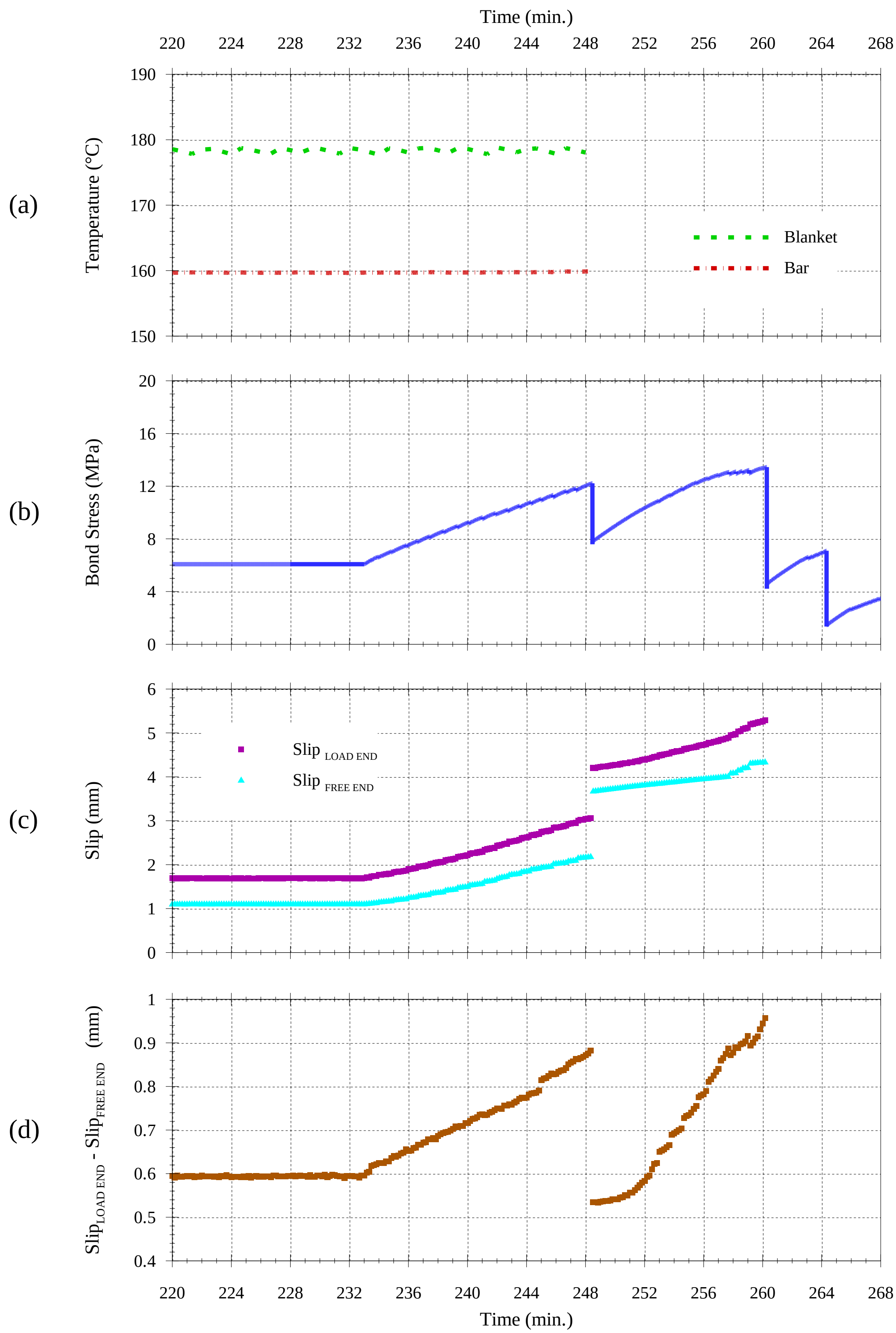

Figure 4.53: Zoom-in at failure for Steel_37%_e2

In Figure 4.54, 13.45 MPa was the maximum average bond stress observed. After failure there were local failures which occurred at the bond interface up until the bond stress capacity dropped to zero. The digital image correlation analysis used to measure the slip measured until a maximum slip of 5.5 mm.

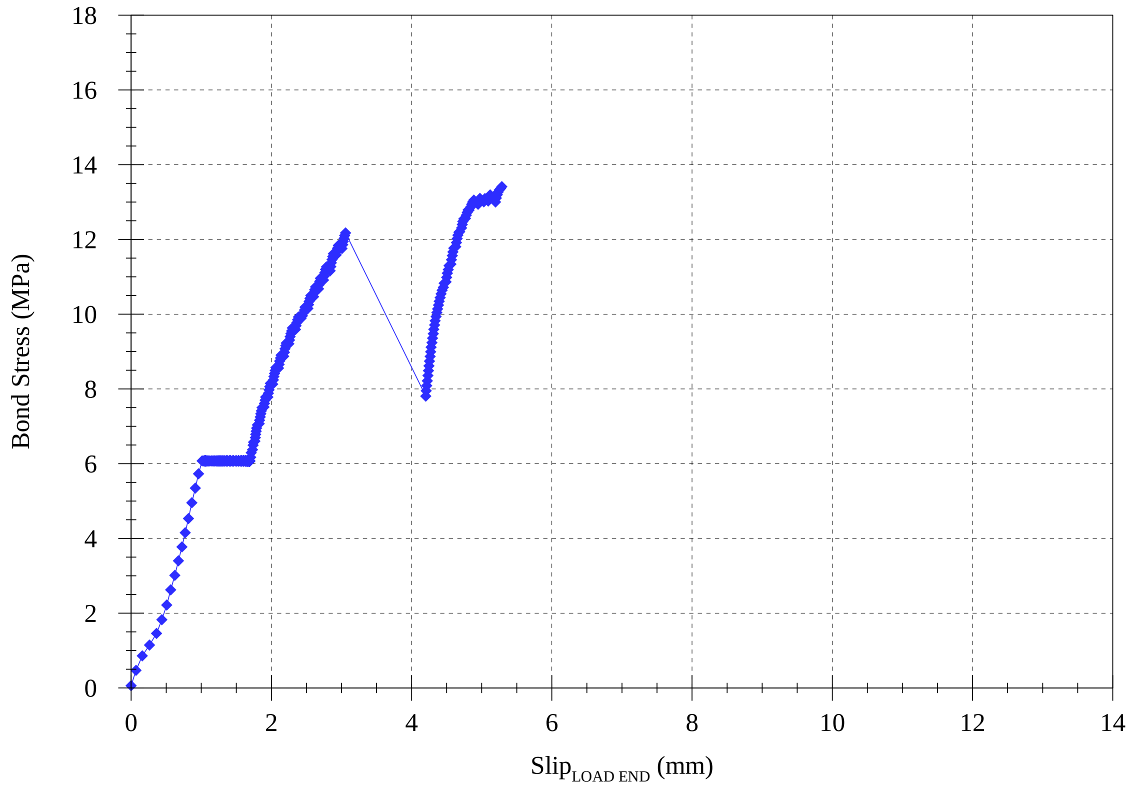

Figure 4.54: Bond stress versus loaded end slip for Steel_37%_e2

Again, in this test the bond interface did not fail as expected (it was assumed that the bond would fail as the tendon's temperature increased), but it failed as the load was increased with the tendon at a temperature of 160°C, and an initial average bond stress of 6.07 MPa. Nonetheless, Figure 4.55 is instructive to display that the failure occurred at a tendon's temperature of 160°C.

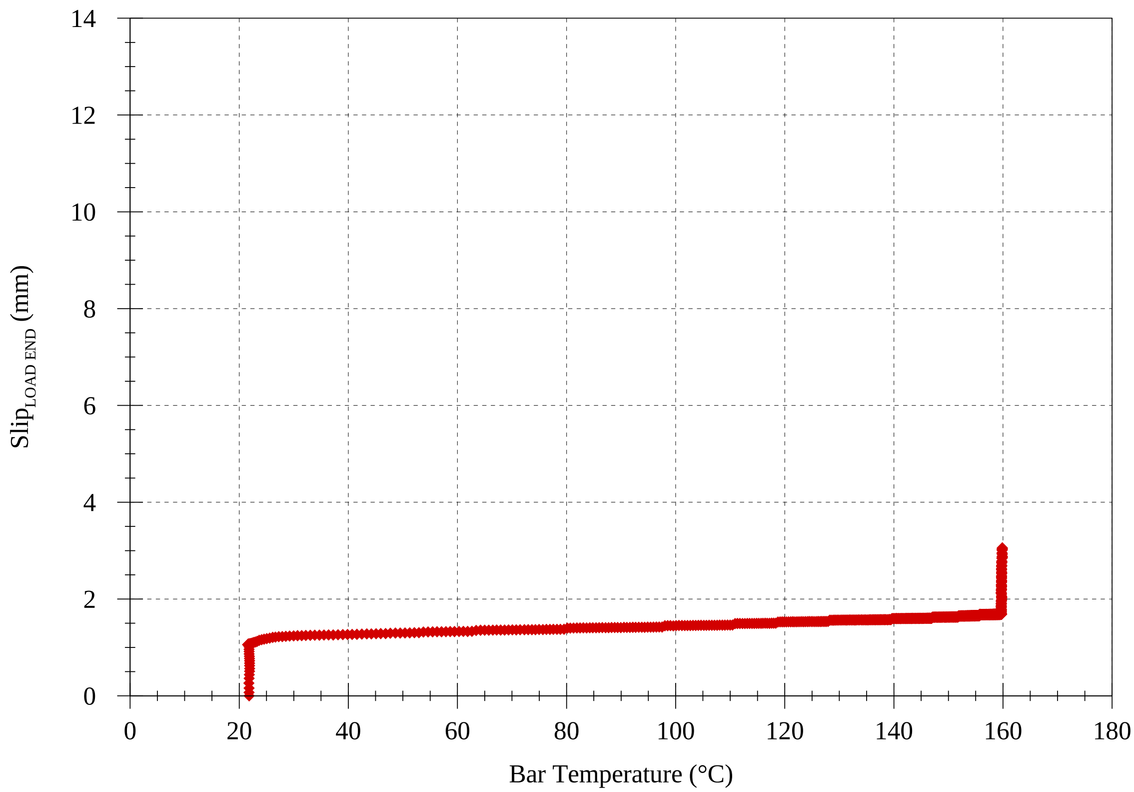

Figure 4.55: Bar temperature versus loaded end slip for Steel_37%_e2

After the heating blanket was turned on at minute 15, the average bond stress remained constant over time while the difference between the loaded and the free end slip increased, as shown in Figure 4.52(d). A zoom-in of the slip readings (see Figure 4.56) reveals that the increase of the slip difference after minute 15 is a result of the increase of the slip readings at both ends, with a more pronounced rise of the free end slip.

This phenomenon is a result of the concrete cylinder and steel prestressing wire combined thermal expansion as noted and explained in Section 5.4.

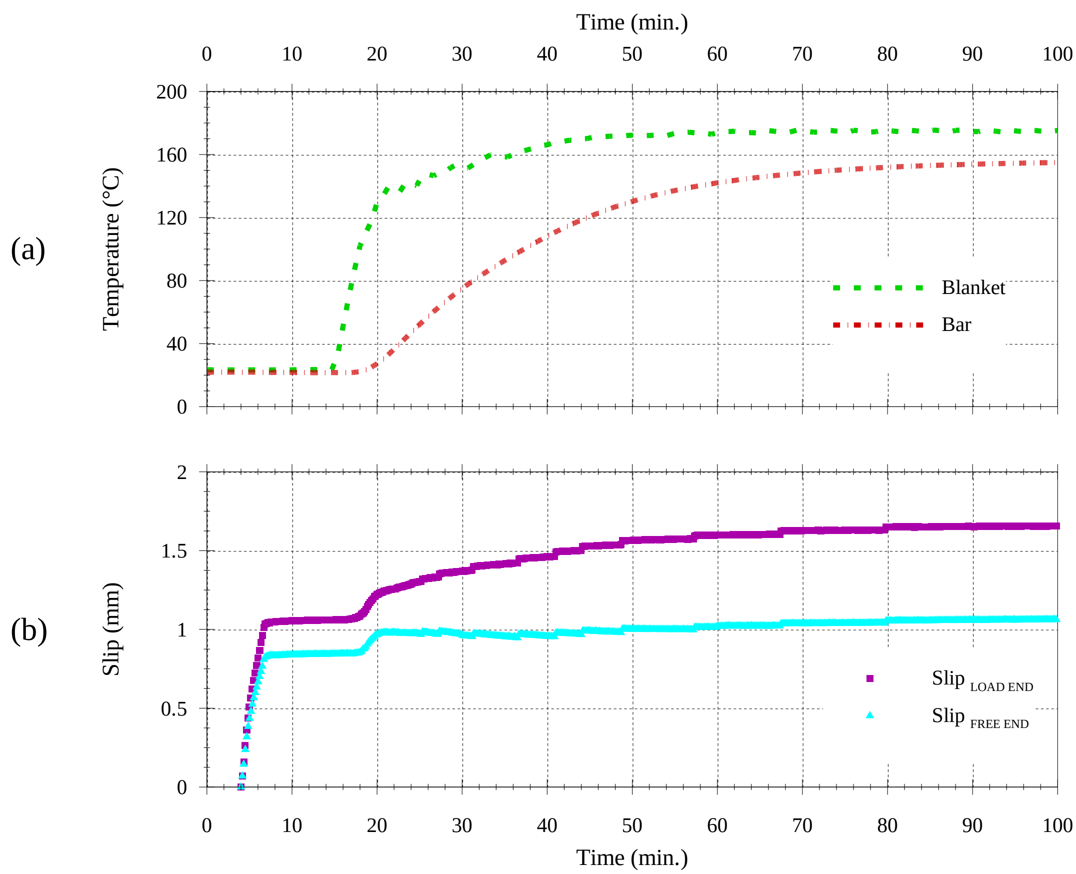

Figure 4.56: Zoom-in of temperature and slip for Steel_37%_e2

4.1.14 Steel_46%_e1

This was a PHPOT done on a steel pullout sample. This sample was stressed up to 46% (7.59 MPa) of the tensile strength capacity measured on the two RPOTs done on the steel pullout samples (Steel_AT_e1 and Steel_AT_e2), because this RPOTs failed at the wire's tensile strength (not at the bond interface). The same loading and heating rate were executed in this test, as for every other PHPOT. The pullout began at minute 4 (see Figure 4.57(b)) and the heating blanket was turned on at minute 15, with the wire's temperature beginning its rise at minute 18 (see Figure 4.57(a)). The Instron machine was configured to pullout from the wire at a bond stress rate of 2.98 MPa/min during the initial loading phase of the tests up until the required sustained load was reached.

Again, failure did not occur as the temperature of the wire increased. The heating rate developed as described in Section 3.4.1.2.2. The wire reached a steady state temperature at 168°C and then, at minute 152, the heating blanket temperature was increased and the wire reached a steady state temperature of 170°C, as shown in Figure 4.57(a).

At minute 233, after not having any signs of failure, with the wire at a steady temperature of 170°C, the Instron machine was configured to pullout until failure occurred at a bond stress rate of 0.40 MPa/min. Failure occurred at about minute 251 with a rapid increase of the slip at both ends, as shown in Figure 4.57(c). The maximum average bond stress was 12.79 MPa, with the wire's temperature at 170°C, and immediately after failure it dropped to zero bond strength capacity. After failure, slip continued and the residual bond strength evolved into an oscillating curve, shown in Figure 4.57(b). This phenomenon is analysed in Section 4.1.12.1.

At the moment of failure there was a sudden drop of the difference between the loaded and the free end slip, as shown in Figure 4.57(d).

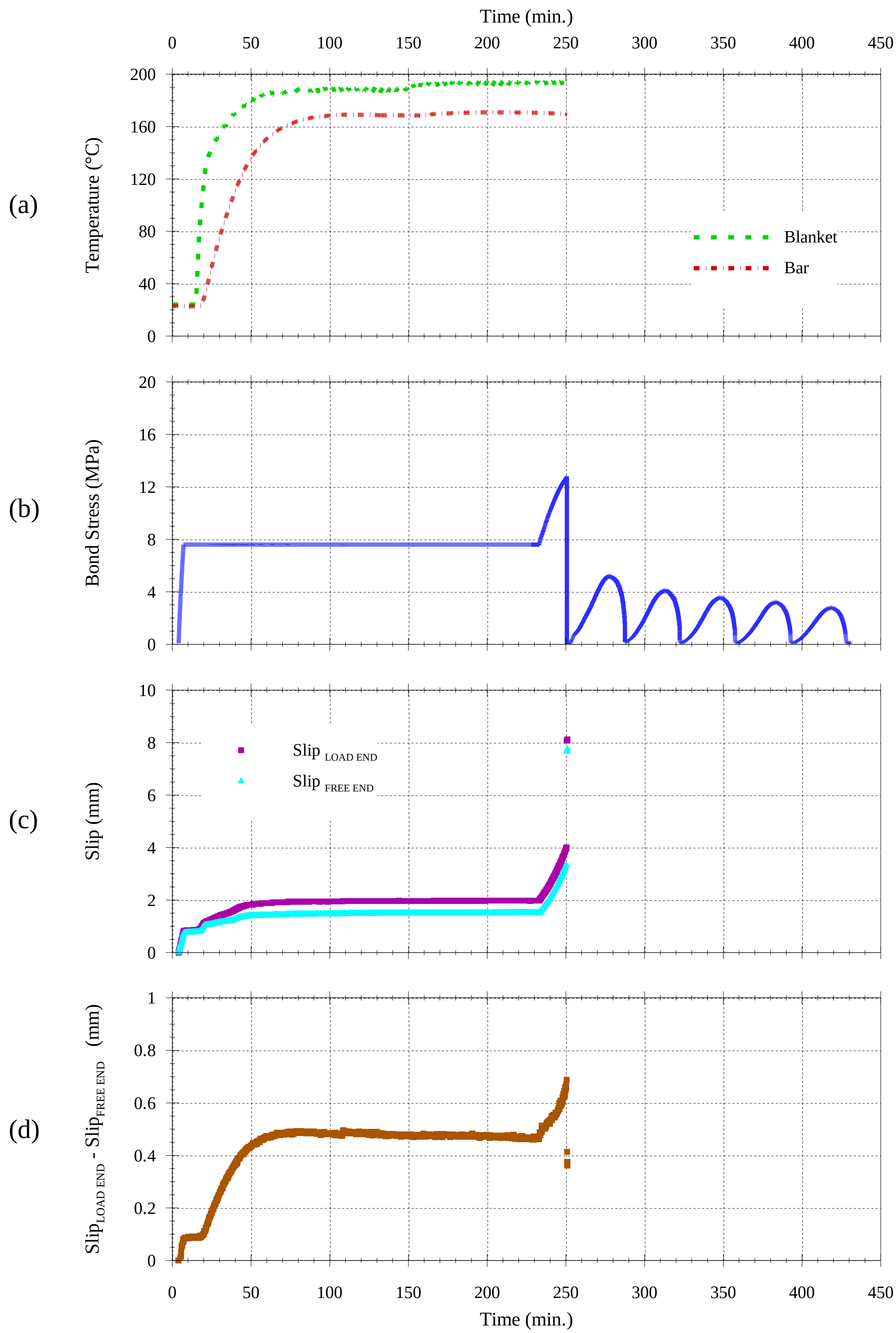

Figure 4.57: Experimental data for Steel_46%_e1

Figure 4.58 illustrates a zoom-in of the experimental data at the moment at which failure occurred. At this moment the wire’s temperature was at a steady state of 170°C, with the heating blanket at 192°C, as shown in Figure 4.58(a). Every parameter was steady up until minute 233, at which further loading was applied in order to produce a bond failure of the sample.

The average bond stress was steady at 7.59 MPa up until minute 233 at which point it started increasing at rate of 0.40 MPa/min. Bond stress increased until minute 251 at which point a maximum bond stress of 12.79 MPa was achieved, as shown in Figure 4.58(b), and dropped to zero bond stress capacity only thirty seconds later.

Slip at both ends remained steady, and started increasing as further pullout began. Both ends started slipping at the same time (minute 233) with a more pronounced increase at the loaded end, up until minute 251 at which point a relatively large slip occurred, as shown in Figure 4.58(c). At this point (bond failure), the difference between the loaded and the free end slip dropped, as shown in Figure 4.58(d).

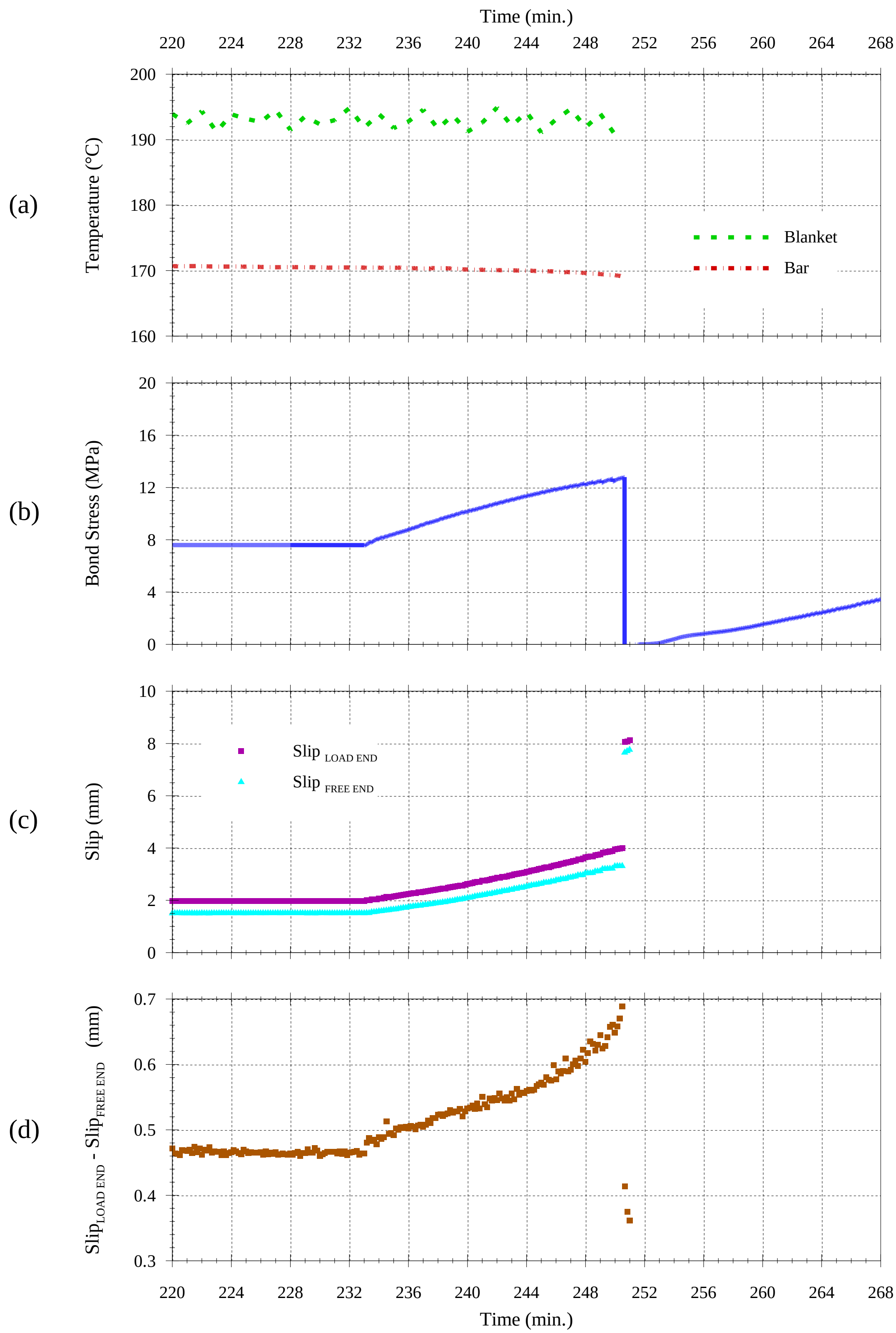

Figure 4.58: Zoom-in at failure for Steel_46%_e1

In Figure 4.59, 12.79 MPa was the maximum average bond stress observed. After failure there were local failures which occurred at the bond interface up until the bond stress capacity dropped to zero. The digital image correlation analysis used to measure the slip measured until a maximum slip of 8 mm.

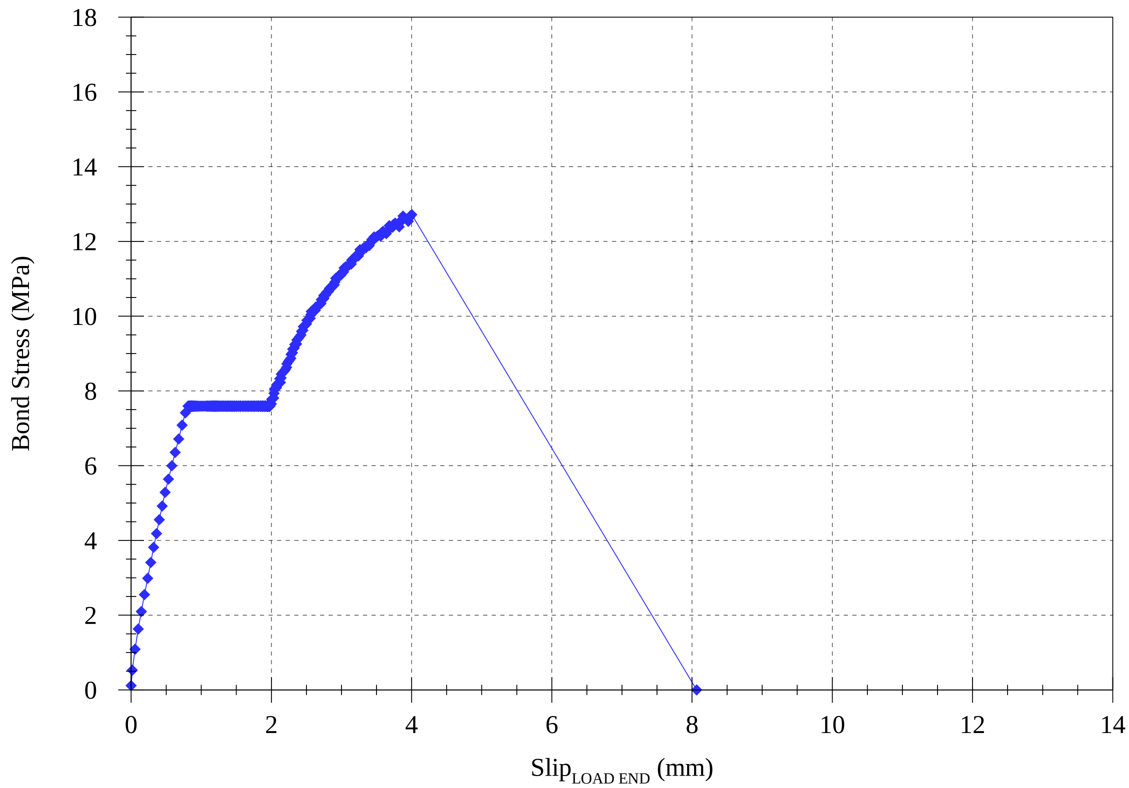

Figure 4.59: Bond stress versus loaded end slip for Steel_46%_e1

Again, in this test the bond interface did not fail as expected (it was assumed that the bond would fail as the tendon's temperature increased), but it failed as the load was increased with the tendon at a temperature of 170°C, and an initial average bond stress of 7.59 MPa. Nonetheless, Figure 4.60 is instructive to display that the failure occurred at a tendon's temperature of 170°C.

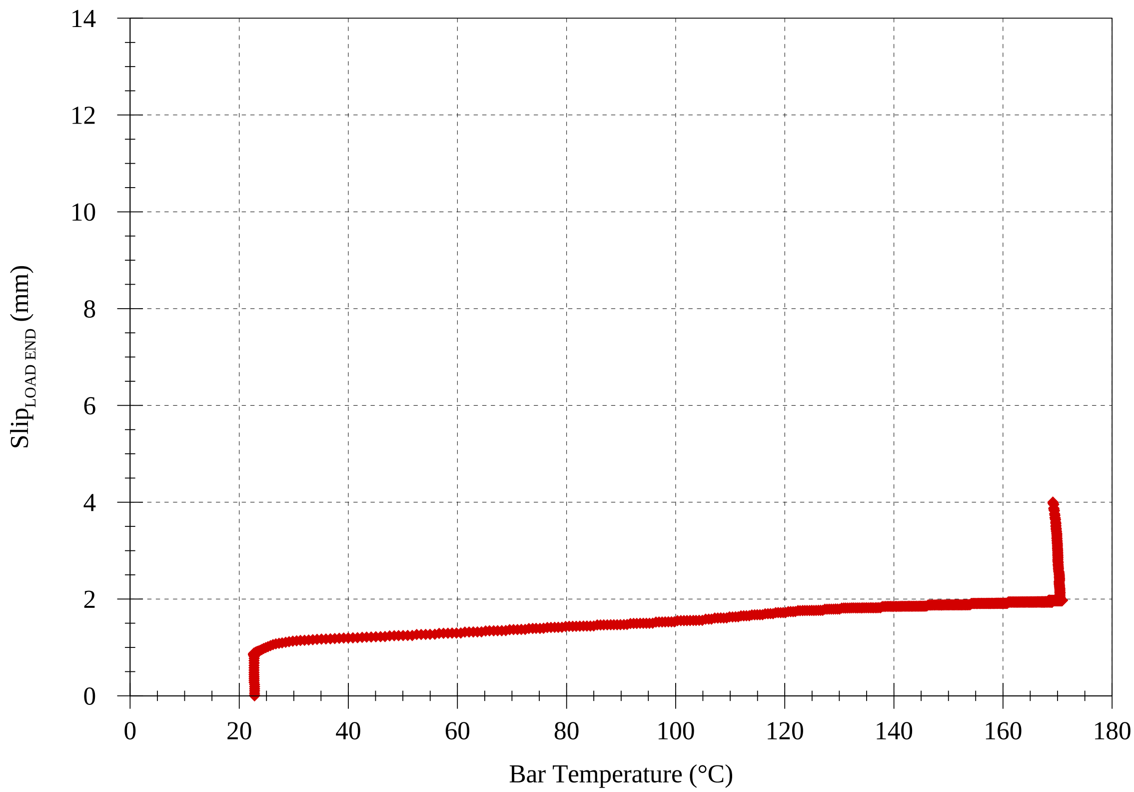

Figure 4.60: Bar temperature versus loaded end slip for Steel_46%_e1

After the heating blanket was turned on at minute 15, the average bond stress remained constant over time while the difference between the loaded and the free end slip increased, as shown in Figure 4.57(d). A zoom-in of the slip readings (see Figure 4.61) reveals that the increase of the slip difference after minute 15 is a result of the increase of the slip readings at both ends, with a more pronounced rise of the free end slip.

This phenomenon is a result of the concrete cylinder and steel prestressing wire combined thermal expansion as noted and explained in Section 5.4.

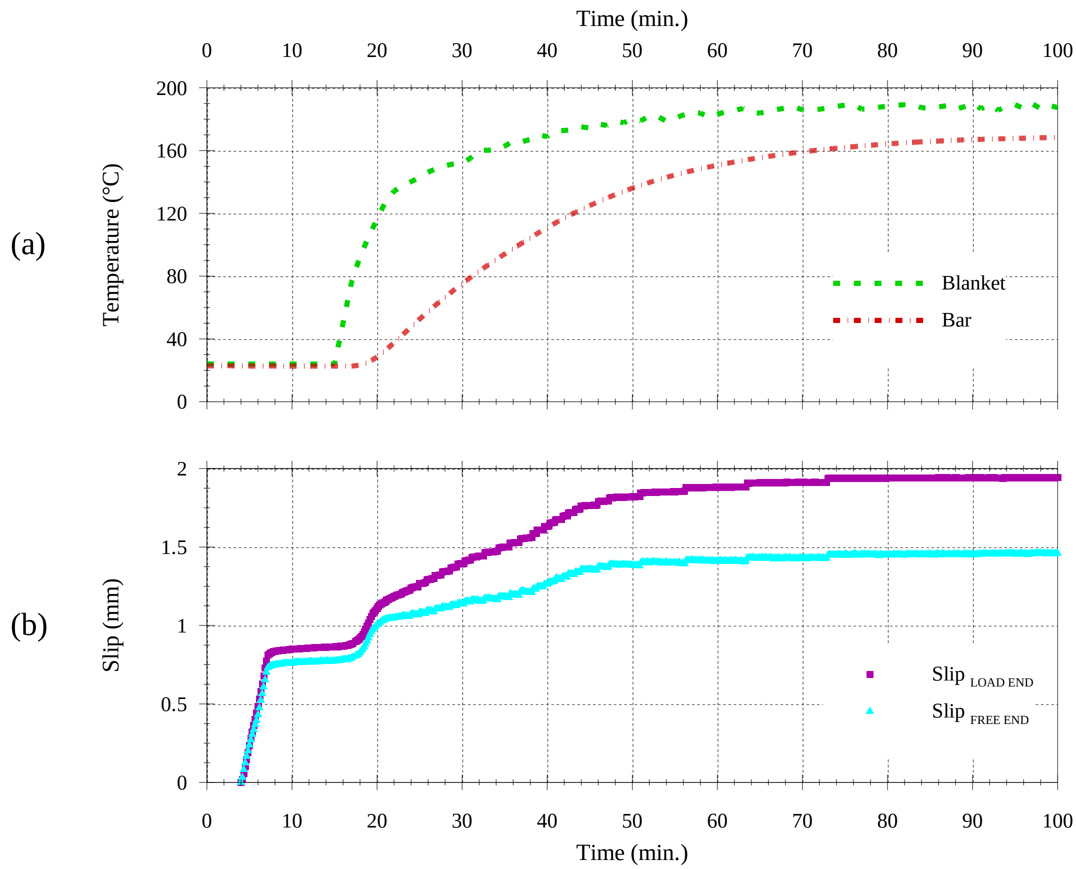

Figure 4.61: Zoom-in of temperature and slip for Steel_46%_e1

4.1.15 Steel_46%_e2

This was a PHPOT done on a steel pullout sample. This sample was stressed up to 46% (7.59 MPa) of the tensile strength capacity measured on the two RPOTs done on the steel pullout samples (Steel_AT_e1 and Steel_AT_e2), because this RPOTs failed at the wire's tensile strength (not at the bond interface). The same loading and heating rate were executed in this test, as for every other PHPOT. The pullout began at minute 4 (see Figure 4.62(b)) and the heating blanket was turned on at minute 15, with the wire's temperature beginning its rise at minute 18 (see Figure 4.62(a)). The Instron machine was configured to pullout from the wire at a bond stress rate of 2.51 MPa/min during the initial loading phase of the tests up until the required sustained load was reached.

Again, failure did not occur as the temperature of the wire increased. The heating rate developed as described in Section 3.4.1.2.2. The wire reached a steady state temperature at 158°C and then, at minute 152, the heating blanket temperature was increased and the wire reached a steady state temperature of 162°C, as shown in Figure 4.62(a).

At minute 233, after not having any signs of failure, with the wire at a steady temperature of 162°C, the Instron machine was configured to pullout until failure occurred at a bond stress rate of 0.50 MPa/min. Failure occurred at about minute 249 with a rapid increase of the slip at both ends, as shown in Figure 4.62(c). The maximum average bond stress was 13.68 MPa, with the wire's temperature at 162°C, and immediately after failure it dropped to zero bond strength capacity. After failure, slip continued and the residual bond strength evolved into an oscillating curve, shown in Figure 4.62(b). This phenomenon is analysed in Section 4.1.12.1.

At the moment of failure there was a sudden drop of the difference between the loaded and the free end slip, as shown in Figure 4.62(d).

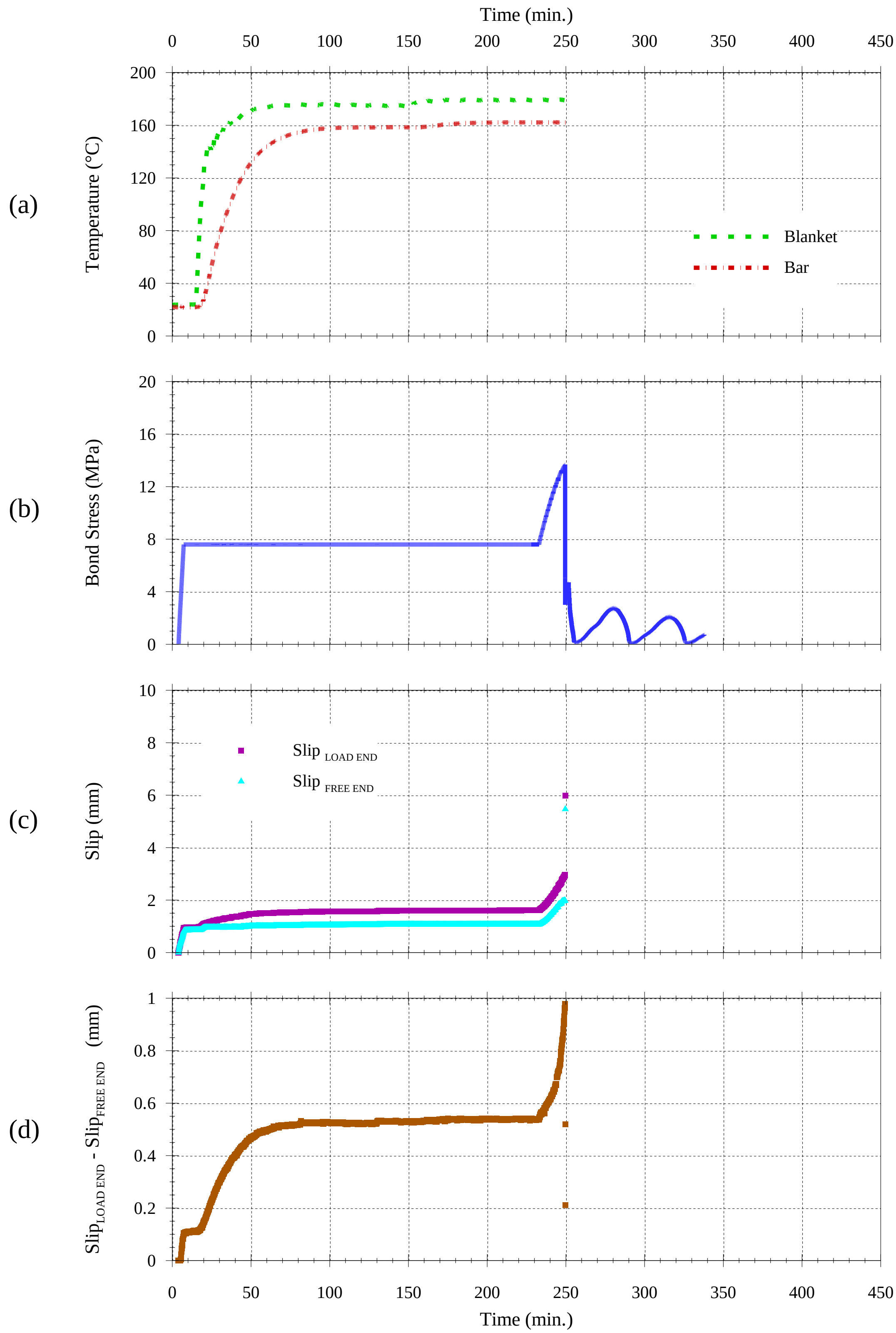

Figure 4.62: Experimental data for Steel_46%_e2

Figure 4.63 illustrates a zoom-in of the experimental data at the moment at which failure occurred. At this moment the wire's temperature was at a steady state of 162°C, with the heating blanket at 179°C, as shown in Figure 4.63(a). Every parameter was steady up until minute 233, at which further loading was applied in order to produce a bond failure of the sample.

The average bond stress was steady at 7.59 MPa up until minute 233 at which point it started increasing at rate of 0.50 MPa/min. Bond stress increased until minute 249 at which point a maximum bond stress of 13.68 MPa was achieved, as shown in Figure 4.63(b), and dropped to zero bond stress capacity at minute 255.

Slip at both ends remained steady, and started increasing as further pullout began. Both ends started slipping at the same time (minute 233) with a more pronounced increase at the loaded end, up until minute 249 at which point a relatively large slip occurred, as shown in Figure 4.63(c). At this point (bond failure), the difference between the loaded and the free end slip dropped, as shown in Figure 4.63(d).

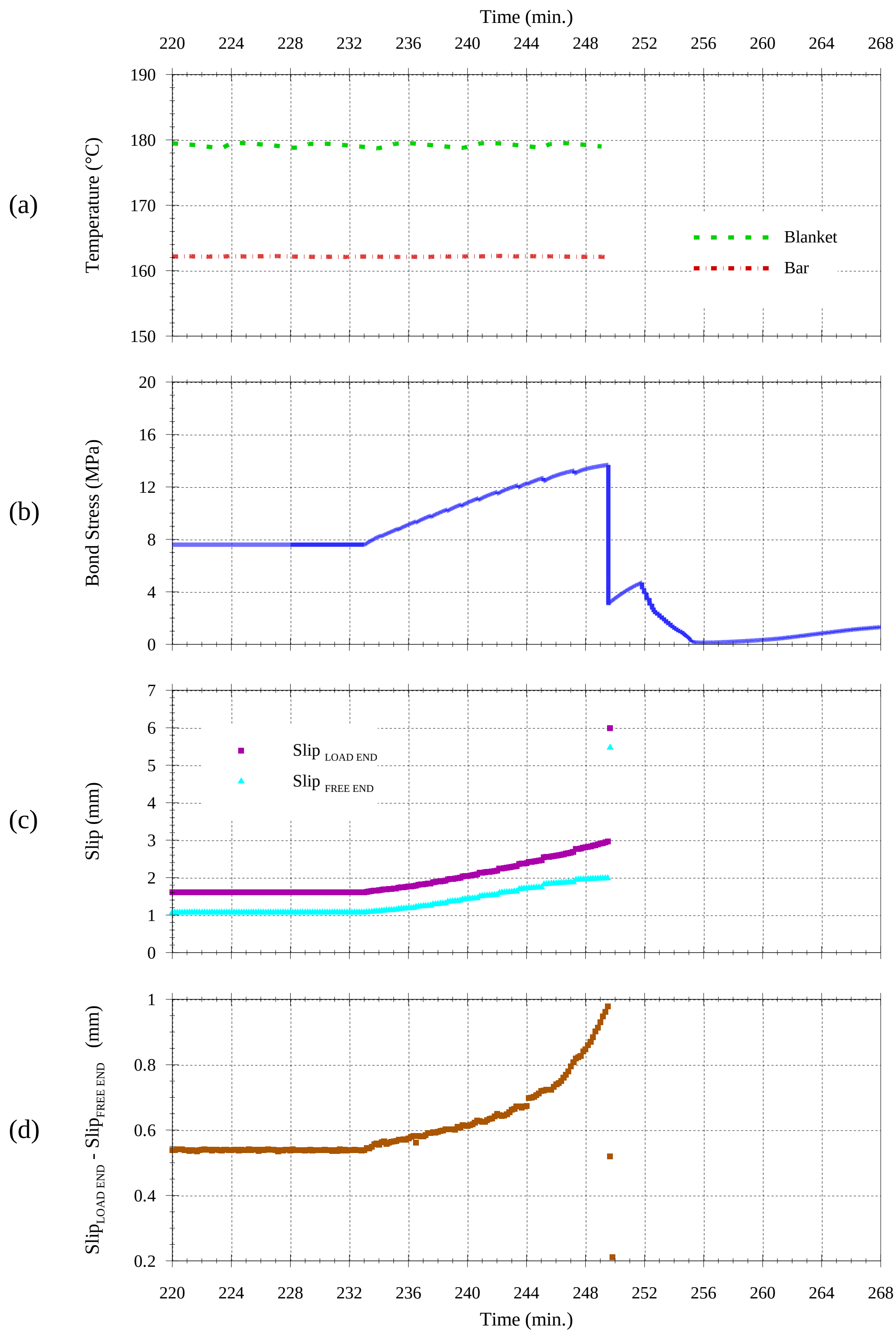

Figure 4.63: Zoom-in at failure for Steel_46%_e2

In Figure 4.64, 13.68 MPa was the maximum average bond stress observed. After failure there were local failures which occurred at the bond interface up until the bond stress capacity dropped to zero. The digital image correlation analysis used to measure the slip measured until a maximum slip of 6 mm.

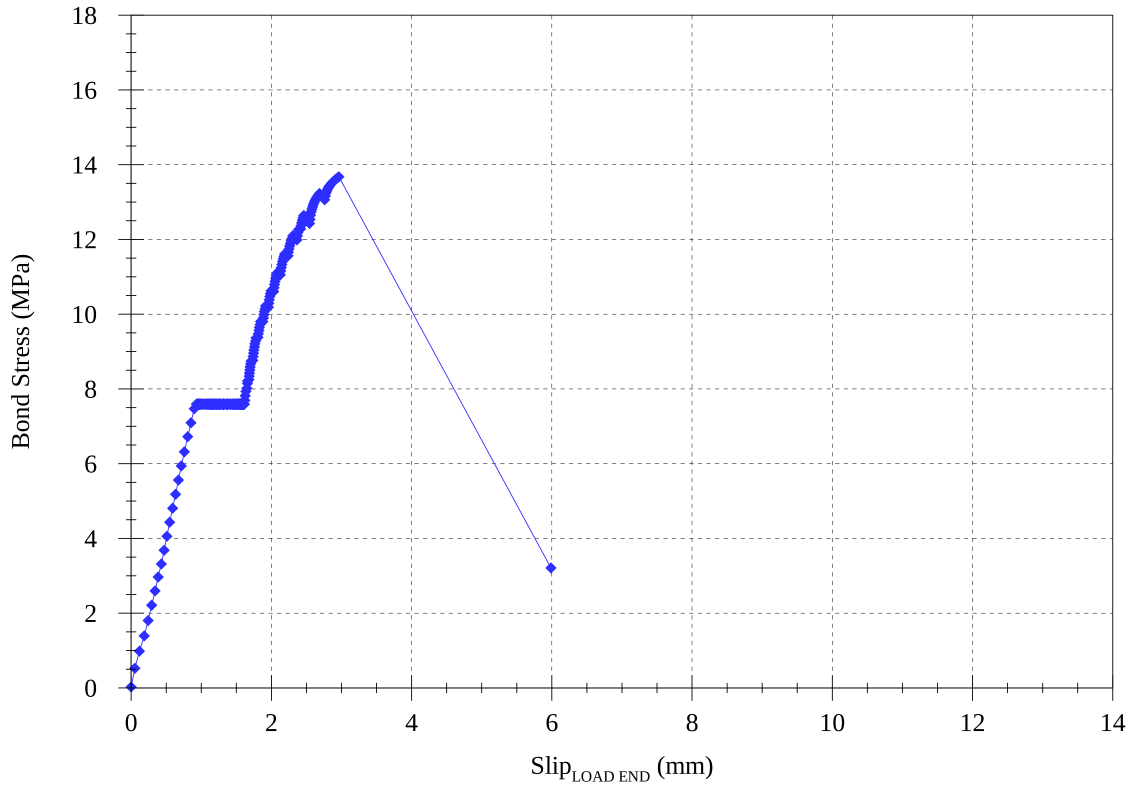

Figure 4.64: Bond stress versus loaded end slip for Steel_46%_e2

Again, in this test the bond interface did not fail as expected (it was assumed that the bond would fail as the tendon's temperature increased), but it failed as the load was increased with the tendon at a temperature of 162°C, and an initial average bond stress of 7.59 MPa. Nonetheless, Figure 4.65 is instructive to display that the failure occurred at a tendon's temperature of 162°C.

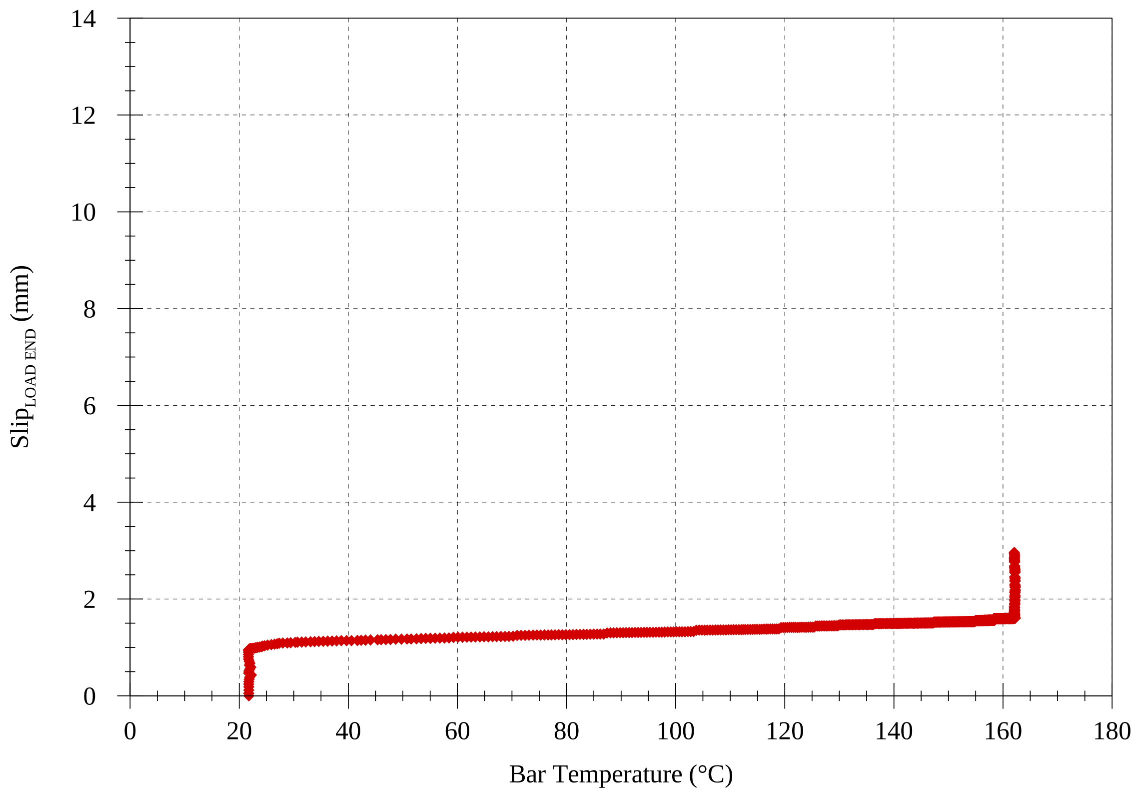

Figure 4.65: Bar temperature versus loaded end slip for Steel_46%_e2

After the heating blanket was turned on at minute 15, the average bond stress remained constant over time while the difference between the loaded and the free end slip increased, as shown in Figure 4.62(d). A zoom-in of the slip readings (see Figure 4.66) reveals that the increase of the slip difference after minute 15 is a result of the increase of the slip readings at both ends, with a more pronounced rise of the free end slip.

This phenomenon is a result of the concrete cylinder and steel prestressing wire combined thermal expansion noted and explained in Section 5.4.

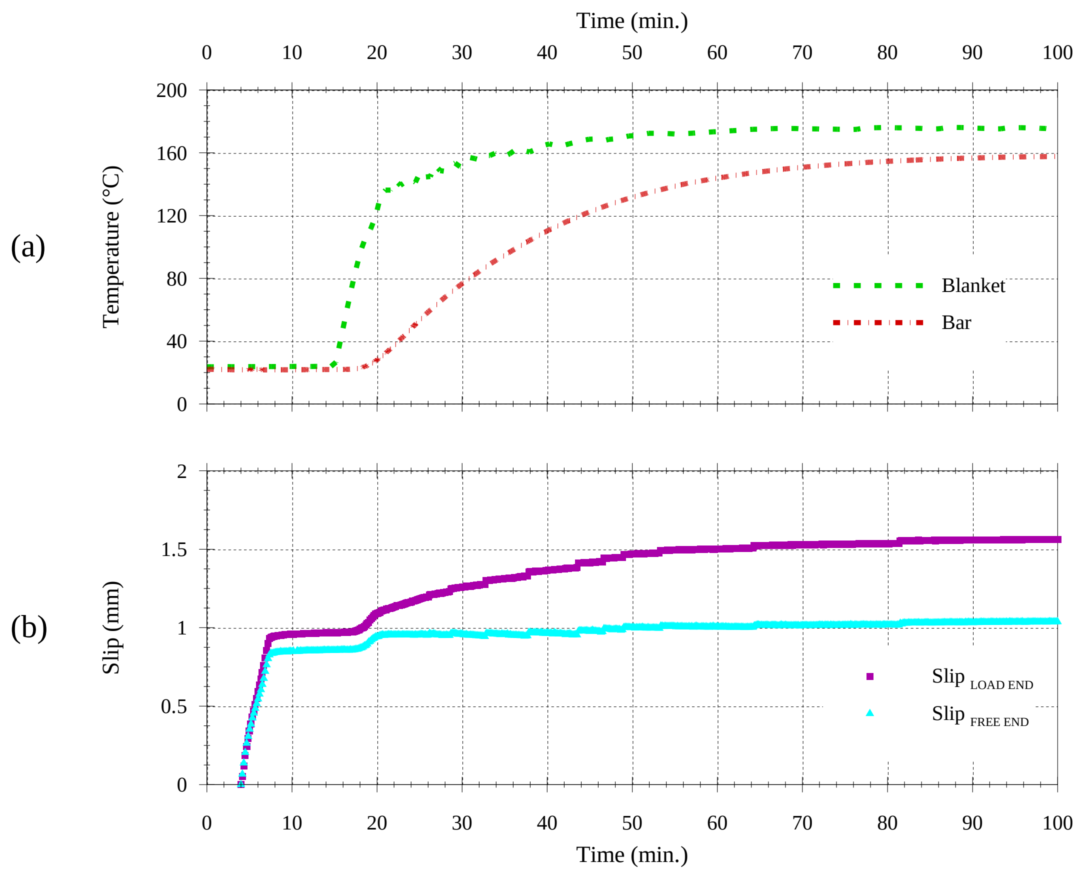

Figure 4.66: Zoom-in of temperature and slip for Steel_46%_e2

4.1.16 Steel_55%_e1

This was a PHPOT done on a steel pullout sample. This sample was stressed up to 55% (9.11 MPa) of the tensile strength capacity measured on the two RPOTs done on the steel pullout samples (Steel_AT_e1 and Steel_AT_e2), because this RPOTs failed at the wire's tensile strength (not at the bond interface). The same loading and heating rate were executed in this test, as for every other PHPOT. The pullout began at minute 4 (see Figure 4.67(b)) and the heating blanket was turned on at minute 15, with the wire's temperature beginning its rise at minute 18 (see Figure 4.67(a)). The Instron machine was configured to pullout from the wire at a bond stress rate of 2.39 MPa/min during the initial loading phase of the tests up until the required sustained load was reached.

In this test, failure occurred at an early stage by concrete's splitting failure, soon after the heating blanket started heating up. This failure generated a radial cracks on both ends of the concrete cylinder and longitudinal cracks at the cylinder's surface, as shown in Figure 4.68, producing a total loss of the sample's bond strength capability. This failure was the result of the concrete's tensile strength failure due to the summation of the mechanical stresses produced by the pullout conditions and the thermal stresses produced by the thermal gradient within the concrete.

Failure started at minute 16 with an increase of the slip at both ends (see Figure 4.67(c)) and a total loss of the bond strength capability at minute 20.6.

(a)

(b)

(c)

(d)

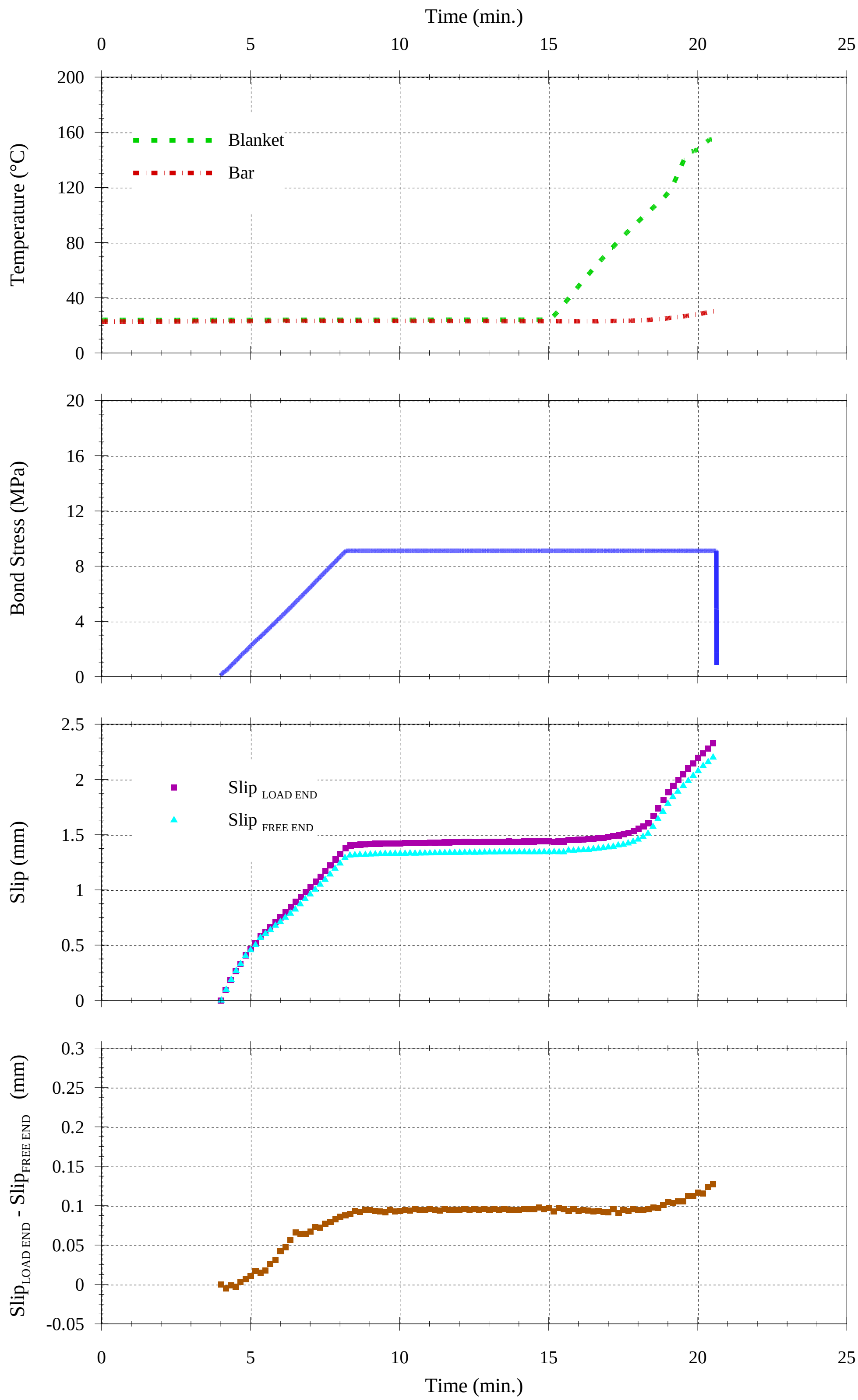

Figure 4.67: Experimental data for Steel_55%_e1

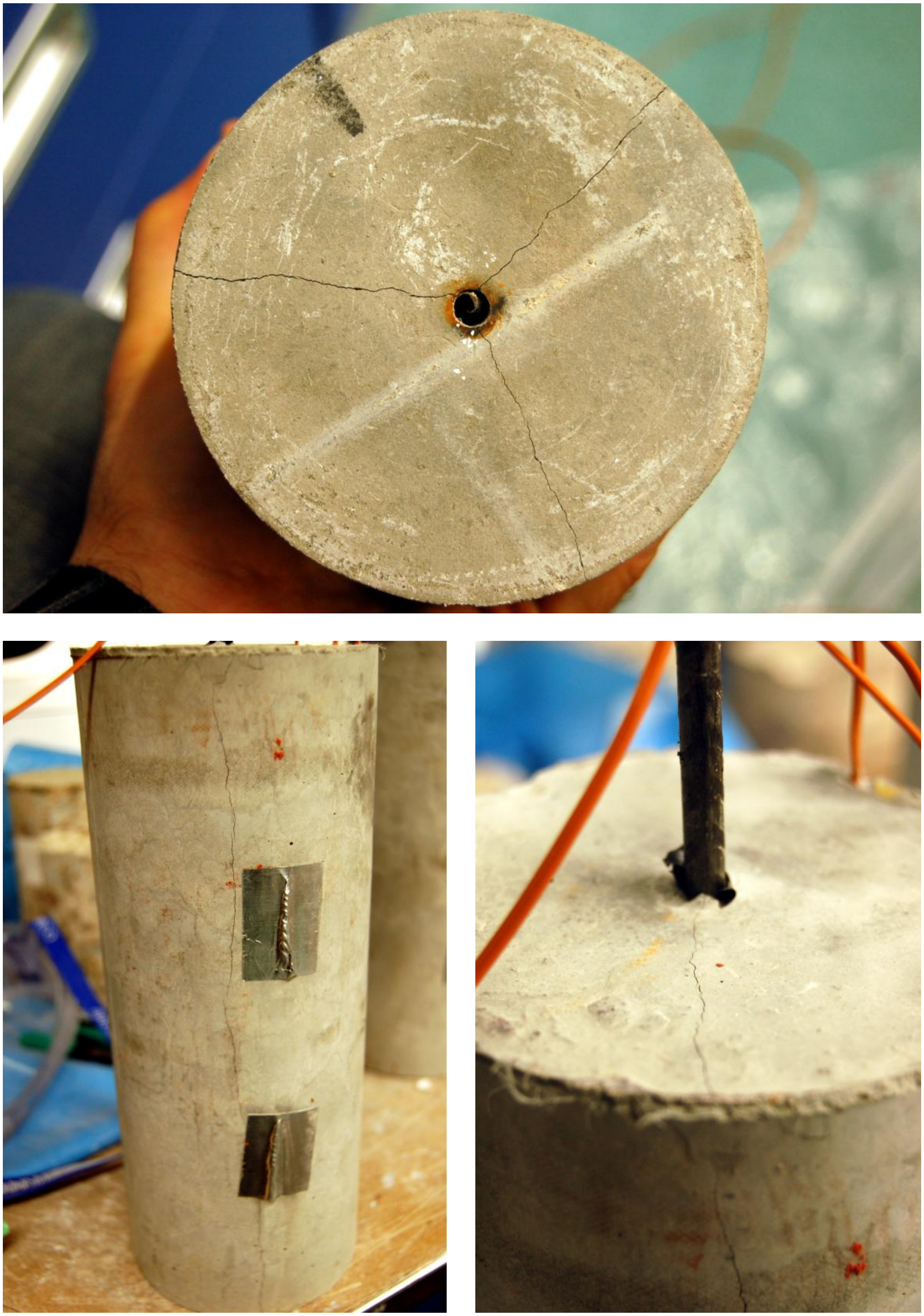

Figure 4.68: Pullout failure by concrete splitting failure (Steel_55%_e1)

Figure 4.69 illustrates a zoom-in of the experimental data at the moment at which failure occurred. Failure started at minute 16 with an increase of the slip at both ends, as shown in Figure 4.69(c). At this moment the steel prestressing wire temperature was 23°C and the heating blanket temperature was 35°C.

In Figure 4.69(d), at minute 18 (after failure had already started) with the steel prestressing wire at 24°C and the heating blanket at 95°C, the difference between the loaded and the free end slip started increasing. This is the effect of a progressive collapse propagating from the loaded end towards the free end. Even though failure in this particular test was the result of the concrete’s splitting failure, this phenomenon occurred indirectly because the confinement capability of the concrete cylinder decreased as failure took place.

At minute 20.6, the average bond stress suddenly dropped generating high slip on both ends, with the steel prestressing wire at 31°C and the heating blanket at 155°C.

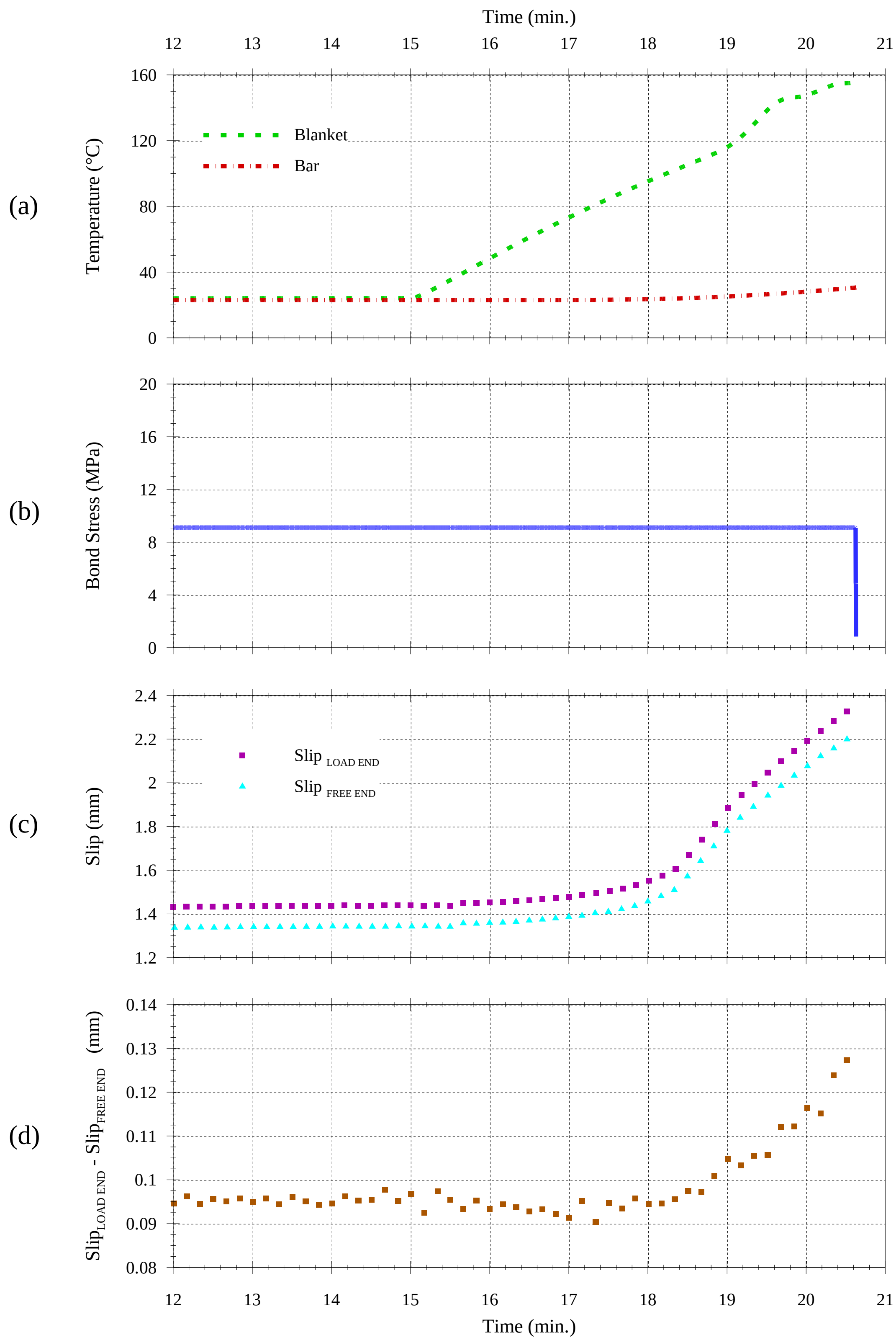

Figure 4.69: Zoom-in at failure for Steel_55%_e1

As failure occurred, the Instron machine tried to keep the average bond stress at the predetermined sustained level (9.11 MPa) in load-control testing mode; this is the reason why the bond stress suddenly dropped and the slip accelerated rapidly toward failure. At this high slip, the slip measurement systems were unable to continue measuring. This is why the residual bond strength relative to the Instron's crosshead displacement was determined (see Figure 4.70), rather than relative to the loaded end slip. After failure, the bond strength dropped to a value close to zero, and then evolves into an oscillating curve. This phenomenon was previously noted and explained in Section 4.1.12.1.

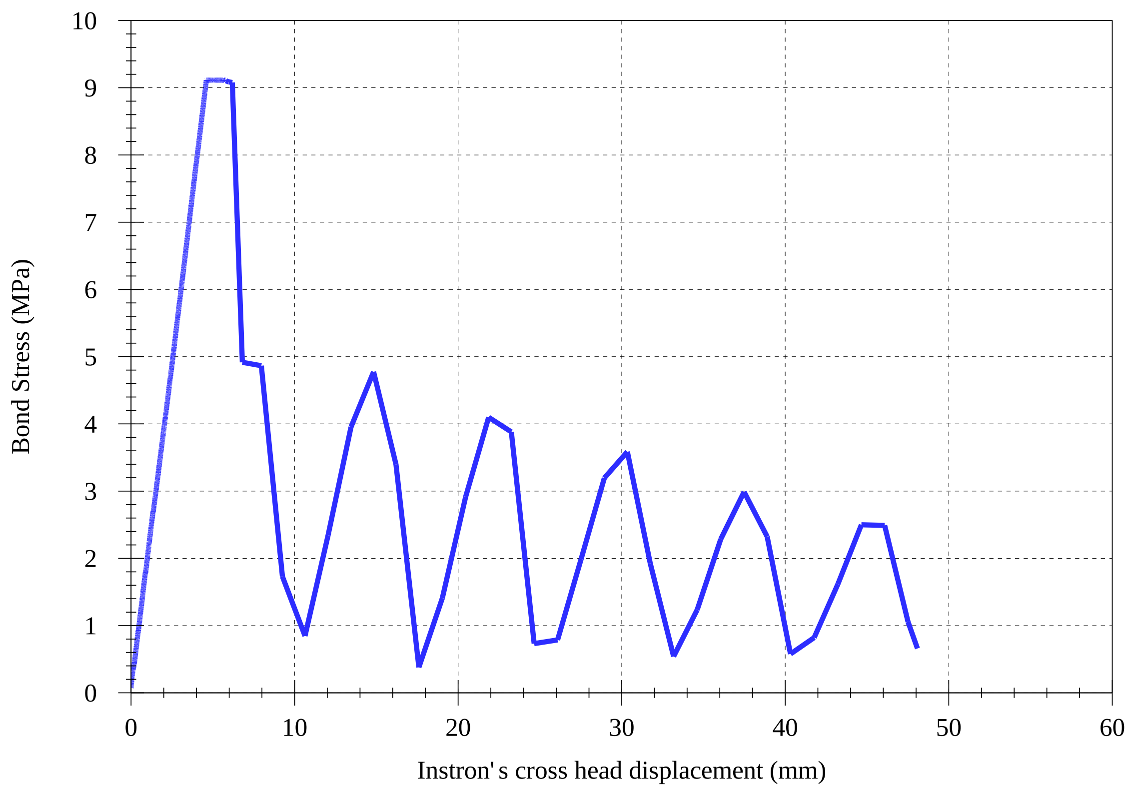

Figure 4.70: Bond stress versus Instron's crosshead displacement for Steel_55%_e1

4.1.17 Steel_55%_e2

This was a PHPOT done on a steel pullout sample. This sample was stressed up to 55% (9.11 MPa) of the tensile strength capacity measured on the two RPOTs done on the steel pullout samples (Steel_AT_e1 and Steel_AT_e2), because this RPOTs failed at the wire's tensile strength (not at the bond interface). The same loading and heating rate were executed in this test, as for every other PHPOT. The pullout began at minute 4 (see Figure 4.71(b)) and the heating blanket was turned on at minute 15, with the wire's temperature beginning its rise at minute 18 (see Figure 4.71(a)). The Instron machine was configured to pullout from the wire at a bond stress rate of 2.51 MPa/min during the initial loading phase of the tests up until the required sustained load was reached.

Again, in this test failure occurred at an early stage by concrete's splitting failure, soon after the heating blanket started heating up. This failure was the result of the concrete's tensile strength failure due to the summation of the mechanical stresses produced by the pullout conditions and the thermal stresses produced by the thermal gradient within the concrete.

Failure started at minute 16 with an increase of the slip at both ends (see Figure 4.71(c)) and a total loss of the bond strength capability at minute 18.7.

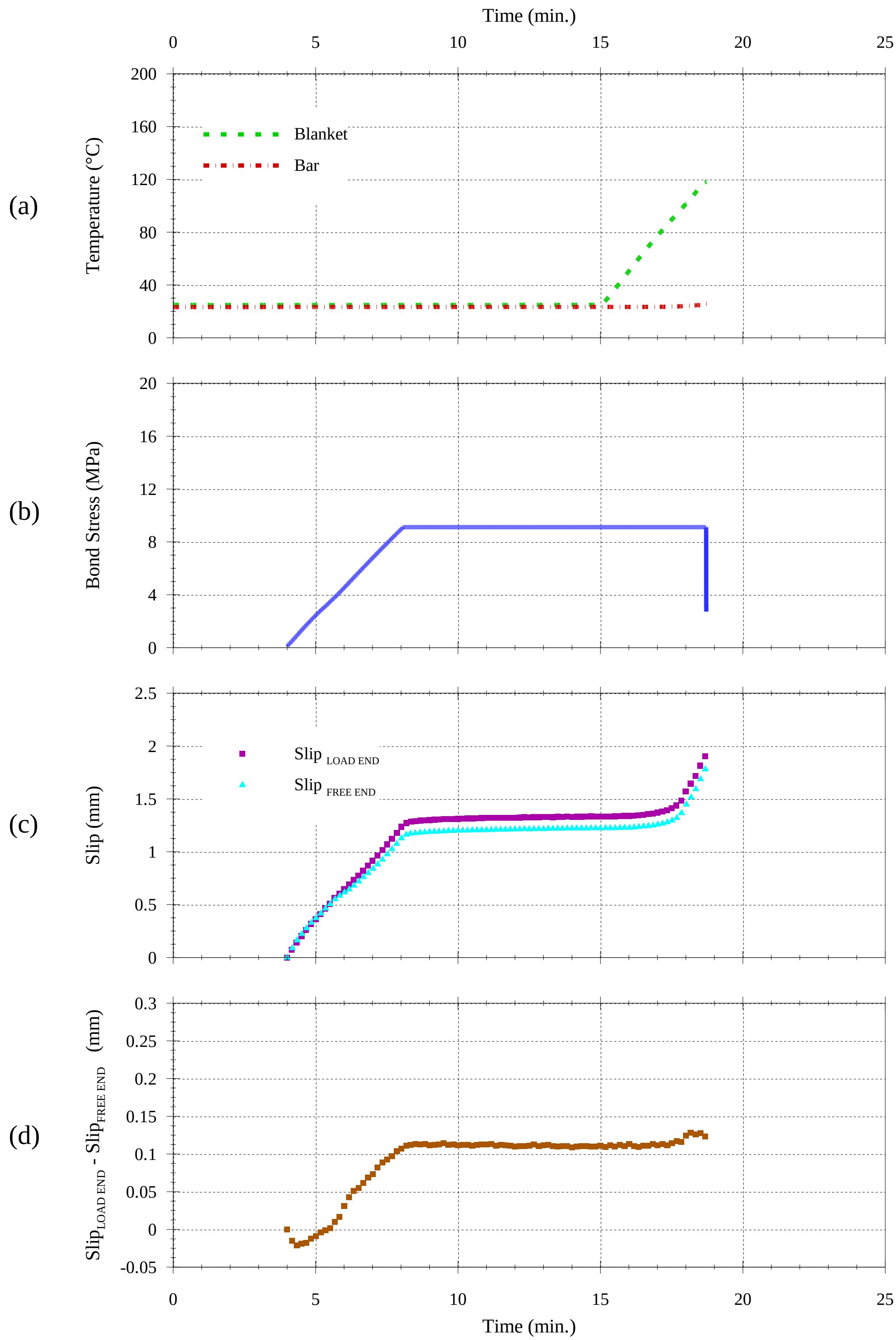

Figure 4.71: Experimental data from the Steel_55%_e2 test

Figure 4.72 illustrates a zoom-in of the experimental data at the moment at which failure occurred. Failure started at minute 16 with an increase of the slip at both ends, as shown in Figure 4.72(c). At this moment the steel prestressing wire temperature was 23°C and the heating blanket temperature was 51°C.

In Figure 4.72(d), at minute 17.4 (after failure had already started) with the steel prestressing wire at 24°C and the heating blanket at 87°C, the difference between the loaded and the free end slip started increasing. This is the effect of a progressive collapse propagating from the loaded end towards the free end. Even though failure in this particular test was the result of the concrete's splitting failure, this phenomenon occurred indirectly because the confinement capability of the concrete cylinder decreased as failure took place.

At minute 18.7, the average bond stress suddenly dropped generating high slip on both ends, with the steel prestressing wire at 25°C and the heating blanket at 118°C.

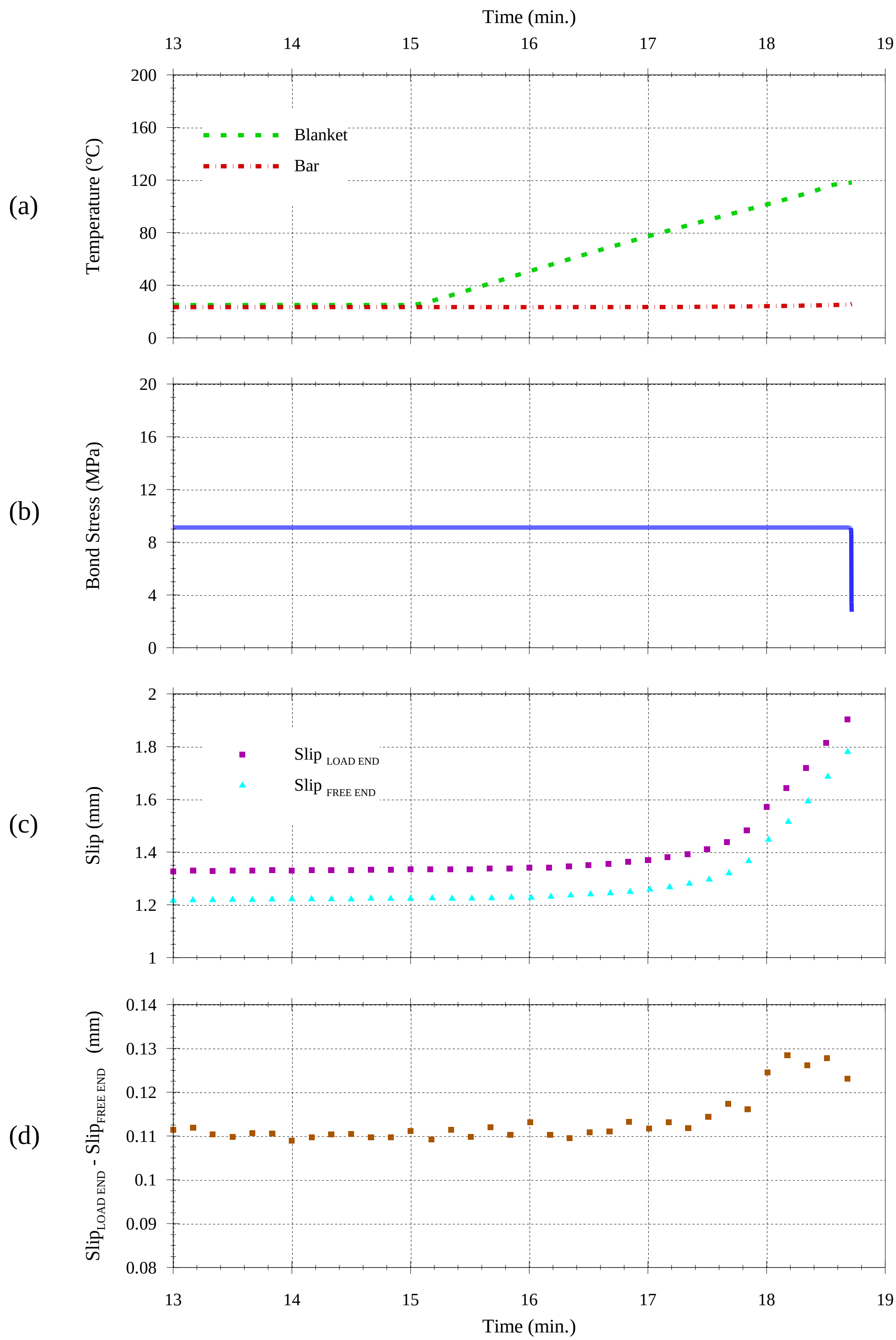

Figure 4.72: Zoom-in at failure for Steel_55%_e2

As failure occurred, the Instron machine tried to keep the average bond stress at the predetermined sustained level (9.11 MPa) in load-control testing mode; this is the reason why the bond stress suddenly dropped and the slip accelerated rapidly toward failure. At this high slip, the slip measurement systems were unable to continue measuring. This is why the residual bond strength relative to the Instron's crosshead displacement was determined (see Figure 4.73), rather than relative to the loaded end slip. After failure, the bond strength dropped to a value close to zero, and then evolves into an oscillating curve. This phenomenon was previously noted and explained in Section 4.1.12.1.

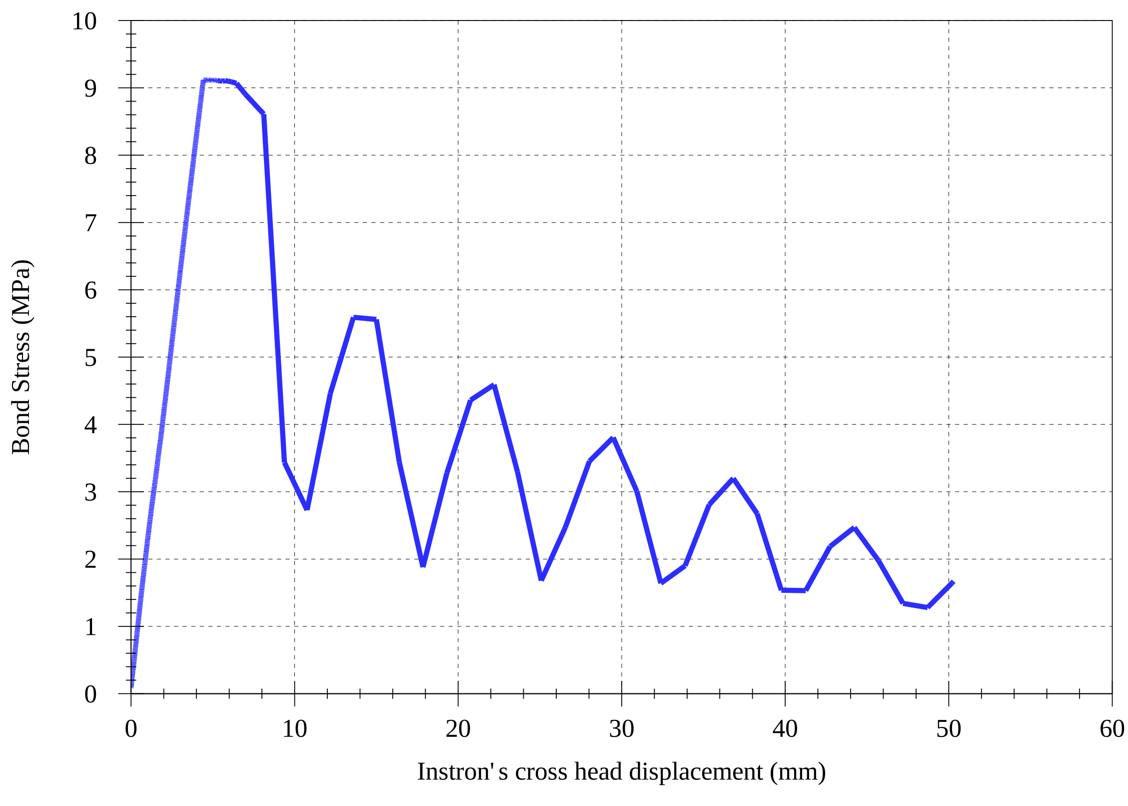

Figure 4.73: Bond stress versus Instron's crosshead displacement for Steel_55%_e2

4.1.18 Steel_55%_e3

This was a PHPOT done on a steel pullout sample. This sample was stressed up to 55% (9.11 MPa) of the tensile strength capacity measured on the two RPOTs done on the steel pullout samples (Steel_AT_e1 and Steel_AT_e2), because this RPOTs failed at the wire's tensile strength (not at the bond interface). The same loading and heating rate were executed in this test, as for every other PHPOT. The pullout began at minute 4 (see Figure 4.74(b)) and the heating blanket was turned on at minute 15, with the wire's temperature beginning its rise at minute 18 (see Figure 4.74(a)). The Instron machine was configured to pullout from the wire at a bond stress rate of 2.42 MPa/min during the initial loading phase of the tests up until the required sustained load was reached.

Again, in this test failure occurred at an early stage by concrete's splitting failure, soon after the heating blanket started heating up. This failure was the result of the concrete's tensile strength failure due to the summation of the mechanical stresses produced by the pullout conditions and the thermal stresses produced by the thermal gradient within the concrete.

Failure started at minute 16 with an increase of the slip at both ends (see Figure 4.74(c)) and a total loss of the bond strength capability at minute 19.2.

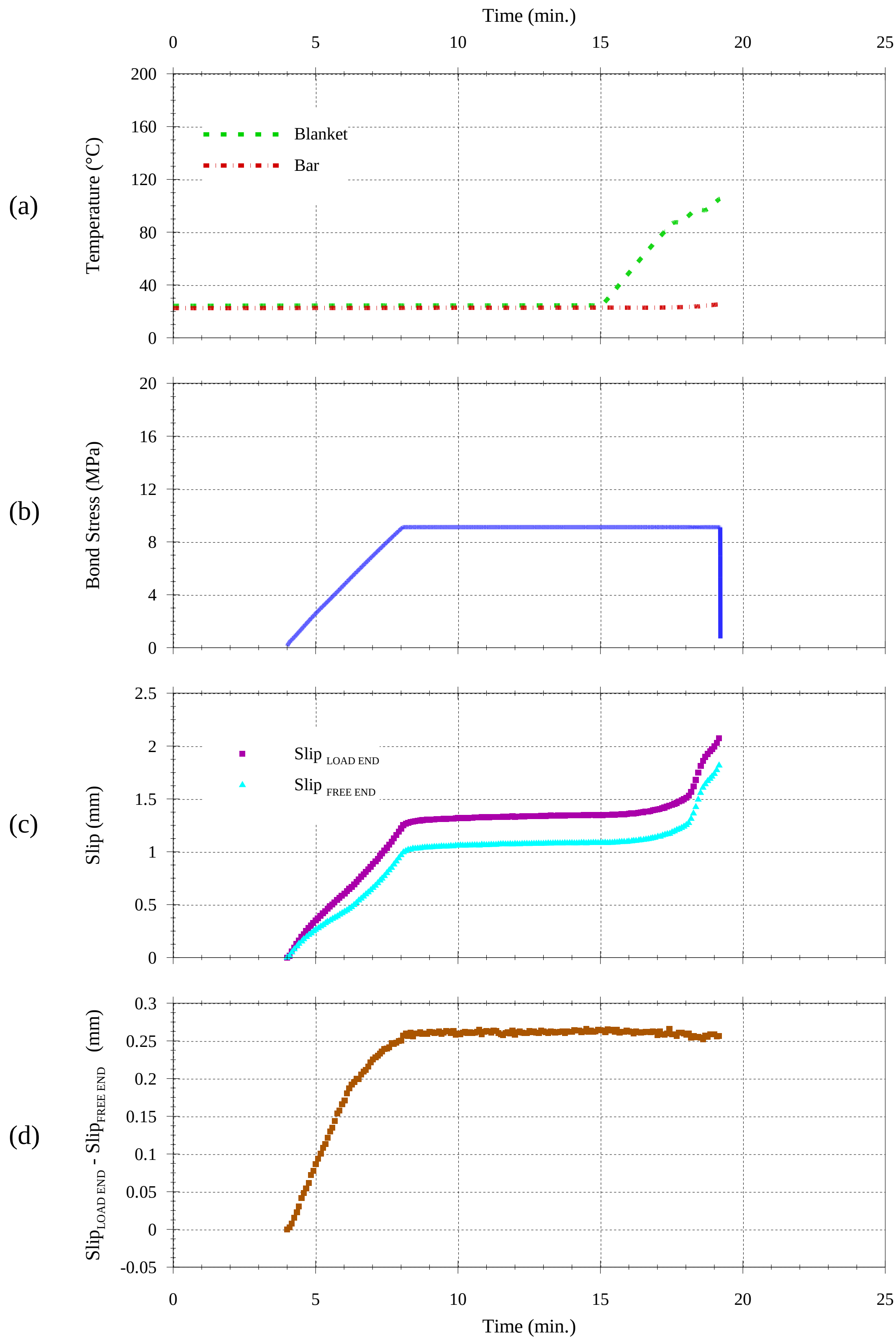

Figure 4.74: Experimental data for Steel_55%_e3

Figure 4.75 illustrates a zoom-in of the experimental data at the moment at which failure occurred. Failure started at minute 16 with an increase of the slip at both ends, as shown in Figure 4.75(c). At this moment the steel prestressing wire temperature was 23°C and the heating blanket temperature was 49°C.

In Figure 4.75(d), at minute 18.6 (after failure had already started) with the steel prestressing wire at 24°C and the heating blanket at 97°C, the difference between the loaded and the free end slip started increasing. This is the effect of a progressive collapse propagating from the loaded end towards the free end. Even though failure in this particular test was the result of the concrete’s splitting failure, this phenomenon occurred indirectly because the confinement capability of the concrete cylinder decreased as failure took place.

At minute 19.2, the average bond stress suddenly dropped generating high slip on both ends, with the steel prestressing wire at 25°C and the heating blanket at 105°C.

(a)

(b)

(c)

(d)

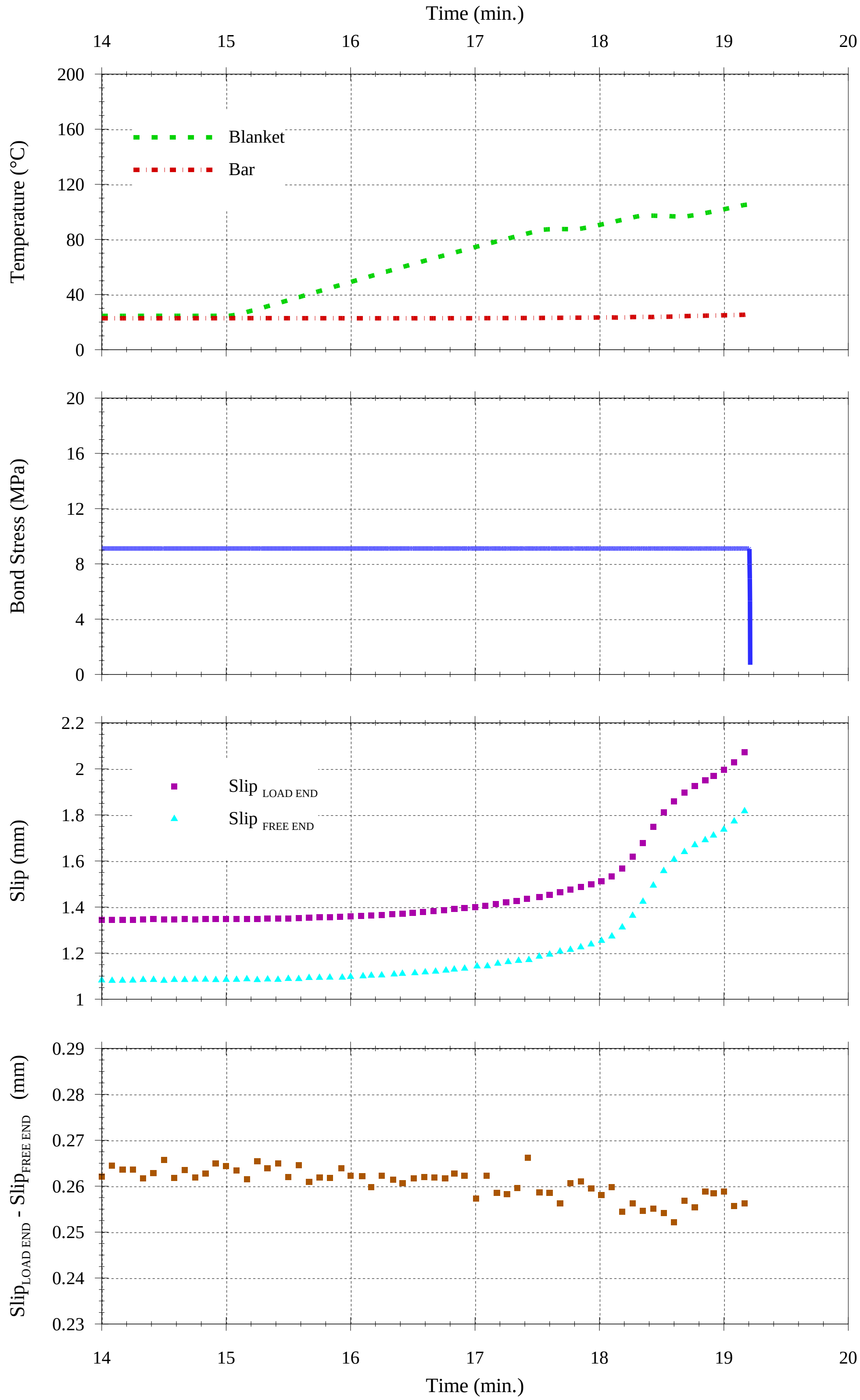

Figure 4.75: Zoom-in at failure for Steel_55%_e3

As failure occurred, the Instron machine tried to keep the average bond stress at the predetermined sustained level (9.11 MPa) in load-control testing mode; this is the reason why the bond stress suddenly dropped and the slip accelerated rapidly toward failure. At this high slip, the slip measurement systems were unable to continue measuring. This is why the residual bond strength relative to the Instron's crosshead displacement was determined (see Figure 4.76), rather than relative to the loaded end slip. After failure, the bond strength dropped to a value close to zero, and then evolves into an oscillating curve. This phenomenon was previously noted and explained in Section 4.1.12.1.

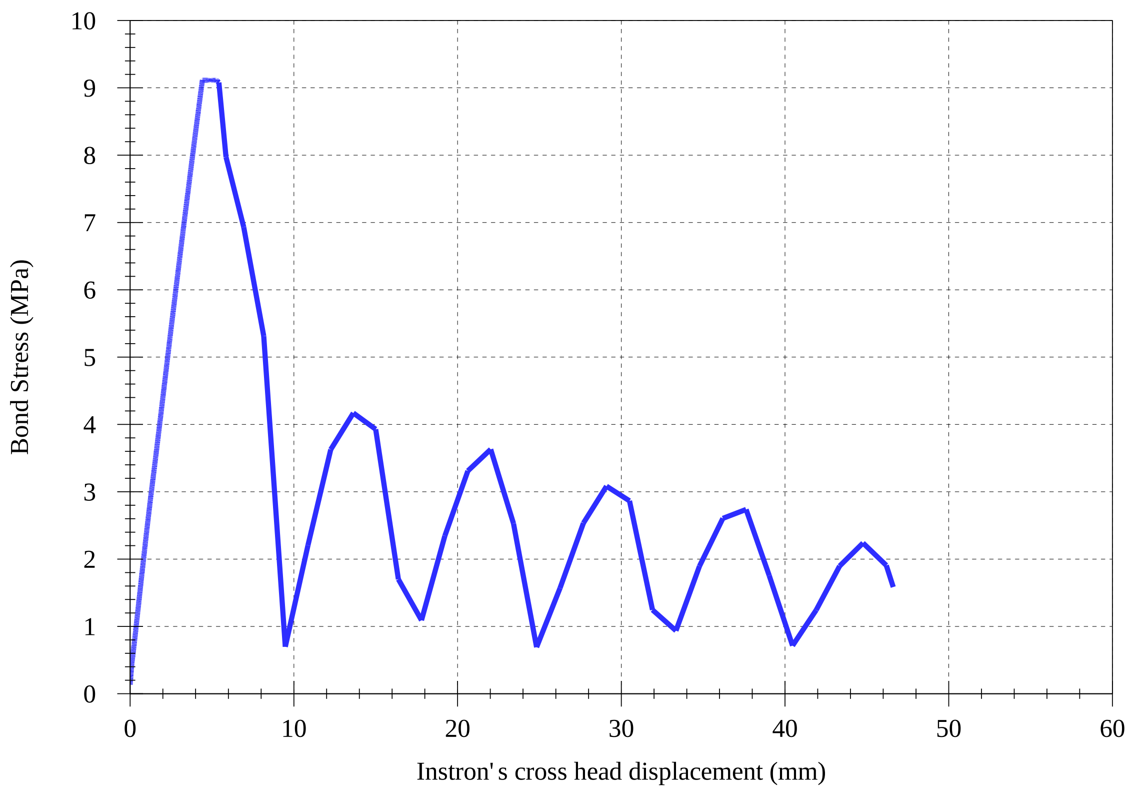

Figure 4.76: Bond stress versus Instron's crosshead displacement for Steel_55%_e3

4.1.19 Summary

4.1.19.1 CFRP pullout comments

CFRP pullouts executed at room temperature (RPOTs) failed at the bond interface. After failure occurred, pullout continued and a residual strength of 66-77% of the bond strength capacity was measured.

For the tests prestressed at 15, 30 and 38%, the bond stress was not high enough to produce a failure of the bond interface as the temperature of the tendon increased. After heating the sample for almost four hours at steady state temperature, the bond stress was further increased until failure occurred at similar bond stresses to those achieved with pullout tests executed at room temperature. These tests were labelled as "extended PHPOTs" on CFRP pullout samples. After failure occurred, pullout continued and a residual strength was measured, which tended to a value of 44-58% of the bond strength at high temperature. The residual bond strengths calculated in these tests were always larger than the minimum bond stresses at which the bond interface did failed as the temperature increased (when prestressed at 45, 53 and 60%).

For the tests prestressed at 45, 53 and 60%, the bond interface failed as the temperature of the tendon increased. After failure occurred, pullout continued and a residual strength was measured, which tended to a value of 29-35% of the bond stress at which the tendons were prestressed. An obvious correlation between the bond prestress level and the failure temperature was determined from these tests, at higher prestress levels failure occurred at lower temperatures. These tests were labelled as "regular PHPOT" on CFRP pullout samples.

For the test prestressed at 68%, the bond interface failed soon after the heating blanket was turned on. The pullout sample failed because of the slip produced by the concrete's thermal expansion slip added to the high bond stress produced by the prestress load.

Pullout samples executed in RPOTs, regular PHPOTs and extended PHPOTs were examined after testing. A circular saw was used to cut the concrete cylinders in a plane across the cylinders' length (see Figure 4.77). Because residues of the CFRP tendons' sand coating were found in the cavity where the CFRP tendon used to be, it could be concluded that the reduction in the bond strength was attributed to the detachment of the sand coating from the CFRP tendon.

In RPOTs post-pullout examination, the sand coating was found to be adhered to concrete at the section in which the CFRP tendon was previously bonded to concrete (see Figure 4.77(c)). In regular and extended PHPOTs post-pullout examination, remains of the sand coating were found adhered to concrete only at the top end of the bonded length (loaded end), indicating that high temperatures to which the CFRP tendons were subjected, degraded the bonding between the sand coating and the concrete.

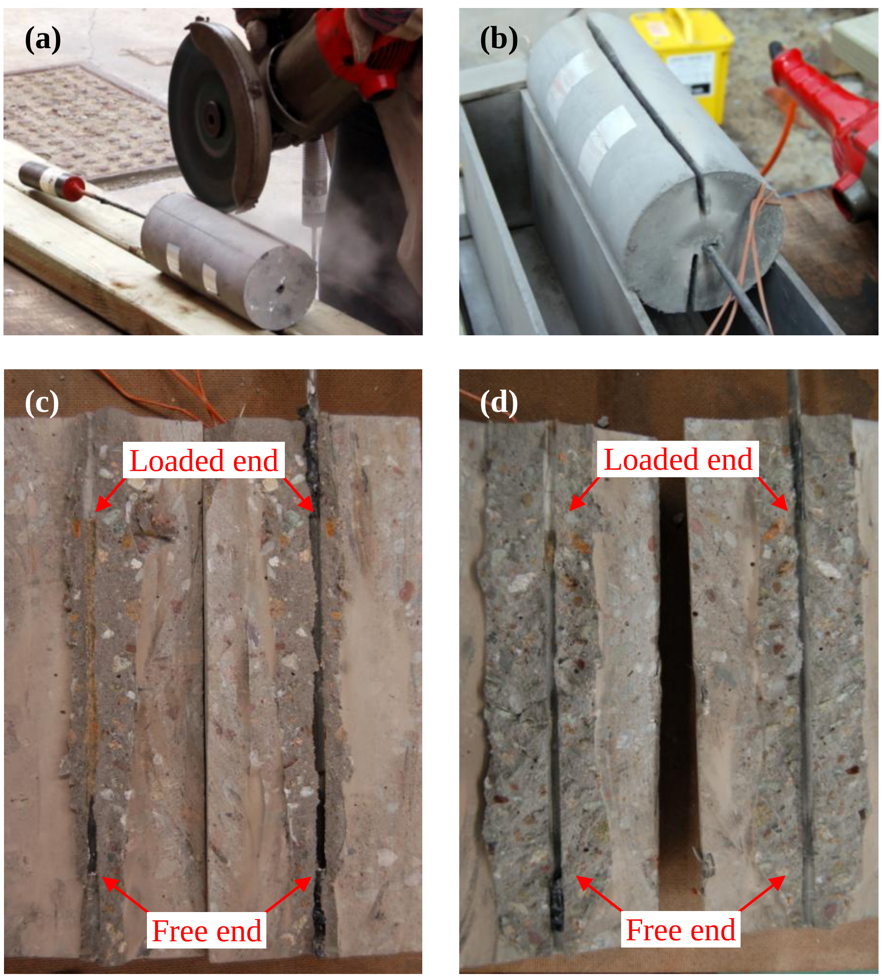

Figure 4.77: (a) Cutting of a pullout specimen with a circular saw, **(b)** longitudinal cuts across the cylinder's diameter, **(c)** CFRP_AT_e1 post-pullout examination **(d)** and CFRP_53% post-pullout examination

4.1.19.2 Steel pullout comments

Steel pullouts executed at room temperature (RPOTs) failed because of yielding and eventual rupture of the steel prestressing wire at the loaded end. In steel pullout sample the bond strength of the steel prestressing wire was actually greater than the tensile capacity of the wire.

For the tests prestressed at 37% and 46%, the bond stress was not high enough to produce a failure of the bond interface as the temperature of the wire increased. After heating the sample for almost four hours at steady state temperature, the bond stress was further increased until failure occurred at bond stresses between 71 and 82% of the maximum bond stress achieved at room temperature (at room temperature the bond strength was not determined because this samples failed by rupture of the steel prestressing wire). These tests were labelled as “extended PHPOT” on steel pullout samples. After failure occurred, pullout continued and a residual strength was measured. Contrary from what happened in the CFRP pullout test, bond strength capacity dropped to zero after failure occurred and as slip continued the bond residual strength evolve into an oscillating curve, as explained in Section 4.1.12.1.

For the tests prestressed at 55%, failure occurred by the concrete’s splitting failure. In these tests failure occurred soon after the heating blanket was turned on, moment at which the thermal gradient within the concrete was higher. Failure of these tests was the result of the concrete’s tensile strength failure due to the summation of the mechanical stresses produced by the pullout conditions and the thermal stresses produced by the thermal gradient within the concrete.

Table 4.1: Results summary for CFRP pullout tests

Test	Prestress Conditions			Failure Conditions					Bond residual strength (MPa)
	Bond Stress (MPa)	Tensile Stress (MPa)	Pullout Load (kN)	Bond Stress (MPa)	Tensile Stress (MPa)	Pullout Load (kN)	Temperature		
							Bar (°C)	Blanket (°C)	
CFRP_AT_e1	-	-	-	5.34	632.52	14.49	21	24	4.09
CFRP_AT_e2	-	-	-	4.42	524.08	12.00	20	24	2.90
CFRP_15%	0.74	87.33	2.00	3.89	460.72	10.55	166	182	2.26
CFRP_30%	1.47	174.66	4.00	5.07	601.21	13.77	166	182	2.21
CFRP_38%	1.84	218.32	5.00	4.33	513.16	11.75	164	185	2.29
CFRP_45%	2.21	261.98	6.00	-	-	-	109	169	0.65
CFRP_53%	2.58	305.65	7.00	-	-	-	102	155	0.89
CFRP_60%	2.95	349.31	8.00	-	-	-	95	148	0.92
CFRP_68%	3.32	392.98	9.00	-	-	-	21	76	-

Table 4.2: Results summary for steel pullout tests

Test	Prestress Conditions			Failure Conditions				
	Bond Stress (MPa)	Tensile Stress (MPa)	Pullout Load (kN)	Bond Stress (MPa)	Tensile Stress (MPa)	Pullout Load (kN)	Temperature	
							Bar (°C)	Blanket (°C)
Steel_AT_e1*	-	-	-	16.63	1774.14	50.16	22	24
Steel_AT_e2*	-	-	-	16.61	1771.97	50.10	21	24
Steel_37%_e1	6.07	647.94	18.32	11.78	1256.61	35.53	164	184
Steel_37%_e2	6.07	647.94	18.32	13.45	1434.36	40.56	160	178
Steel_46%_e1	7.59	809.92	22.90	12.79	1364.79	38.59	170	192
Steel_46%_e2	7.59	809.92	22.90	13.68	1459.59	41.27	162	179
Steel_55%_e1	9.11	971.91	27.48	-	-	-	31	155
Steel_55%_e2	9.11	971.91	27.48	-	-	-	25	118
Steel_55%_e3	9.11	971.91	27.48	-	-	-	25	105

* This tests failed because of yielding and eventual rupture of the steel wire at the loaded end.

In order that similar mechanical conditions were produced in every pullout sample, special care was given to the application of the bond stress rate at which the pullouts were executed. Because the Instron machine pullout rate worked by setting the crosshead displacement rate (mm/min), a calculation (explained in Section 3.4.1.2.1) had to be done in order to apply the desired bond stress rate.

For extended PHPOTs, a second loading phase (labelled as N°2 in Table 4.3) was executed to produce the bond failure, after no failure occurred for the prestress level at which the tendon/wire was initially subject to.

Table 4.3: Bond stress rates for CFRP and steel pullout tests

Test	**Bond stress rate (MPa/min)**	
	N°1	**N°2**
CFRP_AT_e1	0.71	-
CFRP_AT_e2	4.96	-
CFRP_15%	2.64	0.52
CFRP_30%	2.43	0.48
CFRP_38%	2.36	0.45
CFRP_45%	2.33	-
CFRP_53%	3.23	-
CFRP_60%	2.71	-
CFRP_68%	2.78	-

Test	**Bond stress rate (MPa/min)**	
	N°1	**N°2**
Steel_AT_e1	3.27	-
Steel_AT_e2	2.71	-
Steel_37%_e1	2.72	0.42
Steel_37%_e2	2.58	0.44
Steel_46%_e1	2.98	0.40
Steel_46%_e2	2.51	0.50
Steel_55%_e1	2.39	-
Steel_55%_e2	2.51	-
Steel_55%_e3	2.42	-

4.2 CFRP Transient Thermal Tensile Test

This test's objective was to characterize the high temperature tensile strength of the CFRP tendons. A series of nine transient high temperature tensile tests was performed on the CFRP tendons at sustained stress levels between 800 MPa and 1200 MPa (a realistic stress range for pretensioning applications). The tendons were stressed to sustained loads of approximately 800, 1000, or 1200 MPa and then heated, at 10°C/min, to failure. The anchorages were protected from high temperature.

Table 4.4: Test results of the CFRP transient thermal tensile tests

Test	Prestress Conditions		Failure Conditions		
	Tensile Stress (MPa)	Load (KN)	Failure Temperature (°C)	Average Failure Temperature (°C)	Standard Deviation (°C)
CFRP_800MPa_1	800	22.62	393	358.7	35.6
CFRP_800MPa_2			361		
CFRP_800MPa_3			322		
CFRP_1000MPa_1	1000	28.27	331	334.3	2.9
CFRP_1000MPa_2			336		
CFRP_1000MPa_3			336		
CFRP_1200MPa_1	1200	33.93	320	317.3	3.1
CFRP_1200MPa_2			314		
CFRP_1200MPa_3			318		

The ACI (1989) defines as "critical temperature"; 50% loss of the room temperature strength of any structural material. The tests executed at 1000 MPa, 50% of the design tensile strength of the CFRP tendon (2000 MPa), indicated an average failure temperature of 334°C.

4.3 CFRP Dynamic Mechanical Analysis

This test was executed in five samples. In two of them, a heating ramp extracted from the pullout tests was used, as explained in Section 3.4.3. In the three others samples a constant ramp of 3 °C/min is used. Both heating ramps are displayed in Figure 4.78.

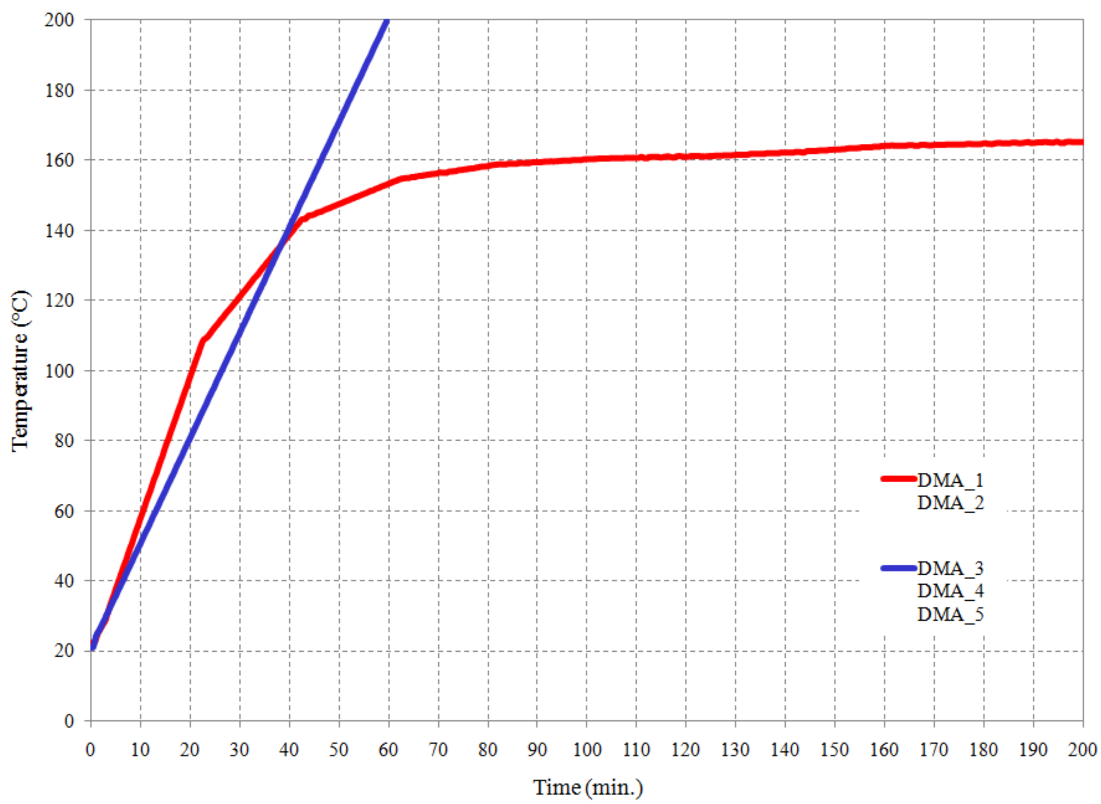

Figure 4.78: DMA heating ramps

4.3.1 DMA_1

The heating ramp, showed in Figure 4.78, was extracted from the temperature data recorded in the CFRP pullout tests. The results from this test are displayed from the retained elastic modulus over time (see Figure 4.79) and over temperature (see Figure 4.80).

The sample was tested twice in order to check variations in the glass transition temperature, which would mean that the CFRP's epoxy cured during the first test.

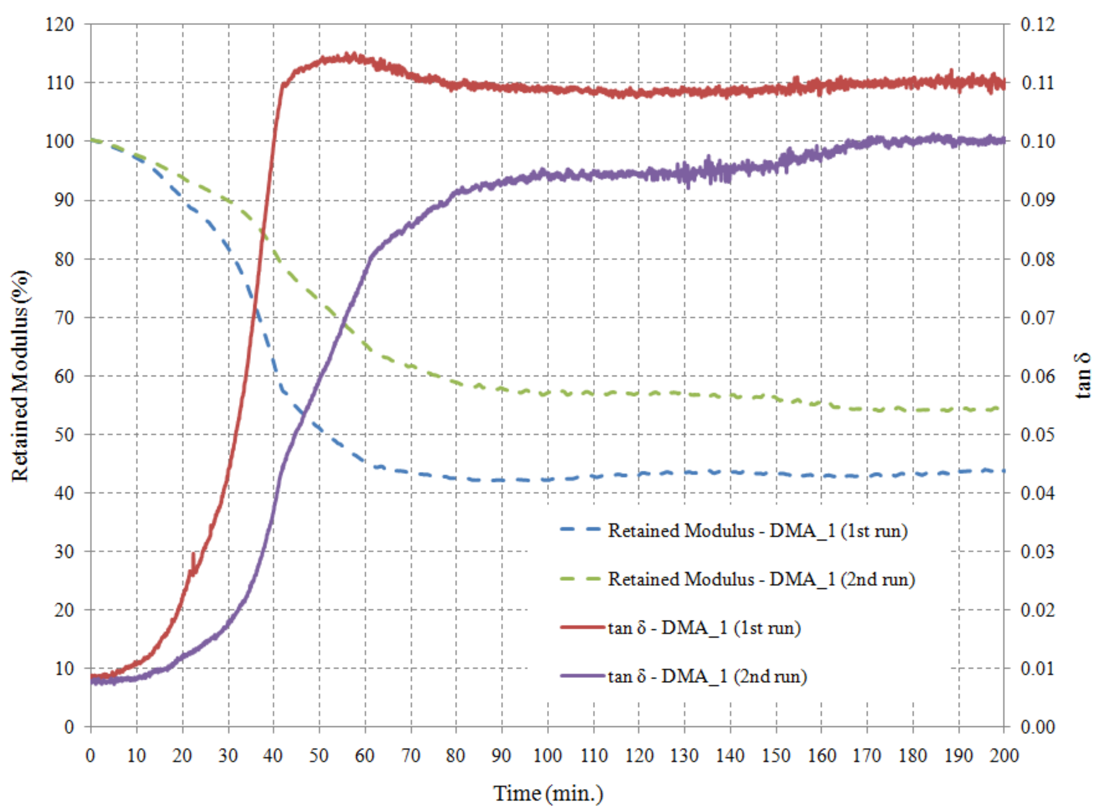

Figure 4.79: DMA_1 test results over time

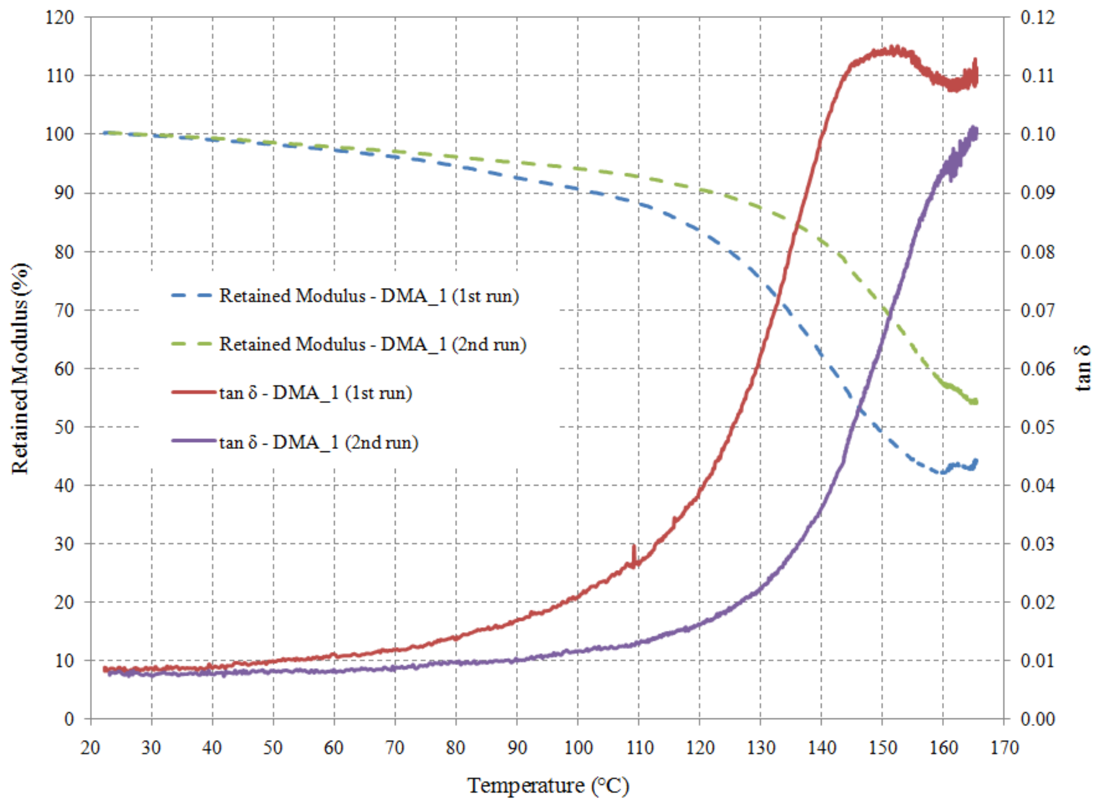

Figure 4.80: DMA_1 test results over temperature

The first time the sample was tested, the T_g was calculated at 152°C, according to the tan δ peak criteria. At this temperature, the epoxy retained a 47% of its room temperature elastic modulus.

For the second time the sample was tested, the tan δ peak did not occurred for the maximum temperature (165°C) reached by the heating ramp extracted from the CFRP pullout tests. Anyway, at 165°C the epoxy retained 54% of its room temperature elastic modulus.

This means that the sample experience an increase of 13°C between the first and the second test, due to curing of the sample's epoxy during the first test.

4.3.2 DMA_2

The heating ramp, showed in Figure 4.78, was extracted from the temperature data recorded in the CFRP pullout tests. The results from this test are displayed from the retained elastic modulus over time (see Figure 4.81) and over temperature (see Figure 4.82).

The sample was tested twice in order to check variations in the glass transition temperature, which would mean that the CFRP's epoxy cured during the first test.

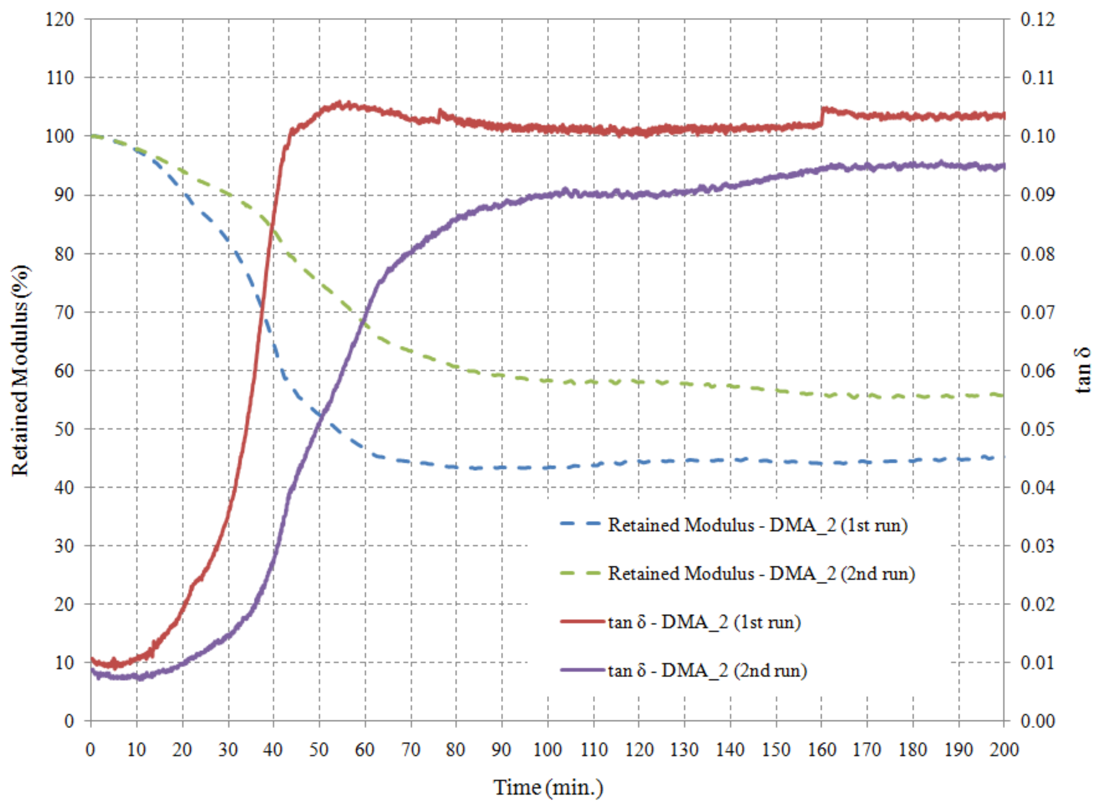

Figure 4.81: DMA_2 test results over time

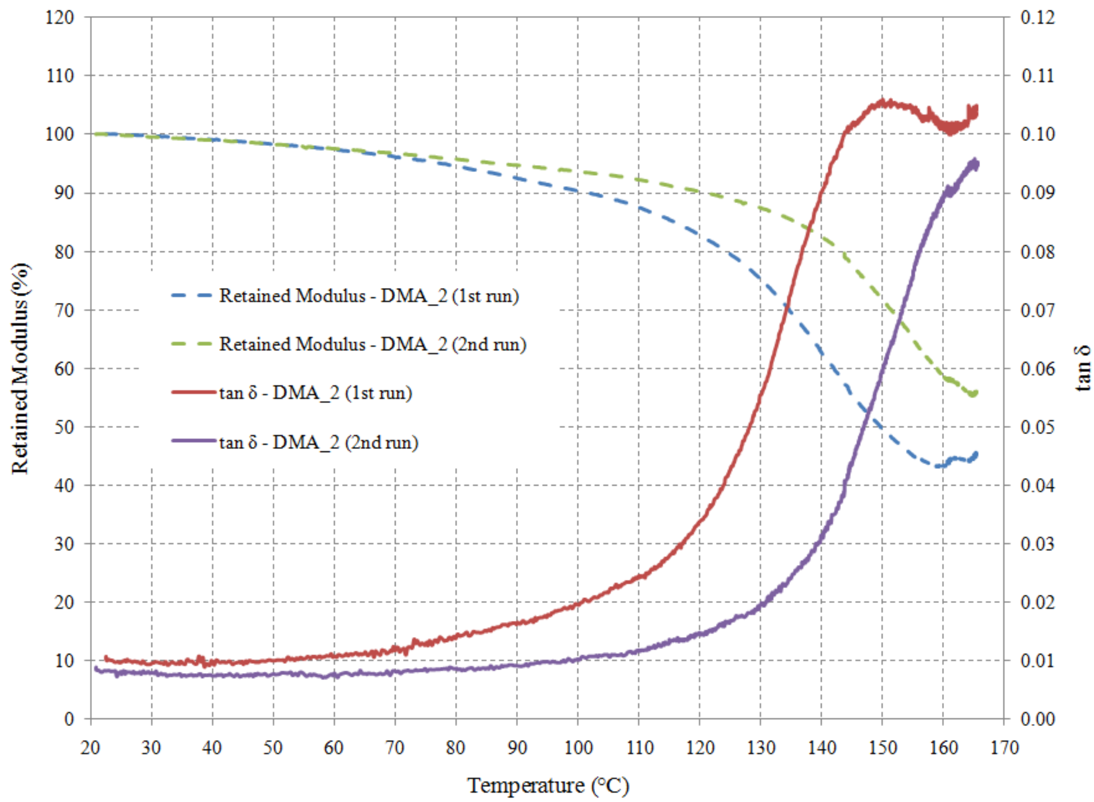

Figure 4.82: DMA_2 test results over temperature

The first time the sample was tested, the T_g was calculated at 150°C, according to the tan δ peak criteria. At this temperature, the epoxy retained a 49% of its room temperature elastic modulus.

For the second time the sample was tested, the tan δ peak did not occurred for the maximum temperature (165°C) reached by the heating ramp extracted from the CFRP pullout tests. Anyway, at 165°C the epoxy retained 55% of its room temperature elastic modulus.

This means that the sample experience an increase of 15°C between the first and the second test, due to curing of the sample´s epoxy during the first test.

4.3.3 DMA_3

The heating ramp, showed in Figure 4.78, was determinate at 3.0 °C/min. The results from this test are displayed from the retained elastic modulus over time (see Figure 4.83) and over temperature (see Figure 4.84).

The sample was tested twice in order to check variations in the glass transition temperature, which would mean that the CFRP's epoxy cured during the first test.

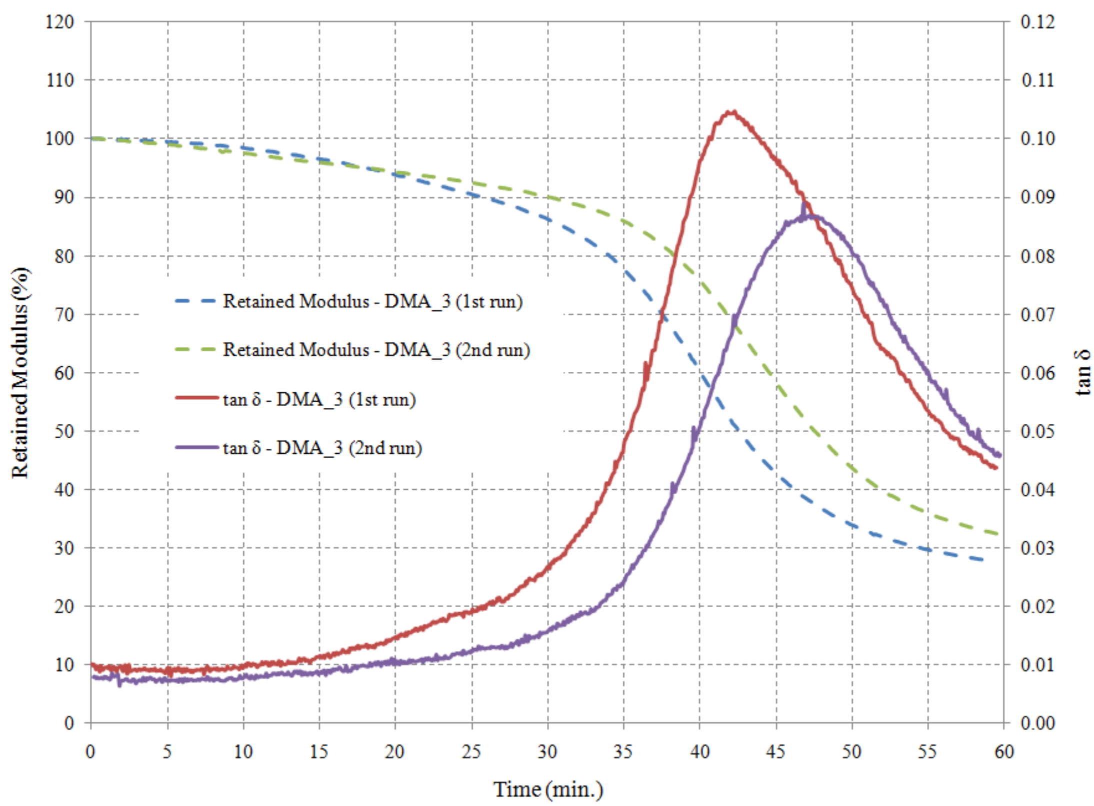

Figure 4.83: DMA_3 test results over time

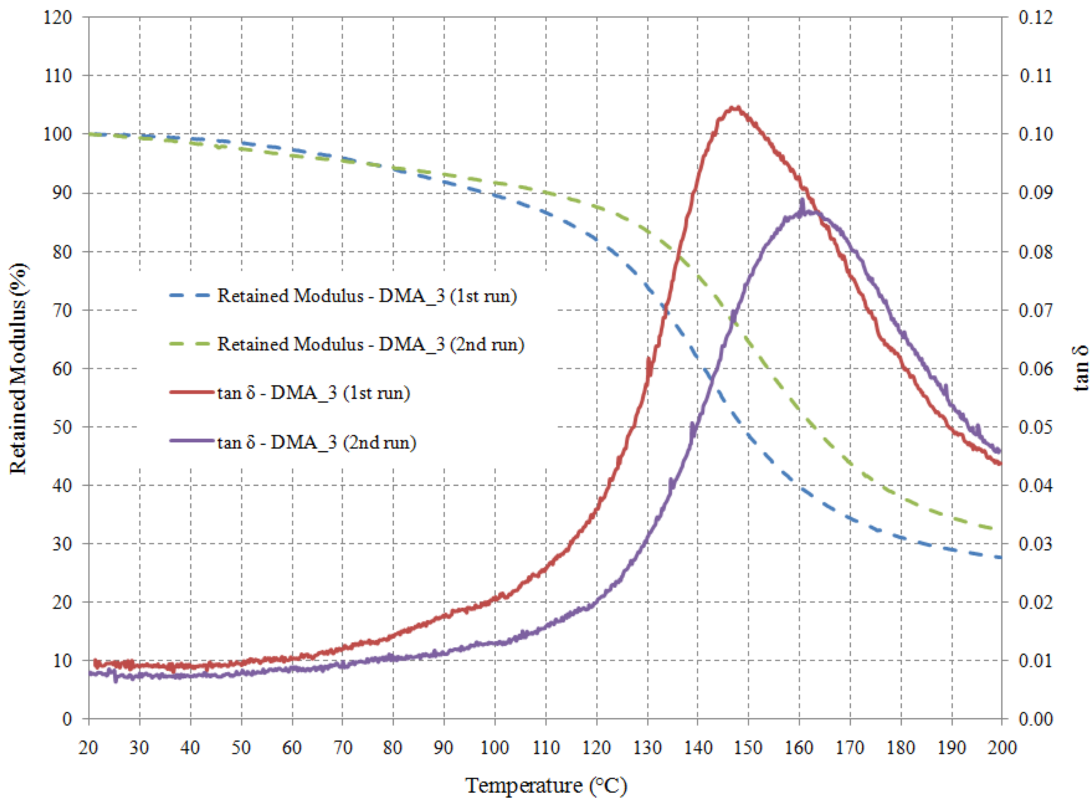

Figure 4.84: DMA_3 test results over temperature

The first time the sample was tested, the T_g was calculated at 148°C, according to the tan δ peak criteria. At this temperature, the epoxy retained a 51% of its room temperature elastic modulus.

For the second time the sample was tested, the T_g was calculated at 161°C, at which the sample's epoxy retained 52% of its room temperature elastic modulus.

This means that the sample experience an increase of 13°C between the first and the second test, due to curing of the sample´s epoxy during the first test.

4.3.4 DMA_4

The heating ramp, showed in Figure 4.78, was determinate at 3.0 °C/min. The results from this test are displayed from the retained elastic modulus over time (see Figure 4.83) and over temperature (see Figure 4.84).

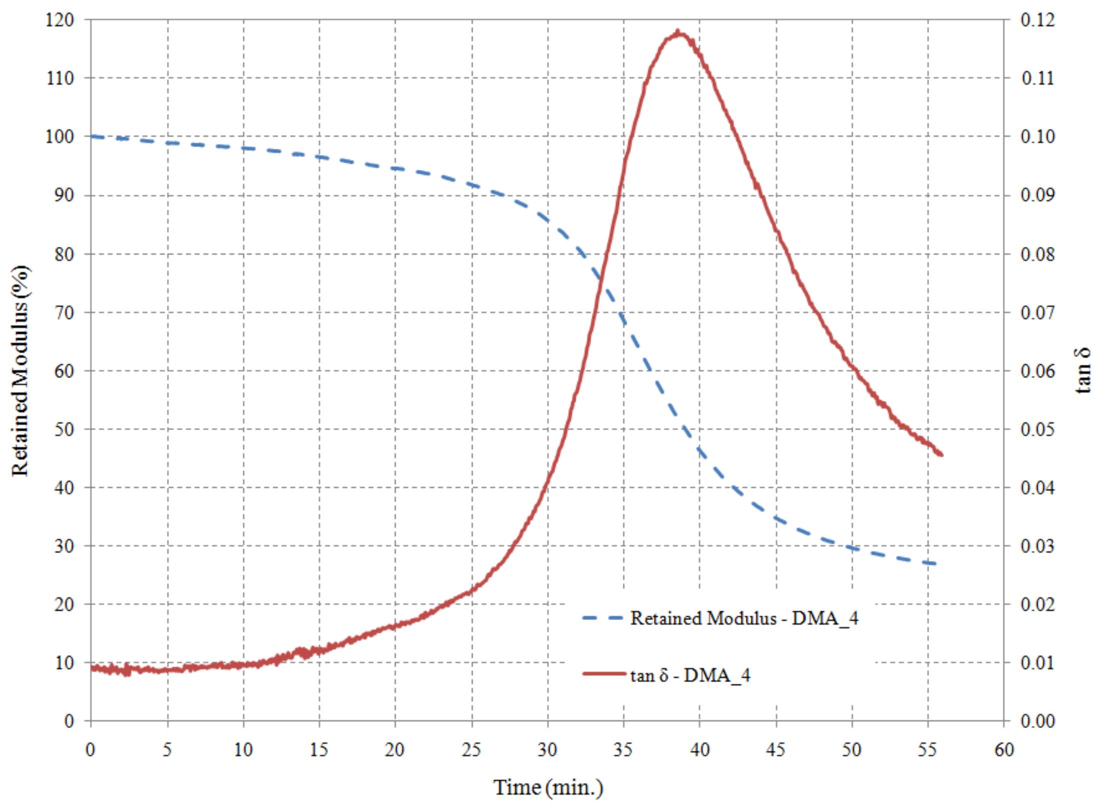

Figure 4.85: DMA_4 test results over time

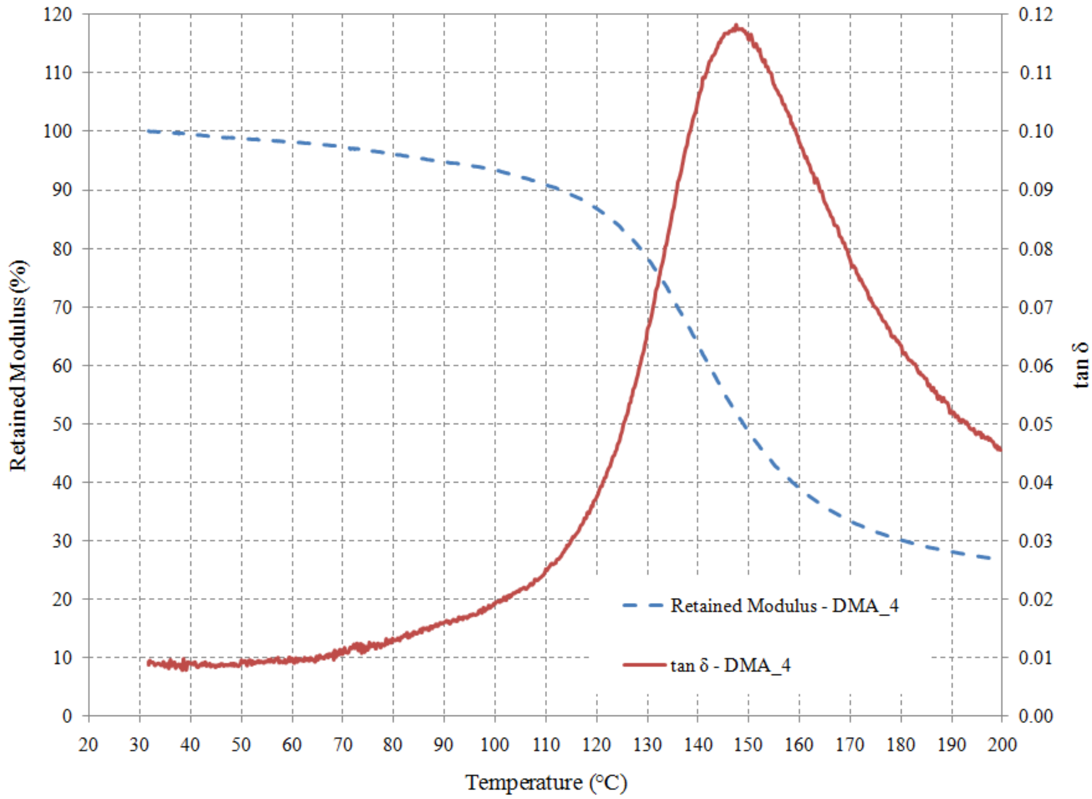

Figure 4.86: DMA_4 test results over temperature

The first time the sample was tested, the T_g was calculated at 147°C, according to the tan δ peak criteria. At this temperature, the epoxy retained a 52% of its room temperature elastic modulus.

4.3.5 DMA_5

The heating ramp, showed in Figure 4.78, was determinate at 3.0 °C/min. The results from this test are displayed from the retained elastic modulus over time (see Figure 4.87) and over temperature (see Figure 4.88).

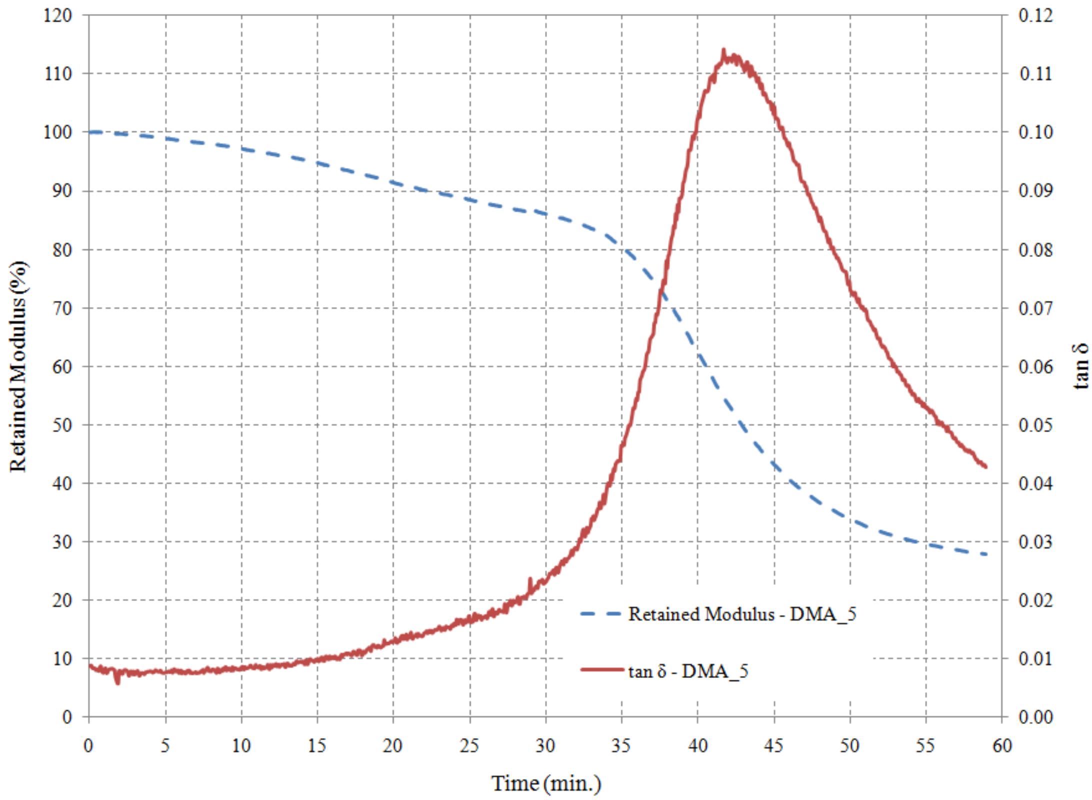

Figure 4.87: DMA_5 test results over time

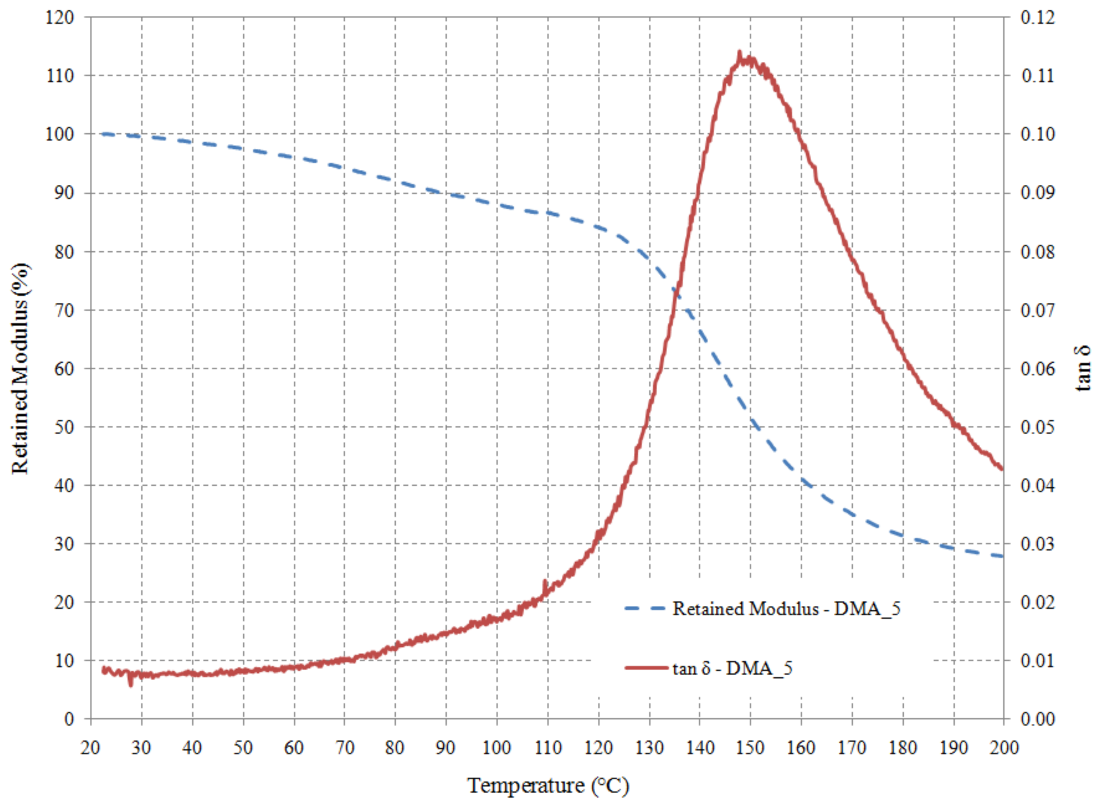

Figure 4.88: DMA_5 test results over temperature

The first time the sample was tested, the T_g was calculated at 148°C, according to the tan δ peak criteria. At this temperature, the epoxy retained a 55% of its room temperature elastic modulus.

4.3.6 Summary

From the five DMA tests an average T_g of 149°C was calculated, according to the tan δ peak criteria. The heating ramp didn't had considerable effect in the T_g determination.

In DMA_1, DMA_2 and DMA_3 the CFRP sample was tested twice. In DMA_1 and DMA_2, the heating ramp maximum temperature was 165°C, which wasn't enough to reach the T_g of the epoxy, the second time the sample was tested. In DMA_3 the T_g occurred both times the sample was tested, showing an increase of 13°C was measured between the first and the second test, due to curing of the epoxy in the first test.

Table 4.5: DMA test results

<table>
<tr><th rowspan="2">Test</th><th rowspan="2">Heating Ramp (°C/min)</th><th colspan="2">T_g</th><th rowspan="2">Tg increase between the 1st and 2nd run (°C)</th></tr>
<tr><th>Temperature</th><th>Retained Modulus</th></tr>
<tr><td>DMA_1 (1st run)</td><td rowspan="4">Extracted from the pullout tests average</td><td>152</td><td>47%</td><td rowspan="2">13 *</td></tr>
<tr><td>DMA_1 (2nd run)</td><td>165 *</td><td>54% *</td></tr>
<tr><td>DMA_2 (1st run)</td><td>150</td><td>49%</td><td rowspan="2">15 *</td></tr>
<tr><td>DMA_2 (2nd run)</td><td>165 *</td><td>55% *</td></tr>
<tr><td>DMA_3 (1st run)</td><td rowspan="4">3 °C/min</td><td>148</td><td>51%</td><td rowspan="2">13</td></tr>
<tr><td>DMA_3 (2nd run)</td><td>161</td><td>52%</td></tr>
<tr><td>DMA_4</td><td>147</td><td>52%</td><td></td></tr>
<tr><td>DMA_5</td><td>148</td><td>55%</td><td></td></tr>
</table>

* tan δ peak did not occurred for this test's maximum temperature (165°C), being this value, the maximum temperature reached.

DMA test showed very good repeatability within tests executed with the same heating ramp (see Figure 4.89 and Figure 4.90).

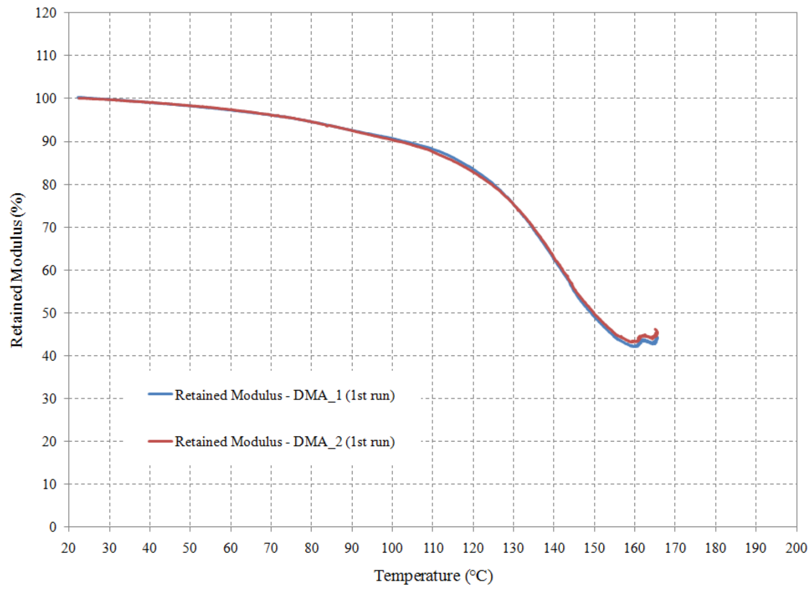

Figure 4.89: Results comparison in DMA tests with heating ramps extracted for the CFRP pullout tests

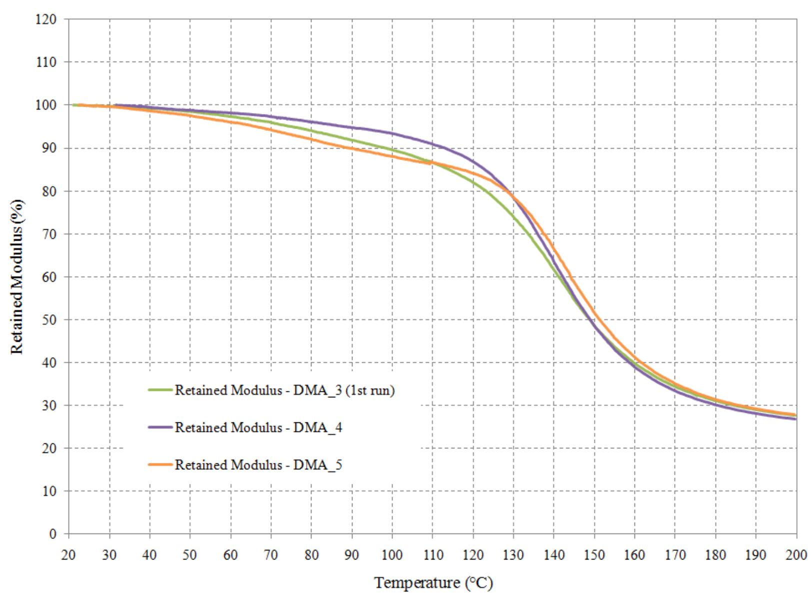

Figure 4.90: Results comparison in DMA tests with 3 °C/min heating ramps

4.3.7 Effect of the heating ramp in the DMA results

For the DMA tests, two heating ramps were executed. For tests DMA_1 and DMA_2 a heating ramp was extracted from the measured temperature in the CFRP pullout tests, as explained in Section 3.4.3. For tests DMA_3, DMA_4 and DMA_5 a constant heating ramp of 3 °C/min was executed. Both ramps are displayed in Figure 4.78.

From Figure 4.91, both samples have the same behaviour up until the 155°C. This occurs because at this temperature the heating rate of DMA_1 test is very close to zero as it approaches the maximum temperature of 165°C in a period of 190 minutes. Opposite to what happens with DMA_3 test which has a constant heating ramp of 3 °C/min. Apparently the heating rate at which the sample is tested has an effect in the retained elastic modulus of the epoxy.

This analysis was performed to know the retained elastic modulus of the samples at for the extended PHPOT, which had the same heating ramp as DMA_1 and DMA_2 tests.

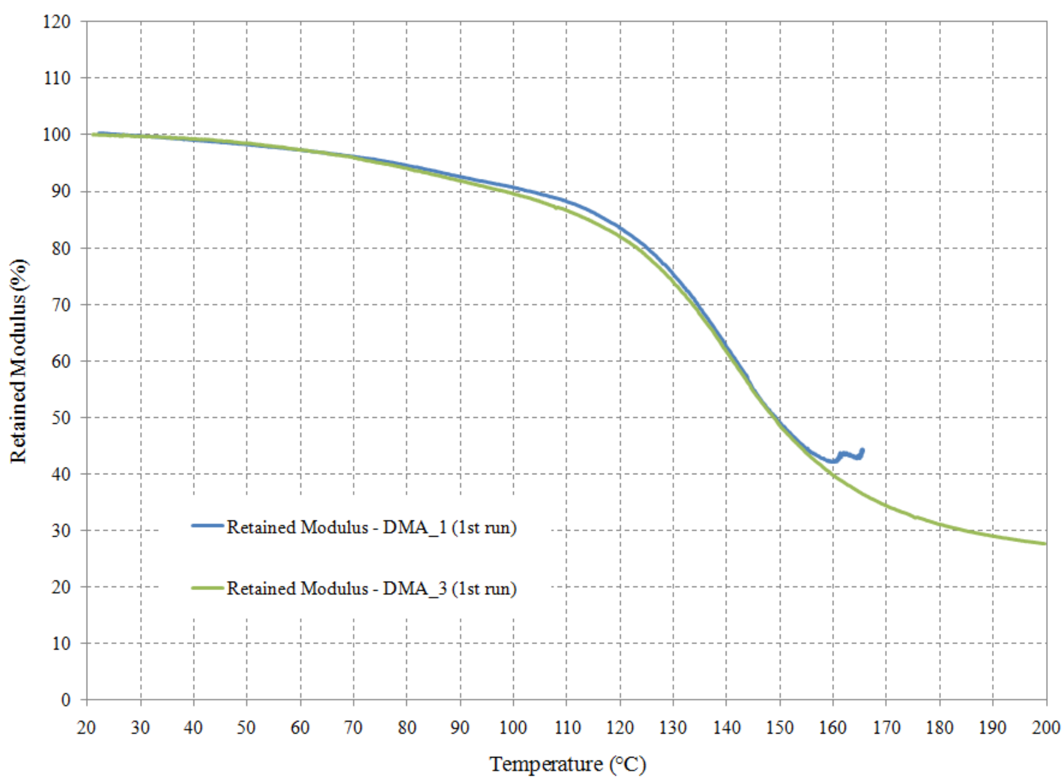

Figure 4.91: Results comparison in DMA tests with different heating ramps

4.4 EMPA Large Scale Fire Tests

Large scale fire tests executed at the EMPA laboratories evidenced that the fire resistance of the slabs varied between 24min and 91min, with the thicker slabs generally achieving higher fire endurances (see Table 4.6). The notable exception was the steel prestressed slab, which suffered severe spalling early in the test (likely due to its very young age at the time of testing).

Table 4.6: Fire test programme and selected results (Reefer to Figure 3.58)

No.	Age (mths)	Tendon type	Prestress (MPa)	Cover *c* (mm)	Thickness *t* (mm)	Overhang (mm)	Failure time	Failure mode
4	9.3	CFRP	1200	19.8	45	160	26'12"	spalling → crushing
7	8.8	CFRP	1200	20.3	46	280	34'36"	spalling → crushing
8	8.4	CFRP	1200	28.3	62	280	24'12"	spalling → crushing
5	8.4	CFRP	1200	27.8	61	160	47'00"	spalling → crushing
9	9.3	CFRP	1200	34.8	75	280	1h00'24"	spalling → crushing
6	9.3	CFRP	1200	34.8	75	160	1h31'36"	spalling → crushing
40	1.0	Steel	1200	34.8	75	160	29'00"	spalling → crushing

Despite including PP fibers in the mix, the dominant failure mode was sudden collapse due to accumulated HSPCC spalling, which reduced the slabs' cross-sections until they failed in bending due to crushing of the remaining concrete under the service load. Spalling was first localized in the shear and bending span (i.e. near the supports where the bending moment is low and the exposed face of the slab is most precompressed). It is widely known that concrete's propensity for spalling is increased by compressive stress, so the location of first spalling is unsurprising.

Longitudinal splitting cracks were observed on the exposed and unexposed surface prior to failure for both 45 mm thick slabs and, to a smaller extent, for the 60 mm slabs. These were possibly caused by thermal incompatibility between the CFRP tendons and the

HPSCC. Most 75 mm slabs displayed single longitudinal cracks. Significantly, tendon slip versus time measurements showed no evidence of slip increases during the tests, indicating that the anchorage length of 160 mm was sufficient to prevent bond failure. Tendon temperatures recorded in the fire exposed spans during these tests indicated that the tensile strength of the CFRP was maintained at temperatures above 330°C. Nevertheless, it appears that a fire resistance of 30min is achievable for these slabs when a concrete cover of 35 mm or more is used and a 160 mm cold anchorage is provided.

5 DISCUSSION

5.1 Bond Failure at High Temperature

5.1.1 Effect of sustained load level for CFRP regular PHPOT

For CFRP regular PHPOTs the experimental data was shown by plotting slip on the horizontal axis and temperature on the vertical axis, as shown in Sections 4.1.6, 4.1.7 and 4.1.8. By plotting the experimental data from the three regular PHPOTs, it could be concluded that as the sustained load increased from test to test, failure occurred at a lower temperature. Experimental results presented in Figure 5.1 identified failure as a sudden increase of slip at a certain temperature. The practical consequences of this behaviour for the response of CFRP prestressed concrete members in real buildings are that ultimate failure may occur, caused by excessive cracking at the tension face of the member, which wont longer be reinforced, leading to a sudden collapse of the member.

The non correlative magnitude of the total slip and sustained bond stress was attributed to the variability in bond stiffness of pullout at ambient temperature, shown later in Figure 5.17 of Section 5.3, since initial pullout of PHPOTs was done at ambient temperature.

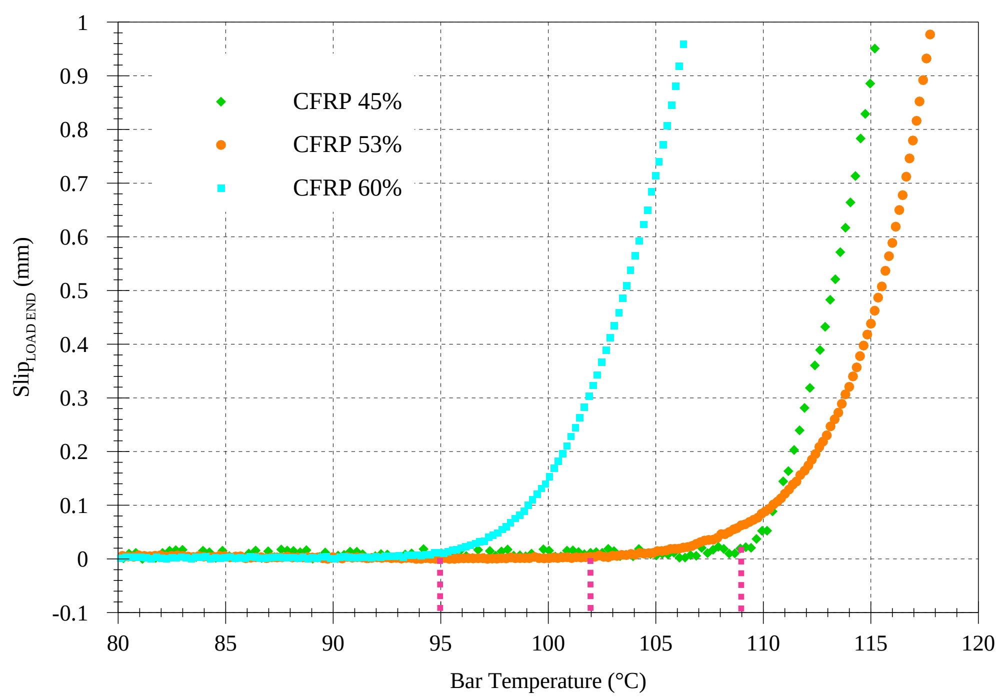

Figure 5.1: Bar temperature versus loaded end slip for regular PHPOTs

5.1.2 Epoxy's retained elastic modulus and sustained bond stress correlation

One of the objectives of this study was to determine a correlation between the CFRP tendon's prestress load and the epoxy's retained elastic modulus at the moment of failure. Table 5.1 shows the epoxy's residual elastic modulus, determined from the DMA results in Section 4.2, for the temperature of the CFRP tendon on PHPOTs at the moment of failure, and also for CFRP_68% which failed before the tendon's temperature increased. Extended PHPOT failure did not occur as the temperature of the CFRP tendon increased, and after almost four hours of steady state temperature, the sample was loaded until failure occurred (second loading phase). Table 5.2 shows the epoxy's residual elastic modulus for the RPOTs which were executed at ambient temperature.

In Figure 5.3, Figure 5.4 and Figure 5.5 the experimental data for regular PHPOTs is shown as presented in Sections 4.1.6, 4.1.7 and 4.1.8, with the inclusion of the epoxy's residual elastic modulus (determined from the DMA showed in Section 4.3), in order to demonstrate how the bond strength failure is influenced by degradation of the epoxy's residual elastic modulus.

Table 5.1: Results for extended and regular PHPOTs done on CFRP pullout samples

	Test	Prestress Conditions			Failure Conditions		Bond residual strength (MPa)
		Bond Stress (MPa)	Tensile Stress (MPa)	Pullout Load (kN)	Tendon's Temperature (°C)	Epoxy's Residual Modulus (%)	
Extended PHPOT	CFRP_15%	0.74	87.33	2.00	166	44.68 *	2.26 **
	CFRP_30%	1.47	174.66	4.00	166	44.68 *	2.21 **
	CFRP_38%	1.84	218.32	5.00	164	43.49 *	2.29 **
Regular PHPOT	CFRP_45%	2.21	261.98	6.00	109	88.23	0.65
	CFRP_53%	2.58	305.65	7.00	102	90.06	0.89
	CFRP_60%	2.95	349.31	8.00	95	91.50	0.92
	CFRP_68% ***	3.32	392.98	9.00	21	100.00	-

* Value for which bond did not failed with the applied prestress conditions.

** Value measured after failure occurred by applying the second loading phase.

*** Test in which bond failure occurred before temperature of the tendon increased.

Table 5.2: Results for RPOTs done on CFRP pullout samples

	Test	Failure Conditions			Failure Conditions		Bond residual strength (MPa)
		Bond Stress (MPa)	Tensile Stress (MPa)	Pullout Load (kN)	Tendon's Temperature (°C)	Epoxy's Residual Modulus (%)	
RPOT	CFRP_AT_e1	5.34	632.52	14.49	21	100.00	4.09
	CFRP_AT_e2	4.42	524.08	12.00	20	100.00	2.90

By elaborating a graph which plots residual elastic modulus of the epoxy, at the moment of failure, versus sustained bond stress (regular PHPOTs) or failure bond stress (RPOT and extended PHPOTs), it is evident that as the sustained load increased from test to test, less degradation of the epoxy's elastic modulus (larger residual elastic modulus) was needed for bond failure to occur. For extended PHPOT, the epoxy's degradation did not generate bond failure for the prestress conditions. The practical consequences of this behaviour for the response of CFRP prestressed concrete members in real buildings are that a critical prestressing level can be determined for bond failure not to occur under severe fire conditions.

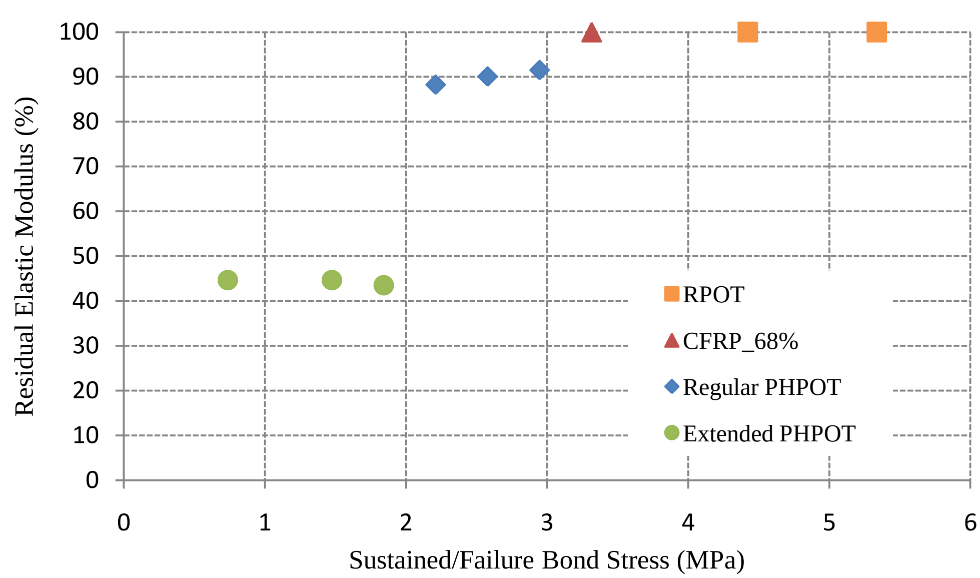

Figure 5.2: Experimental data correlation between CFRP tendon's prestress load and epoxy's retained elastic modulus (determined from DMA)

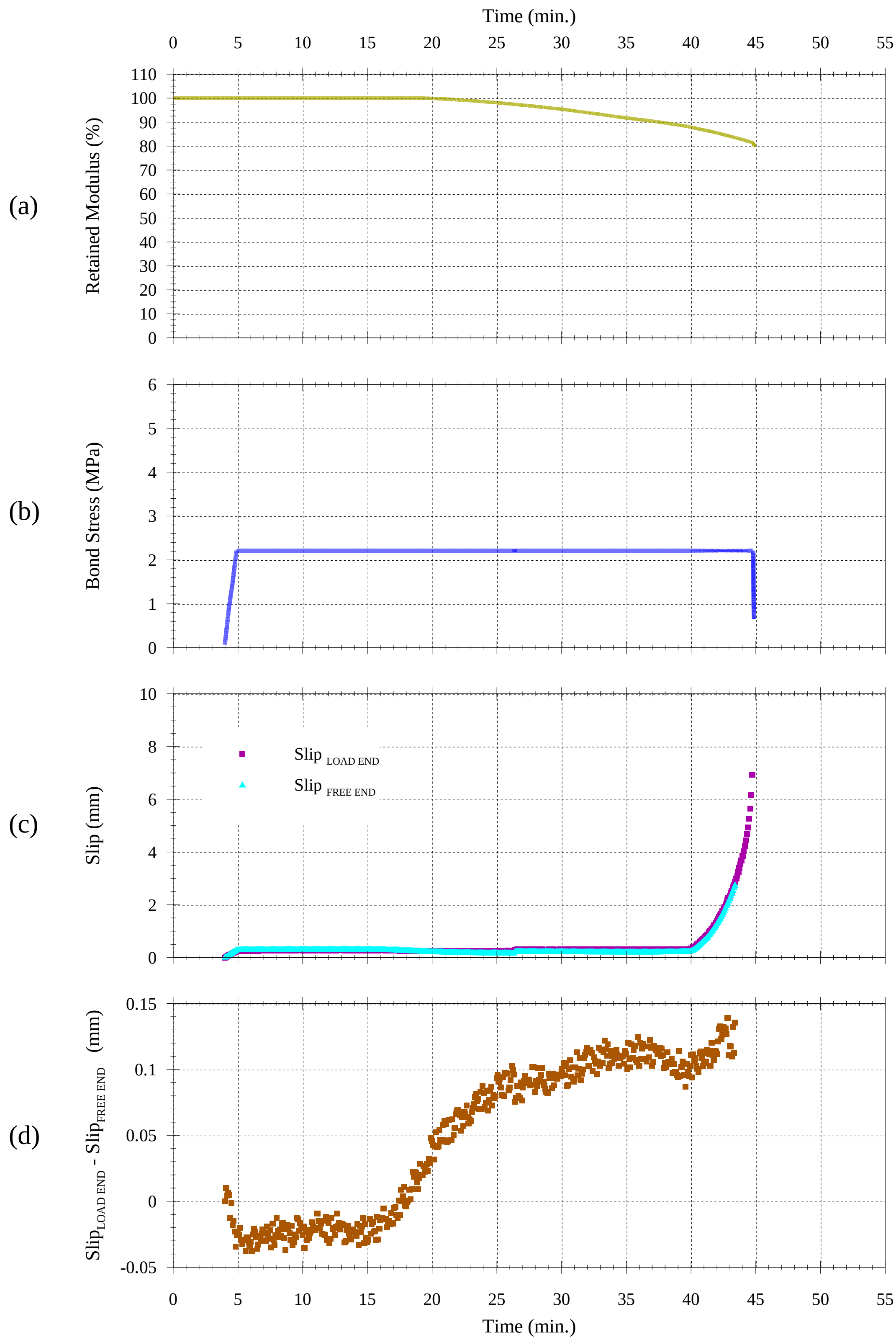

Figure 5.3: Experimental data for CFRP_45% and epoxy's residual elastic modulus (DMA test)

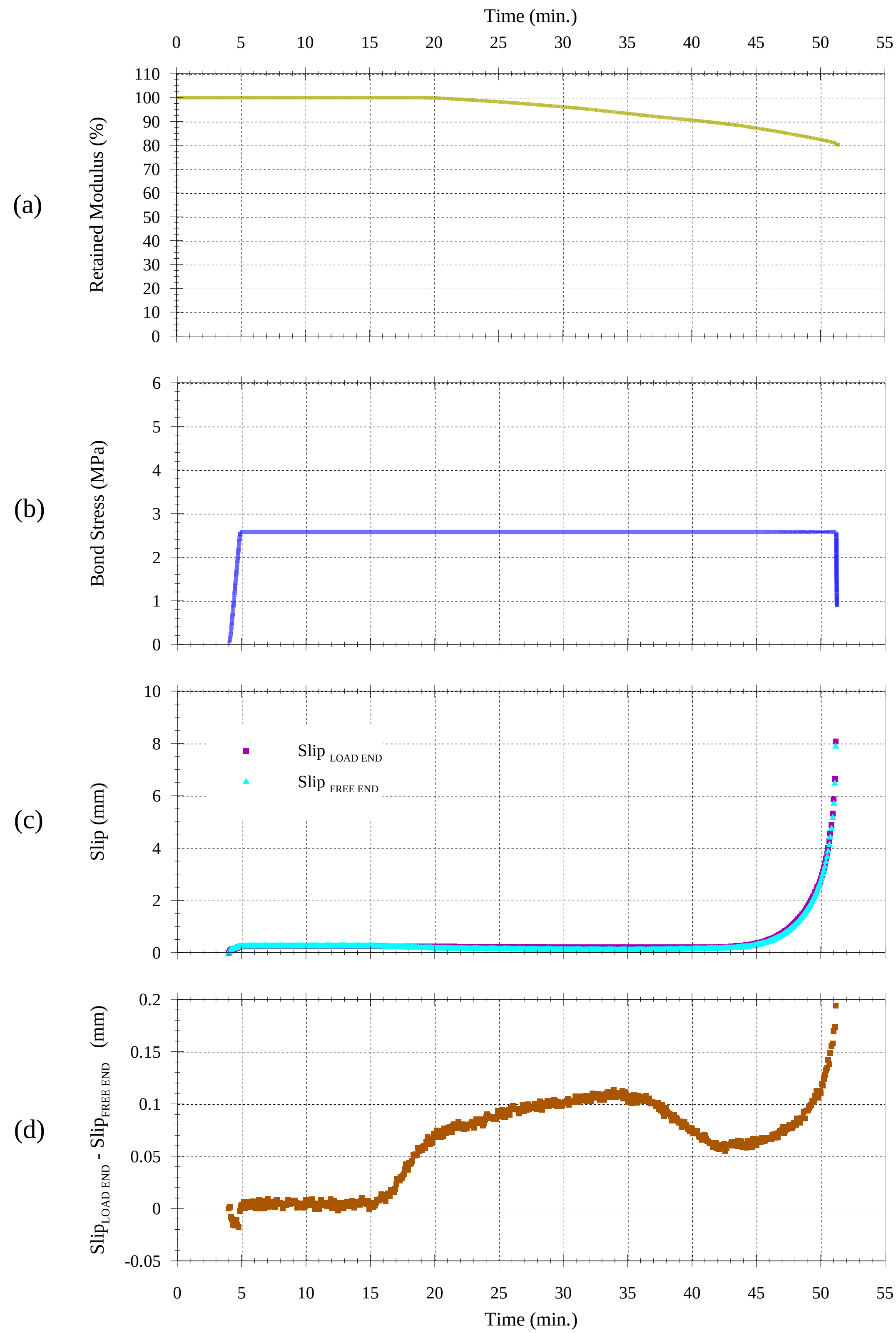

Figure 5.4: Experimental data for CFRP_53% and epoxy's residual elastic modulus (DMA test)

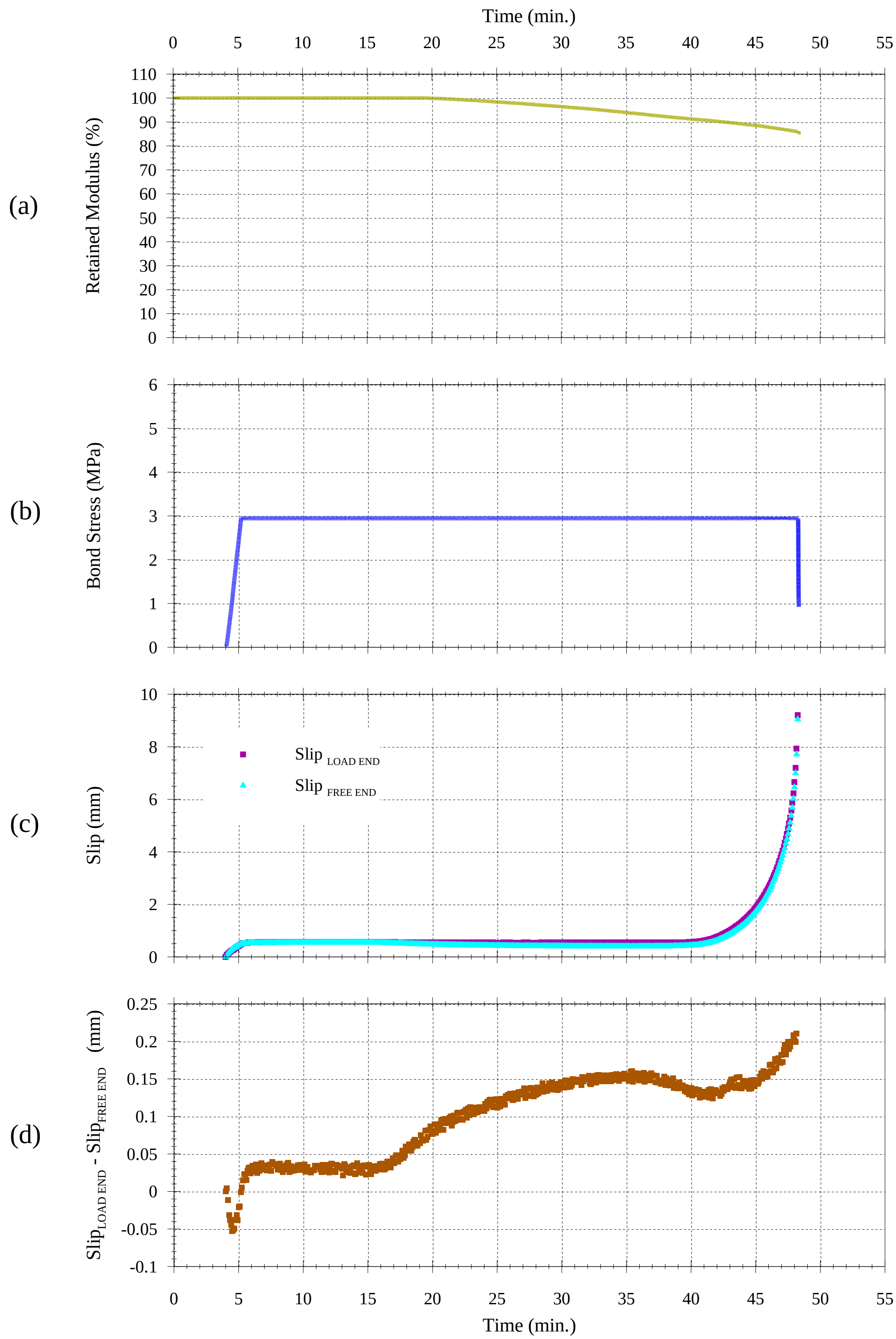

Figure 5.5: Experimental data for CFRP_60% and epoxy's residual elastic modulus (DMA test)

5.1.2.1 Model of the prestress level effect on the epoxy's degradation at the moment of bond failure

The proposed model that describes the correlation between CFRP tendon's prestress load and epoxy's retained elastic modulus at failure of regular PHPOT is a semi-empirical one. The general form of the equation is determined in order to follow the trends presented in Figure 5.7. However, almost all the constants in the model represent actual material properties. An equation of the form $y = \tanh(x)$ was chosen to describe the correlation between CFRP tendon's prestress load and epoxy's retained elastic modulus at failure of regular PHPOT. To take onto account the physical properties of the phenomenon, a modified equation is described in Equation (5.1) and presented in Figure 5.6.

$$y = \mathrm{a} \cdot \tanh[b \cdot (x - c)] + d \qquad (5.1)$$

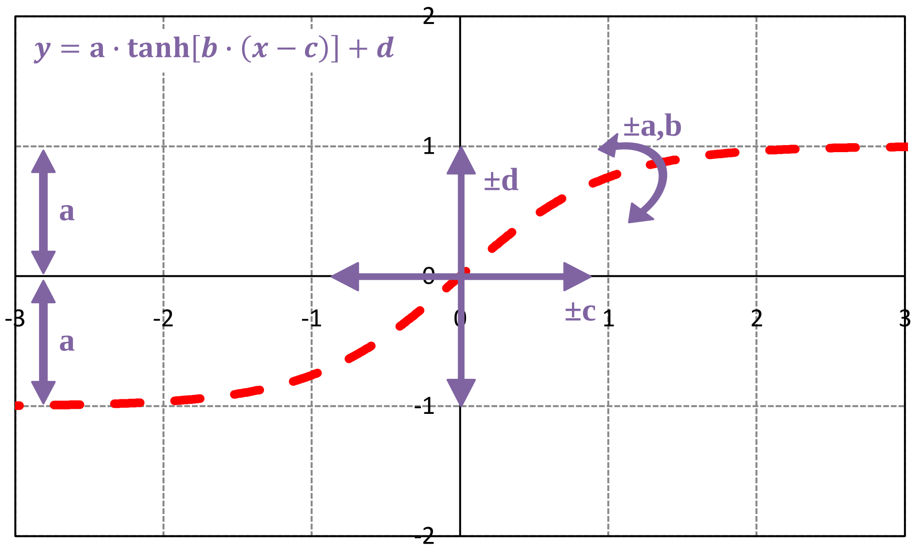

Figure 5.6: Schematic presentation of the $y = \tanh(x)$ proposed model

For this proposed model, the y-axis represents the epoxy's residual elastic modulus and x-axis represents the sustained bond stress at the moment of failure (failure bond stress in RPOTs and extended PHPOTs). a and b govern the vertical location of the curve on the y-axis. According to the definition presented in Figure 5.6, the value of a is given by:

$$a = 0.5 \qquad (5.2)$$

Assuming that at room temperature tests (RPOTs) the epoxy retains all its elastic modulus and the bond stress failure is bond strength at room temperature. For large values of x, Equation (5.1) gets the value $(a + d)$.

$$a + d = 1 \tag{5.3}$$

Introducing Equation (5.2) in Equation (5.3) provides the following value for d:

$$d = 0.5 \tag{5.4}$$

c and d govern the location on the horizontal axis where the transition from the upper to the lower asymptote takes place. The value of c is determined from two limit bond stresses. The maximum bond stress for which failure did not occurred as temperature increased (CFRP_38%) and the minimum bond stress for which failure did occurred as temperature increased (CFRP_45%). The average of these two values is:

$$c = (1.84 + 2.21)/2 = 2.03\ [MPa] \tag{5.5}$$

The coefficient b is the only parameter that could not be directly related to a physical property of the modelled phenomenon. Instead, it was determined experimentally by best fit of the test results, by using the least square method.

$$b = 1.8 \tag{5.6}$$

Introducing all the values for a, b, c and d into Equation (5.1) yields the overall expression for the epoxy's residual elastic modulus, E_r (see Equation (5.7)) for failure in the bond interface at a sustained bond stress, σ_{bond}.

$$E_r = 0.5 \cdot \tanh[2.1 \cdot (\sigma_{bond} - 2.03)] + 0.5 \tag{5.7}$$

This model must be considered only as a rough approximation of the epoxy's residual elastic modulus and sustained stress correlation. The sustained load for the extended PHPOTs (see Figure 5.7) was not enough for the bond interface to fail at the residual elastic modulus (high temperature) accomplished by the experimental setup.

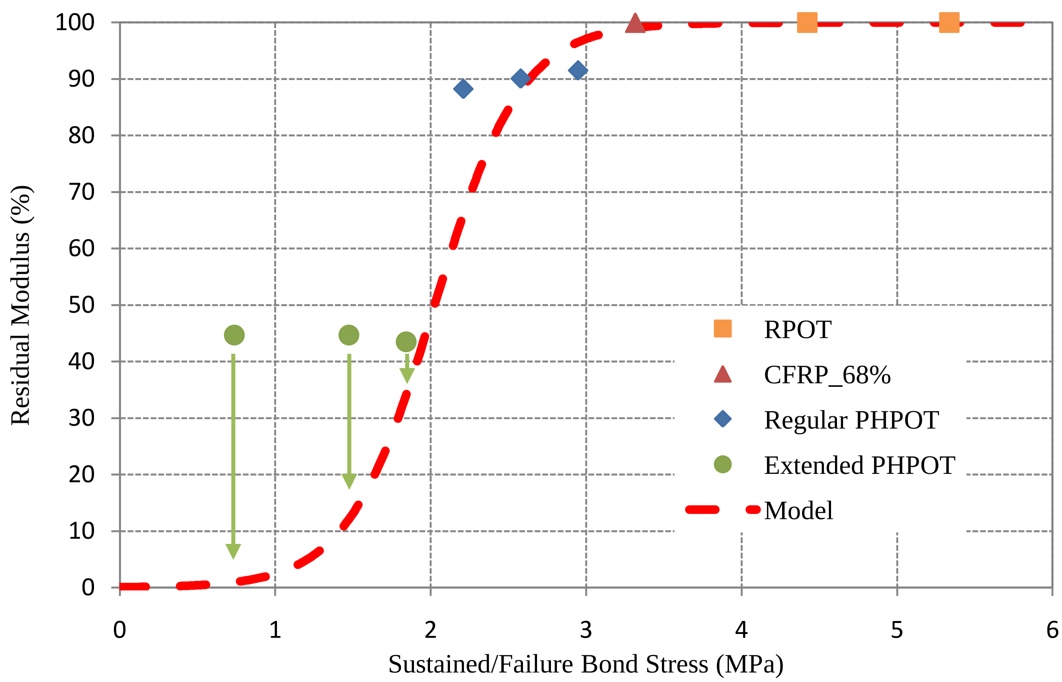

Figure 5.7: Model correlation between CFRP tendon's prestress load and epoxy's retained elastic modulus (determined from DMA)

More work needs to be done, executing a wider range of regular PHPOTs for the lower sustained bond stress values. For this, higher temperature should be accomplished in the pullout tests, in order to obtain a higher degradation of the epoxy's elastic modulus. In conclusion, a correlation between the bond strength, the temperature of the CFRP tendon and the residual elastic modulus of the epoxy was found to be in accordance with the model described above.

5.2 Residual Bond Strength

In tests where failure occurred with the loading frame working under a displacement-control mode (RPOTs with CFRP tendon and extended PHPOT with both types of prestressing bar) an apparent residual bond strength was measured after failure, as pullout continued at a constant crosshead displacement rate, with the free end of the bar slipping into the already failed bonded length.

In tests where failure occurred with the loading frame working under load-control mode, residual bond strength was the result of an abrupt slip of the bar executed by the Intron's attempt in keeping the sustained load at the predefined level.

5.2.1 Effect of the bar type for extended PHPOT

For CFRP pullout tests, the residual strength is attributed to the friction between the tendon and its sand coating, while for steel pullout tests it is attributed to the wire's ribs slipping along the already failed bonded length and crushing the steel-concrete interface as the wire slips, a phenomenon previously analysed and discussed in Section 4.1.12.1. As mentioned in Section 3.2.1.1, both types of bars were treated so that the last 40 mm from the bottom and at the first 50 mm from the top had no adhesion, friction, or mechanical interlocking with the surrounding concrete (see Figure 3.10).

For the CFRP pullout tests, the sand coating was removed from the length of the bar which protruded (approximately 20 mm) from the bottom of the cylinder (free end), so it could be assumed that the free end at the bottom of the cylinder was not generating any friction or mechanical interlocking with concrete, as the tendon slipped into the cylinder after bond failure occurred.

For the steel pullout tests, the length of the bar which protruded (see Figure 5.8) from the bottom of the cylinder did not received any such smoothing treatment, which meant that after bond failure occurred the steel prestressing wire's ribs continued to generate friction and mechanical interlocking with concrete as the wire slipped into the already failed concrete cylinder.

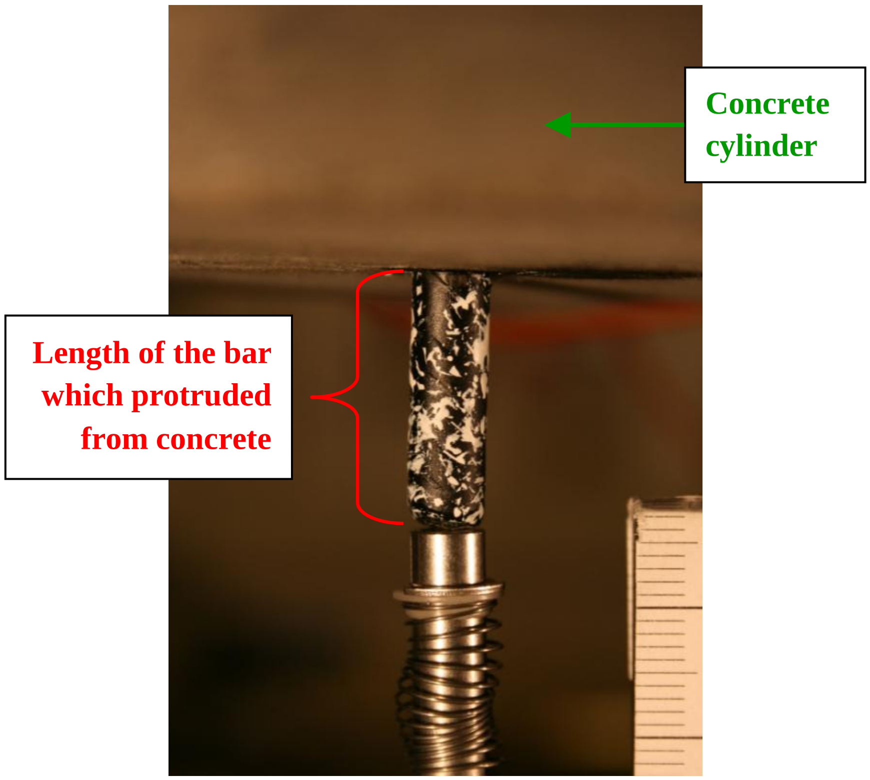

Figure 5.8: Free end's photo of a typical pullout sample

In extended PHPOTs the bond interface did not occur as the temperature of the tendon increased, the heating blanket was left on until the bar reached a steady state temperature of about 160°C (calculated as mentioned in Section 3.4.3) which was further increased at minute 151 to reach a steady state bond line temperature of about 165°C.

In extended PHPOTs, at minute 232 (with the exception of CFRP_15%, at minute 212), after not having any signs of failure, the loading frame was configured to pull out the bars until failure occurred, at a rate between 0.40 and 0.52 MPa/min as shown in Table 4.3. In this second loading phase, the system was configured under a displacement-control mode, allowing for the pullout to continue at a constant crosshead displacement rate after failure occurred, with the free end of the bar slipping into the already failed bonded length.

For the CFRP extended PHPOT (see Figure 5.9), the second loading phase achieved a maximum average bond stress between 3.89 and 5.07 MPa, after which every tested specimen experienced an immediate 12% to 19% drop of its average bond stress. The tendon then kept on slipping and the samples exhibited a residual bond strength which tended to a value between 2.21 and 2.29 MPa. It should be recalled that the second loading phase for CFRP_15% started at minute 212, while CFRP_30% and CFRP_38% started at minute 232.

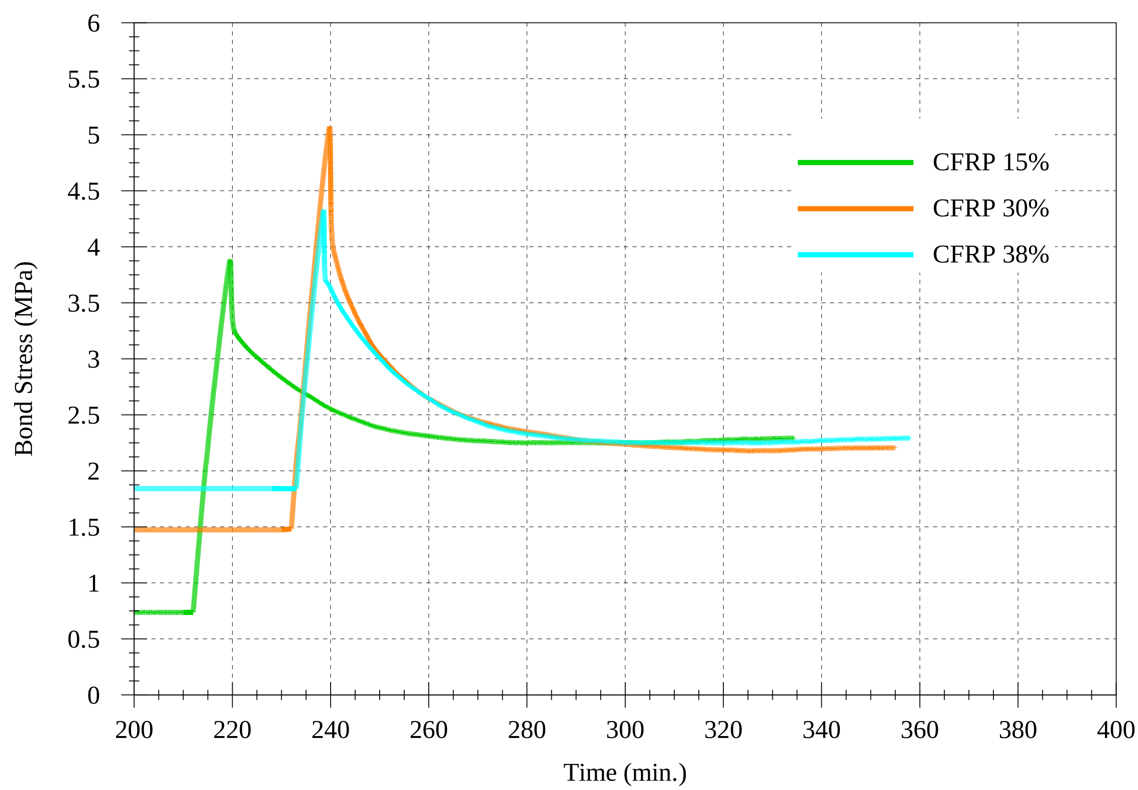

Figure 5.9: Failure curve for extended PHPOT with CFRP tendon

For the steel extended PHPOTs (see Figure 5.10), the second loading phase achieved a maximum average bond stress between 11.78 and 13.68 MPa, after which, every test experience a total drop of its bond strength capacity between 0 and 12 minutes after the maximum average bond stress was achieved. For the test in which it took 12 minutes for to totally loose bond strength capacity (Steel_37%_e2), the wire slipped 2.6 mm. The wire then kept on slipping and the bond stress versus time plot developed into an oscillating curve (see Figure 5.11), generated from the wire's ribs slipping along the already failed bonded length. Unlike the residual bond strength measured in the CFRP pullout tests, the phenomenon measured in the steel pullout tests cannot be considered as the residual bond strength capacity of the steel prestressing wire in reinforced concrete members in real buildings, because once the bond stress capacity drops to zero, excessive cracking at the concrete's tension face will occur, leading to a sudden collapse of the prestressed concrete member.

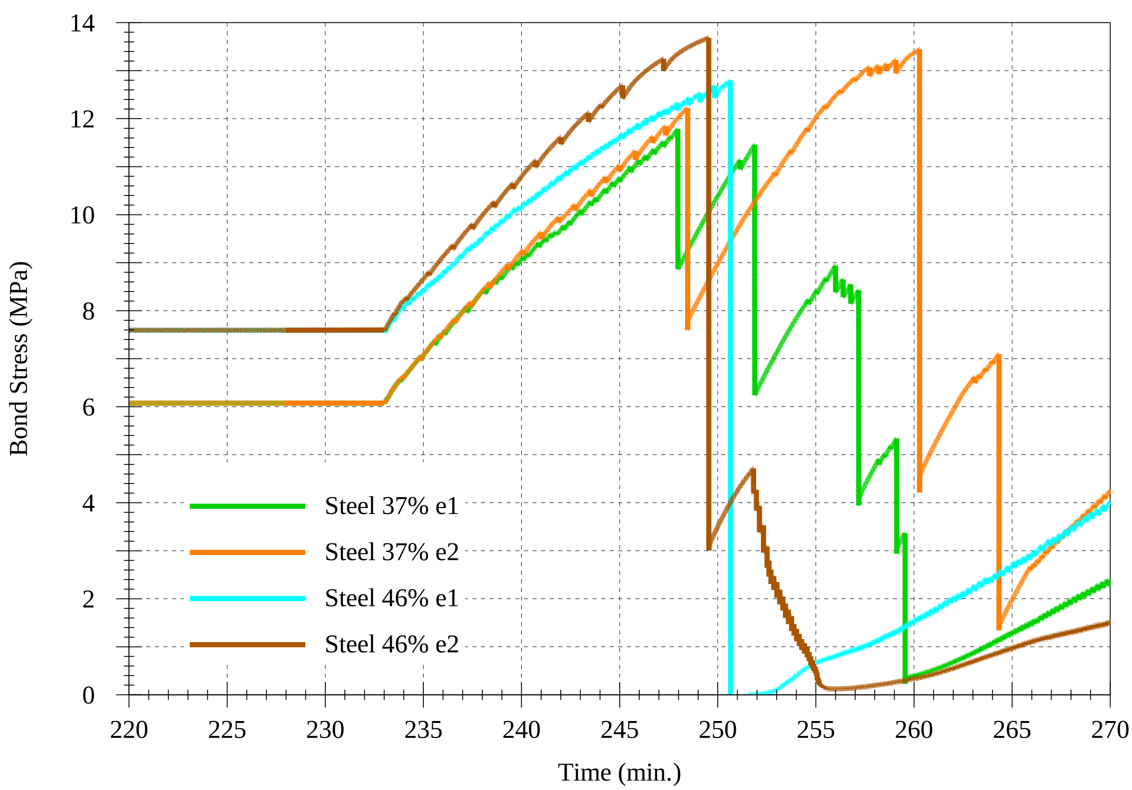

Figure 5.10: Failure curve for extended PHPOT with steel prestressing wire

No correlation between the sustained load and the final bond strength could be determined from the three CFRP and four steel extended PHPOTs. Figure 5.11 shows a comparison between the residual bond strength measured in CFRP and steel pullout tests.

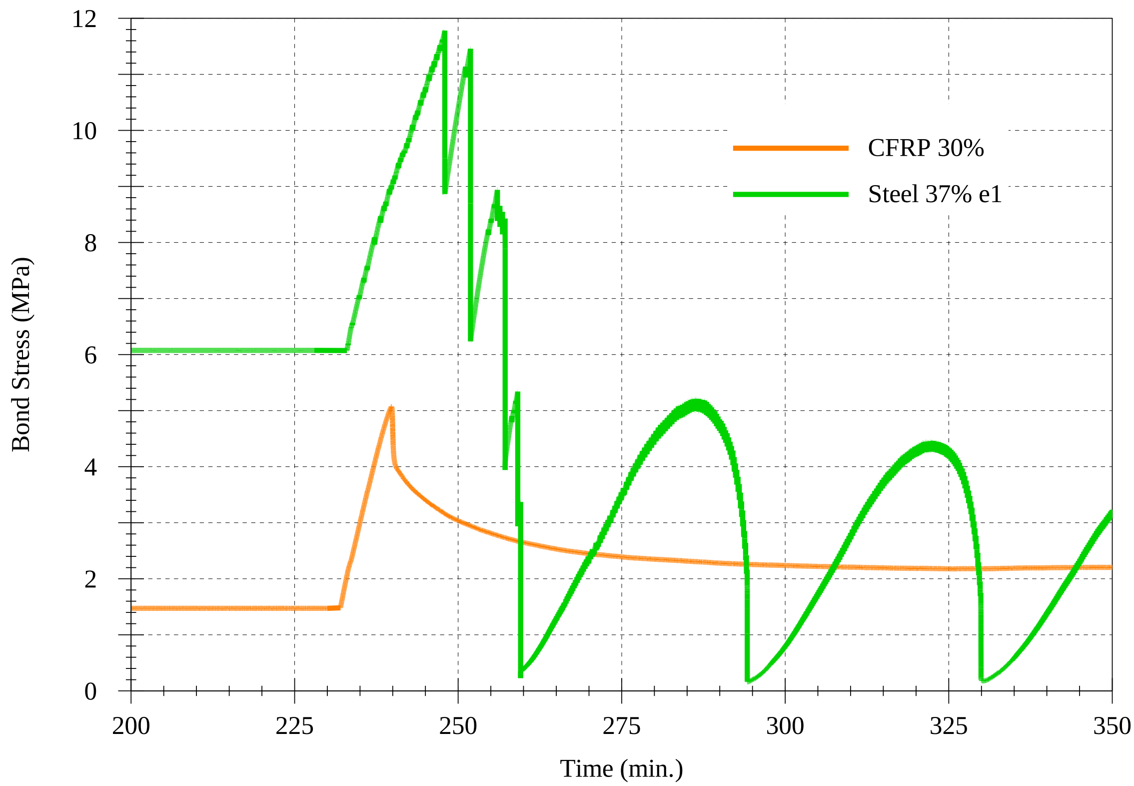

Figure 5.11: Apparent residual bond strength for extended PHPOT with CFRP tendon (CFRP_30%) and steel prestressing wire (Steel_37%)

The apparent residual bond strength measured for the steel pullout test was a phenomenon related to how the pullout test was setup. In a reinforced concrete member, once the bond strength of the reinforcing bars is lost, the tensile stresses in the load bearing element will generate the total failure of such element, as previously explained.

5.3 Analytical Model of Bond Stress-Slip Relationship in CFRP Pullout Tests

The B.E.P. model (Eligehausen, Papov & Bertero, 1983) elaborated to represent the bond phenomenon of deformed steel reinforcing bars to concrete was extended, in this study, to be used with CFRP reinforcement. It has been already successfully applied to FRP tendons and strips by others (Faoro, 1992; Rossetti, Galeota & Giammatteo, 1995; Cosenza, Manfredi & Realfonzo, 1995; De Lorenzis, Rizzo & La Tegola, 2002; Sena Cruz & Barros, 2004). The local bond stress-slip relationship ($\tau - s$ curve) is composed by the following two equations, which define an ascending branch ($s \leq s_m$) and a descending branch ($s \leq s_m$).

$$\tau(s) = \begin{cases} \tau_m \times \left(\frac{s}{s_m}\right)^{\alpha} & if \;\; s \leq s_m \\ \\ \tau_m \times \left(\frac{s}{s_m}\right)^{\alpha'} & if \;\; s > s_m \end{cases} \tag{5.8}$$

Where τ_m and s_m are the bond strength and its corresponding slip, at the loaded end. α and α' are parameters obtained experimentally which define the shape of the curves. This relationship was selected because of its simplicity and ability to simulate the phenomena under discussion.

The corrector coefficients β and β' were included in the analytical model to take into account the influence of high temperature in the stress-slip relationship for PHPOT. The modified B.E.P. model is as follows:

$$\tau(s) = \begin{cases} \tau_m \times \left(\frac{s}{s_m}\right)^{\alpha} \times \beta & if \;\; s \leq s_m \\ \\ \tau_m \times \left(\frac{s}{s_m}\right)^{\alpha'} \times \beta' & if \;\; s > s_m \end{cases} \tag{5.9}$$

Using the experimental results from the CFRP pullout tests, the purpose was to obtain the parameters α, α', β and β' which fit the experimental data as best as possible by evaluating the experimental and analytical data fitting by the least square method. The values of the parameters and the error obtained in each analysis are included in Table 5.3.

The analytical modelling of bond between CFRP and concrete is shown from Figure 5.12 through Figure 5.16.

Table 5.3: Values of parameters defining the bond stress-slip relationship (B.E.P. model)

Pullout test	τ_m (MPa)	s_m (mm)	Assending Branch			Descending Branch		
			α	β	Error (%)	α'	β'	Error (%)
CFRP_AT_e1	5.34	0.87	0.785	1.039	2.31%	-0.049	0.941	0.71%
CFRP_AT_e2	4.21	0.64	0.861	1.059	3.88%	-0.027	0.967	4.36%
CFRP_15%	3.88	0.89	0.731	0.819	0.78%	-0.157	0.736	0.87%
CFRP_30%	5.07	0.72	0.708	0.766	2.17%	-0.429	0.699	2.80%
CFRP_38%	4.33	0.91	0.604	0.597	0.58%	-0.349	0.570	7.18%

It should be recalled that, in extended PHPOTs, the sample was loaded at room temperature to a prescribed load under a load control mode; after this the specimen was heated up without any signs of bond failure; finally, after almost four hours of steady state temperature, the sample was then loaded until pullout occurred. In extended PHPOTs the analytical model described in this section only represents the phenomenon occurring in the second loading phase (ascending branch) and the subsequent post failure residual strength (descending branch).

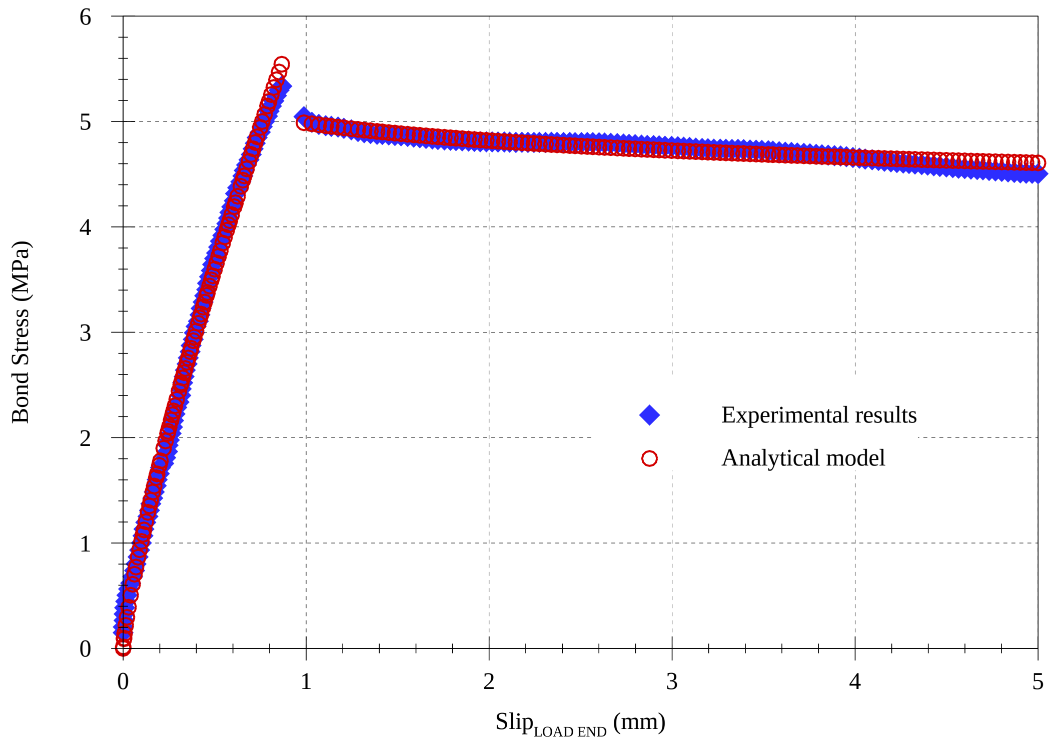

Figure 5.12: Numerical and experimental results for CFRP_AT_e1 stress-slip relationship

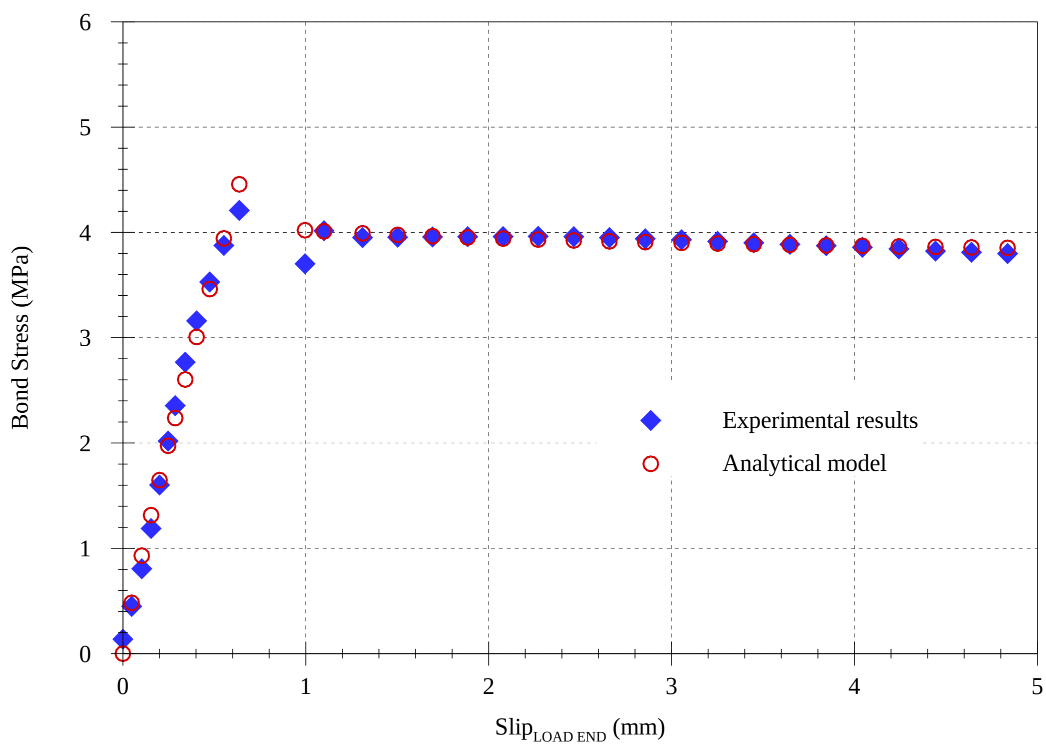

Figure 5.13: Numerical and experimental results for CFRP_AT_e2 stress-slip relationship

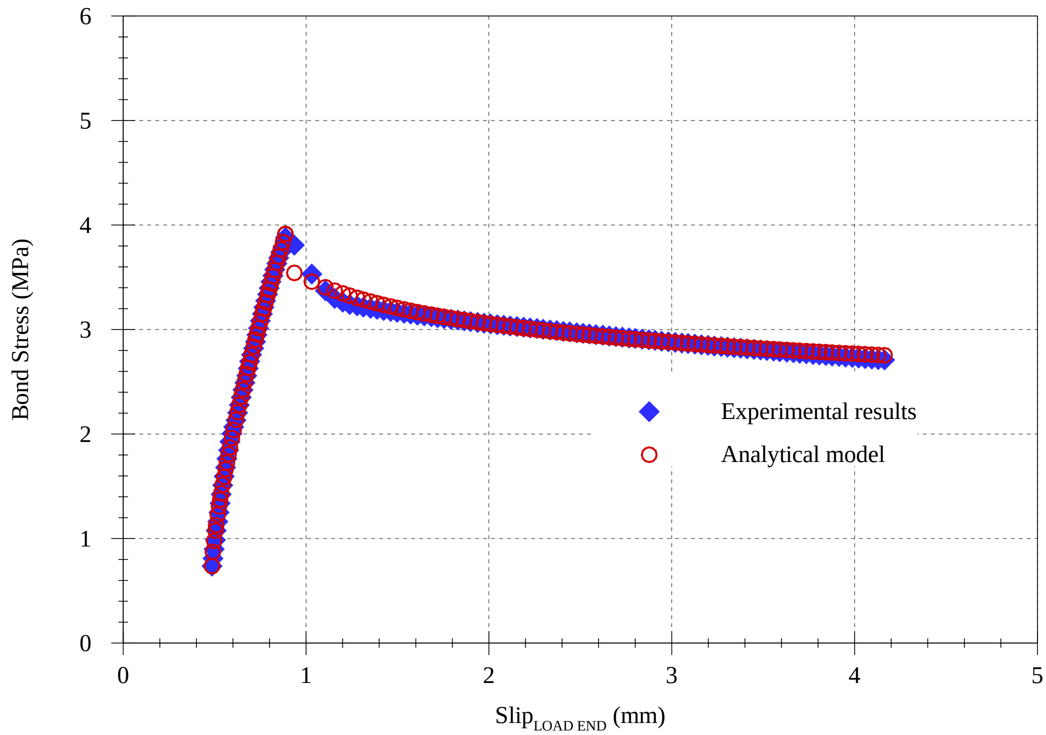

Figure 5.14: Numerical and experimental results for CFRP_15% stress-slip relationship

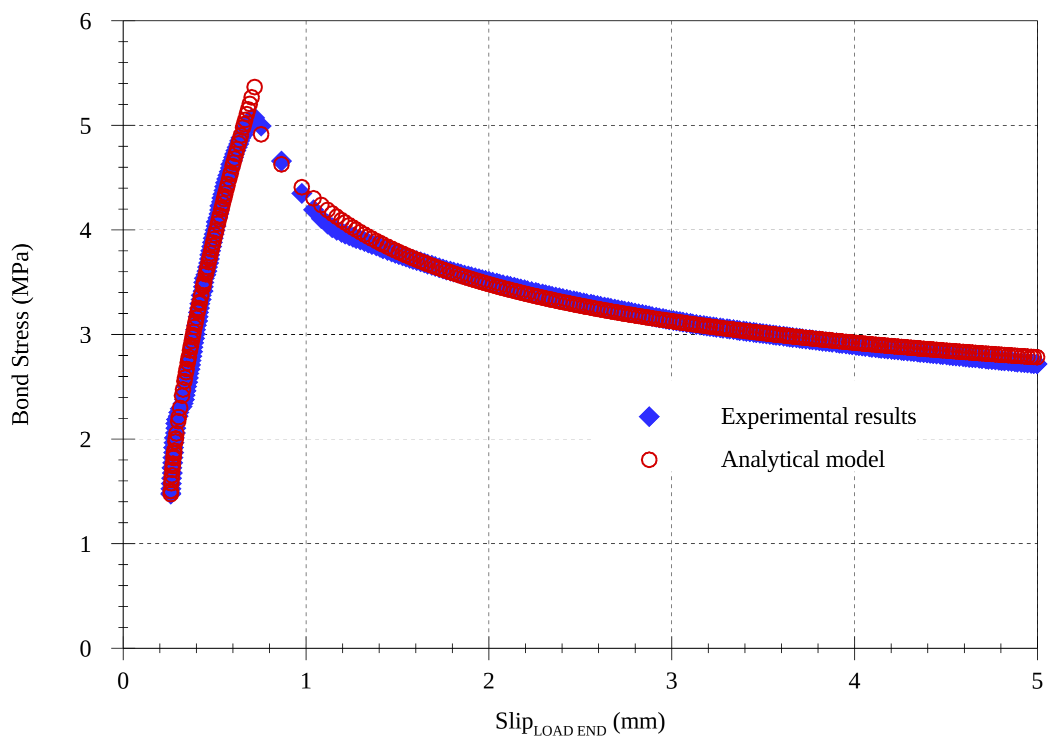

Figure 5.15: Numerical and experimental results for CFRP_30% stress-slip relationship

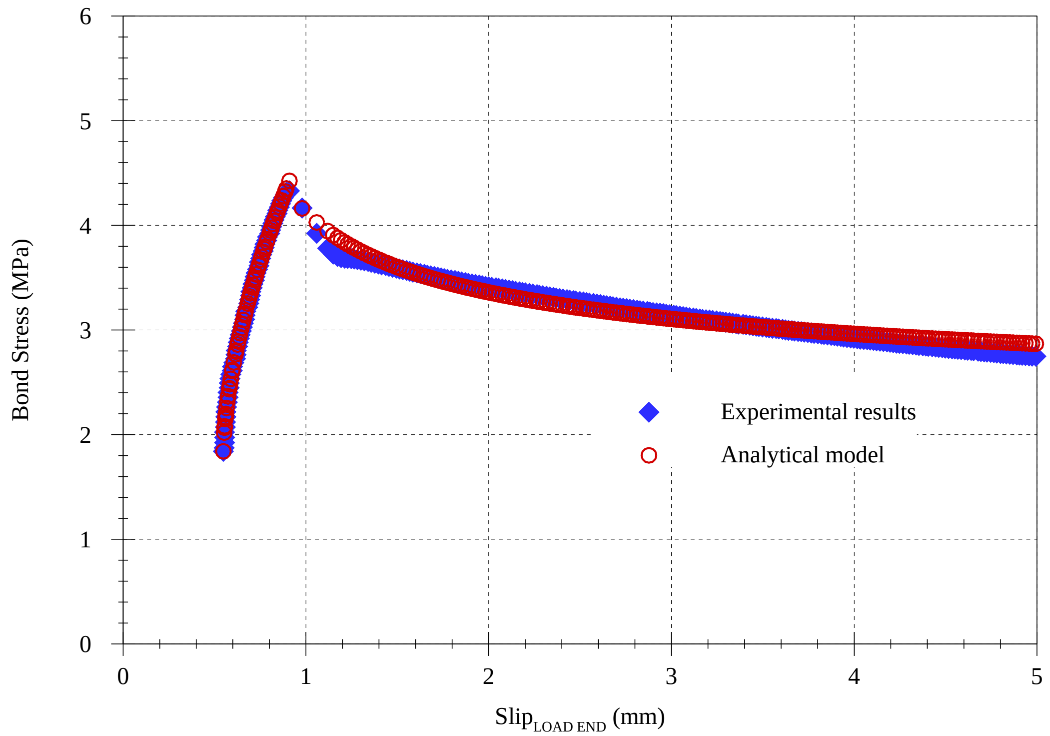

Figure 5.16: Numerical and experimental results for CFRP_38% stress-slip relationship

As mentioned before, the inclusion of the parameters β and β' intended to take into account the reduction of bond stiffness at the ascending branch when the pullout was performed at high temperatures. The B.E.P. model has been widely used, with very good results, in tests executed at ambient temperature. This is the reason why the values of β and β' defined for CFRP_AT_e1 and CFRP_AT_e2 (tests executed at ambient temperature) are very close to 1, as shown in Table 5.3.

The value of β decreases for PHPOT (CFRP_15% , CFRP_30%, and CFRP_38%) as seen from Table 5.3, with a correlation between the prestress load (at which the sample is sustained under load-control mode as the temperature increased) and the β value defined for each test.

From the modified B.E.P. model, the bond stiffness of the ascending branch is given by the following equation:

$$\frac{d\tau(s)}{ds} = \alpha \cdot \beta \cdot \frac{\tau_m}{s_m^{\alpha}} \cdot s^{\alpha-1} \tag{5.10}$$

In Figure 5.17, the ascending branch of the modified B.E.P. model and the evolution of the bond stiffness is plotted for the RPOTs and extended PHPOTs executed with CFRP tendons. Every curve tends to a bond stiffness value as pullout reaches the peak bond stress (bond strength). For the extended PHPOTs, the bond stress and bond stiffness correspond to the second loading phase, with the CFRP tendons at elevated temperature.

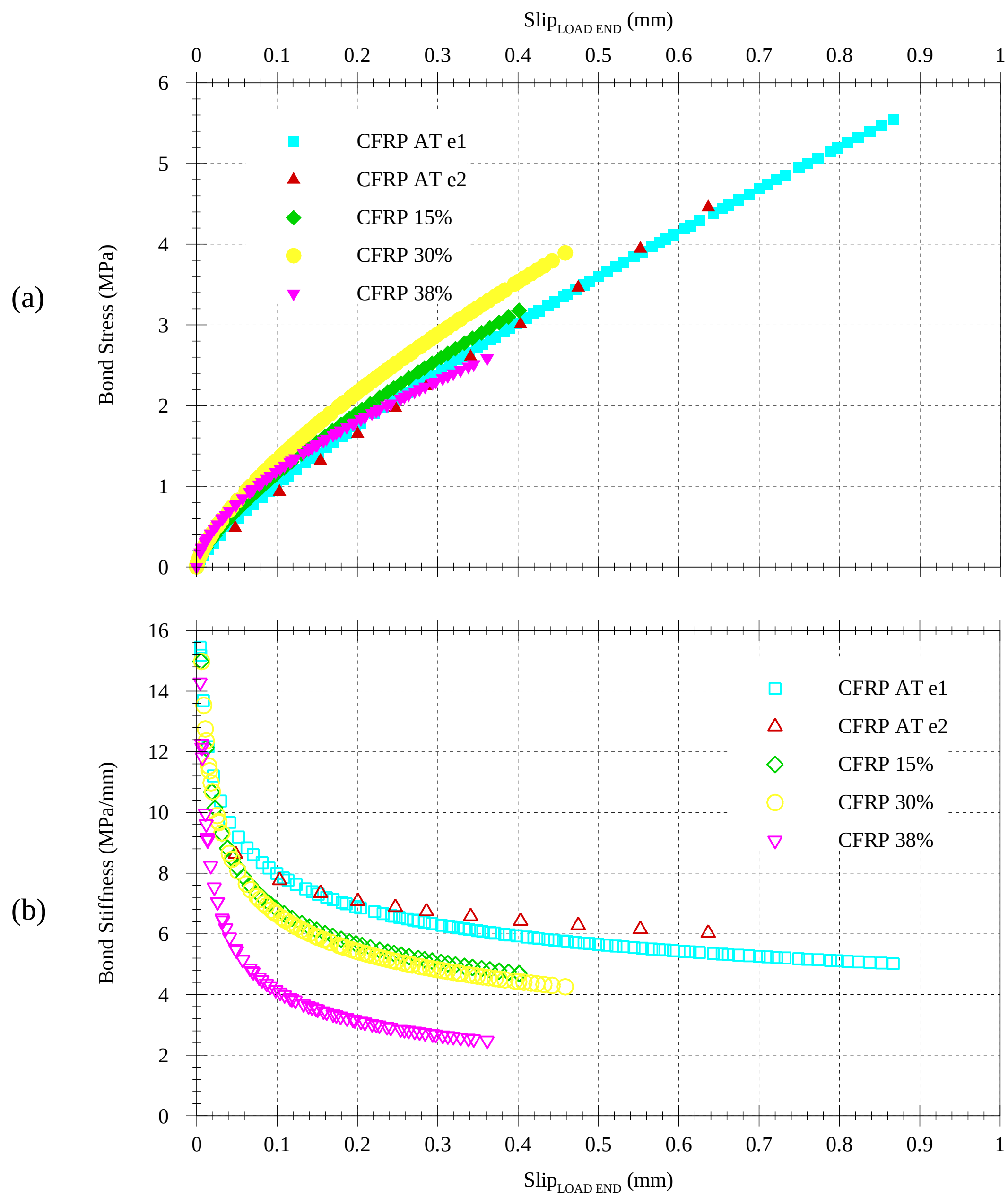

Figure 5.17: (a) Ascending branch from the bond stress-slip modified B.E.P model for CFRP pullout tests and **(b)** their corresponding bond stiffness evolution

The bond stiffness, in the ascending branch, tends to a lower value as the prestress load (sustained as the sample was heated) increased from test to test, as shown in Figure 5.17(b) for CFRP_15%, CFRP_30 and CFRP_38%. In these tests the bond stiffness tended to a value which was always lower than the one determined for CFRP_AT_e1 and CFRP_AT_e2, executed at ambient temperature.

The phenomenon explained above its related to what took place in the pullout tests performed in this study and is another tool to be used to compare different type of reinforcement. Is the author's opinion that future studies might find a correlation between the bond stiffness measured in pullout tests and development length, of CFRP tendons prestressed concrete members in real buildings.

5.4 Analytical Model for Longitudinal Thermal Expansion Effect on Slip Measurement

Special consideration was given to the accuracy of the measurements of bar slip at both the loaded and free ends of the pullout tests' specimens (see Section 3.3.6). Since thermal and mechanical events took place in the pullout tests, the data had to be filtered to determine what was the phenomena for which slip occur.

As temperature was increased in the PHPOTs, a variation of the slip measured at the loaded and free ends of the bar was recorded. This phenomenon was the result of the concrete cylinder and CFRP tendon or steel prestressing wire's combined thermal linear expansion. An analytical model was elaborated to predict the effect of the linear expansion of the concrete and bar in the recording of slip at the loaded and free end.

This model considers that the rise in temperature generates three phenomena which generate false slip measured by the slip recording systems.

1. Thermal expansion of the concrete restrained by the frame's top reference plate (see Figure 3.41) results in negative slip at the loaded and free ends.
2. Thermal expansion of the CFRP tendon or steel prestressing wire results in a positive slip at the loaded end (restrained by the top of the bonded length) and negative slip at the free end (restrained by the bottom of the bonded length).
3. The Instron's crosshead displaced because of the machine's effort to maintain the sustained load at load-control mode.

This model assumes perfect bonding between the concrete and the bar. The false slip recorded by the slip measurement systems is shown in Figure 5.18 and given by the following equations:

$$Slip_{LE}^{T} = -\Delta L_{c\_LE}^{T} + \Delta L_{bar\_LE}^{T} + \delta_{Instron} \tag{5.11}$$

$$Slip_{FE}^{T} = -\Delta L_{c\_FE}^{T} - \Delta L_{bar\_FE}^{T} + \delta_{Instron} \tag{5.12}$$

Considering that the coefficients of thermal expansion (α_c and α_{bar}) are not significantly temperature dependant for the range of temperatures in which PHPOTs were executed, Equations (5.13) and (5.14) can be calculated.

$$Slip_{LE}^{T} = -(50)mm \cdot \alpha_c \cdot \Delta T_c[t] \\ +l_{patch} \cdot \alpha_{bar} \cdot \Delta T_{ber\_LE}[t] + \delta_{Instron}[t] \tag{5.13}$$

$$Slip_{FE}^{T} = -(50+160)mm \cdot \alpha_c \cdot \Delta T_c[t] \\ -(40+20)mm \cdot \alpha_{bar} \cdot \Delta T_{bar\_FE}[t] + \delta_{Instron}[t] \tag{5.14}$$

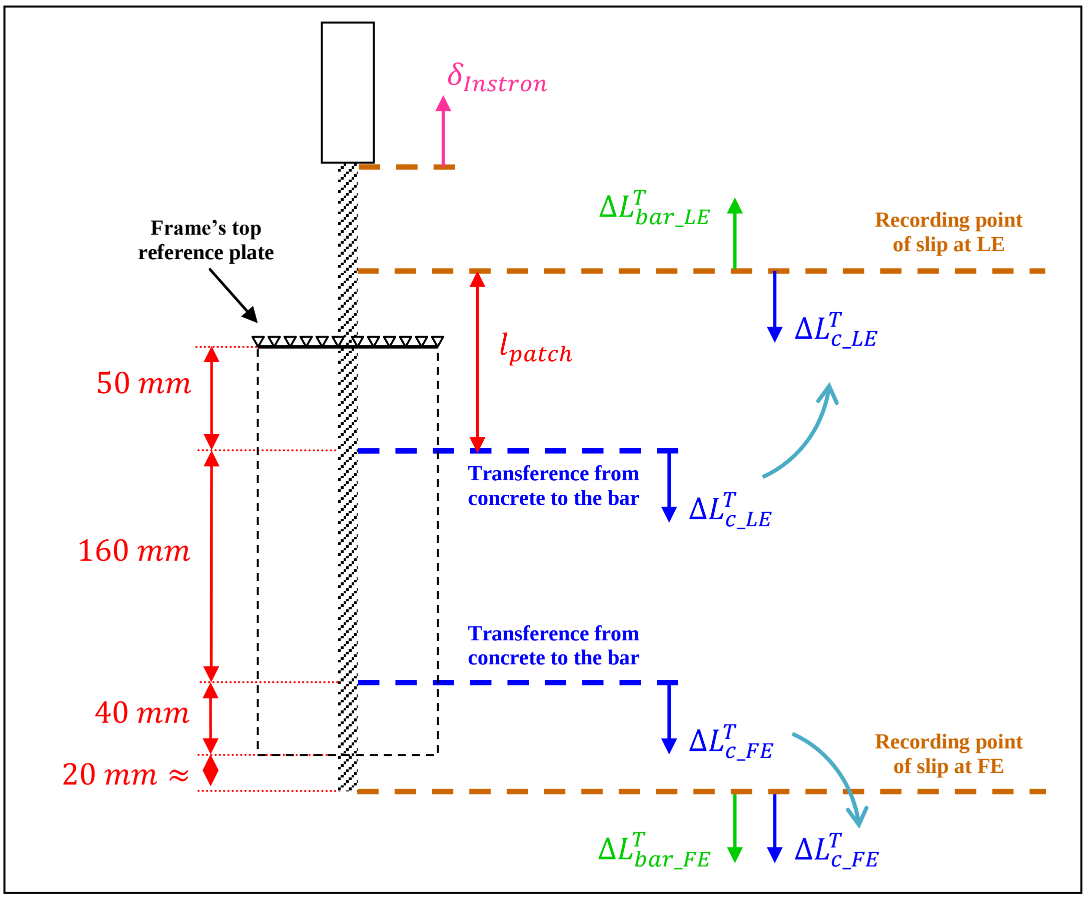

Figure 5.18: Diagram of the pullout test's thermal linear expansion phenomena

The temperature variation of the concrete (ΔT_c) used as an input for this model is the mean temperature recorded by the thermocouples at the bar (top, middle and bottom of the bonded length) as determined in Section 3.4.3. This is the temperature of the concrete in direct contact with the bar and is used as input temperature because the increase it is assumed that the bar moves with the concrete in direct contact with it, and the temperature gradient within concrete generate stresses inside the concrete cylinder without affecting the slip of the bar. The thermal gradient between the heating blanket (concrete surface) and the bar was large when the heating blanket was initially turned on and decreased as the PHPOTs continued.

The temperature variation used as an input for the bar thermal expansion at loaded end (ΔT_{bar_LE}) and free end (ΔT_{bar_FE}) calculations, were the temperatures recorded by the thermocouples at the top and bottom of the bonded length respectively.

The coefficient of thermal expansion of concrete (α_c) was extracted from a study made in concrete containing similar volume of silica as the one design for this research (Whiting & Detwiler, 1998). The coefficient of thermal expansion of the steel prestressing wire (α_{Steel}) was extracted from the recommendations given by the Eurocode 2 (2002) for common steel reinforcing bars. The longitudinal coefficient of thermal expansion of the CFRP tendons $(\alpha_{CFRP\_longitudinal})$ was extracted from a study made with similar CFRP tendons as the ones used in past research (Lublóy, Balázs, Borosnyuói & Nehme, 2005).

$$\alpha_c = 13 \times 10^{-6} \left[{}^{1}/_{\circ C}\right] \tag{5.15}$$

$$\alpha_{Steel} = 14 \times 10^{-6} \left[{}^{1}/_{\circ C}\right] \tag{5.16}$$

$$\alpha_{CFRP\_longitudinal} = 0.2 \times 10^{-6} \left[{}^{1}/_{\circ C}\right] \tag{5.17}$$

The analytical model elaborated above was compared against experimental data from extended PHPOTs. The results are displayed in three graphs per test:

(a) Temperature of the heating blanket and the three thermocouples located at the bar (top, middle and bottom of the bonded length).

(b) Instron’s crosshead displacement after the heating blanket is turned on (minute 15).

(c) Experimental slip readings and analytical model comparison from the moment in which the heating blanket was turned on (minute 15).

The analytical model was performed for the following tests:

- Steel_37%_e1, Steel_37%_e2, Steel_46%_e1 and Steel_46%_e2,
- CFRP_15%, CFRP_30% and CFRP_38%

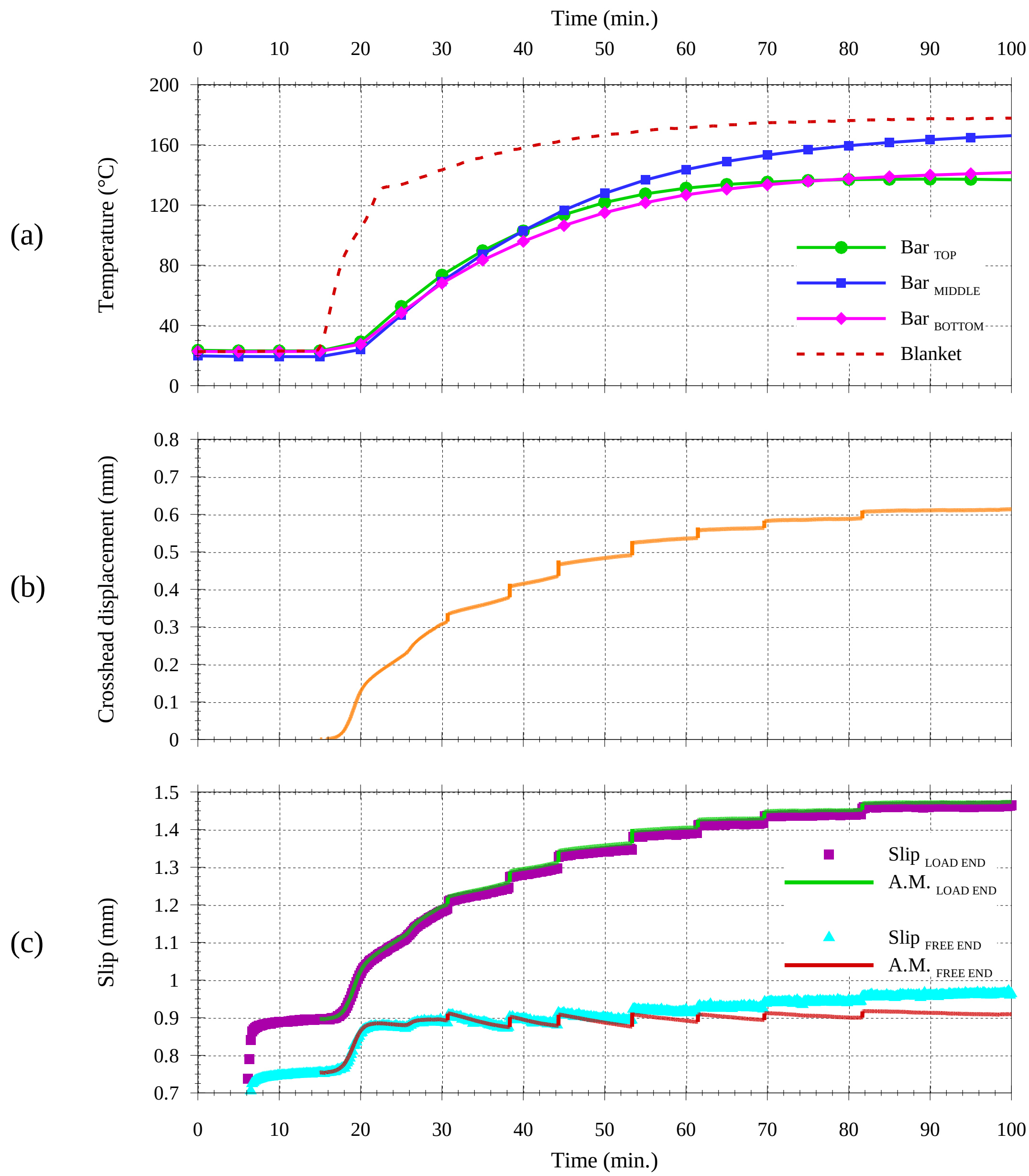

Figure 5.19: (a) Temperature evolution, **(b)** crosshead displacement due to materials thermal expansion and **(c)** slip readings and thermal longitudinal compatibility analytical model of slip for Steel_37%_e1

(a)

(b)

(c)

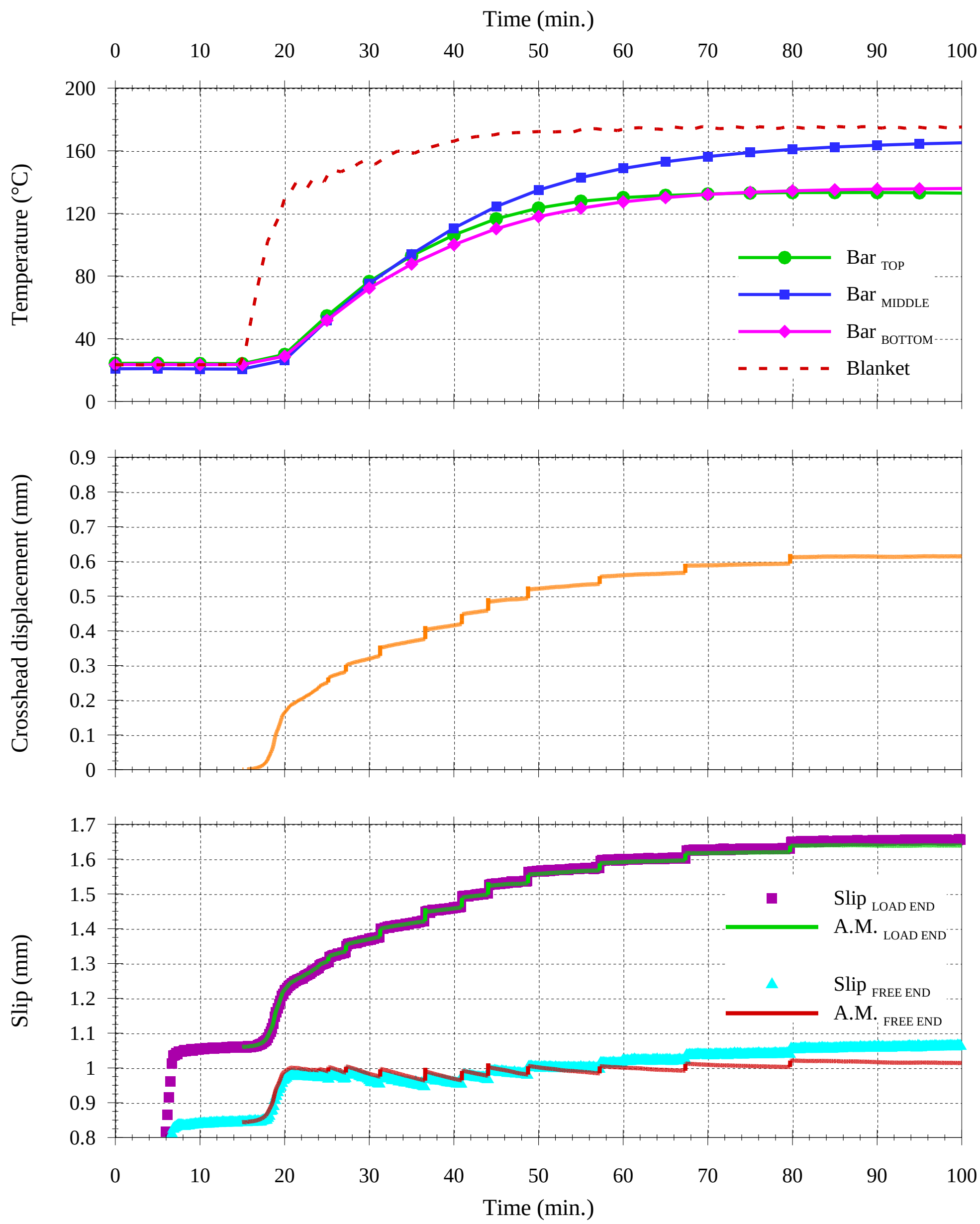

Figure 5.20: (a) Temperature evolution, **(b)** crosshead displacement due to materials thermal expansion and **(c)** slip readings and thermal longitudinal compatibility analytical model of slip for Steel_37%_e2

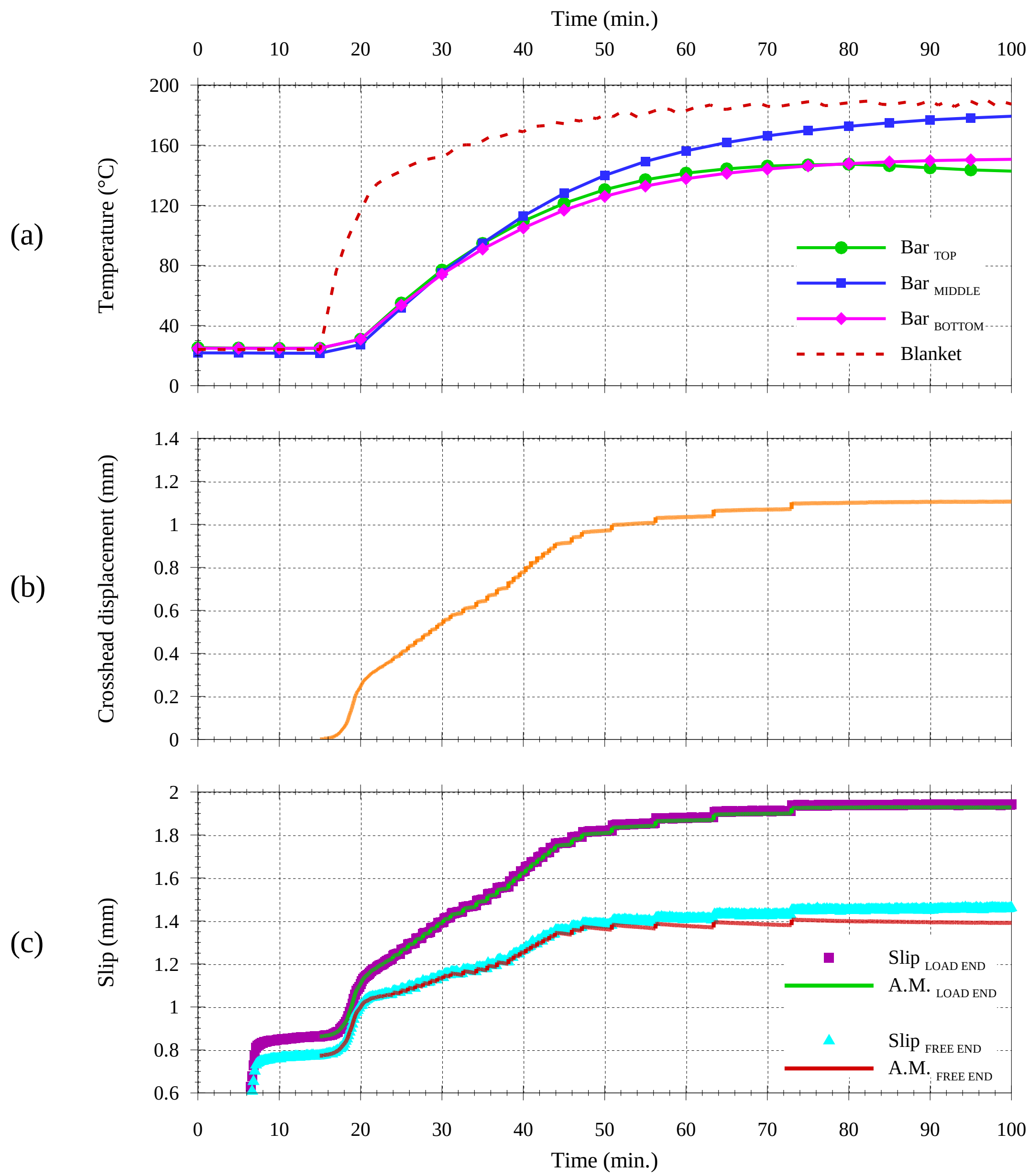

Figure 5.21: (a) Temperature evolution, **(b)** crosshead displacement due to materials thermal expansion and **(c)** slip readings and thermal longitudinal compatibility analytical model of slip for Steel_46%_e1

(a)

(b)

(c)

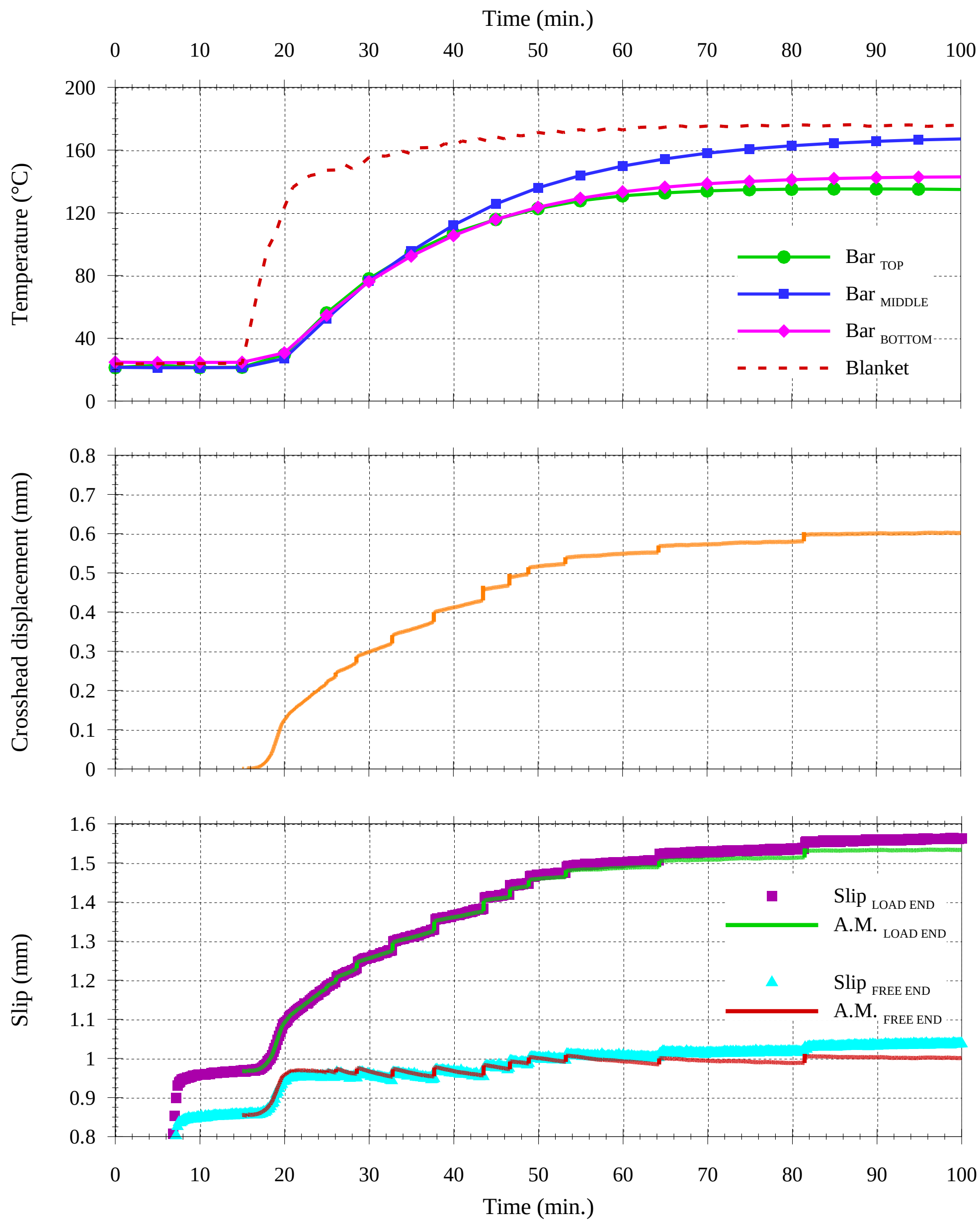

Figure 5.22: (a) Temperature evolution, **(b)** crosshead displacement due to materials thermal expansion and **(c)** slip readings and thermal longitudinal compatibility analytical model of slip for Steel_46%_e2

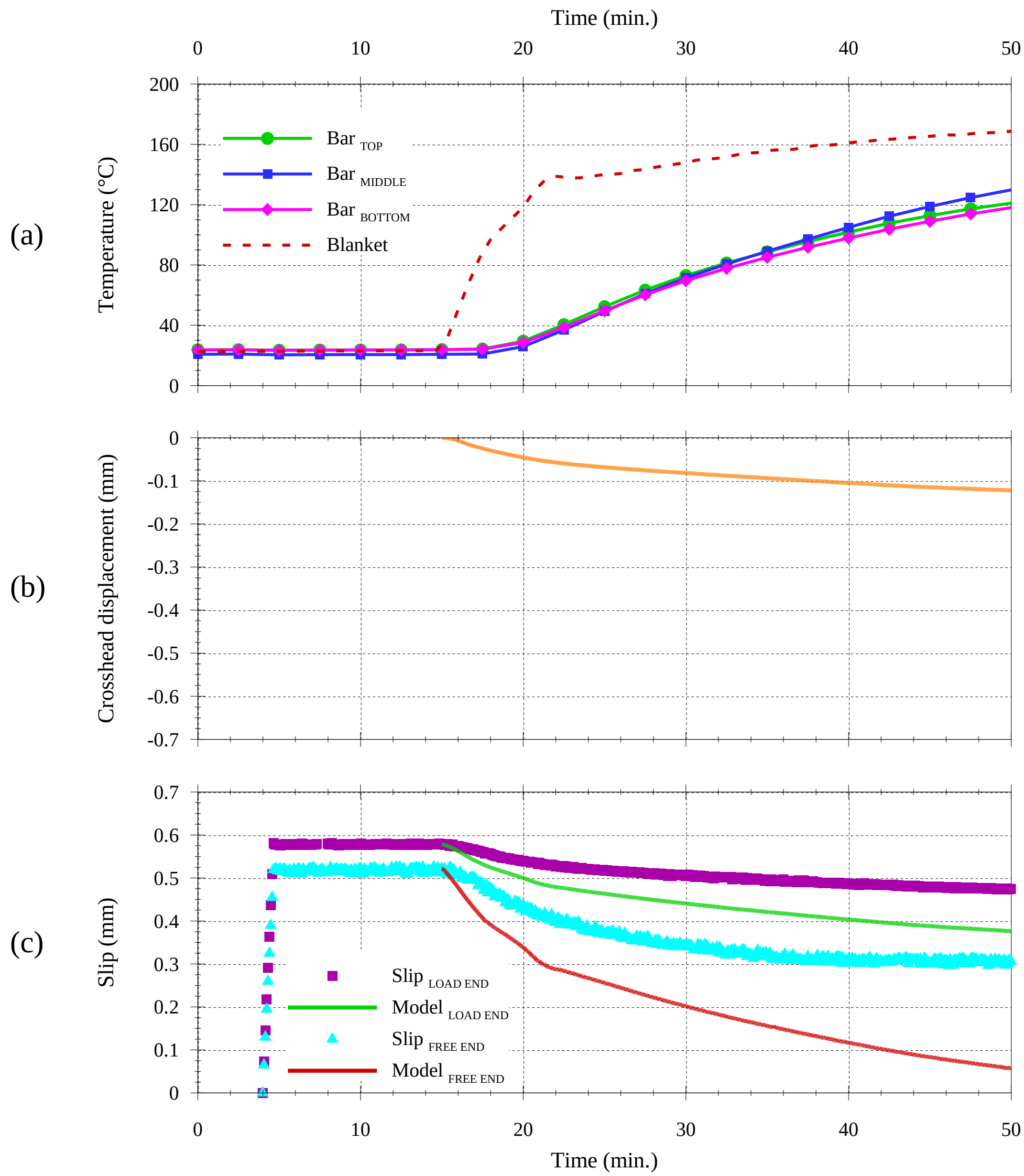

Figure 5.23: (a) Temperature evolution, **(b)** crosshead displacement due to materials thermal expansion and **(c)** slip readings and thermal longitudinal compatibility analytical model of slip for CFRP_15%

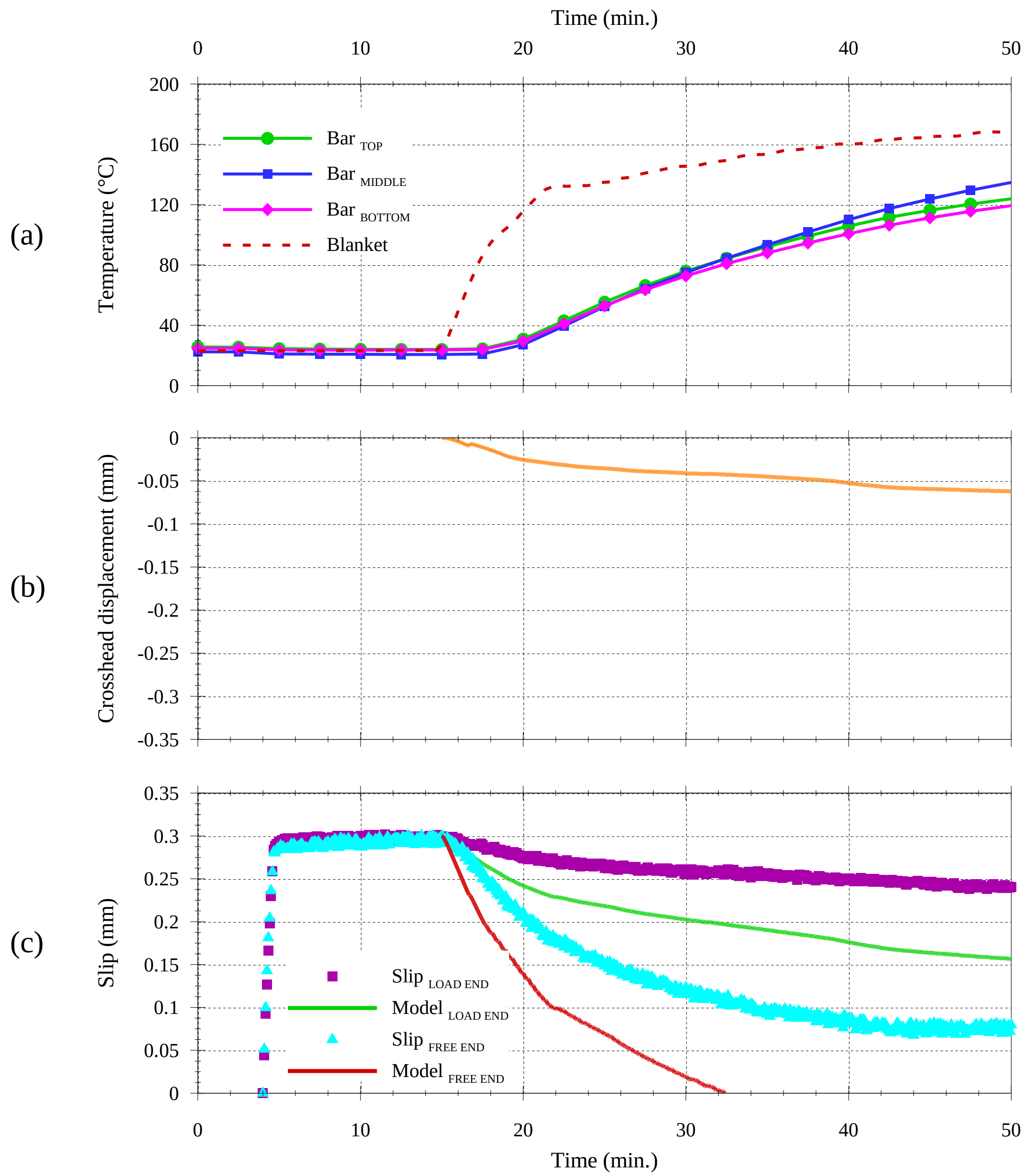

Figure 5.24: (a) Temperature evolution, **(b)** crosshead displacement due to materials thermal expansion and **(c)** slip readings and thermal longitudinal compatibility analytical model of slip for CFRP_30%

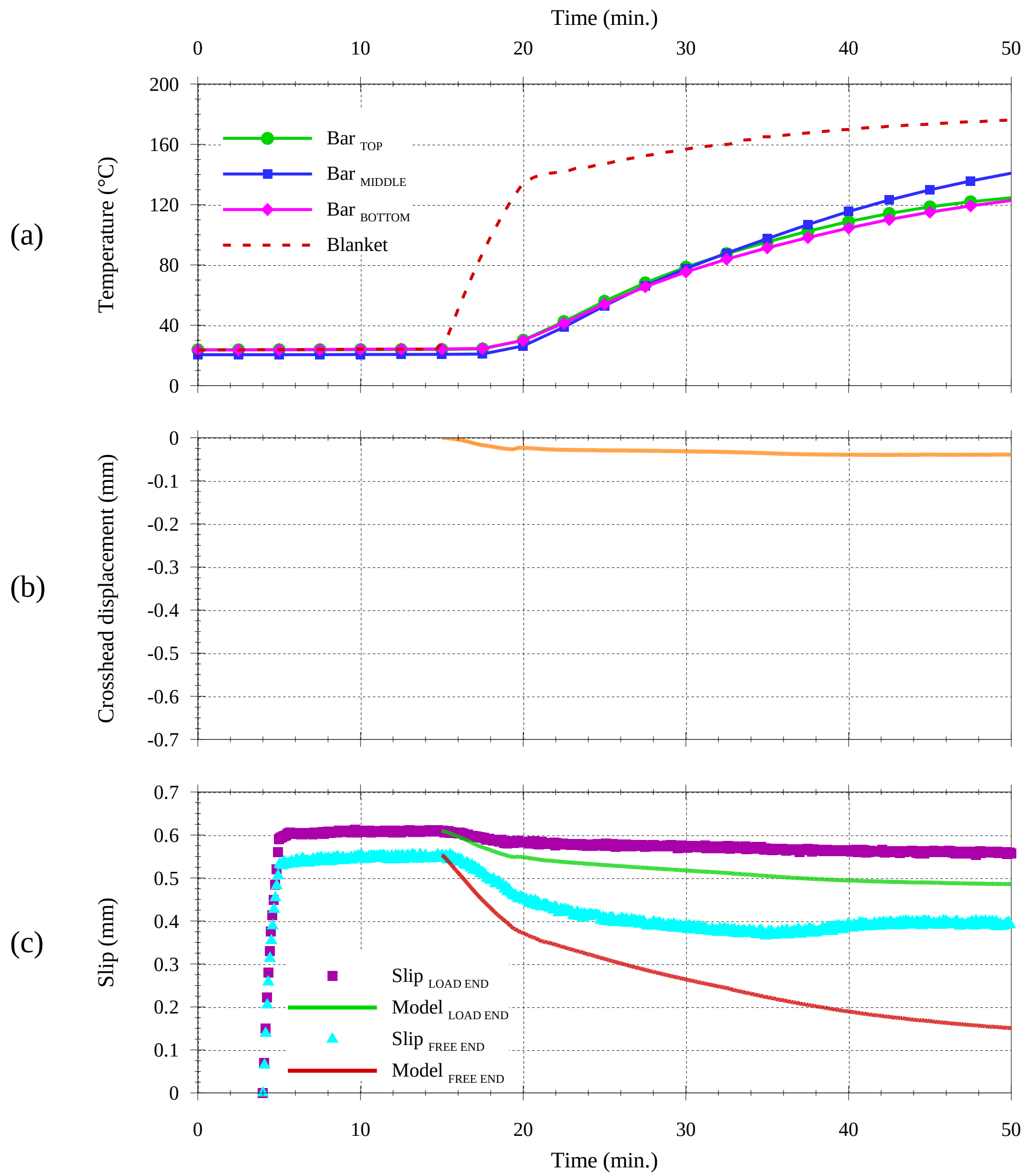

Figure 5.25: (a) Temperature evolution, **(b)** crosshead displacement due to materials thermal expansion and **(c)** slip readings and thermal longitudinal compatibility analytical model of slip for CFRP_38%

The analytical model to describe the linear expansion of concrete and bar effects on slip recording was performed for steel extended PHPOTs (Figure 5.19 till Figure 5.22) and CFRP extended PHPOTs (Figure 5.23 till Figure 5.25).

The model gave negligible error values for steel pullout tests but did not performed as good for CFRP pullout tests, as shown in Table 5.4.

Table 5.4: Error of the analytic model of the longitudinal thermal expansion effect in slip readings

Pullout test	**Analytic model error**	
	Loaded End	**Free end**
CFRP_15%	13.07%	43.02%
CFRP_30%	22.03%	84.90%
CFRP_38%	9.51%	34.97%
Steel_37%_e1	0.90%	2.47%
Steel_37%_e2	0.48%	2.34%
Steel_46%_e1	0.56%	2.38%
Steel_46%_e2	0.93%	1.56%

5.4.1 Bond degradation assumption

It should be recalled that this analytical model assumes perfect bonding between the concrete and the bar. The reason for the analytical model not fitting the CFRP pullout test's experimental data (Figure 5.23 till Figure 5.25) could be related to the apparent degradation of the bond strength with the increase in temperature of the CFRP tendon.

In previous sections it was predicted that bond strength of the sand coated CFRP tendons could be related to the reduction of elastic modulus suffered by the epoxy, from which the CFRP is manufactured, when it is at high temperature. Because bond strength degradation is obviously not simply affected only by the epoxy's retained elastic modulus $\left(E_{retained}^{epoxy}\right)$, a corrector value (θ_{bond}) is added to the model.

Because at the loaded end, the concrete's thermal expansion is transmitted to the CFRP tendon only by the top of the bonded length, it is reasonable to assume that none of the concrete's expansion is transmitted to the CFRP tendon.

At the free end, the concrete's thermal expansion is transmitted to the CFRP tendon all along the bonded length (160 mm), in which case is a good assumption to assume that the bond strength is directly affected by the epoxy's retained elastic modulus, as discussed before.

The analytical model for the CFRP pullout tests is now as follows:

$$Slip_{LE}^{T} = l_{patch} \cdot \alpha_{bar} \cdot \Delta T_{bar\_LE}[t] + \delta_{Instron}[t] \tag{5.18}$$

$$\begin{aligned} Slip_{FE}^{T} = &-(50+160)mm \cdot \alpha_{c} \cdot \Delta T_{c}[t] \cdot E_{retained}^{epoxy}[t] \cdot \theta_{bond} \\ &-(40+20)mm \cdot \alpha_{bar} \cdot \Delta T_{bar\_FE}[t] + \delta_{Instron}[t] \end{aligned} \tag{5.19}$$

The comparison of the new model, which assumes bond degradation of the CFRP tendon, with the experimental data is showed in Figure 5.26, Figure 5.27 and Figure 5.28, and their respective errors are shown in Table 5.5. As expected, the errors of the model which assumes bond degradation of the CFRP tendon are much lower than the ones from the first model which assumed perfect bonding.

Table 5.5: Error of the analytic model of the longitudinal thermal expansion effect in slip readings (assuming bond degradation of the CFRP tendon)

Pullout test	**θ_{bond}**	**Analytic model error (assuming bond degradation)**	
		Loaded End	**Free end**
CFRP_15%	0.55	1.95%	2.16%
CFRP_30%		0.56%	12.55%
CFRP_38%		1.08%	2.01%

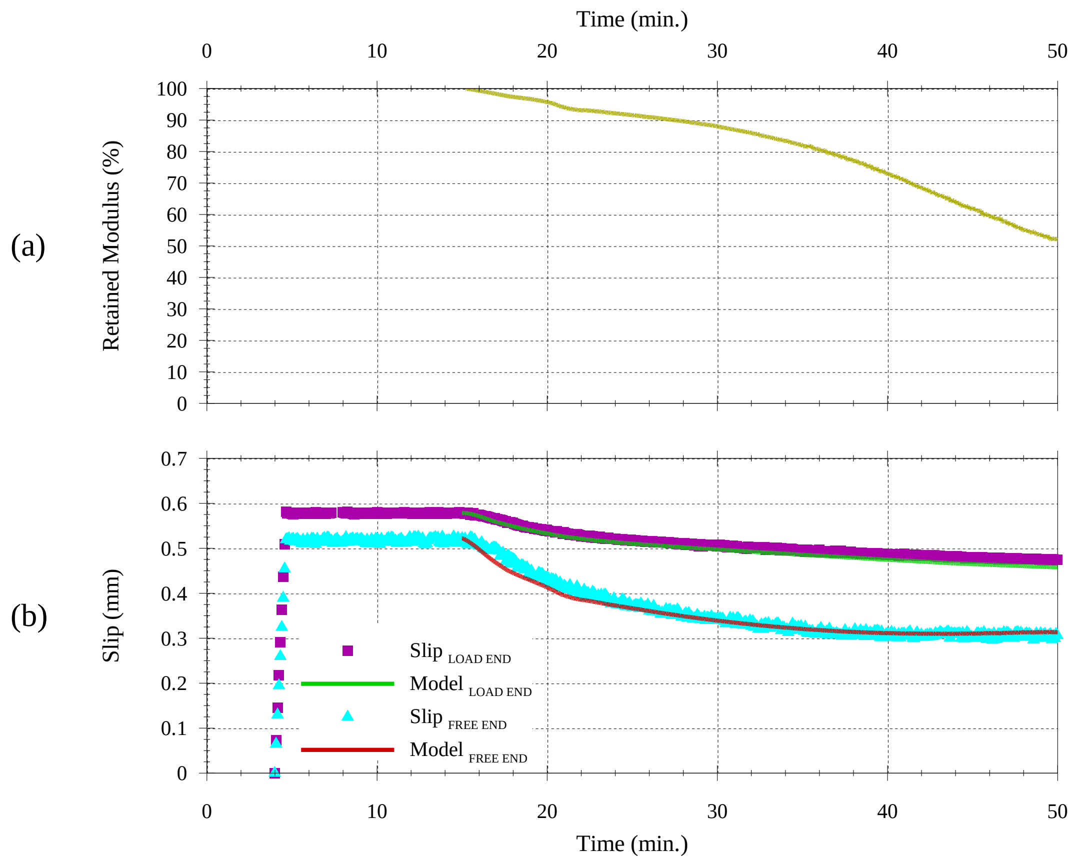

Figure 5.26: (a) Tendon's epoxy retained elastic modulus and **(b)** slip readings for CFRP_15% and thermal longitudinal compatibility analytical model of slip corrected assuming bond degradation

(a)

(b)

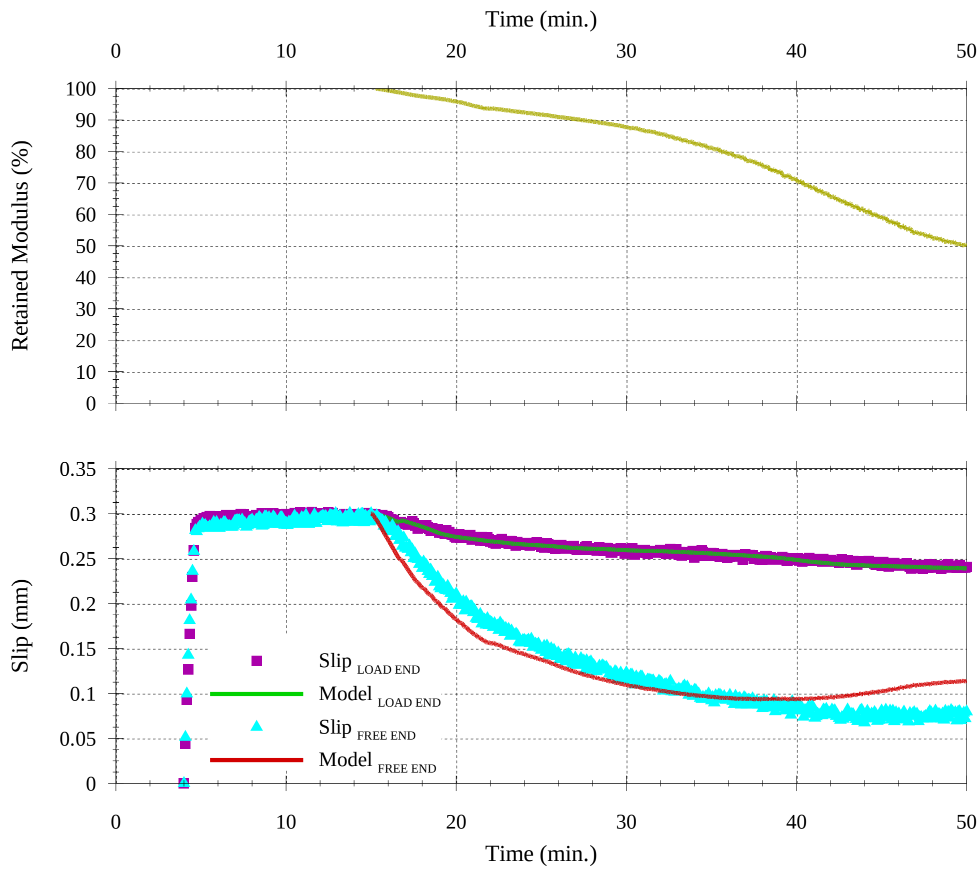

Figure 5.27: (a) Tendon's epoxy retained elastic modulus and **(b)** slip readings for CFRP_30% and thermal longitudinal compatibility analytical model of slip corrected assuming bond degradation

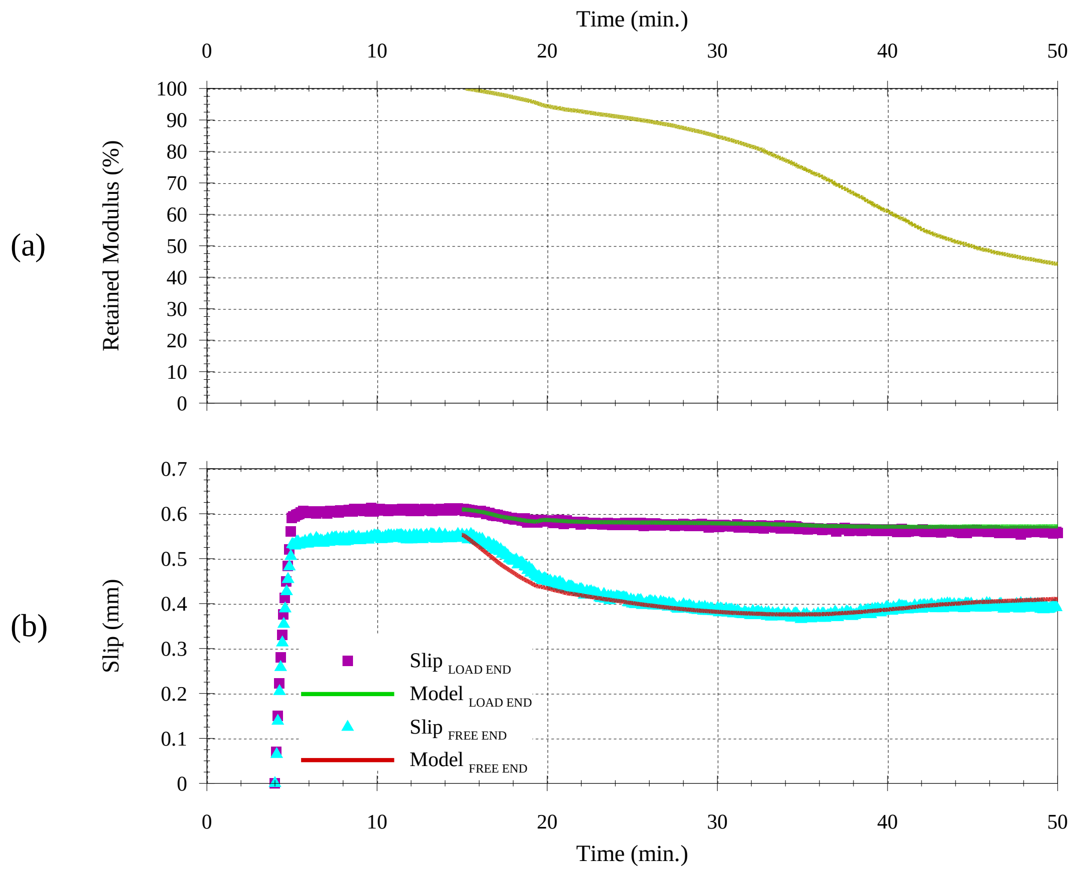

Figure 5.28: (a) Tendon's epoxy retained elastic modulus and **(b)** slip readings for CFRP_38% and thermal longitudinal compatibility analytical model of slip corrected assuming bond degradation

5.5 Comparison Between Tensile Strength of CFRP and Steel at High Temperature

The tensile strength of both CFRP and steel prestressing reinforcements can be expected to be reduced at elevated temperatures. For cold-drawn steel wire the relationship between temperature and tensile strength is relatively well established and is available, for example, in Eurocode 2 (2002). The effects of elevated temperature on the specific strength of the CFRP tendons used in the current study are not known. Thus, a series of nine transient high temperature tensile tests were performed on the CFRP tendons at sustained stress levels between 800 MPa and 1200 MPa (a realistic stress range for pretensioning applications), and the results are shown in Section 4.2. The results of these tests are also given in Figure 5.29, along with the yield stress reduction curve recommended by the Eurocode 2 (2002) for Class A cold-drawn prestressing steel.

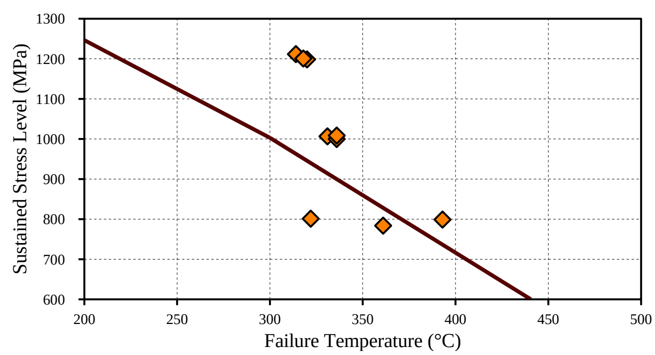

Figure 5.29: Results of transient thermal tensile tests on CFRP tendons at high temperature and yield stress reduction curve for prestressing steel (Eurocode 2, 2002)

It is evident that the performance of the CFRP tendons is similar to steel prestressing in terms of retention of tensile strength at elevated temperature, and that CFRP tendons stressed to 1000 MPa can be expected to fail at about 334°C.

Analysis and discussions were developed in the current section, with the objective of better understanding the experimental data from the pullout tests by developing models to simulate and better understand the theory behind the way results were measured.

6 NUMERICAL MODELING

6.1 Heat Transfer Model

A heat transfer model of the pullout tests was developed for this study, using the finite volume computational fluid dynamics (CFD) tool FLUENT (Fluent Inc., 2005). To assess the capabilities of the computational numerical model, two of the pullout tests executed on steel prestressing wire (Steel_37%_e1 and Steel_46%_e1) were modelled and compared to the experimental data. One quarter of the system was modelled, using symmetry boundary conditions, to optimize the computational requirements of the model, as shown later in Figure 6.7.

Three mechanisms of heat transfer (conduction, convection and radiation) contribute in every fire (Drysdale, 1998). In the pullout experiments executed for this study, concrete was heated up by using a heating blanket directly placed on the concrete surface. This meant that the concrete cylinder was heated mainly by conduction, and convection occurred at both top (metal plate) and bottom (concrete cylinder) of the specimen, as shown in Figure 6.1. In a fire, substantial amount of heat released in flames is transmitted by radiation to the surroundings, phenomena avoided in this experimental work.

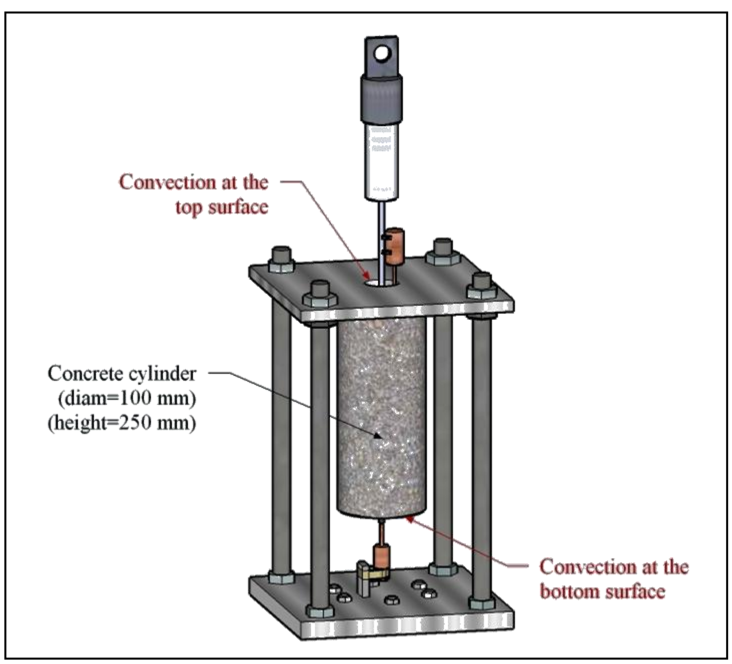

Figure 6.1: Location of the pullout test's top and bottom convective heat transfer surfaces.

6.1.1 Conduction

Conduction is the mode of heat transfer associated with the solids of the model (concrete and CFRP). Heat transfer in a solid can be described by the heat diffusion differential equation (Incropera & DeWitt, 2002), where k is the thermal conductivity of the solid, T is the temperature, t is time, ρ is the concrete's density, C_P is the specific heat, and $\dot{q}$ is a term representing heat generation within the material.

$$\frac{\delta}{\delta x}\left(k\frac{\delta T}{\delta x}\right)+\frac{\delta}{\delta y}\left(k\frac{\delta T}{\delta y}\right)+\frac{\delta}{\delta z}\left(k\frac{\delta T}{\delta z}\right)+\dot{q}=\rho C_P\frac{\delta T}{\delta t} \tag{6.1}$$

Each of the first three terms represents heat transfer into or out of the differential volume due to heat conduction, and the term on the right hand side represents the heat (energy) stored in the differential volume per unit time.

The thermal conductivity (k) of concrete was determined from the experimental results shown in Appendix C. The variation of this value with temperature was reproduced from past studies performed by Lie (1992). The value and variation of the heat capacity of concrete C_P was reproduced from work developed by Lie (1992). The density (ρ) of concrete, was determined from the experimental data shown in Table A.2, and was assumed to evolve with temperature as determined by past studies (Schneider, 1988).

The variation of thermal conductivity and specific heat of the steel prestressing wire was reproduced from Lie (1992).

6.1.2 Convection

Free convection was assumed to occur at the top and bottom of the concrete cylinder, as shown in

Figure **6.2**. The heat transfer coefficient $[W/m^2 \cdot K]$ is given by:

$$\bar{h}=\frac{\overline{Nu}_L \cdot k}{L} \tag{6.2}$$

With:

$$\overline{Nu}_L = \begin{cases} 0.54 \cdot Ra_L^{1/4} & \text{for the top surface} \\ 0.27 \cdot Ra_L^{1/4} & \text{for the bottom surface} \end{cases} \quad (6.3)$$

$$k = 2574 \ \left[{}^{W}/_{m \cdot K}\right] \quad \text{for air at T=20°C} \quad (6.4)$$

$$L = \frac{A_s}{P} \quad (6.5)$$

Where:

$$Ra_L = \frac{g \cdot \beta \cdot (T_s - T_\infty) \cdot L^3}{\nu \cdot \alpha} \quad (6.6)$$

$$g = 9.82 \left[{}^{m}/_{s^2}\right] \quad (6.7)$$

$$\beta(T_\infty = 293\ K \mid T_\infty = 473\ K\ ) = 0.00261\ [K^{-1}] \quad (6.8)$$

$$\nu(T_\infty = 293\ K) = 15.27 \times 10^{-6} \quad (6.9)$$

$$\alpha(T_\infty = 293\ K) = 21.58 \times 10^{-6} \quad (6.10)$$

$$A_s = \text{Top/Bottom surface} = \pi \cdot r_c^2 \quad (6.11)$$

$$P = \text{Top/Bottom perimeter} = 2 \cdot \pi \cdot r_c \quad (6.12)$$

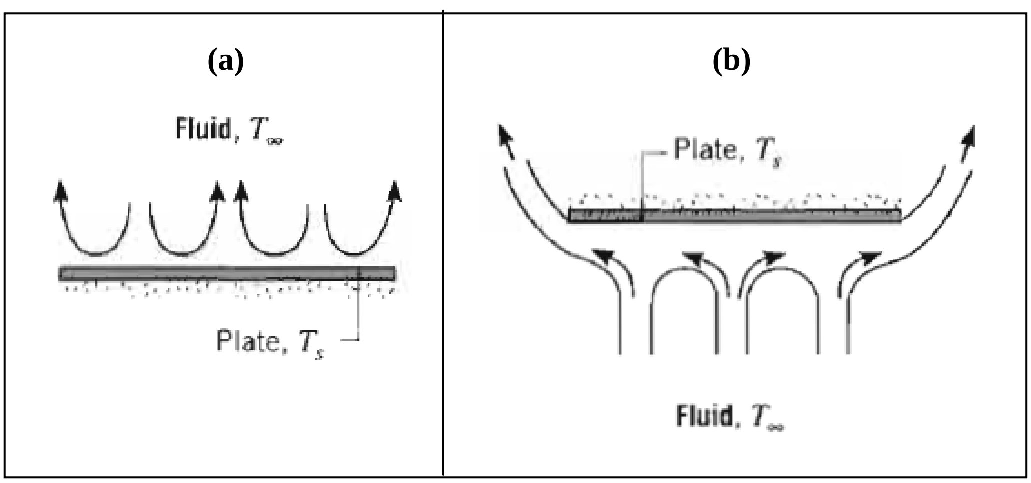

Figure 6.2: Buoyancy-driven flows on horizontal hot plates ($T_s > T_\infty$); **(a)** top surface and **(b)** bottom surface (Incropera & DeWitt, 2002)

6.1.3 Input temperature

The heating ramp was determined from each of the pullout tests by using the experimental data from the four thermocouples at the blanket-concrete interface (see Section 3.2.1.3). The average readings from the four thermocouples were used as an input for the model.

6.1.4 Parametric adjustment with experimental data

The parameters of the model were adjusted by comparing the model results with the experimental data obtained from the three thermocouples placed at the bonded length of the bar (see Section 3.2.1.2). The results of a first version of the model, with the material properties experimentally determined, is showed in Figure 6.3 and Figure 6.4, compared to the measurements from tests Steel_37%_e1 and Steel_46%_e1, respectively. Since the thermal properties of the CFRP tendons are not well known, the model was only developed for pullout samples with steel prestressing wire.

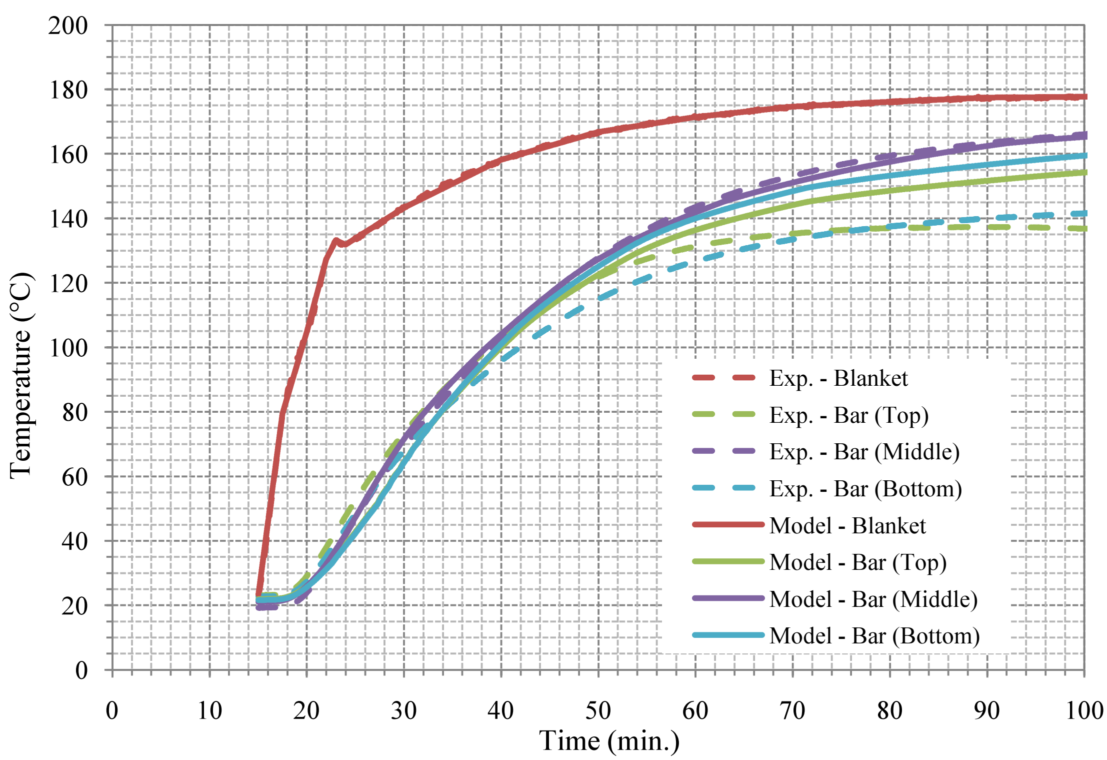

Figure 6.3: Temperature comparison between heat transfer model and experimental results from Steel_37%_e1

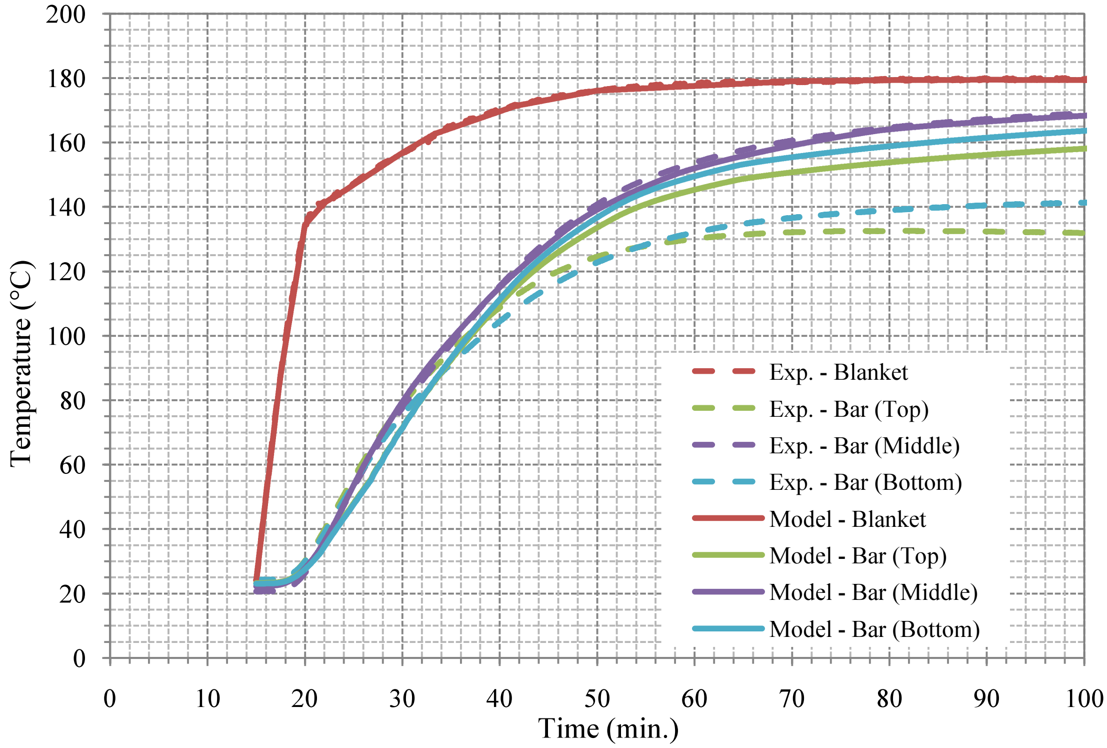

Figure 6.4: Temperature comparison between heat transfer model and experimental results from Steel_46%_e1

The temperature at the middle of the bonded length (purple line) determined by the model seems to fit the experimental data relatively well, while the temperature at the top and bottom of the bonded length are overestimated by the model after minute 40. The author believes that the temperature at the middle of the bonded length is not affected by the convection phenomena at the top and bottom of the concrete cylinder. It might be assumed that at the middle of the bonded length the thermal conditions behave as if it would be an in infinitely long cylinder.

The poor attempt in predicting the convection effect on the experiment was likely caused by the unknown ventilation conditions in the laboratory in which the pullout tests were executed (although it is unlikely that ideal free convection was occurring).

It should be recalled that in every pullout test, the heating blanket was turned on exactly at minute 15, as described in Section 3.4.1.2.2.

An increment of the values for the heat transfer coefficient in the convection at the top and bottom of the concrete cylinder was done in order to fit the temperature with the experimental data obtained from the pullout tests. The heat transfer coefficient values were increased by three times for the bottom surface (concrete cylinder) and twice its value for the top surface (steel plate), assuming the presence of forced convection (Incropera & DeWitt, 2002). The results from this correction are shown in Figure 6.5 and Figure 6.6.

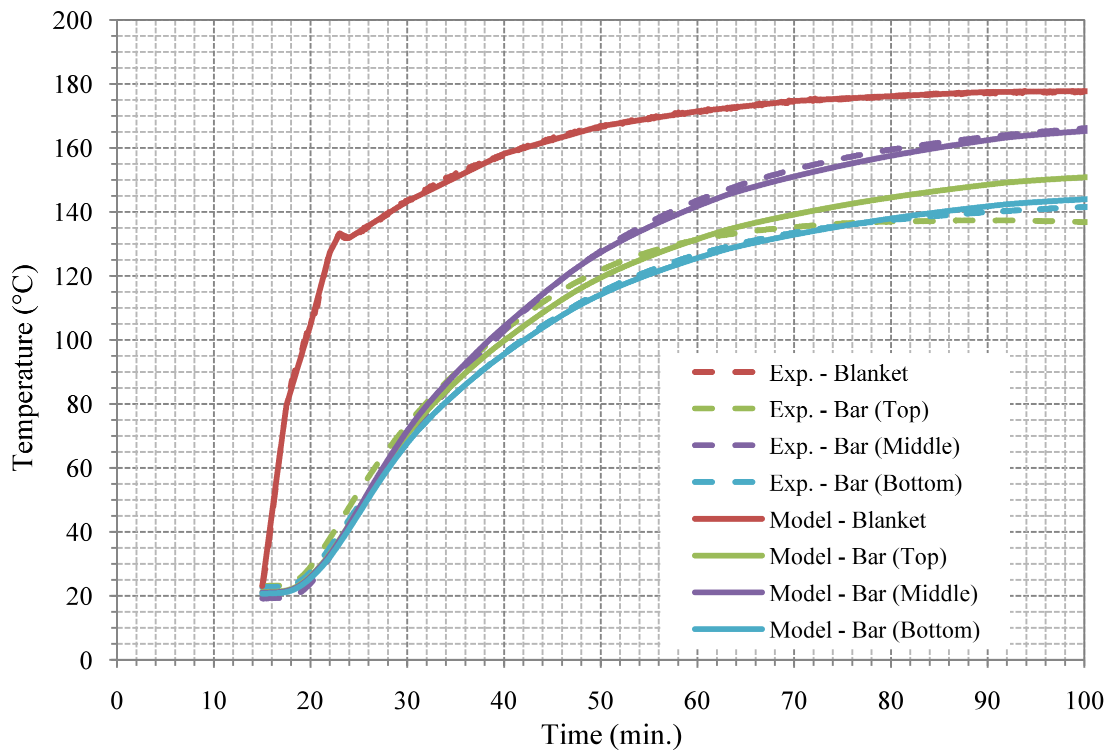

Figure 6.5: Temperature comparison between heat transfer model (with correction of the convective heat transfer coefficient) and experimental results from Steel_37%_e1

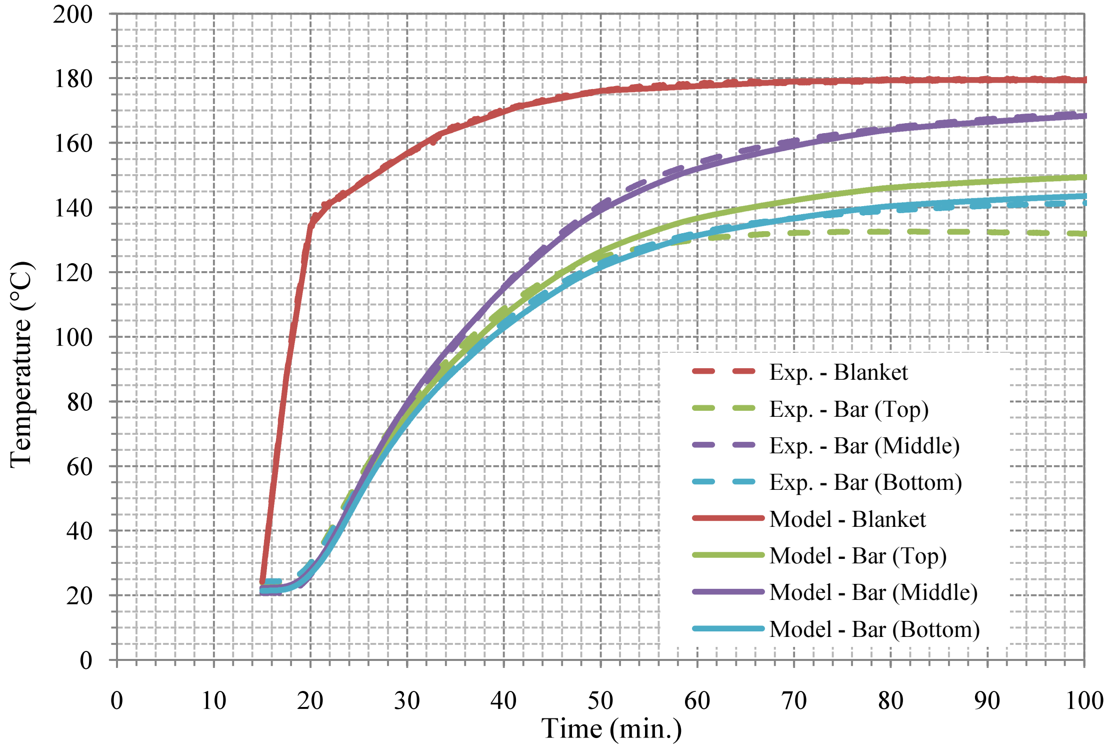

Figure 6.6: Temperature comparison between heat transfer model (with correction of the convective heat transfer coefficient) and experimental results from Steel_46%_e1

In the corrected model, the temperature at the bottom of the bonded length is fairly accurately estimated. The temperature at the top of the bonded length is overestimated after minute 60 and 50, for specimens Steel_37%_e1 and Steel_46%_e1 respectively. Typically it is hard to predict heat transfer on concrete above 100°C because of the various transient phenomena (vapour pressure of capillarity and gel water, decomposition of cement hydration products, and collapse of filling aggregate). And at temperatures even higher (160-170°C), the PP fibres melt.

This model could be the first step into the development of a heat transfer model capable of predicting temperatures within a reinforced concrete member, with concrete as the one used for this study. This could be an important addition to the cracking model described in Section 6.2, where the stresses produced by the thermal gradient were not considered in the analysis, but might be considered for future studies. In Figure 6.7, the mesh of the modelled system and a contour plot of the temperature distribution are displayed for test Steel_37%_e1 at minute 240.

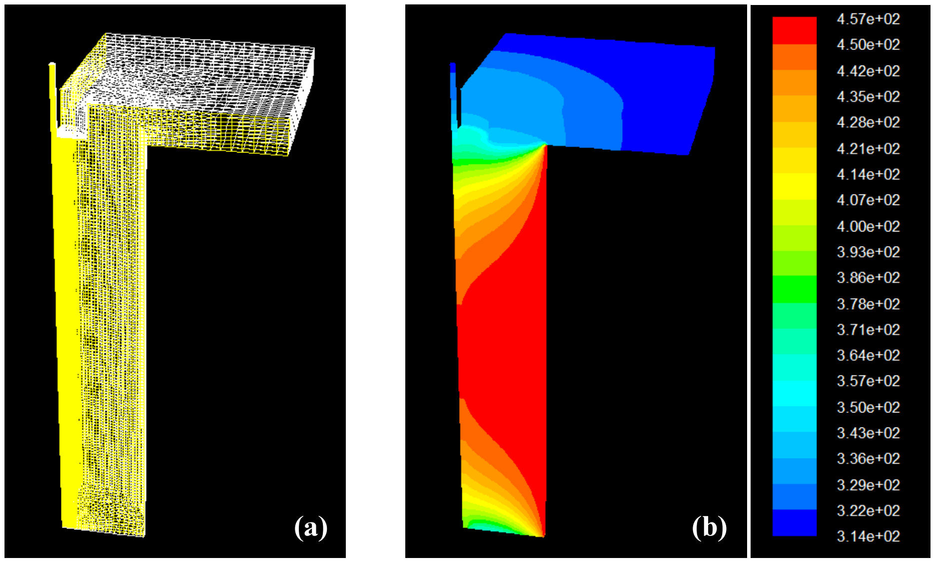

Figure 6.7: (a) Mesh of the heat transfer model and **(b)** contour plot of the steady state temperature (K) distribution for test Steel_37%_e1 at minute 240 (CFD tool FLUENT)

6.2 CFRP-Concrete Thermal Incompatibility Model

From the experimental data recorded in the EMPA large scale fire tests (see Sections 3.4.4 and 4.4), longitudinal splitting cracks were extensively observed for 45 mm thick slabs and to a smaller degree for thicker slabs, in particular for the surfaces not exposed to fire. Past research has shown that longitudinal splitting cracks are generated due to the large thermal expansion of CFRP tendons relative to that of concrete (Abdalla, 2006).

Past studies have been carried out to determine the effects of the difference in thermal expansion between CFRP tendons and the surrounding concrete, which may cause significant splitting stresses within the concrete cover during temperature increases (Aiello, Focacci & Nanni, 2001; Masmoudi, Zaidi & Gérard, 2005). Figure 6.8 shows the thermal incompatibility cracks for the slabs' top surface (non-exposed to high temperature) in the EMPA large scale fire tests.

Figure 6.8: Longitudinal thermal incompatibility cracks on the slabs' top surface after large scale fire test

6.2.1 Analytical model

An analytical model proposed by Aiello et al. (2001) was modified to determine the temperatures corresponding to the first appearance of longitudinal cracks in the large scale fire tests performed at EMPA. This is a first approach into the development of a more complex finite element model, which will be developed in future studies. The transverse section of a slab (45 mm thick) tested in the large scale fire tests, is shown in Figure 6.9.

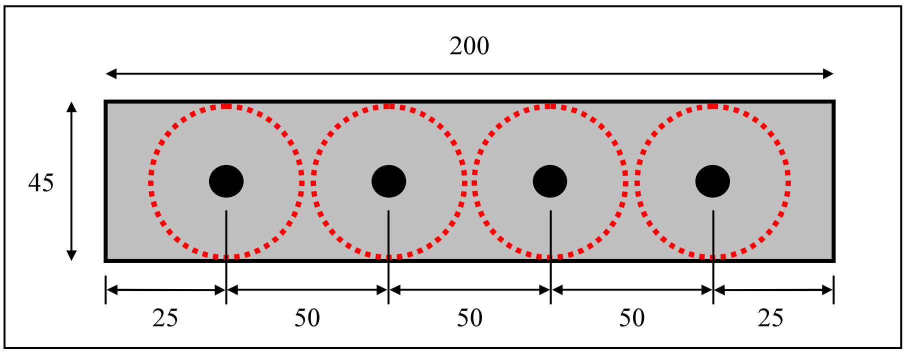

Figure 6.9: CFRP tendon and concrete effective area (red circles) for a 45 mm thick slab from the EMPA large scale fire test

This model is a theoretical, analytical approach to predicting the cracking phenomenon observed in these tests, and is based on the assumptions that:

- each CFRP tendon is treated independently, meaning that the clear spacing between two adjacent tendons is sufficient to avoid the occurrence of horizontal splitting cracks at the tendon's level;
- absence of CFRP tendon's boundary conditions at the bar terminations with the aim of focusing the analysis on the effects of stress interaction between CFRP tendons and HPSCC produced by thermal actions;
- the temperature in the CFRP tendon and the concrete increases uniformly (i.e. there is no thermal gradient) with the aim of focusing the analysis on the effects mentioned the previous assumption; and
- the elastic modulus and tensile strength of HPSCC decreases at high temperatures.

This analytical model describes the effect of a temperature increase (ΔT) on a CFRP tendon embedded in a concrete cylinder, the diameter of which is equal to the slab's thickness. A radial stress (σ_T) acts at the concrete cover, as shown in Figure 6.10.

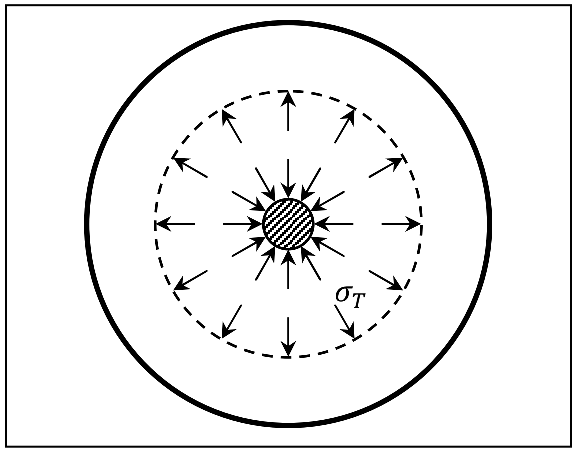

Figure 6.10: Radial stress acting at the interface CFRP-concrete under temperature increase

Three cases must be considered (see Figure 6.11); (a) before the stress in concrete reaches the tensile strength, (b) after the first cracks appear within the concrete, and (c) after the cracks reach the outer radius of the cylinder.

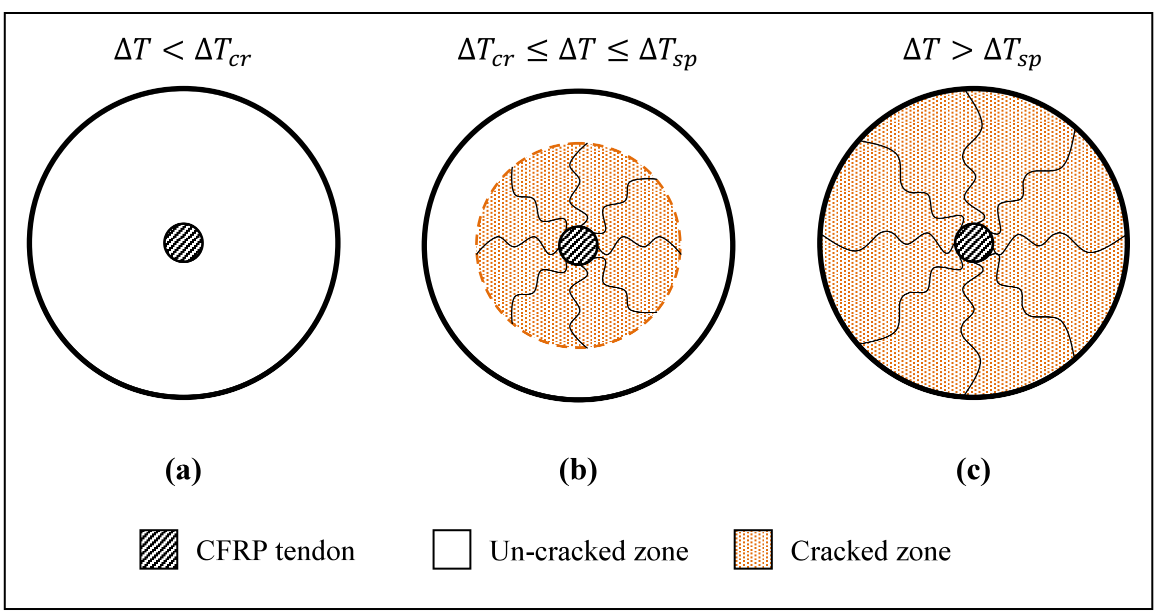

Figure 6.11: Three cases of the thermal incompatibility analytical model

Taking into account the axial symmetry of the system in the hypothesis of plane elasticity at a generic point in the concrete with a distance equal to x from the centreline of the CFRP tendon, the following equations were determined:

(a) $\Delta T \leq \Delta T_{cr}$ $\quad [\ \sigma_T \leq \sigma_\theta(r_{CFRP})\ ]$

$$\sigma_T = \frac{(T - T_i) \cdot \left(\alpha_{CFRP,tr} - \alpha_c\right)}{\frac{1}{E_c}\left(\frac{r_c^2 + r_{CFRP}^2}{r_c^2 - r_{CFRP}^2} + \nu_c\right) + \frac{1}{E_{CFRP,tr}}(1 - \nu_{CFRP.tr})} \tag{6.13}$$

– In concrete ($r_{CFRP} \leq x < r_c$)

$$\sigma_\rho(x) = \frac{r_{CFRP}^2}{r_c^2 - r_{CFRP}^2}\left(1 - \frac{r_c^2}{x^2}\right)\sigma_T \tag{6.14}$$

$$\sigma_\theta(x) = \frac{r_{CFRP}^2}{r_c^2 - r_{CFRP}^2}\left(1 + \frac{r_c^2}{x^2}\right)\sigma_T \tag{6.15}$$

(b) $\Delta T > \Delta T_{cr}$ $\quad [\ \sigma_T > \sigma_\theta(r_{CFRP})\ ]$

$$\sigma_T = \frac{(T - T_i) \cdot \left(\alpha_{CFRP,tr} - \alpha_c\right)}{\frac{1}{E_c}\left(\ln\frac{r_{cr}}{r_{CFRP}} \cdot \frac{r_c^2 + r_{cr}^2}{r_c^2 - r_{cr}^2} + \nu_c\right) + \frac{1}{E_{CFRP,tr}}\left(1 - \nu_{CFRP,tr}\right)} \tag{6.16}$$

– Inside the cracked zone ($r_{CFRP} \leq x < r_{cr}$)

$$\sigma_\rho(x) = \frac{r_{CFRP}^2}{r_c^2 - r_{CFRP}^2}\left(1 - \frac{r_c^2}{x^2}\right)\sigma_T \tag{6.17}$$

$$\sigma_\theta(x) = \frac{r_{CFRP}^2}{r_c^2 - r_{CFRP}^2}\left(1 + \frac{r_c^2}{x^2}\right)\sigma_T \tag{6.18}$$

– Outside the cracked zone ($r_{cr} \leq x < r_c$)

$$\sigma_\rho(x) = \frac{r_c}{x}\sigma_T \tag{6.19}$$

$$\sigma_\theta(x) = 0 \tag{6.20}$$

(c) $\Delta T > \Delta T_{sp}$ $[\ \sigma_T > \sigma_\theta(r_c)\ ]$

$$\sigma_T = \frac{(T - T_i) \cdot (\alpha_{CFRP} - \alpha_c)}{\frac{1}{E_c}\left(\ln\frac{r_{cr}}{r_{CFRP}} \cdot \frac{r_c^2 + r_{cr}^2}{r_c^2 - r_{cr}^2} + \nu_c\right) + \frac{1}{E_{CFRP,tr}}(1 - \nu_{TT})} \tag{6.21}$$

– In concrete ($r_{CFRP} \leq x < r_c$)

$$\sigma_\rho(x) = \frac{r_c}{x}\sigma_T \tag{6.22}$$

$$\sigma_\theta(x) = 0 \tag{6.23}$$

The notation in the model is as follows:

T	=	Temperature
T_i	=	Initial temperature
ΔT_{cr}	=	Temperature increase at which the first crack appears
ΔT_{sp}	=	Temperature increase at which the first crack reaches the cylinder's surface
σ_T	=	Radial compression acting in the concrete zone
σ_ρ	=	Concrete's stress in the radial direction
σ_θ	=	Concrete's stress in the circumferential direction
f_{st_crack}	=	Concrete's tensile strength determined from splitting tensile strength test
x	=	Distance from the centreline of the CFRP tendon
r_c	=	Radius of concrete cylinder
r_{CFRP}	=	Radius of CFRP tendon
r_{cr}	=	Radius of cracked concrete
α_c	=	Coefficient of thermal expansion of concrete
$\alpha_{CFRP,tr}$	=	Coefficient of thermal expansion of CFRP tendon in transverse direction
$E_{c,T}$	=	Elastic modulus of concrete at temperature T
$E_{c,0}$	=	Elastic modulus of concrete at ambient temperature
$E_{CFRP,tr}$	=	Elastic modulus of CFRP tendon in transverse direction
ν_c	=	Poisson's ratio of concrete at ambient temperature
$\nu_{CFRP,tr}$	=	Poisson's ratio of CFRP tendon in transverse direction

As mentioned in Section 3.1.2, CFRP tendons are made of longitudinal fibres and an epoxy resin. The epoxy resin plays an important role in the thermo-mechanical properties of the CFRP tendon's transverse direction. Steel reinforcements have relatively similar values of the coefficient of thermal expansion (CTE) to that of concrete. The CTE in the transverse direction of similar CFRP tendons to the ones used in this study is more than double the CTE of concrete (ACI, 2004). The transverse CTE of CFRP tendons can be up to six times that of concrete in some commercial FRPs brands (Gentry & Hudak, 1996).

The values of the CTE of the concrete and the CFRP tendon (transverse direction) were taken from past studies made by Whiting and Detwiler (1998) and ACI (2004). The value from a common brand of CFRP tendon is used. No variation of the thermo-mechanical properties of concrete and CFRP were considered to vary within the range of temperature in which the experiments were executed.

$$\alpha_c = 13 \times 10^{-6} \left[{}^{1}/{}_{\circ C}\right] \tag{6.24}$$

$$\alpha_{CFRP,tr} = 27 \times 10^{-6} \left[{}^{1}/{}_{\circ C}\right] \quad (transverse\ direction) \tag{6.25}$$

The elastic modulus of the CFRP tendon in the transverse direction was given by ACI (2004), for a common brand of CFRP tendon.

$$E_{CFRP,tr} = 10.3\ [GPa] \tag{6.26}$$

The values of Poisson's ratio for concrete and the CFRP tendons are considered not to be temperature dependant at the temperatures at which the model will be executed. The value of the Poisson's ratio for the CFRP tendons was taken from Vogel and Svecova (2007). Based on AASHTO (2005), if Poisson's ratio of the concrete is not determined by physical test, Poisson's ratio may be assumed as 0.20.

$$\nu_{CFRP,tr} = 0.35 \tag{6.27}$$

$$\nu_c = 0.20 \tag{6.28}$$

The tensile strength of the concrete at ambient temperature was determined from the measurements made in the splitting tensile strength tests (see Appendix B.2).

$$f_{st\_crack} = 5.30\ [MPa] \tag{6.29}$$

Very little attention has been devoted so far to the behaviour of concrete in tension, be it direct or indirect tension (splitting), at high temperatures (Li & Guo, 1993; Xu & Xu, 2000). Sri Ravindrarajah et al. (2002) executed several tests on concrete samples made from concrete containing fly ash and silica fume, similar to the mixture developed for this study. Tests were performed by measuring the splitting tensile strength of concrete samples after being exposed to high temperature (see Figure 6.12). Even though, for this model, it would be preferable to know the splitting tensile strength of concrete under high temperature, and not after the samples are subject to high temperature, data from past studies is scarce in literature and it is assumed that the splitting tensile strength of concrete under high temperature is similar to the splitting tensile strength after high temperature.

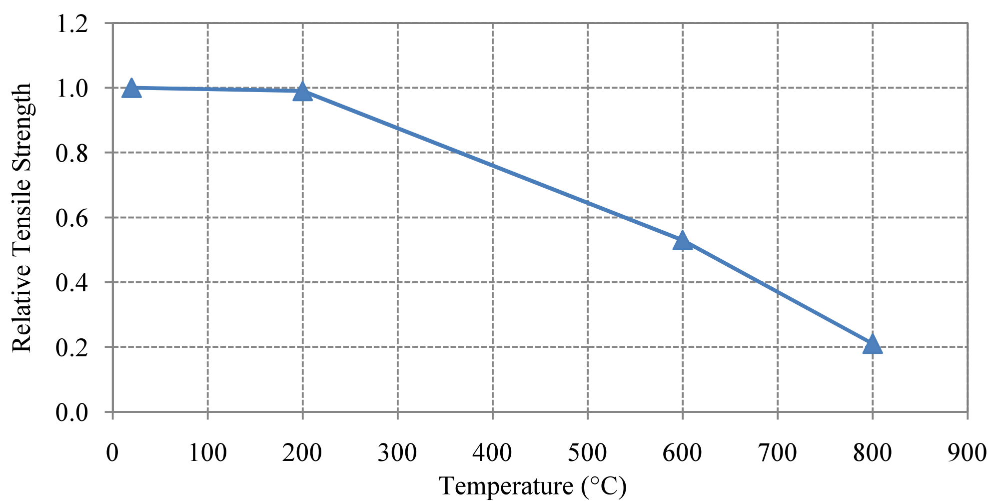

Figure 6.12: Variation of the tensile strength of concrete with increase in temperature

The modulus of elasticity of the concrete at ambient temperature was determined from the measurements executed in the compressive strength tests (see Appendix A.2).

$$E_{c,0} = 35.4\ [GPa] \tag{6.30}$$

Past studies have proven that there is a significant decrease in the modulus of elasticity of concrete with increased temperature (Xiao & König, 2004; Schneider, 1988), which is dependent on aggregate type, cement type and less significant original strength and water-cement ratio. A prior study, executed on a similar concrete mix as the one used for this study, concluded that the variation of the modulus of elasticity of concrete is as shown in Figure 6.13 (Kim, Kim & Lee, 2009). These data were obtained by measuring the modulus of elasticity in compressive strength tests executed under high temperatures.

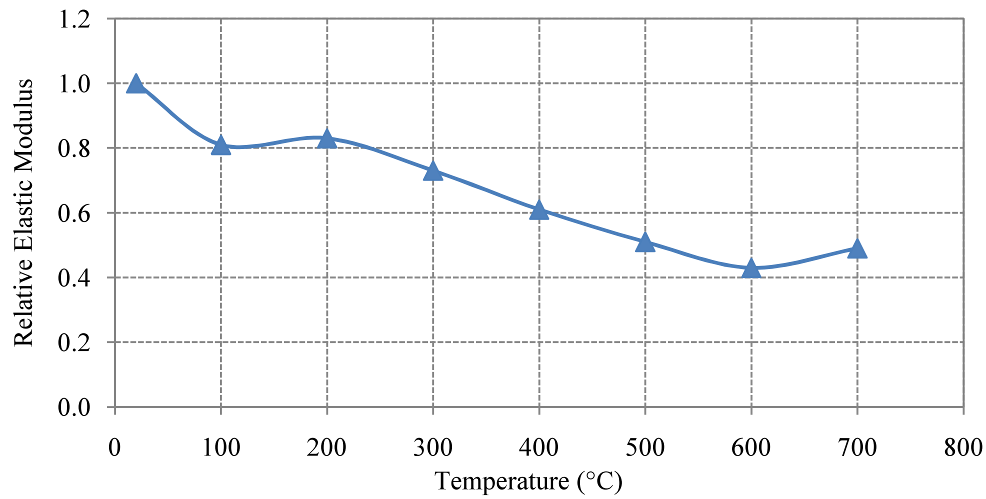

Figure 6.13: Variation of the concrete's modulus of elasticity with increase in temperature

6.2.2 Parametric study

The analytical model to predict longitudinal appearence was executed for the slabs tested in the EMPA large scale fire test with 45, 62 and 75 mm thickness. The temperature at which longitudinal splitting cracks first appeared on the slabs' top surface in the large scale fire tests was not recorded. Further experimental tests should be executed to validate this model. The model was executed under two conditions:

1. The system (CFRP tendon and concrete) increases its temperature uniformly, which is a first order approximation modelling of what happens at the fire exposed surface of the slab.
2. The concrete was kept at ambient temperature (20°C) while the tendon was heated, which is a first order approximation modelling of what happens at the non-fire exposed surface of the slab – ST.

Results of the model were plotted in a temperature-crack tip location graph for both conditions (see Figure 6.14). The plot indicates the temperature at which the crack first initiated (red circle) and the temperature at which the crack reached the outer radius of concrete (green rhombus).

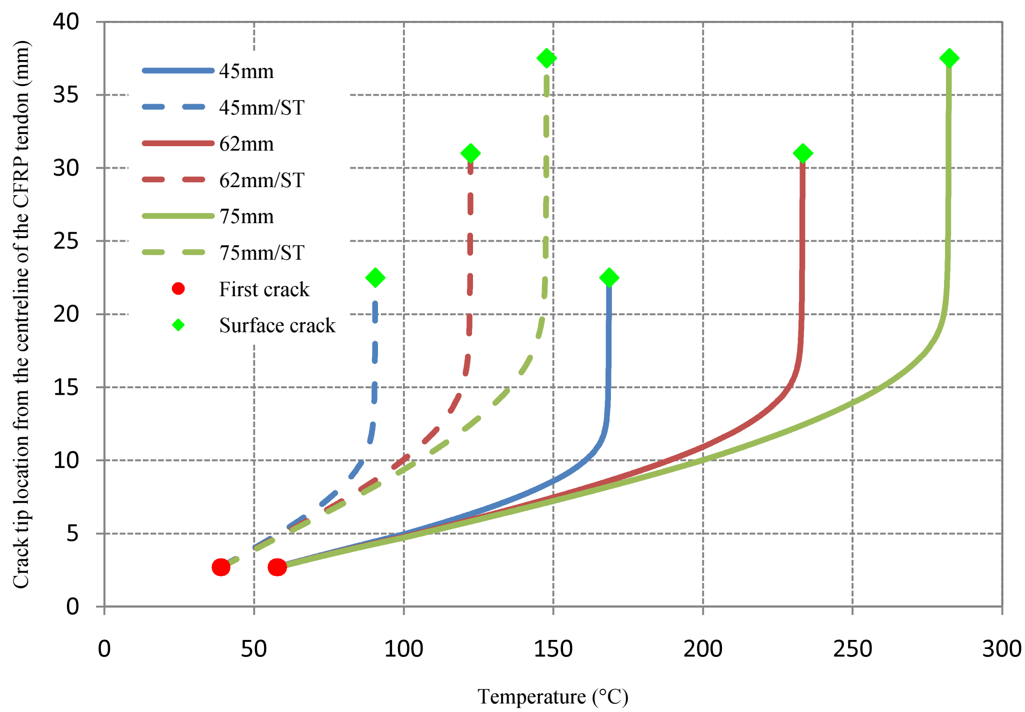

Figure 6.14: Relationship between crack propagation and temperature in the model

Independent of the amount of concrete cover, the crack first initiated at 58°C for the models in which the concrete experienced a uniform increase of temperature, and at 39°C for the models in which concrete was kept at ambient temperature while only the tendon was heated.

As the crack propagated from the CFRP tendon, unstable crack propagation occurred as it approached the outer radius of concrete. Relative to the concrete cover, the crack reached the outer radius of the concrete at 169, 233 and 282°C (for slabs 45, 62 and 75 mm thick, respectively) for the models in which concrete uniformly increased in temperature. For the models in which concrete was kept at ambient temperature while the tendon was heated, the crack reached the outer radius at 91, 122 and 148°C (for slabs 45, 62 and 75 mm thick, respectively).

The model revealed an explanation for why, in the large scale fire tests, more longitudinal cracks were observed on the top (unheated) surface of the slabs. Even though the exposed surface of the slab suffered tensile strength and modulus of elasticity degradation of concrete, the crack initiated and reached the surface of the slab at lower temperatures for the case of cracking on the unexposed face. Additional modelling is needed to better understand the implications of the thermal gradient in the concrete in the real fire tests on the appearance of splitting cracks in the concrete during the transient heating of a fire test.

The concrete's stresses in the circumferential direction, from the centreline of the CFRP tendon up to the outer radius of the concrete cover, were plotted for the models executed under both conditions (see Figure 6.15). This scenario is the moment before the crack first initiates ($\Delta T = \Delta T_{cr}$ and $\sigma_T = \sigma_\theta(r_{CFRP})$). From this graph, it can be concluded that when the crack first initiates at the CFRP tendon-concrete interface, the circumferential stresses were relative to the concrete cover, with slight difference as the cover increases (reason why the stress-axis was plotted in logarithmic scale).

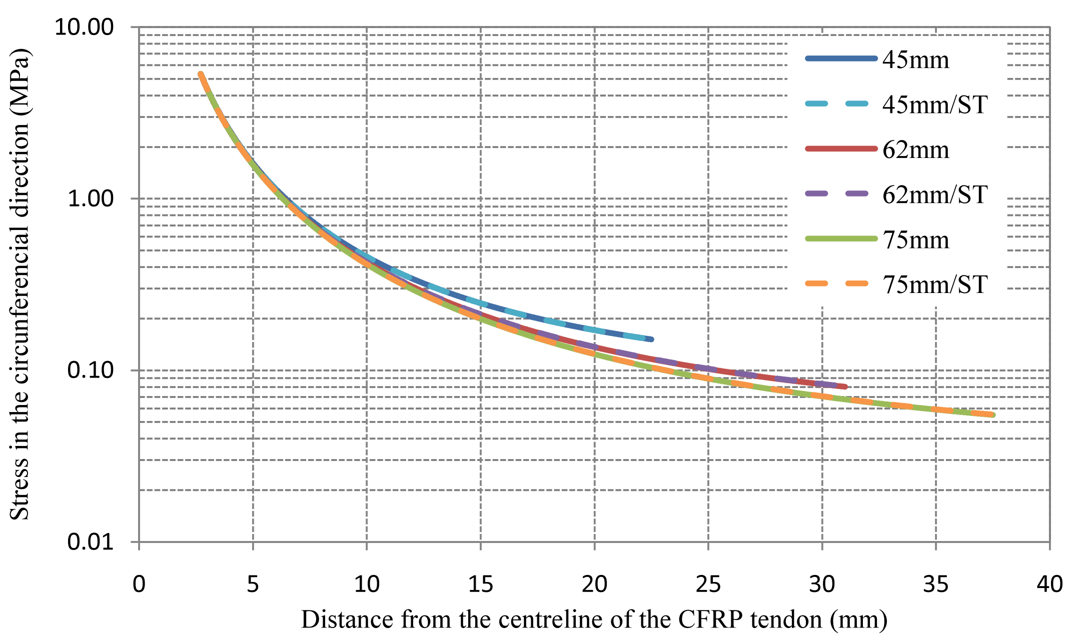

Figure 6.15: Stress in the circumferential direction before crack first initiated in the model

7 SUMMARY AND CONCLUSIONS

7.1 Summary

The experimental and numerical studies presented in this thesis sought to examine and compare the bond deterioration of CFRP tendons and steel prestressing wire with HPSCC at high temperatures. To achieve this objective, a detailed literature review was conducted; pullout tests of CFRP tendons and steel prestressing wire were executed at high temperature; various ancillary tests were performed to determine the mechanical and thermal properties of the steel prestressing wire, CFRP tendons, and HPSCC; analytical and numerical models were developed to better comprehend the observed phenomena involved in pullout tests at high temperatures; and results of a complementary research project (performed by others) of seven large scale fire tests on CFRP prestressed HPSCC slabs were analyzed.

CFRP pullout tests failed within the tendon and sand coating interface, either at ambient or high temperature. From post-pullout examination of the CFRP pullout samples, it was found that at ambient temperature the bond strength between the sand coating and the tendon degraded and at high temperatures the bond strength between the sand coating and the HPSCC degraded.

Steel pullout tests performed at ambient temperature failed because of yielding and eventual rupture of the steel prestressing wire at the loaded end, with maximum bond stresses almost three times higher than the bond strength developed in CFRP pullout samples. When the steel pullout sample where prestressed at high bond stresses, splitting failure of the concrete occurred few minutes after the heating blanket was turned on (moment at which the thermal gradient within concrete was higher).

In CFRP pullout tests, after bond failure, the sample developed residual bond strength, unlike steel pullout samples, which after failure experienced a total drop of its bond strength capacity.

7.2 Conclusions

A number of significant conclusions can be drawn from the experimental and numerical studies presented and discussed in this thesis. The key conclusions are:

- From the pullout tests executed on the CFRP tendons it was concluded that for sustained bond stresses below 45% of the bond strength at ambient temperature (approx. 20°C), no failure occurred as temperature increased.
- A clear and predictable correlation was found between the bond failure temperature of the regular PHPOT executed on CFRP pullout samples and the prestress load. As the prestress load increased the bond failure occurred at lower temperatures. A correlation between the CFRP tendon's prestress load and the epoxy's retained elastic modulus (determined with DMA) at the moment of failure was proposed. Since FRP bars are made by different manufacturer techniques, the correlation found in this study may only apply to this particular FRP bar, but could be reproduced for other FRP bars commercially available by performing DMA tests on representative samples of the bars.
- Loss of bond (anchorage) is potentially a governing factor for CFRP prestressing tendons in concrete at elevated temperatures. It seems that temperatures close to the value of the glass transition temperature (T_g) of the tendon's epoxy matrix (used also for adhering the bond enhancing sand coating to the surface of the bars) are critical for maintaining anchorage during a fire.
- From the pullout tests executed on the steel prestressing wire it was concluded that bond strength degraded between 18 and 29%, from the maximum stressed reached at ambient temperature pullout tests, when loaded at high temperature (160-170°C).
- A heat transfer model was developed and validated against the experimental data. It was found that it is hard to predict heat transfer on concrete above 100°C because of the various transient phenomena not considered by the model developed for this study (vapour pressure of capillarity and gel water,

decomposition of cement hydration products, collapse of filling aggregate, and melting of the PP fibres).

- The analytical model developed to predict the formation of longitudinal cracks observed at the large scale fire tests, revealed a possible explanation for why in the large scale fire tests more longitudinal cracks were observed on the top (unheated) surface of the slabs.
- Many aspects of bond performance at elevated temperature (for both FRP tendons and steel prestressing wires) remain poorly understood and require additional investigation.
- Critical temperatures for CFRP reinforced concrete members should not be determined in the same way as is done for steel reinforced concrete members.

7.3 Further Work

While the analytical and numerical models presented previously suggest that CFRP bars-concrete bond degradation at elevated temperatures can be characterized by pullout tests executed at high temperature, an effort should be made to correlate the bond degradation with the simpler tests, as the Dynamic Mechanical Analysis (DMA). An attempt to indicate the procedure in which this correlation could be determined was made in this study, limited by the maximum temperature accomplish by the pullouts experimental setup (190°C). CFRP pullout tests performed at higher temperatures, will allow for bond failure to occur as temperature increases in those pullout samples sustained at the lower stressing levels, which in this study did not failed. The following are additional recommended areas for future research:

- Test data is required on the deterioration of strength and stiffness for all FRP materials available for reinforcement of concrete. Standard test methods for characterization of thermo-mechanical deterioration would be helpful in this regard.

- Large scale fire tests should be performed with the objective of measuring the deterioration of bond strength of the CFRP tendons, keeping in mind that various, still undefined, phenomena will occur in an experimental test in which mechanical and thermal conditions are imposed.
- A discussion should be made about the appearance of longitudinal cracks for slabs tested in large scale fire tests was an effect of the thermal incompatibility of the orthotropic CFRP tendon with the HPSCC. The experimental data from the EMPA large scale fire tests and the thermal incompatibility model proved that cracking was more common on the non-exposed (unheated) surface of the slab.
- The influence of continuity and restraint on the fire performance of FRP reinforced concrete members should be investigated, both numerically and experimentally.

REFERENCES

AASHTO (2005). LRFD Bridge Design Specifications (3rd ed.). *American Association of State Highway and Transportation Officials*, Washington, D.C.

Abbasi, A. & Hogg, P.J. (2005). Temperature and environmental effects on glass fibre rebar: modulus, strength and interfacial bond strength with concrete. *Composites Part B: Engineering*, 36 (5), 394-404.

Abbasi, A. & Hogg, P.J. (2006). Fire testing of concrete beams with fibre reinforced plastic rebar. *Composites Part A: Applied Science and Manufacturing*, 37 (8), 1142-1150.

Abdalla, H. (2006). Concrete cover requirements for FRP reinforced members in hot climates. *Composite Structures*, 73 (1), 61-69.

ACI (1989). ACI 216R-89: Guide for Determining the Fire Endurance of Concrete Elements (Reapproved 2001). *American Concrete Institute*, Farmington Hills, MI.

ACI (2003). ACI 408R-03: Bond and development of straight reinforcing bars in tension. *American Concrete Institute*, Farmington Hills, MI.

ACI (2004). ACI 440.4R-04: Prestressing concrete structures with FRP tendons. *American Concrete Institute*, Farmington Hills, MI.

Aiello, M.A., Focacci, F. & Nanni, A. (2001). Effects of thermal loads on concrete cover of fibre-reinforced polymer reinforced elements: theoretical and experimental analysis. *ACI Materials Journal*, 98 (4), 332-339.

ASTM (2001). Test Method E119-01: Standard methods of fire test of building construction and materials. *American Society for Testing and Materials*, West Conshohocken, PA.

ASTM (2002). Test Method C469-02: Standard test method for static modulus of elasticity and Poisson's ratio of concrete in compression. *American Society for Testing and Materials*, West Conshohocken, PA.

ASTM (2003a). Test Method D3418-03: Standard test method for transition temperatures of polymers by differential scanning calorimetry. *American Society for Testing and Materials*, West Conshohocken, PA.

ASTM (2003b). Test Method C39/C39M-03: Standard test method for compressive strength of cylindrical concrete specimens. *American Society for Testing and Materials*, West Conshohocken, PA.

ASTM (2003c). Test Method A370-03: Standard test method and definitions for mechanical testing of steel products. *American Society for Testing and Materials*, West Conshohocken, PA.

ASTM (2004). Test Method C496-04: Standard test method for splitting tensile strength of cylindrical concrete specimens. *American Society for Testing and Materials*, West Conshohocken, PA.

ASTM (2009). Test Method C1611-09: Standard test method for slump flow of self-consolidating concrete. *American Society for Testing and Materials*, West Conshohocken, PA.

Bakis, C.E. (2008, October). Elevated temperature capability of epoxy resins: issues and developments. In *U.S.-South America Workshop: Innovative Materials for Civil Infrastructure, Research and Education*, Santiago, Chile.

Bingöl, A.F. & Gül, R. (2009). Residual bond strength between steel bars and concrete after elevated temperatures. *Fire Safety Journal*, 44 (6), 854-859.

Bisby, L.A., Green, M.F. & Kodur, V.K.R. (2005). Response to fire of concrete structures that incorporate FRP. *Progress in Structural Engineering and Materials*, 7 (3), 136–149.

Bisby L.A. & Kodur V.K.R. (2007). Evaluating the fire endurance of concrete slabs reinforced with FRP bars: Considerations for a holistic approach. *Composites Part B: Engineering*, 38 (5-6), 547-558.

Buchanan, A.H. (2001). *Structural Design for Fire Safety*. West Sussex, UK: John Wiley & Sons Ltd.

Burgoyne, C.J. (2001). Ductility and deformability in beams prestressed with FRP tendons (keynote paper). *Proceedings from CICE2001 FRP Composites in Civil Engineering* J.G. Teng, (Ed.), 1, 15-26.

Chen, A.C.T. & Chen, W.F. (1976). Nonlinear analysis of concrete splitting tests. *Computers & Structures*, 6 (6), 451-457.

Choi, Y. & Yuan, R.L. (2004). Experimental relationship between splitting tensile strength and compressive strength of GFRC and PFRC. *Cement and Concrete Research*, 35 (8), 1587-1591.

Cosenza, E., Mannfredi, G. & Realfonzo, R. (1995). Analytical modelling of bond between FRP reinforcing bars and concrete. *Proceedings from 2nd International RILEM Symposium on Non-matallic (FRP) Reinforcement for Concrete Structures*. L. Taerwe (Ed.), 164-171.

CNR (2004). CNR-DT 200/2004: Guide for the design and construction of externally bonded FRP systems for strengthening existing structures. *National Research Council*, Rome, Italy.

CNR (2006). CNR-DT 203/2006: Guide for the design and construction of concrete structures reinforced with fiber-reinforced polymer bars. *National Research Council*, Rome, Italy.

CSA (2002). CSA-S806-02: Design and construction of building components with fibre-reinforced polymers – Annex D: Test method for development length of FRP reinforcements. *Canadian Standards Association*, Mississauga, Ontario.

De Lorenzis, L., Rizzo, A. & La Tegola, A. (2002). A modified pull-out test for bond of near-surface mounted FRP rods in concrete. *Composites Part B: Engineering*, 33 (8), 589-603.

Drysdale, D. (1998). *An Introduction to Fire Dynamics* (2nd ed.). West Sussex, UK: John Wiley & Sons Ltd.

Eligehausen, R., Popov, E.P. & Bertero V.V. (1983). Local bond stress–slip relationships of deformed bars under generalized excitations. *Earthquake Engineering Research Center Report No. 83/23*, Berkeley, CA: University of California.

Eurocode 2 (2002). EN 1992-1-2:2002: Design of concrete structures - Part 1.2: General rules - Structural fire design. *European Committee for Standardization*, Brussels, Belgium.

Faoro, M. (1992). Development and conversion of the properties of ACM into prestressing tendons for bridges and structures. *1st International Conference on Advanced Composite Materials in Bridges and Structures*, Sherbrooke, Quebec.

fib (2007). fib TG 9.3: FRP reinforcement for RC structures. *Fédération Internationale du Béton*, Lausanne, Switzerland.

Findley, W.N., Lai, J.S. & Onaran, K. (1976). *Creep and relaxation of nonlinear viscoelastic materials*. Toronto, Onatario: North Holland Publishing Company.

Fluent Inc. (2005). FLUENT 6.2 user's guide. Lebanon, NY: Fluent Inc.

Fujisaki, T., Nakatsuji, T. & Sugita, M. (1993). Research and development of grid shaped FRP reinforcement. *American Concrete Institute Special Publication*, 138, 177-192.

Gentry, T.R. & Hudak, C.E. (1996, August), Thermal Compatibility of Plastic Concrete Composite Reinforcement and Concrete. *Proceedings from Second International Conference on Advanced Composites Material in Bridges and Structures (ACMBS-II)*, Montréal, Québec. 149-156.

Ghaffar, A., Chaundhry, M.A. & Kamran Ali, M. (2005). A new approach for measurement of tensile strength of concrete. *Journal of Research (Science), Bahauddin Zakariya University, Multan, Pakistan*, 16 (1), 1-9.

ISIS (2006). Design Manual 3 (v2): Reinforcing concrete structures with fibre reinforced polymers. *Intelligent Sensing for Innovative Structures*, Winnipeg, Canada.

IEC (1982). IEC 584-2: Couples thermoélectriques – Part 2: Tolérances. *International Electrotechnical Commission*, Genève, Suisse.

Incropera, F.P. & DeWitt, D.P. (2002), *Fundamentals of Heat and Mass Transfer*. New York, NY: John Wiley & Sons.

ISO (1999). ISO 834-1:1999: Fire Resistance Tests - Elements of Building Construction - Part 1: General Requirements. *International Organization for Standardization*, Geneva, Switzerland.

Katz, A., Berman, N. & Bank, L.C. (1999). Effect of high temperature on bond strength of FRP rebars. *Journal of Composites for Construction*, 3 (2), 73-81.

Katz, A. & Berman, N. (2000). Modelling the effect of high temperature on the bond of FRP reinforcing bars to concrete. *Cement & Concrete Composites*, 22 (6), 433-443.

Khoury, G.A. (2000). Effect of fire on concrete and concrete structures. *Progress in Structural Engineering and Materials*, 2 (4), 429-447.

Khoury, G.A. (2008). Polypropylene fibres in heated concrete. Part 2: Pressure relief mechanisms and modelling criteria. *Magazine of Concrete Research*, 60 (3), 189-204.

Kim, G.Y., Kim, Y.S. & Lee, T.G. (2009) Mechanical properties of high-strength concrete subjected to high temperature by stressed test. *Transaction of Nonferrous Metals Society of China*, 19 (s1), s128-s133.

Kodur, V.K.R. & Baingo, D. (1998). *Fire resistance of FRP reinforced concrete slabs. IRC Internal Report No. 758*. Ottawa, ON: National Research Council of Canada.

Kuennen, T. (1996). *Silica fume resurges*. New York, NY: Concrete Products®.

Lamond, J.F. (1983). Twenty-five years' experience using fly ash in concrete. *American Concrete Institute Special Publication*, 79, 47-70.

Li, W. & Guo, ZhH. (1993). Experimental investigation on strength and deformation of concrete under high temperature. *China Journal of Building Structures*, 14 (1), 8–16 [in Chinese].

Li, G., Lee-Sullivan, P. & Thring R.W. (2000). Determination of activation energy for glass transition of an epoxy adhesive using dynamic mechanical analysis. *Journal of Thermal Analysis and Calorimetry*, 60 (2), 377-390.

Lie, T.T. (1992). *Structural Fire Protection: Manuals and Reports on Engineering Practice No. 78*. New York, NY: American Society of Civil Engineers [ASCE].

Lubin, G. (Ed.). (1981). *Handbook of composites*. New York, US: Van Nostrand Reinhold.

Lublóy, É., Balázs, G.L., Borosnyói, A. & Nehme, S.G. (2005, December). Bond of CFRP wires under elevated temperature. In *International Symposium on Bond of FRP in Structures (BBFS 2005)*, Hong Kong, China.

Malhotra, V.M. & Mehta, P.K. (1996). *Pozzolanic and cementitious materials*. Amsterdam, Netherlands: Overseas Publisher Association.

Masmoudi, R., Zaidi, A. & Gérard, P. (2005). Transverse thermal expansion of FRP bars embedded in concrete. *Journal of Composites for Construction © ASCE*, 9 (5), 377-387.

Morley, P. & Royles, R. (1983). Response of the bond in reinforcing concrete to high temperatures. *Magazine of Concrete Research*, 35 (123), 67-74.

Nakagawa, H., Kobayashi, M., Suenaga, T., Ouchi, T., Watanabe, S. & Satoyama, K. (1993). Application of three-dimensional fabric reinforced concrete to building panels. *American Concrete Institute Special Publication*, 138, 211-232.

NEFCOM Corporation (1998). *Technical Leaflet 3: Fire resistance of concrete slabs reinforced by NEFMAC*. Tokyo, Japan: NEFCOM Corp.

Nemati, K.M., Gardoni, P. & Noguchi, T. (2008). On modulus of elasticity of high-strength concrete. *Proceedings from International Conference on Construction and Building Technology (ICCBT 2008)*, C (14), 159-172.

OGUC (2001). *Ordenanza General de Urbanismo y Construcciones*. Ministerio de Vivienda y Urbanismo, Chile.

Okamoto, T., Matsubara, S., Tanigaki, M. & Hasuo, K. (1993). Practical application and performance of PPC beams reinforced with braided FRP bars. *American Concrete Institute Special Publication*, 138, 875-894.

Reinhart, T.G. (1998). *Handbook of composites: Overview of composites materials* S.T. Peters, (Ed.). London, UK: Chapman & Hall.

Rossetti, V.A., Galeota, D., & Giammatteo, M.M. (1995). Local bond stress-slip relationships of glass fibre reinforced plastic bars embedded in concrete. *Material and Structures*, 28 (6), 340–344.

Sakashita, M. (1997, October). Deflection of continuous fiber reinforced concrete beams subjected to loaded heating. *Third International Symposium on Non-Metallic (FRP) Reinforcement for Concrete Structures* (pp. 51-58). Sapporo, Japan: Japan Concrete Institute, 2, 51-58.

Sena Cruz, J. & Barros, J. (2004). Modeling of bond between near-surface mounted CFRP laminate strips and concrete. *Computers and Structures*, 82 (17-19), 1513-1521.

Schneider, U. (1988). Concrete at high temperatures – a general review. *Fire Safety Journal*, 13 (1), 55-68.

Schwartz, M.M. (2002). *Encyclopedia of materials, parts and finishes* (2nd ed.). Boca Raton, Florida: CRC Press.

Seica, M.V. & Packer J.A. (2007). FRP materials for the rehabilitation of tubular steel structures for underwater applications. *Journal of Composites Structures*, 80 (3), 440-450.

Senthilkumar, S.R.R & Natesan, S.C. (2004). Effect of polypropylene fibre addition on restrained plastic shrinkage cracking of cement composites. *Journal of the Institution of Engineers (India)*, 85, 100-106.

Sinclair, W. & Groves, G.W. (1986). The microstructure of Portland cement-silica fume pastes. *Journal of Materials Science Letters*, 5 (1), 101-102.

Sri Ravindrarajah, R., Lopez, R. & Reslan, H. (2002, March). Effect of elevated temperature on the properties of high-strength concrete containing cement supplementary materials. In *9th International Conference on Durability of Building Materials and Components*, Brisbane, Australia.

Tanano, H., Masuda, Y., Kage, T., Fukuyama, H., Nishida, I. & Hashimoto, T. (1995). Fire resistance of continuous fibre reinforced concrete. In L. Taerwe (Ed.), *Proceeding of the Second International RILEM Symposium: Non-metallic (FRP) Reinforcement for Concrete Structures* (pp. 368-375). London, UK: E&FN Spon.

Terrasi, G.P. (2007, July). Prefabricated thin-walled structural elements made from HPC prestressed with pultruded carbon wires. In *8th International Symposium on FRPs for Reinforcement Concrete Structures*, Patras, Greece.

Terrasi, G.P., Affolter, Ch., Barbezat, M. & Bättig, G. (2008, July). Increasing the acceptance of high performance concrete prestressed with CFRP. In *Fourth International Conference on FRP Composites in Civil Engineering (CICE 2008)*, Zurich, Switzerland.

Valcuende, M. & Parra, C. (2009). Bond behaviour of reinforcement in self-compacting concretes. *Construction and Building Materials*, 23 (1), 162-170.

Videla C. (2007). Concrete Technology. P*ost-graduate course modules*. Pontificia Universidad Católica de Chile, Santiago, Chile.

Vogel, H. & Svecova, D. (2007). Thermal compatibility and bond strength of FRP reinforcement in prestressed concrete applications. *Journal of Composites for Construction © ASCE*, 11 (5), 459-468.

Wesche, K. (Ed.). (1991). *Fly ash in concrete: properties and performance*. London, UK: E&FN Spon.

White, D.J. & Take, W.A. (2002) GeoPIV: Particle Image Velocimetry (PIV) software for use in geotechnical testing. *Cambridge University Engineering Department Technical Report, CUED/D-SOILS/TR322*.

Whiting, D. & Detwiler, R. (1998) *Report 410: Silica fume concrete for bridge decks.* Washington, DC: National Academy Press.

Wilson, A.F., Tsiatas, G., Taggart, D.G., Doleski, R.F., Kim, T.J., Horii, K., Yoshida, H., Yokoo, M. & Yagi, K. (2002, June). Investigation of interfacial bond strength in CFRP rod reinforced concrete. In *Third International Conference on Composites in Infrastructure*, San Francisco, CA.

Xiao, J. & König, G. (2004). Study on concrete at high temperature in China – an overview. *Fire Safety Journal*, 39 (1), 89-103.

Xu, Y. & Chung, D.D.L. (2000). Cement of high specific heat and high thermal conductivity, obtained using silane and silica fume as admixtures. *Cement and Concrete Research*, 30 (7), 1175-1178.

Xu, Y. & Xu, ZhSh. (2000). Experimental study on strength of concrete after high temperature. *China Concrete 2000* [in Chinese].

Zain, M.F.M., Mahmud, H.B., Ilham, A. & Faizal, M. (2002). Prediction of splitting tensile strength of high-performance concrete. *Cement and Concrete Research*, 32 (8), 1251-1258.

A APPENDIX A: CONCRETE COMPRESSIVE STRENGTH TEST RESULTS

The compressive strength of concrete was experimentally determinate by executing compressive strength tests at 7, 14, 28, 49 and 84 days. Digital image correlation analysis (Section 3.4.5.4) was used on the samples tested at 49 and 84 days. This allowed to experimentally determinate the strains at the sample's surface. Three samples were tested at each date.

A.1 Digital Image Correlation Analysis

This analysis was performed for the samples tested at 49 (date of the first pullout test) and 84 days (date of the last pullout test), and used to calculate the modulus of elasticity of concrete as explained in Section 3.4.5.5.

A.1.1 HPSCC_49d_c1

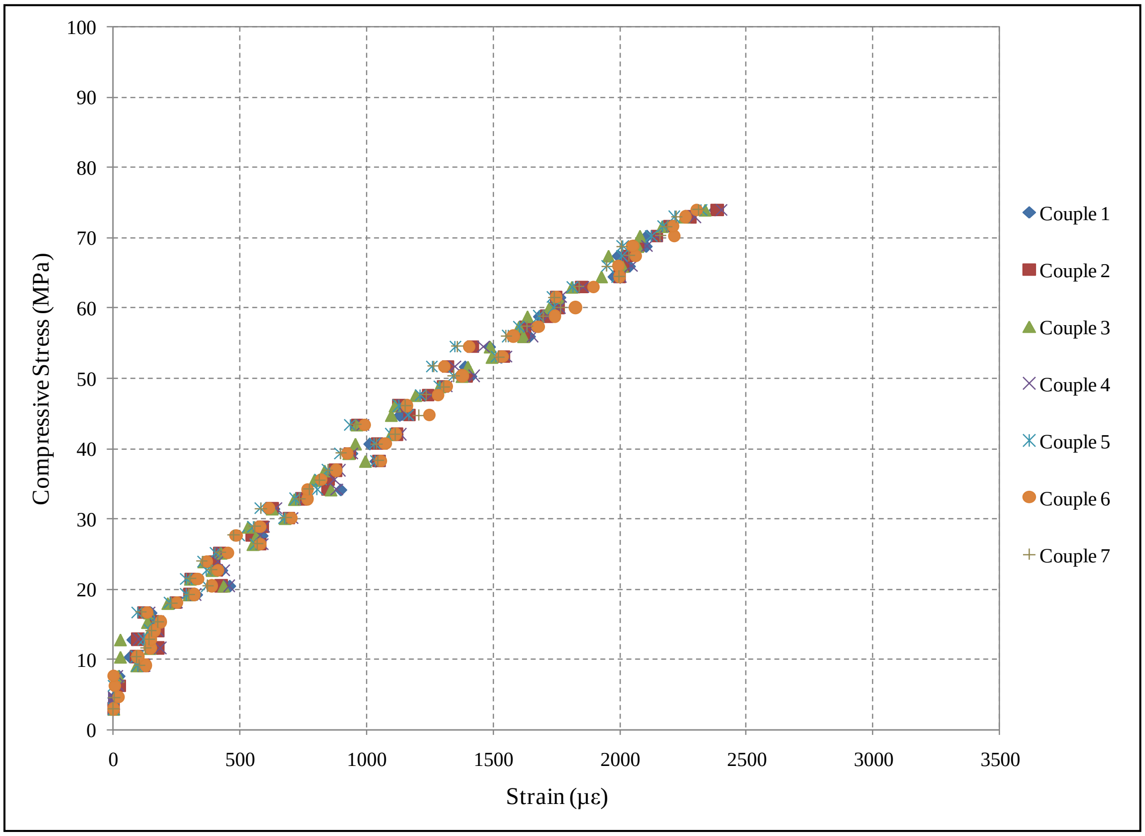

Figure A.1: Stress versus strain curve for HPSCC_49d_c1

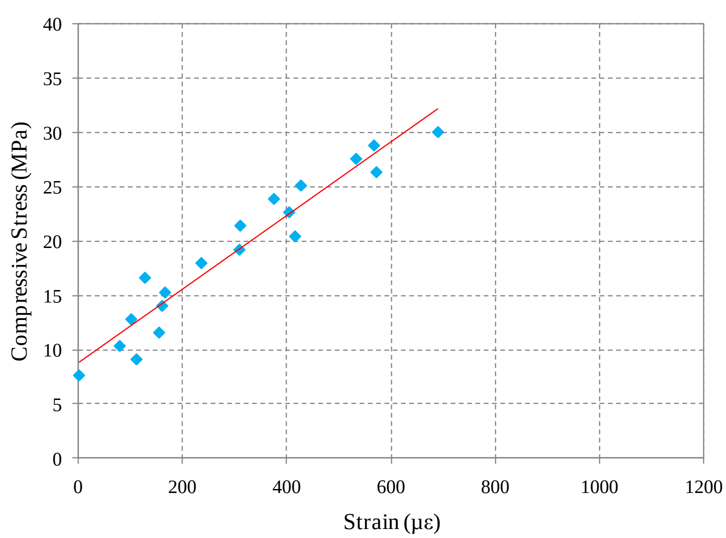

Figure A.2: Modulus of elasticity determination for HPSCC_49d_c1

A.1.2 HPSCC_49d_c2

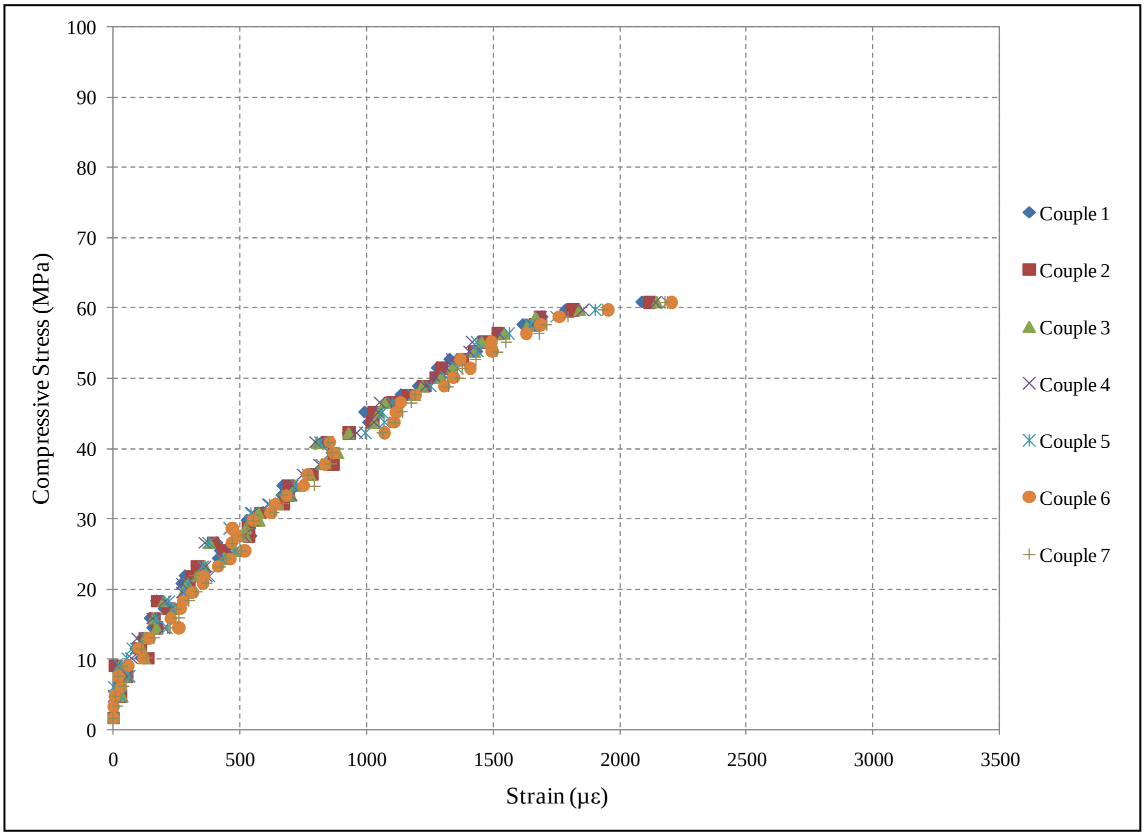

Figure A.3: Stress versus strain curve for HPSCC_49d_c2

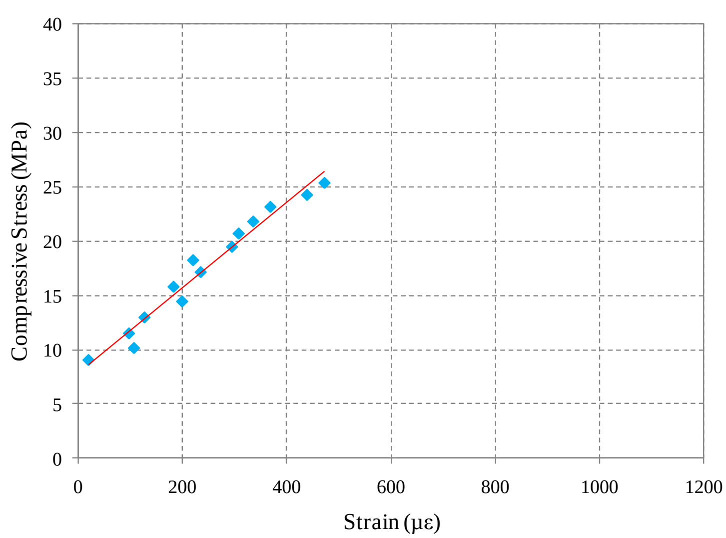

Figure A.4: Modulus of elasticity determination for HPSCC_49d_c2

A.1.3 HPSCC_49d_c3

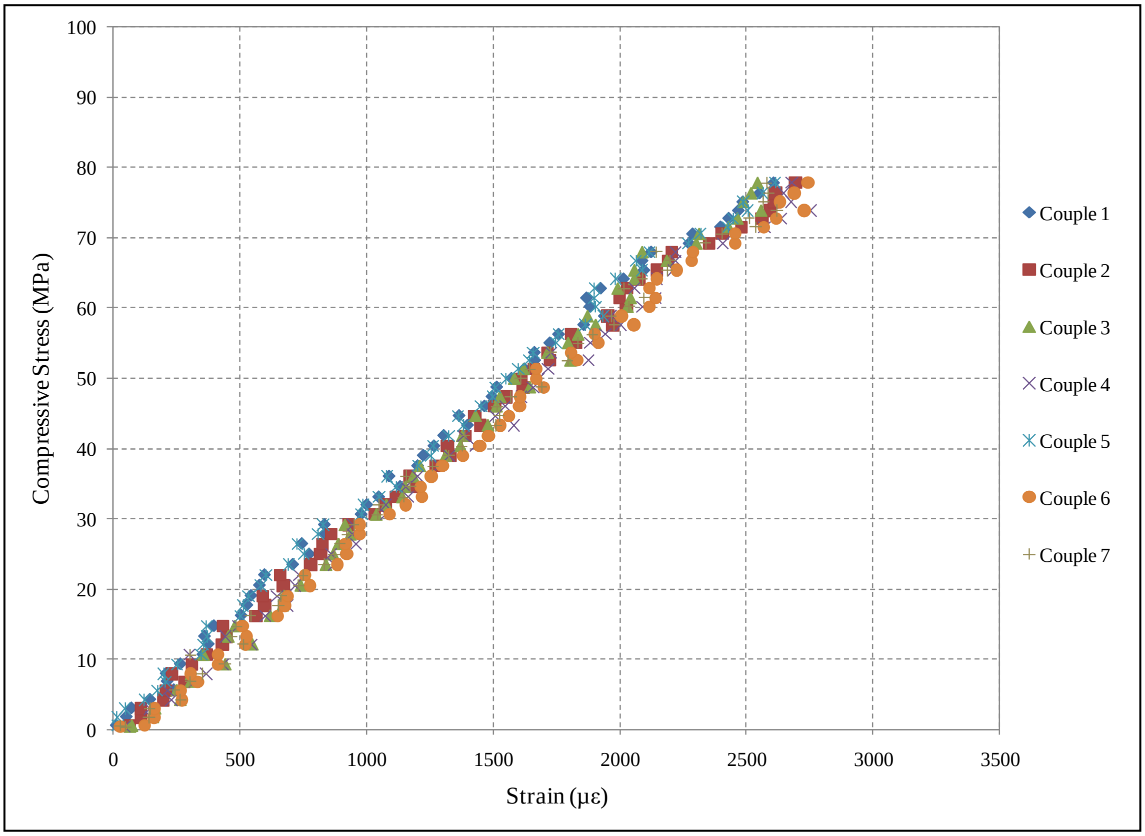

Figure A.5: Stress versus strain curve for HPSCC_49d_c3

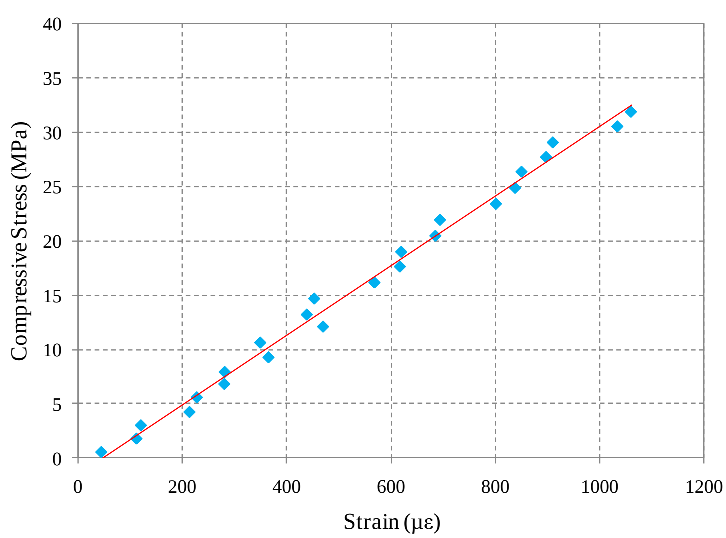

Figure A.6: Modulus of elasticity determination for HPSCC_49d_c3

A.1.4 HPSCC_84d_c1

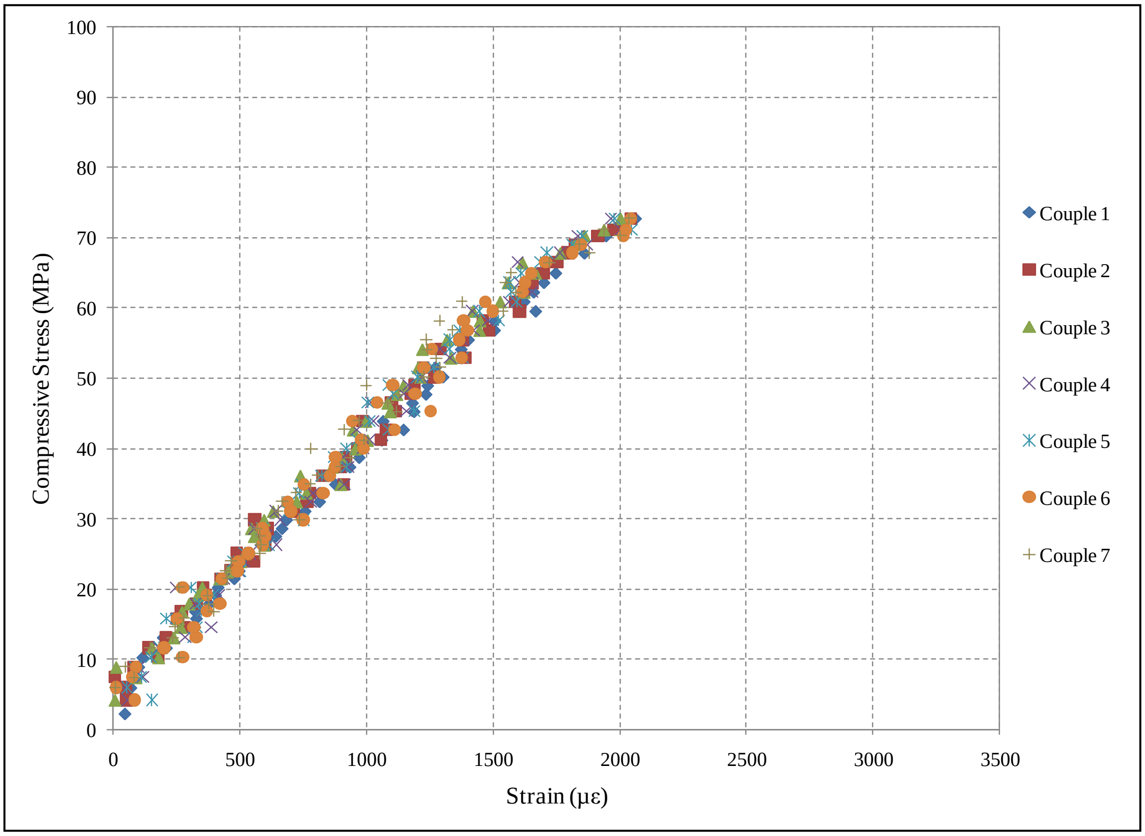

Figure A.7: Stress versus strain curve for HPSCC_84d_c1

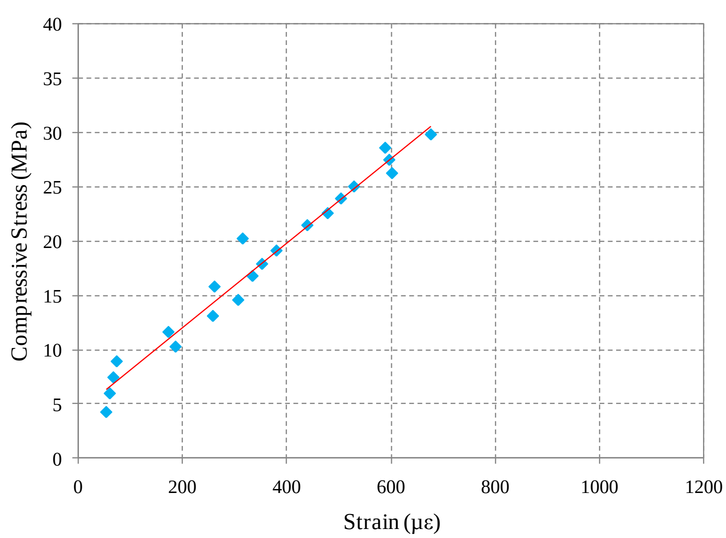

Figure A.8: Modulus of elasticity determination for HPSCC_84d_c1

A.1.5 HPSCC_84d_c2

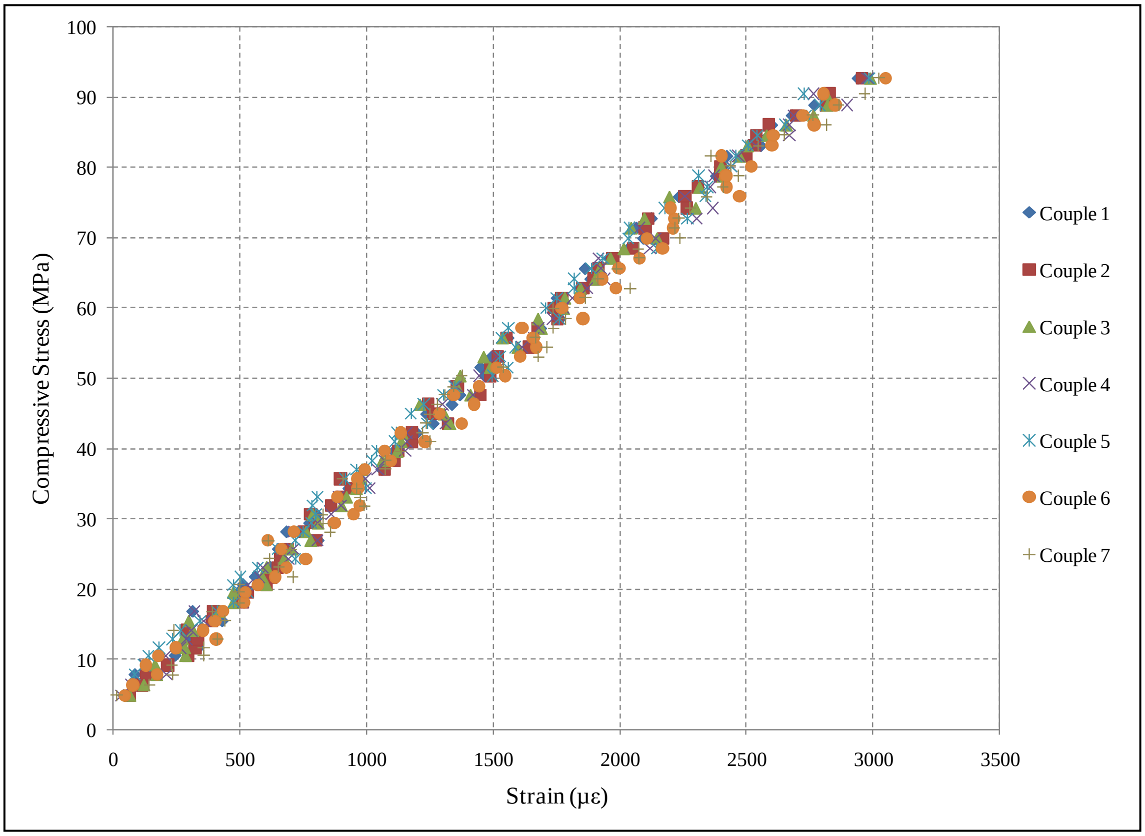

Figure A.9: Stress versus strain curve for HPSCC_84d_c2

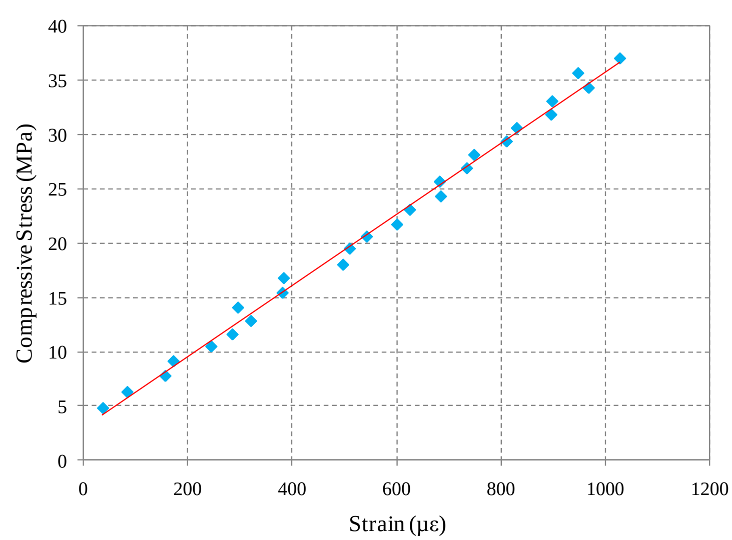

Figure A.10: Modulus of elasticity determination for HPSCC_84d_c2

A.1.6 HPSCC_84d_c3

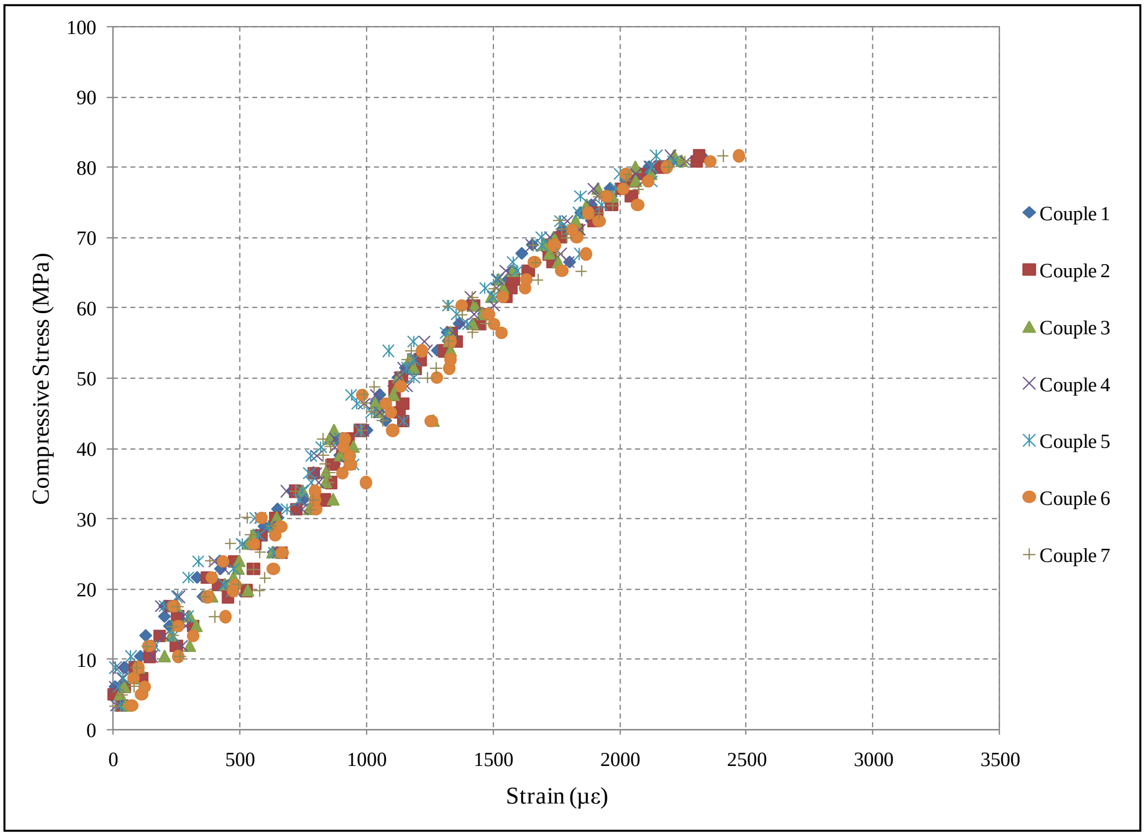

Figure A.11: Stress versus strain curve for HPSCC_84d_c3

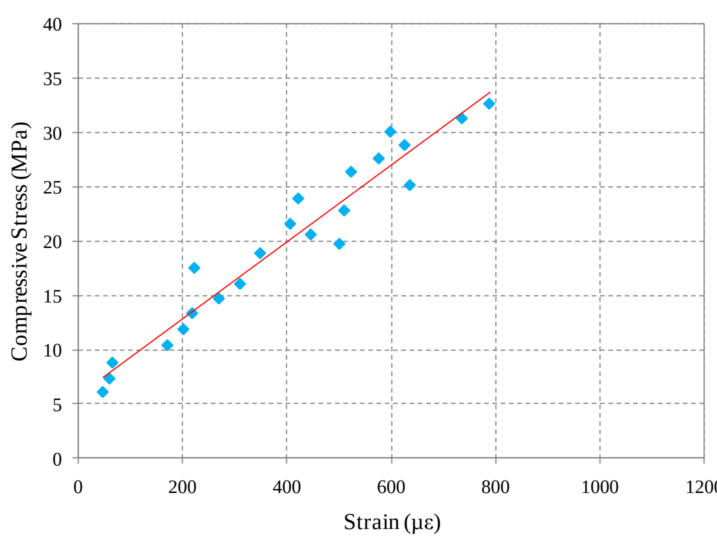

Figure A.12: Modulus of elasticity determination for HPSCC_84d_c3

A.2 Summary

The results are display in Table A.1, for the tests executed at 7, 14, 28, 49 and 84 days.

Table A.1: Test results of the concrete compressive strength tests

Test label	Compressive Strength			Maximum Strain			Modulus of Elasticity		
	f_c' (MPa)	Average f_c' at "t" days (MPa)	Standard Deviation (MPa)	ε_{max} (με)	Average ε_{max} at "t" days (με)	Standard Deviation (με)	E_c (GPa)	Average E_c at "t" days (GPa)	Standard Deviation (GPa)
HPSCC_7d_c1	46.01			-			-		
HPSCC_7d_c2	48.47	48.15	1.99	-	-	-	-	-	-
HPSCC_7d_c3	49.95			-			-		
HPSCC_14d_c1	63.89			-			-		
HPSCC_14d_c2	54.52	58.47	4.86	-	-	-	-	-	-
HPSCC_14d_c3	56.99			-			-		
HPSCC_28d_c1	71.54			-			-		
HPSCC_28d_c2	71.05	70.22	1.87	-	-	-	-	-	-
HPSCC_28d_c3	68.09			-			-		
HPSCC_49d_c1	74.01			2349			33.85		
HPSCC_49d_c2	61.43	71.09	8.58	2028	2338	305	39.38	35.09	3.83
HPSCC_49d_c3	77.83			2638			32.03		
HPSCC_84d_c1	72.77			2019			38.92		
HPSCC_84d_c2	92.76	82.60	10.00	2991	2435	500	32.77	35.72	3.08
HPSCC_84d_c3	82.27			2296			35.46		

Past study performed on high-strength concrete have developed formulations that predict the modulus of elasticity of concrete in terms of its compressive strength and its density (Nemati, Gardoni & Noguchi, 2008). According to this study, the equation to be used to predict the modulus of elasticity calculations is:

$$E_c = k_1 \cdot k_2 \cdot 33.5 \cdot \left(\frac{\gamma}{2.4}\right)^2 \cdot \left(\frac{f_c{}'}{60}\right)^{1/3} \qquad \text{(A.1)}$$

Where:

$$E_c = modulus\ of\ elasticity\ [GPa]$$
$$\gamma = density\ of\ concrete\ [ton/m^3]$$
$$f_c{}' = compressive\ strength\ [MPa]$$
$$k_1 = correction\ factor\ corresponding\ to\ coarse\ aggregates$$
$$k_2 = correction\ factor\ corresponding\ to\ mineral\ admixtures$$

For the compressive strength tests in which the modulus of elasticity was measured using digital image correlation analysis, a comparison was made with the equation developed by Nemati, as showed in Table A.2. The density of each sample was measured before every compressive test.

Table A.2: Correlation between measured and predicted modulus of elasticity of concrete

Test	**f_c' (MPa)**	**Density (ton/m^3)**	**E_c (GPa)**	**Nemati's E_c calculation (GPa)**	**Measured E_c / Predicted E_c**
HPSCC_49d_c1	74.01	2.39	33.85	37.29	0.91
HPSCC_49d_c2	61.43	2.39	39.38	35.20	1.12
HPSCC_49d_c3	77.83	2.40	32.03	38.40	0.83
HPSCC_84d_c1	72.77	2.41	38.92	37.87	1.03
HPSCC_84d_c2	92.76	2.42	32.77	41.26	0.79
HPSCC_84d_c3	82.27	2.43	35.46	40.13	0.88

Figure A.13, shows the compressive and tensile strength development of concrete from the mechanical tests executed in this research. The tensile strength is calculated from the initial crack reduction analysis performed in Appendix B.1.

The compressive strength of the concrete is predicted from the compressive strength tests executed at 7, 14 and 28 days. This was done from the predictive equations developed by Ross, Venuat, Hummel, Gardner, and ACI 209 (Videla, 2007).

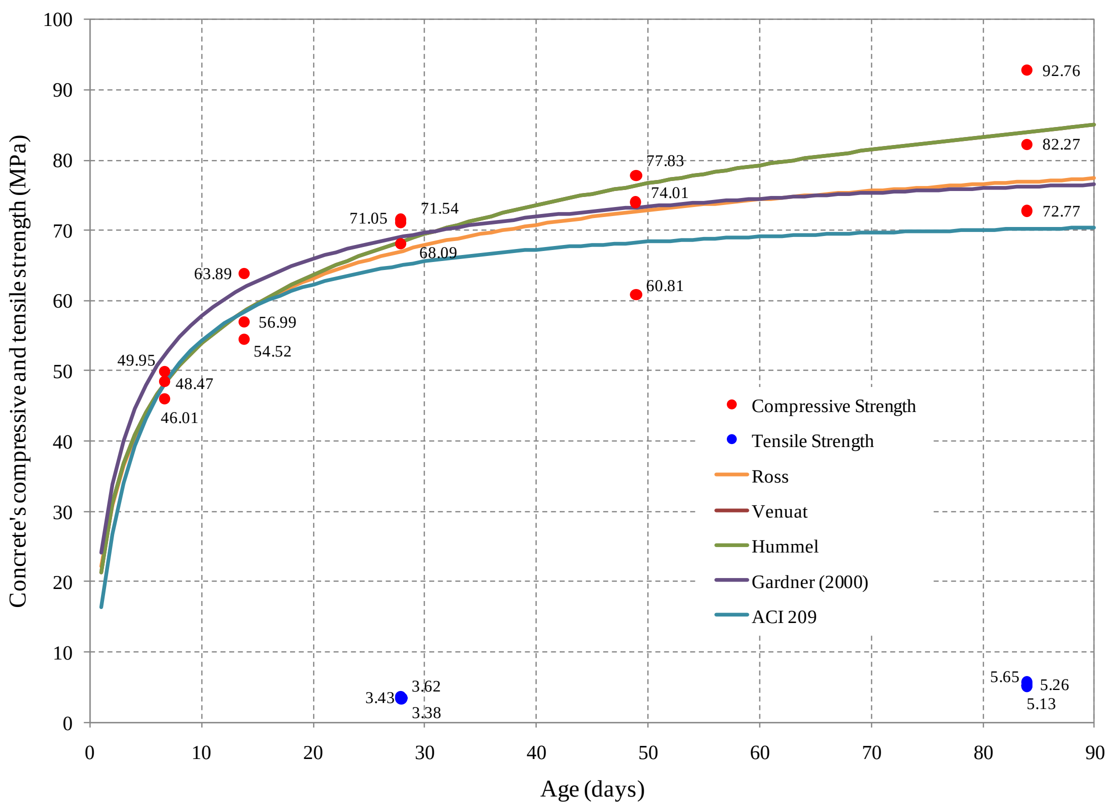

Figure A.13: Concrete's compressive and tensile strength development over time

B APPENDIX B: CONCRETE SPLITTING TENSILE STRENGTH TEST RESULTS

The splitting tensile strength of concrete was experimentally determinate by doing splitting tensile strength tests at 28 and 84 days. Three samples were tested at each date.

B.1 Digital Image Correlation Analysis

Digital image correlation analysis (Section 3.4.6.4) was used on the samples tested at 84 days. This allowed to determinate the horizontal tensile stress at which tensile failure firs occurred.

B.1.1 HPSCC_84d_st1

In this test, the splitting tensile strength was 7.16 MPa. Image correlation analysis determined that there was a significant relative displacement between patches, across the vertical diameter, when 5.13 MPa was the horizontal tensile stress at the centre of the cylinder (maximum horizontal tensile stress). The results from the digital image correlation analysis are shown in Figure B.1, in which each curve represents a moment in time in which the maximum horizontal tensile stress (at the centre of the cylinder) is as labelled in the legend. The first curve labelled as 5.01 MPa presents no significant relative displacement between any of the patches.

The maximum horizontal tensile stress versus the crack opening across the vertical diameter is plot, as shown in Figure B.2. And a zoom-in of the crack opening after the crack first initiate is showed in Figure B.3.

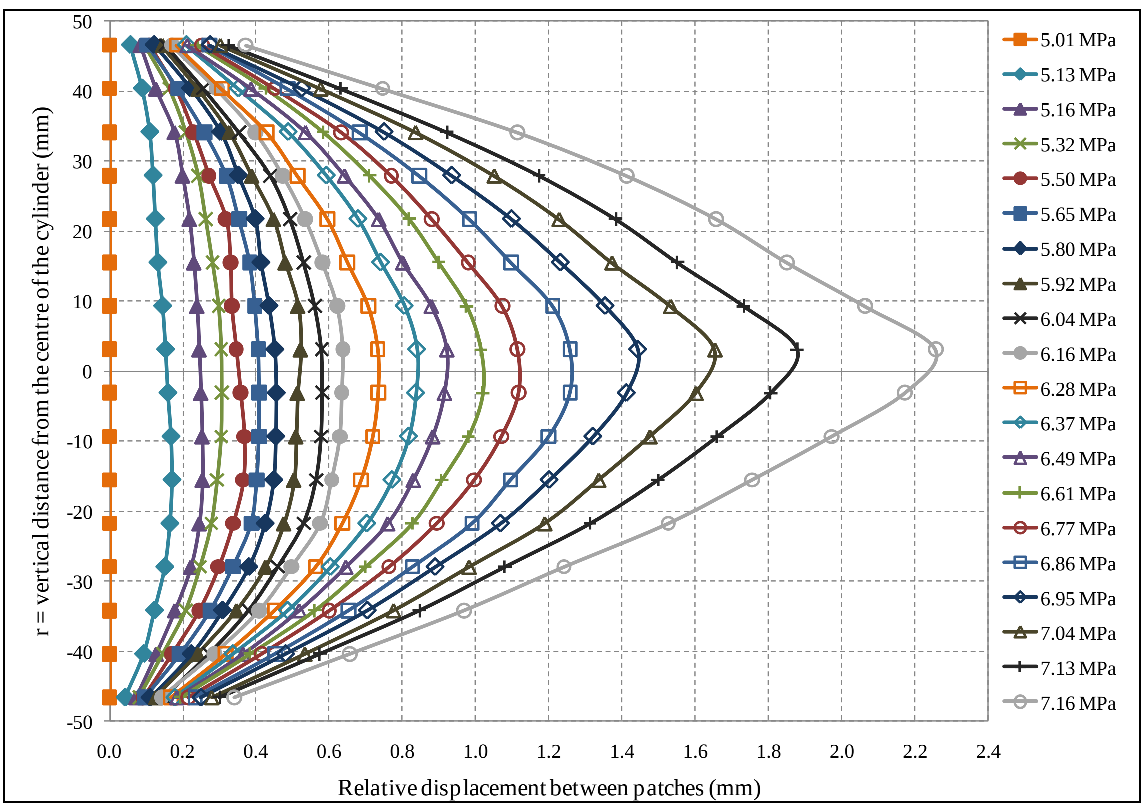

Figure B.1: Relative displacement between patches in HPSCC_84d_st1, for different horizontal tensile stresses at the centre of the cylinder.

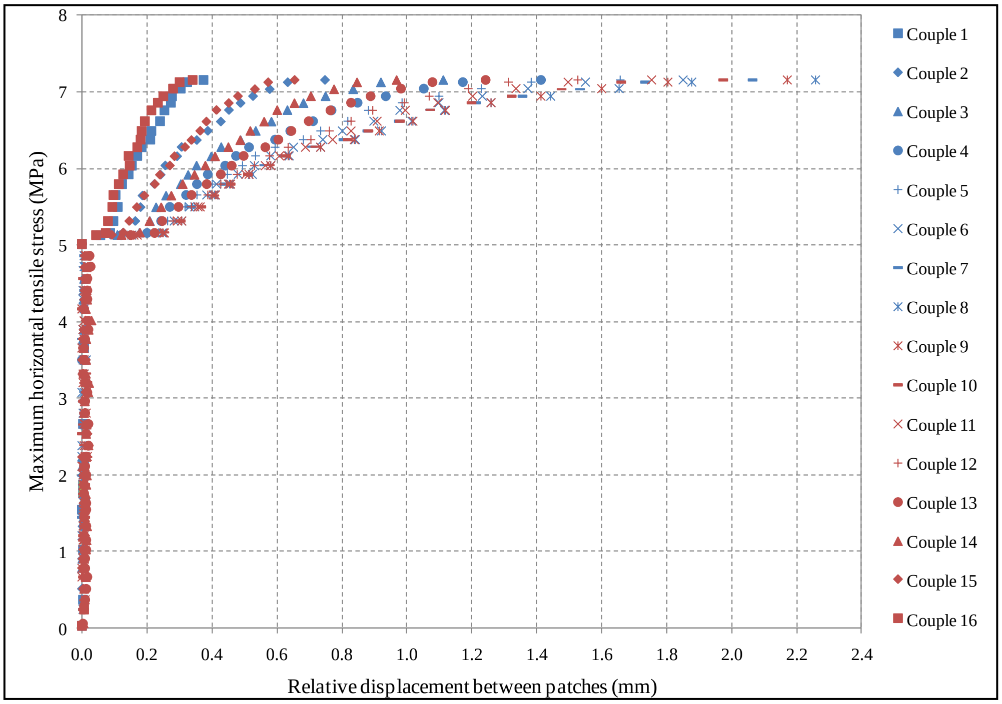

Figure B.2: Relative displacement between patches in HPSCC_84d_st1, for different couple of patches

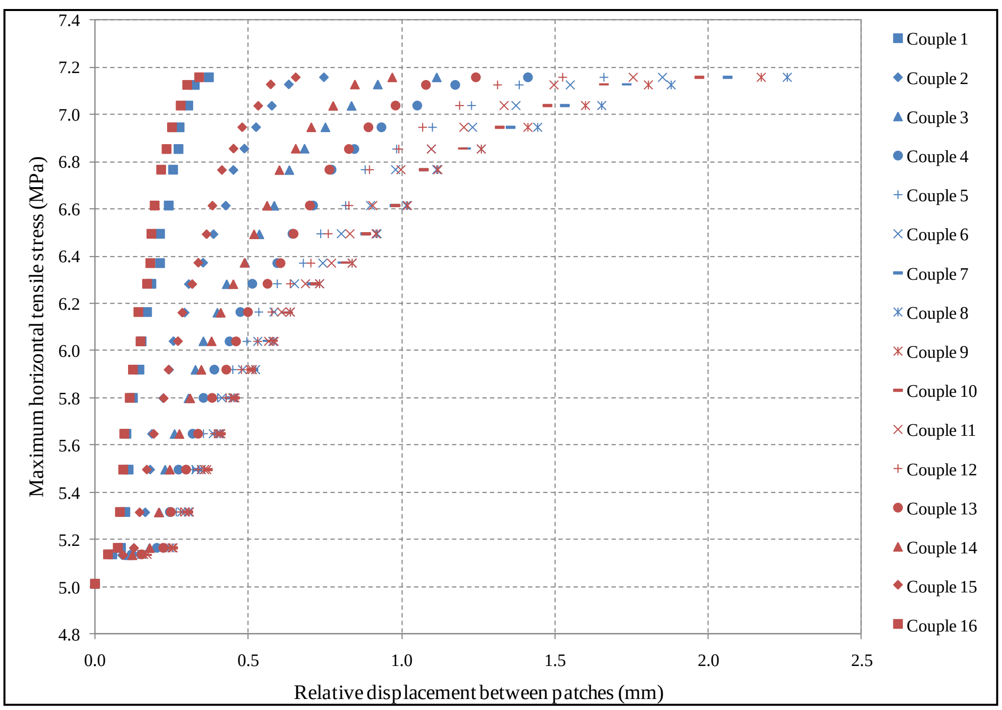

Figure B.3: Zoom-in of the relative displacement between patches in HPSCC_84d_st1 after first vertical crack was first generated, for different couple of patches

B.1.2 HPSCC_84d_st2

In this test, the splitting tensile strength was 6.83 MPa. Image correlation analysis determined that there was a significant relative displacement between patches, across the vertical diameter, when 5.59 MPa was the horizontal tensile stress at the centre of the cylinder (maximum horizontal tensile stress). The results from the digital image correlation analysis are shown in Figure B.4, in which each curve represents a moment in time in which the maximum horizontal tensile stress (at the centre of the cylinder) is as labelled in the legend. The first curve labelled as 5.56 MPa presents no significant relative displacement between any of the patches.

The maximum horizontal tensile stress versus the crack opening across the vertical diameter is plot, as shown in Figure B.5. And a zoom-in of the crack opening after the crack first initiate is showed in Figure B.6.

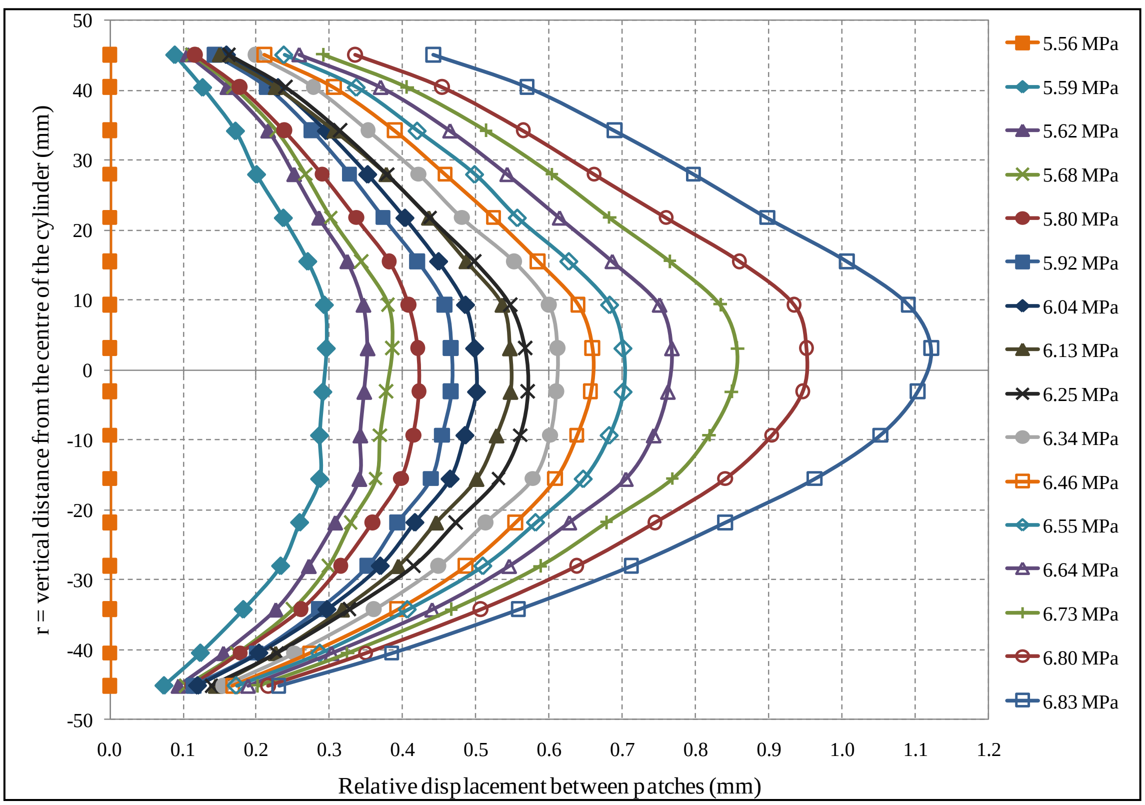

Figure B.4: Relative displacement between patches in HPSCC_84d_st2, for different horizontal tensile stresses at the centre of the cylinder.

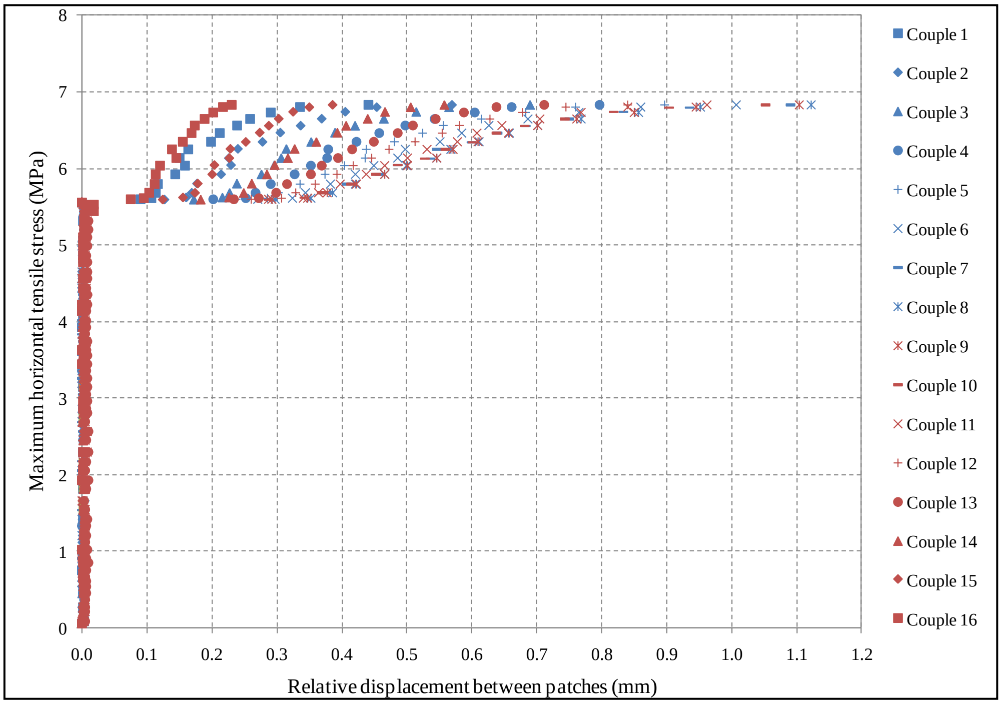

Figure B.5: Relative displacement between patches in HPSCC_84d_st2, for different couple of patches

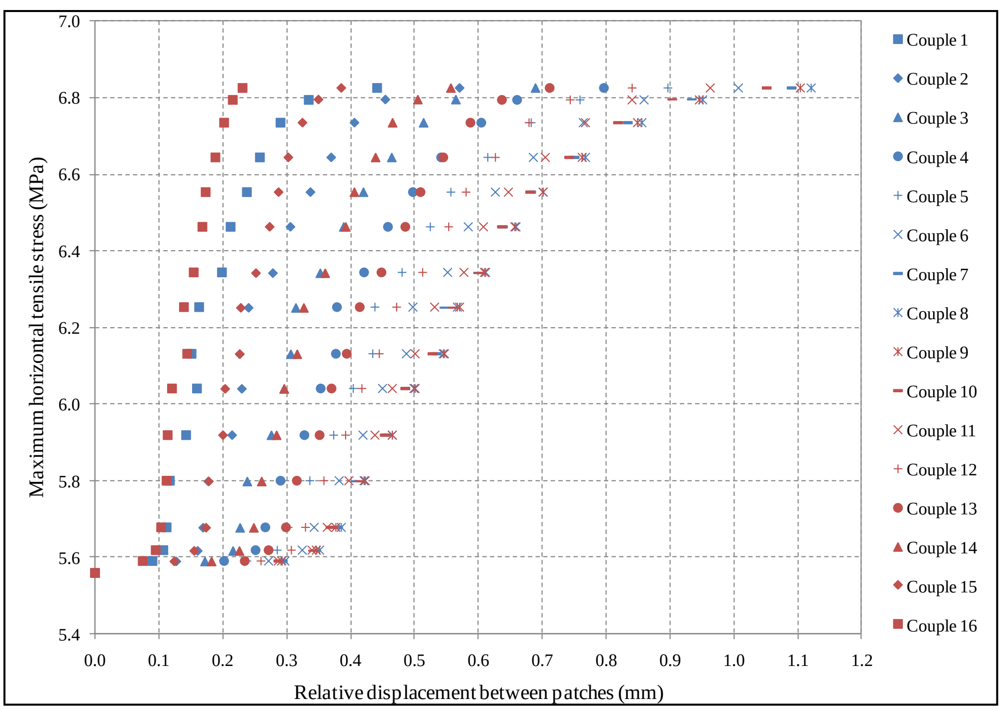

Figure B.6: Zoom-in of the relative displacement between patches in HPSCC_84d_st2 after first vertical crack was first generated, for different couple of patches

B.1.3 HPSCC_84d_st3

In this test, the splitting tensile strength was 6.40 MPa. Image correlation analysis determined that there was a significant relative displacement between patches, across the vertical diameter, when 5.17 MPa was the horizontal tensile stress at the centre of the cylinder (maximum horizontal tensile stress). The results from the digital image correlation analysis are shown in Figure B.7, in which each curve represents a moment in time in which the maximum horizontal tensile stress (at the centre of the cylinder) is as labelled in the legend. The first curve labelled as 5.15 MPa presents no significant relative displacement between any of the patches.

The maximum horizontal tensile stress versus the crack opening across the vertical diameter is plot, as shown in Figure B.8. And a zoom-in of the crack opening after the crack first initiate is showed in Figure B.9.

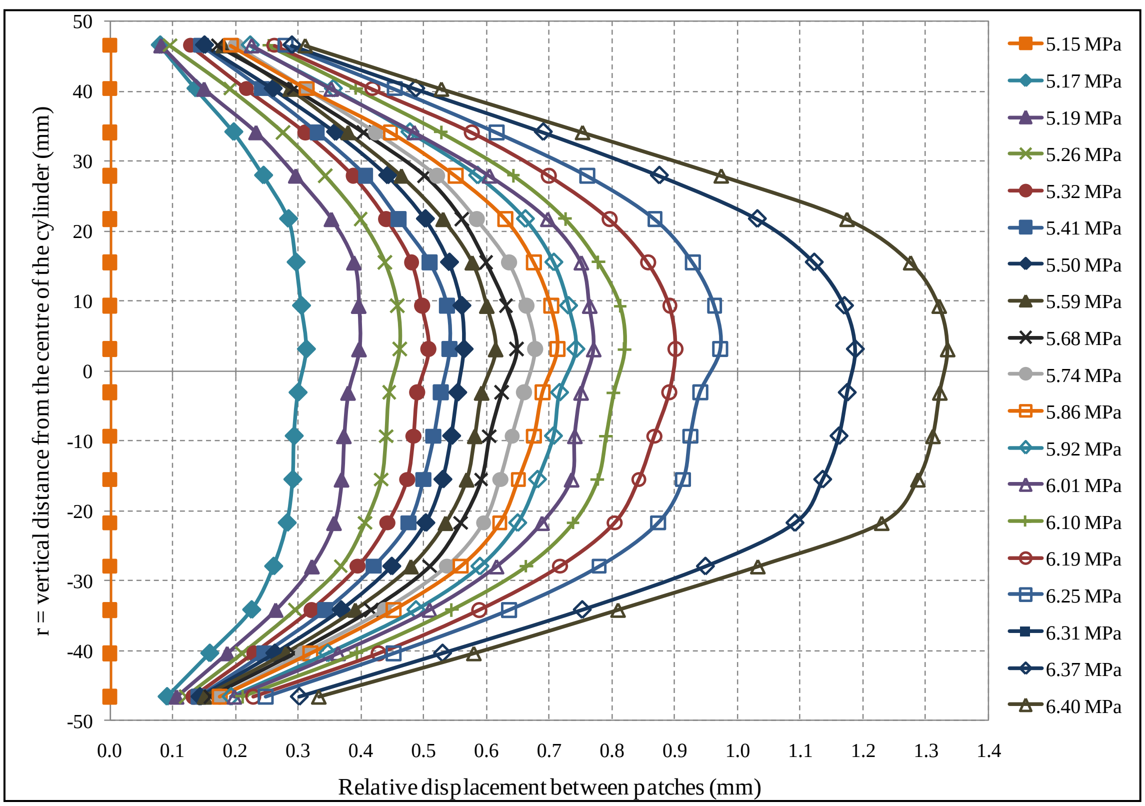

Figure B.7: Relative displacement between patches in HPSCC_84d_st3, for different horizontal tensile stresses at the centre of the cylinder.

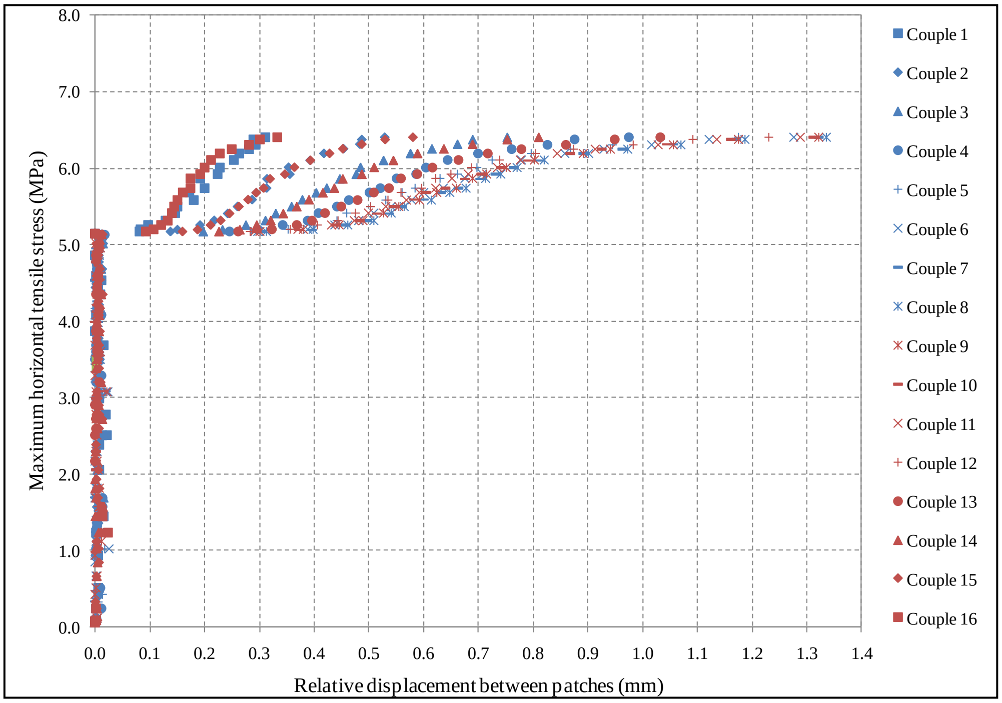

Figure B.8: Relative displacement between patches in HPSCC_84d_st3, for different couple of patches

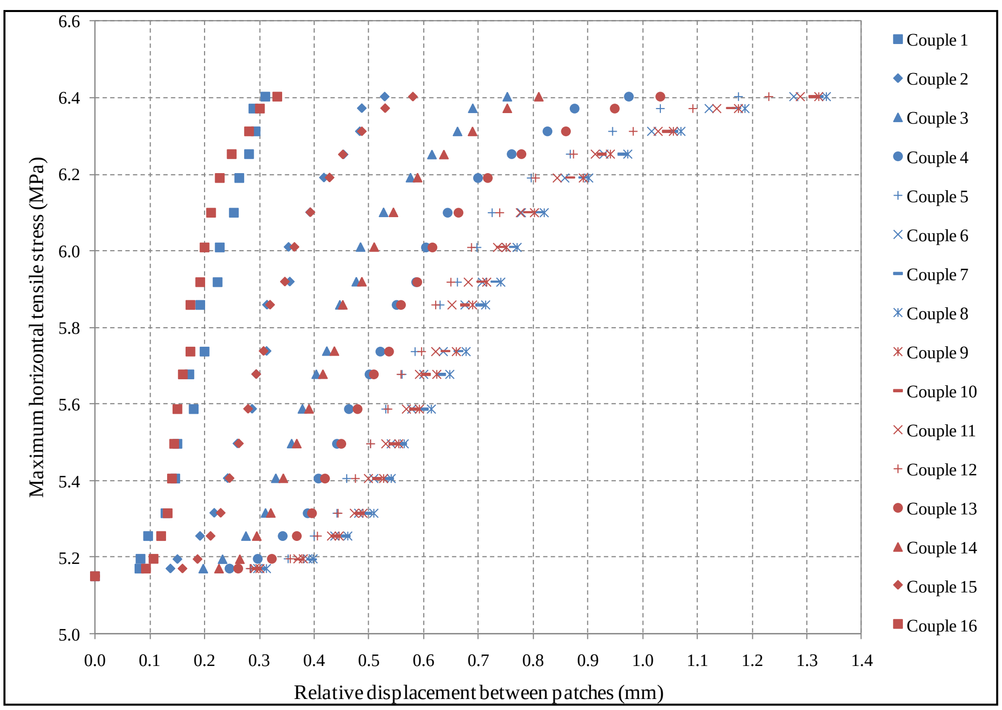

Figure B.9: Zoom-in of the relative displacement between patches in HPSCC_84d_st3 after first vertical crack was first generated, for different couple of patches

B.2 Summary

Digital image correlation analysis was performed only in the 84 days samples. This allowed to determinate a correlation between the splitting tensile strength and the stress at which the crack first initiated, as shown in Table B.1.

Table B.1: Test results of the concrete splitting tensile strength tests

Test label	f_{st} (MPa)	Average f_{st} at "t" days (MPa)	Standard Deviation (MPa)	f_{st_crack} (MPa)	Average f_{st_crack} at "t" days (MPa)	Standard Deviation (MPa)	(f_{st_crack}/f_{st}) *100
HPSCC_28d_st1	4.59			3.59 *			-
HPSCC_28d_st2	4.35	4.41	0.16	3.40 *	3.44 *	0.12 *	-
HPSCC_28d_st3	4.29			3.35 *			-
HPSCC_84d_st1	7.16			5.13			72%
HPSCC_84d_st2	6.83	6.80	0.38	5.59	5.30	0.25	82%
HPSCC_84d_st3	6.40			5.17			81%

* Calculated from the average (f_{st_crack}/f_{st})*100 of the tests done at 84 days.

The average (f_{st_crack} / f_{st})*100 value calculated from the tests executed at 84 days is 79%. As stated in Section 3.4.6.5, the stress at which the crack first initiates is the actual tensile strength of concrete, comparable with the strength obtained by a direct tensile strength test. The correlation determined by Ghaffar et al. (2005) implies that the direct tensile strength is 66% of the splitting tensile strength. Close to the correlation found by this study which states that the stress at which the crack first initiates is 79% of the splitting tensile strength.

For the reasons above, the input tensile strength of concrete used in the finite element models developed in Section 5.5, is 3.48 MPa at 28 days and 5.35 MPa at 84 days.

Past studies have determinate correlations between the splitting tensile strength and the compressive strength for fibre reinforced polypropylene concretes (Choi & Yuan, 2004) and high strength concretes (Zain et al., 2002). These correlations validate the strengths determinate by the splitting tensile strength tests executed at 28 and 84 days.

Table B.2: Concrete splitting tensile strength test validated by correlation with compressive strength

Test label	f_c' (MPa)	Average f_{st} at "t" days (MPa)	(Choi, 2004) f_{st_Choi} (MPa)	Average f_{st_Choi} at "t" days (MPa)	f_{st_Choi} / f_{st} (MPa)	(Zain, 2002) f_{st_Zain} (MPa)	Average f_{st_Zain} at "t" days (MPa)	f_{st_Zain} / f_{st} (MPa)
HPSCC_28d_c1	71.54		4.65			4.99		
HPSCC_28d_c2	71.05	4.41	4.64	4.61	1.05	4.97	4.94	1.12
HPSCC_28d_c3	68.09		4.54			4.87		
HPSCC_84d_c1	72.77		4.69			5.26		
HPSCC_84d_c2	92.76	6.80	5.30	4.99	0.73	5.94	5.60	0.82
HPSCC_84d_c3	82.27		4.99			5.59		

C APPENDIX C: CONCRETE THERMAL CONDUTIVITY TEST RESULTS

This test was executed as a first approach to determinate the thermal conductivity of the concrete design for this study. As explained in Section 3.3.9, the C-Matic machine measures the thermal conductivity of materials at a steady state, without considering any of the transient phenomenon that occur as concrete is heated up. Such transient phenomenons are vapour pressure of capillarity and gel water, decomposition of cement hydration products, collapse of filling aggregate, and melting of the PP fibres.

Any measurement of the thermal conductivity is not valid as the temperature is increasing the sample's temperature, and thermal conductivity can only be measured once a steady state, for which the machine was previously calibrated (76, 114 and 155°C), is reached.

Samples were tested at 76, 114 and 155°C, two at each temperature. The test's results are shown in Figure C.1.

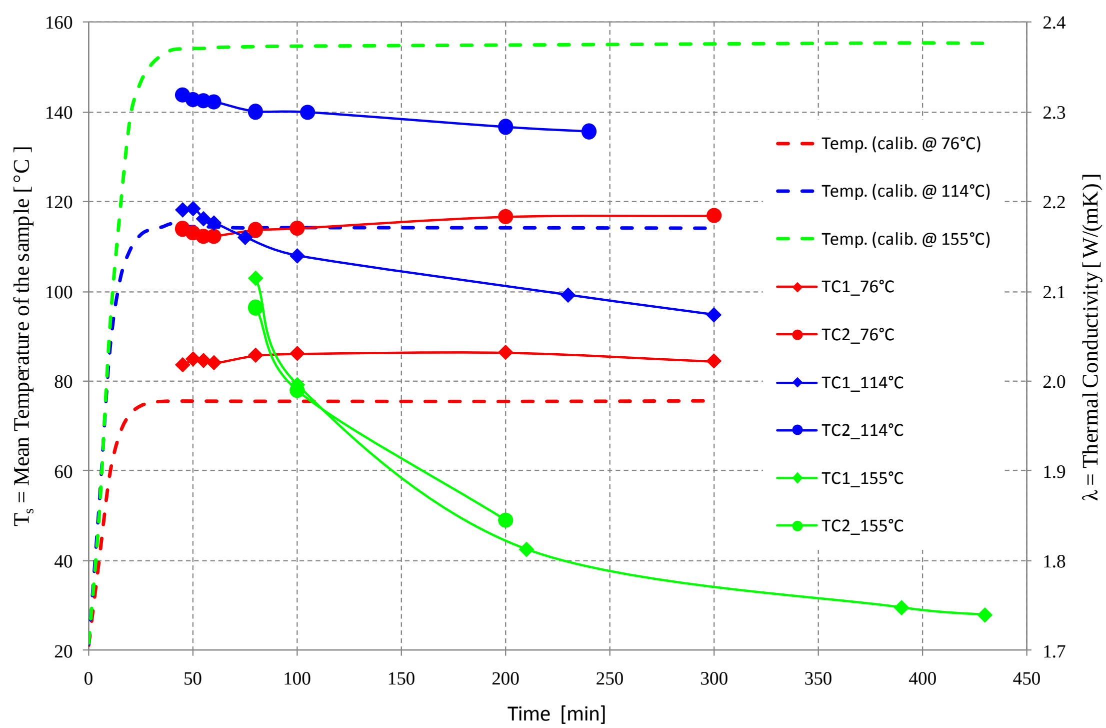

Figure C.1: Concrete thermal conductivity test results

The tests results experience a relatively high standard deviation for the samples tested at 76 and 114°C, but showed a clear trend as the sample's temperature was left in steady over long periods of time (300 minutes).

For the samples tested at 155°C a big drop of the thermal conductivity value was recorded soon after the sample reached the steady state (50 minutes). Thermal conductivity tended to a value after almost 400 minutes of steady temperature. This phenomenon could be the result of the polypropylene fibres include in the concrete mixture, which have a melting point of 160-170°C. It should be recalled that the sample's mean temperature is kept steady at 155°C, but the lower surface temperature records 180°C temperature once the steady state is reached, as explained in Section 3.3.9.

Table C.1: Concrete thermal conductivity test results

Test	**Sample temperature at λ determination (°C)**	**λ trend (W/mK)**	**Average λ (W/mK)**	**Standard Deviation (W/mK)**
T1 @ 76°C **T2 @ 76°C**	76	2.022 2.185	2.10	0.11
T1 @ 114°C **T2 @ 114°C**	114	2.074 2.279	2.18	0.14
T1 @ 155°C **T2 @ 155°C**	155	1.739 1.845 *	-	-

*Test finished before λ tended to any value (200 minutes).

D APPENDIX D: STEEL TENSILE STRENGTH TEST RESULTS

This test was executed to measure the tensile strength capacity of the steel prestressing wires used in this study. Slip of the sample occurred at the Instron's wedge grips, for this reason neither strain nor modulus of elasticity could be determinate from these tests, even though ultimate tensile strength and yield strength were calculated. The results from these tests are display in stress versus crosshead displacement plot, showed in Figure D.1.

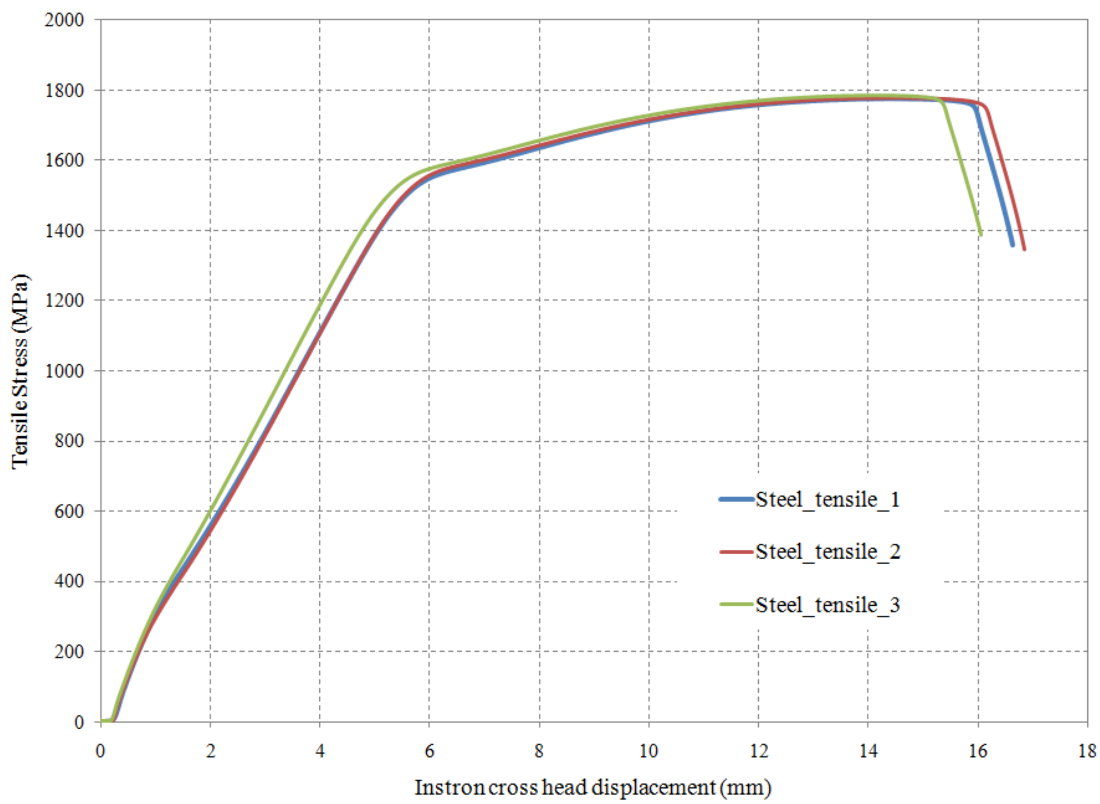

Figure D.1: Steel tensile strength test's results

Every test showed a similar development of tensile stress, with a yield strength around 1500-1600 MPa and an average ultimate tensile strength of 1780 MPa (see Table D.1).

Table D.1: Ultimate strengths determined by steel tensile strength tests

Test	Ultimate Strength (MPa)
Steel_tensile_1	1777
Steel_tensile_2	1780
Steel_tensile_3	1784

The data from this test works in order to validate the specifications indicated by the manufacturer (NEDRI Spanstaal BV), shown in Table D.2.

Table D.2: Mechanical properties of steel prestressing wire (NEDRI Spanstaal BV)

Mechanical Properties of Steel Wire (NEDRI Spanstaal BV)	
Elastic Modulus	210 GPa
Yield stress (0.2% offset)	1592 MPa
Yield strain (0.2% offset)	0.76%
Ultimate stress	1770 MPa
Ultimate strain	5.40%